

Superconducting X-ray Spectrometers for High-Resolution Synchrotron XAS

By

MATTHEW HOLLIS CARPENTER
B.A. (University of California, Berkeley) 2005
M.S. (University of California, Davis) 2010

DISSERTATION

Submitted in partial satisfaction of the requirements for the degree of

DOCTOR OF PHILOSOPHY

in

Applied Science - Engineering

in the

OFFICE OF GRADUATE STUDIES

of the

UNIVERSITY OF CALIFORNIA

DAVIS

Approved:

Chair Stephen P. Cramer

Niels Grønbech-Jensen

C. William McCurdy

Committee in Charge

2015

UMI Number: 3706565

All rights reserved

INFORMATION TO ALL USERS

The quality of this reproduction is dependent upon the quality of the copy submitted.

In the unlikely event that the author did not send a complete manuscript and there are missing pages, these will be noted. Also, if material had to be removed, a note will indicate the deletion.



UMI 3706565

Published by ProQuest LLC (2015). Copyright in the Dissertation held by the Author.

Microform Edition © ProQuest LLC.

All rights reserved. This work is protected against unauthorized copying under Title 17, United States Code



ProQuest LLC.
789 East Eisenhower Parkway
P.O. Box 1346
Ann Arbor, MI 48106 - 1346

Copyright © 2015 by
Matthew Hollis Carpenter
All rights reserved.

*To Lauren, my best coach and fan;
and my parents, Gary and Mary Ann.*

CONTENTS

List of Figures	v
List of Tables	viii
Abstract	ix
Acknowledgments	x
1 Introduction	1
1.1 Energy Levels in Atoms and Molecules	2
1.1.1 Sample Applications	5
1.2 X-ray Absorption Spectroscopy	7
1.2.1 XANES vs. EXAFS, Soft vs. Hard X-rays	8
1.2.2 Synchrotron Radiation	11
1.2.3 XAS Techniques: Transmission vs. EY vs. FY	13
1.3 Motivation for Superconducting X-ray Detectors for PFY-XAS	16
1.3.1 Increased Sensitivity	17
1.3.2 Issue: Non-proportionality of PFY to XAS	18
References	21
2 Superconducting Tunnel Junctions	24
2.1 Superconductivity	24
2.1.1 Tunnel Junctions	29
2.2 SIS Tunnel Junctions as Photon Detectors	33
2.2.1 Mechanism	33
2.2.2 Resolution	35
2.2.3 Operation considerations	38
2.3 Device Fabrication	41
References	47
3 Cryostat Design	50
3.1 Cryogenic Development	50
3.1.1 Overall Structure	52
3.1.2 ADR	57
3.1.3 Cold Finger	63
3.2 Electronics	70
3.2.1 LLNL Preamplifiers	70
3.2.2 XIA Preamplifiers	72
References	76
4 Spectrometer Performance	78
4.1 STJ Device Characterization	78
4.2 Spectral Response	84
4.2.1 Count Rate	87
4.2.2 Homogeneity	89
4.3 Dry ADR Performance	93
4.3.1 IR-Blocking Windows	96
4.3.2 Detector Magnets	101

4.4	XAS Setup	105
	References	111
5	Application	112
5.1	Sample Preparation	113
5.1.1	Sample Characterization	117
5.2	Experimental Setup	121
5.3	Metal-acac XAS	126
5.3.1	Ni(acac) ₂	126
5.3.2	Mn(acac) ₃	132
5.3.3	Cr(acac) ₃	137
5.4	Metal-acac XAS Modeling	140
	References	148
6	Summary and Outlook	150
6.1	Summary of Results	150
6.1.1	STJ Detector	150
6.1.2	Scientific Results	151
6.2	Outlook	153
6.2.1	Future STJ Detector Improvements	153
6.2.2	Scientific Outlook	156
	References	158
	List of Abbreviations	159

LIST OF FIGURES

1.1	Atomic Energy Level Terms	3
1.2	CFT Splitting	4
1.3	d^8 T-S Diagram	6
1.4	NiFe Hydrogenase Structure	7
1.5	Broad XAS	8
1.6	XAS Terms	9
1.7	L-edge XANES	10
1.8	Synchrotron Light Sources	11
1.9	XAS Beam Line Schematic	14
1.10	XAS Mechanisms	15
1.11	STJ vs. SSD Resolution Comparison	19
2.1	Transition to Superconducting State	28
2.2	Gap Parameter vs. Temperature	29
2.3	Tunneling in an SIS Junction	30
2.4	SIS I-V vs. Temperature	32
2.5	STJ Operating Principle	34
2.6	Critical Current vs. Applied Field	41
2.7	Device Cross-Section	42
2.8	STJ Absorption by Layer	43
2.9	STJ Fabrication Die	45
2.10	36-Pixel Array Chip	46
3.1	Cryostat Overview	53
3.2	PT-407 Capacity Curve	54
3.3	Cryostat Internals	55
3.4	FAA Entropy vs. Temperature in Magnetic Fields	59
3.5	ADR Suspension Puck	60
3.6	ADR Cutaway Views	62
3.7	Cold Finger	65
3.8	Blackbody Emitted Power at Room T	66
3.9	Detector Rod Suspension	68
3.10	36-Pixel Array Installed	69
3.11	Preamplifier Principle	71
3.12	LLNL Preamp Circuit Diagram	73
3.13	STAR Preamp Housing	74
3.14	XIA Preamplifier Schematic	74
3.15	XIA 32-Channel Digital Preamplifier	75
4.1	LLNL Test Cryostat	79
4.2	Typical STJ I-V Curve	80
4.3	Pulse Structure	81
4.4	Rise Time Discrimination	82
4.5	Bottom vs. Top Electrode	83
4.6	Detector Response vs. Bias	84

4.7	Resolution vs. Detector Size	86
4.8	Resolution vs. Energy: Direct Illumination	87
4.9	Resolution vs. Energy	88
4.10	Resolution vs. Count Rate	89
4.11	Multiple Pixel X-ray Emission Spectrum, XIA Electronics	91
4.12	Single Pixel X-ray Emission Spectrum, XIA Electronics	92
4.13	Cryostat Cool-down from Room Temperature	94
4.14	ADR Cool-down Performance II	95
4.15	ADR Temperature Regulation	96
4.16	IR Filter Transmission 1	97
4.17	IR Filter Transmission 2	98
4.18	IR Filter Power Spectrum	99
4.19	X-ray Absorbance of IR Filters	100
4.20	X-ray Transmission of IR Filter Stack	100
4.21	STJ Magnet Field	102
4.22	STJ Magnet T_C	103
4.23	I-V Curves vs. Applied Field	104
4.24	I-V Noise vs. Applied Field	105
4.25	Detector Installed on Beam Line	107
4.26	XIA Software	108
4.27	36-pixel Array I-V Curves	109
4.28	36-pixel Spectrometer XES	110
5.1	Metal-acac Structure	115
5.2	Sample X-ray Attenuation	115
5.3	X-ray Transmission Sample Fabrication	116
5.4	Photoresist Thickness Measurement	118
5.5	Ni(acac) ₂ UV-Vis	119
5.6	Mn(acac) ₃ UV-Vis	120
5.7	UV-Vis of metal-acac samples in photoresist	121
5.8	X-ray Transmission Set-up	122
5.9	X-ray Transmission Samples	123
5.10	STJ Detector installed for PFY-XAS	124
5.11	PFY Sample Geometry	125
5.12	Transmission XAS Analysis Method	127
5.13	Ni(acac) ₂ XES	128
5.14	Ni(acac) ₂ STJ XAS	129
5.15	Ni(acac) ₂ STJ XAS L3/L2 Regions	130
5.16	Ni(acac) ₂ XES: STJ vs SDD	131
5.17	Transmission XAS Analysis Method	132
5.18	Mn(acac) ₃ TEY	133
5.19	Mn(acac) ₃ XES	135
5.20	Mn(acac) ₃ STJ XAS	136
5.21	Mn(acac) ₃ STJ XAS L3/L2 Regions	137
5.22	Mn(acac) ₃ XES: STJ vs SDD	138
5.23	Cr(acac) ₃ XES: STJ vs SDD	139
5.24	Cr(acac) ₃ PFY	140

5.25	Ni(acac) ₂ XAS Model	141
5.26	Ni RIXS Calculation	142
5.27	Ni(II) XAS vs. PFY Theory	143
5.28	Mn(acac) ₃ Transmission	145
5.29	Mn RIXS Calculation	146
5.30	Mn XAS vs. PFY Theory	147
6.1	IR Filter Comparison	154
6.2	STJ Sensitivity Improvements	155
6.3	STJ Detector	157

LIST OF TABLES

1.1	Measurement Methods	16
1.2	Detector Comparison	17
2.1	Superconductor Properties	38
3.1	Estimated Cryostat Main Stage Heat Loads	57
3.2	Estimated Cold Finger Heat Loads	70
5.1	AZ-1500 Series Film Thickness	114

ABSTRACT

Superconducting X-ray Spectrometers for High-Resolution Synchrotron XAS

X-ray absorption spectroscopy (XAS) is a powerful technique to determine the structure and function of molecules. It provides element-specific information on geometry, chemical bonding, oxidation state, and spin state, and its applications range from biology to material science. For dilute samples, XAS is measured by partial fluorescence yield (PFY), where the intensity of a weak fluorescence line is recorded as a measure of absorption as the energy of the incident x-ray beam is scanned across an absorption edge of the element of interest. PFY increases the sensitivity for XAS if an x-ray detector is used that can efficiently separate the small fluorescence signal of interest from the x-ray background due to other elements in the sample.

This dissertation describes the development of a high-resolution x-ray detector based on arrays of superconducting tunnel junctions (STJs). It is cooled to its operating temperature below 0.3 K with a liquid-cryogen-free adiabatic demagnetization refrigerator (ADR) cryostat, and offers more than an order of magnitude improvement in energy resolution over conventional Ge or Si-based solid state detectors (SSDs). For operation in XAS experiments at a synchrotron, the STJ detector array is held at the end of a cold finger that can be inserted into a ultra-high vacuum (UHV) endstation. This dissertation describes the design and performance of the STJ x-ray spectrometer, and demonstrates its use in PFY-XAS experiments in metallo-organic compounds at the Advanced Light Source (ALS) synchrotron.

ACKNOWLEDGMENTS

My graduate career has been interesting to say the least. I certainly would not have made it through without some very personal help and support from my colleagues. Between the struggle for funding, dead ends, and inevitable technical challenges, I relied strongly on the guidance of these people.

Stephan Friedrich has been absolutely key to my success. Conversation with him during my first visit to the ALS captured my interest in low-temperature detectors. From there he was a superb help in finishing my MS thesis, and worked tirelessly to develop not just my thesis project, but also orchestrate the funding and collaboration which brought disparate parties together. Along the way, he has been an even better friend and support for my personal struggles, and without his help I would definitely not have made it to the end.

Simon George taught me the most of what I know about XAS. He's a skilled spectroscopist and even better friend. Coming from a physics background, I learned the most from him about biochemistry and lab practices.

Robin Cantor has performed a very different role from the typical grad student mentor. His position as the licensee of the STJ technology from LLNL and recipient of DOE-SBIR grants is a bridge between private industry and academia. His entrepreneurship has breathed new life into both the future of STJs and my dissertation work. As a businessman he had a lot to lose by taking me on and funding me through the end of my project, but we both came out much better for it. Because of his experience, attention, and dedication of resources to the project, we have been able to produce some great science from a new commercially-viable and consumer-friendly product.

Last certainly not least, my advisor Steve Cramer has given me an excellent opportunity to pursue my passion for design and development of experimental hardware, and without the flexible nature of the group at the ALS I would not have learned nearly as much nor found my passion for applications. His long and impactful career in XAS fostered an excellent creative environment to develop techniques. There have been several occasions where one look and suggestion from him was all it took to get past a sticking point in an experiment. This work builds on the foundations he laid first in Fe-S cluster XAS and later in soft XAS of transition metal L-edges. I am deeply grateful to him for his support and patience through my graduate career.

Chapter 1

Introduction

X-ray absorption spectroscopy (XAS), *i.e.* the measurement of the x-ray absorption of a sample as a function of x-ray energy, is an experimental technique that can give element-specific information about the electronic structure and chemical state of atoms and molecules. It is widely used to understand chemical properties of samples in diverse fields from solid state physics and environmental science to inorganic chemistry and biochemistry. Since x-ray absorption is followed by a relaxation to the ground state that produces either an Auger electron or a fluorescence x-ray, there are three methods for measuring an x-ray absorption spectrum (XAS)¹: directly by transmission, or indirectly by measuring electron yield (EY) or fluorescence yield (FY) that are assumed to be proportional to the absorption signal. Partial fluorescence yield (PFY), where just the fluorescence from the element of interest is recorded as a measure of the absorption, can improve the sensitivity for XAS on dilute samples, provided that an energy-resolving detector is used that can separate the weak fluorescence signal from the x-ray background due to the other elements in the sample. Si or Ge solid state detectors (SSDs) are therefore widely used for PFY-x-ray absorption spectroscopy (XAS) on dilute samples.

However, for many samples, especially at low energy, the energy resolution of semiconductor SSDs is not sufficient to separate the x-ray fluorescence of a given element from the x-ray background. This limits the sensitivity and restricts XAS to more concentrated samples. In addition, recent theoretical models suggest that the intensity of certain fluorescence lines may not be proportional to the absorption signal, causing the XAS to be distorted. The models suggest recording alternative (and weaker) fluorescence lines as PFY signals that are not affected by this non-proportionality. Both problems can be addressed with a detector with higher en-

¹The abbreviation XAS is used for both “x-ray absorption spectroscopy” and “x-ray absorption spectrum”

ergy resolution. This dissertation describes the development of such an x-ray detector based on arrays of superconducting tunnel junctions (STJs). The instrument is designed for PFY-XAS in applications where semiconductor SSDs lack energy resolution and grating spectrometers lack efficiency to measure weak fluorescence lines of interest. As an initial application, the STJ x-ray spectrometer is used to compare XAS of dilute organometallic model compounds based on different fluorescence lines of the same element. These experiments are designed to confirm, modify, or refute the model predictions of non-proportionality in PFY-XAS.

1.1 Energy Levels in Atoms and Molecules

A major goal of chemistry is the determination of molecular electronic structure. This encompasses specific details such as the oxidation and spin state of valence electrons, or more general descriptions involving the wave functions and energy levels of all the electrons in the molecule. The states being measured are the solutions to the Schrödinger equation for the system. While there are many theoretical approaches to modeling these states, the systems are in general so complex that precise analytical solutions are not possible. It is therefore up to the spectroscopist to provide the empirical data to constrain the models.

For single-electron atoms, electronic states are described in the most basic way by wave functions built from Legendre polynomials and spherical harmonics as solutions to the Schrödinger equation. Though the situation rapidly becomes complicated as more electrons are added, the basic naming scheme for core orbitals follows the hydrogen-like atomic orbitals, shown in the left panel of figure 1.1. Electrons fill up available empty states from the 1s level upwards according to Fermi statistics so that no two electrons have the same quantum number. The electrons lying in the outermost orbitals (or valence electrons) are the ones that interact with the atom's surroundings, as the inner (core) electrons are effectively shielded from external potentials by the outer electrons and are energetically inaccessible. While hydrogen can be solved analytically, for more complex atoms solutions quickly become unsolvable directly and require numerical approximation. Still, the results of approximations and methods such as the Hartree-Fock approximation and the variational principle can be very accurate.

The theory of chemical bonds has several paradigms that are applied based on the nature and complexity of the system. The first basic distinction is made between ionic and covalent bonds, the former involving the ionization of the bonding atoms (complete transfer of an electron from one to another), and the latter involving the complete sharing of unpaired electrons

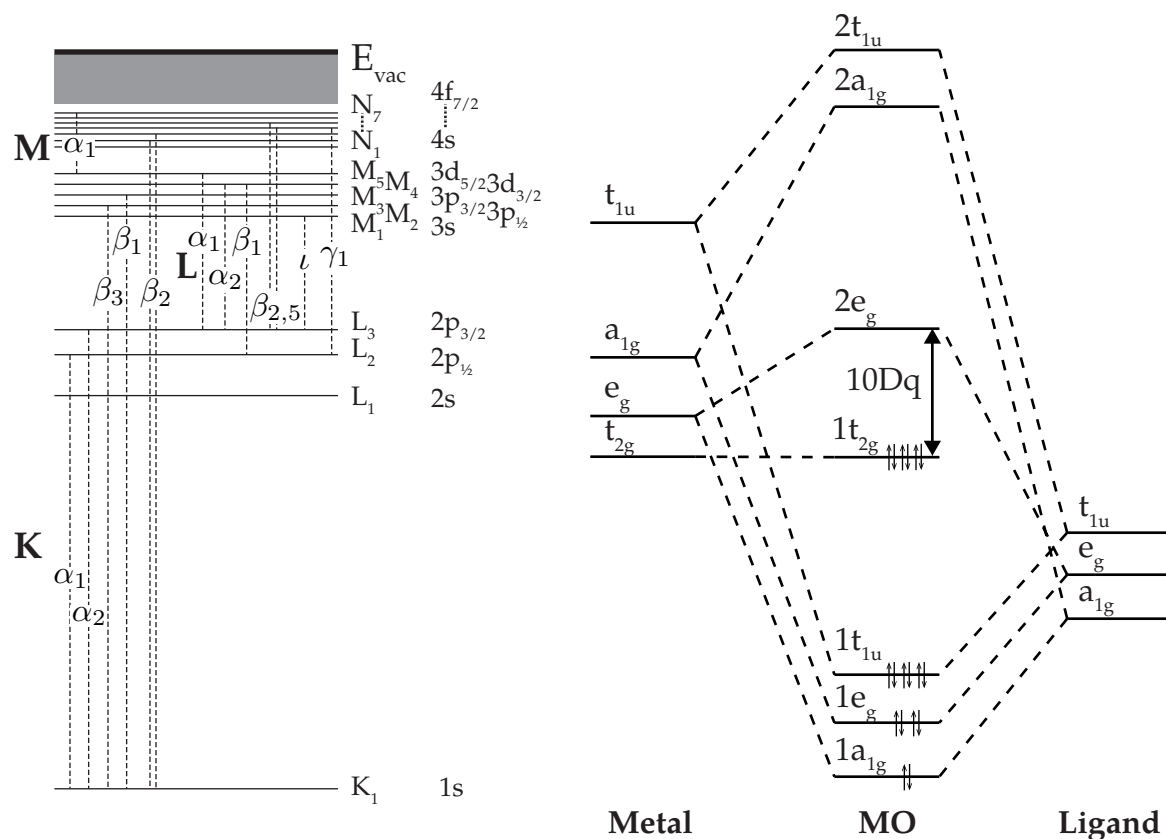


Figure 1.1: Left: Schematic illustration of the arrangement of atomic energy levels and their naming. The terms to the right of the levels name the levels (in lowercase, with spin in subscript) and their associated absorption edges (in capital letters). Common emission lines are plotted over the levels in dotted lines, with their names given in Siegbahn notation. Right: Construction of molecular orbitals out of metal valence and ligand valence orbitals, labeled with terms describing their symmetry in the octahedral point group. Inner orbitals are not shown.

to form new molecular orbitals. The ionic picture is fairly simple to model as the atoms can be considered as independent ions with perturbed atomic levels. The covalent case is more difficult to solve but again may be approximated by several methods, including linear combination of atomic orbitals (LCAO), density functional theory (DFT), or multiplets. The right panel of figure 1.1 shows a simple application of LCAO to approximating the molecular bonds between a metal and a p-block element in octahedral symmetry. The atoms bonded to the central metal atom are called ligands.

As molecules grow in size and complexity, even numerical methods cannot find precise solutions. A basic simplification is the notion of functional groups: for extremely large molecules, small sections and groups of atoms can be treated mostly independently from the rest of the molecule and merged into the whole system with some parameters. In a large protein, for ex-

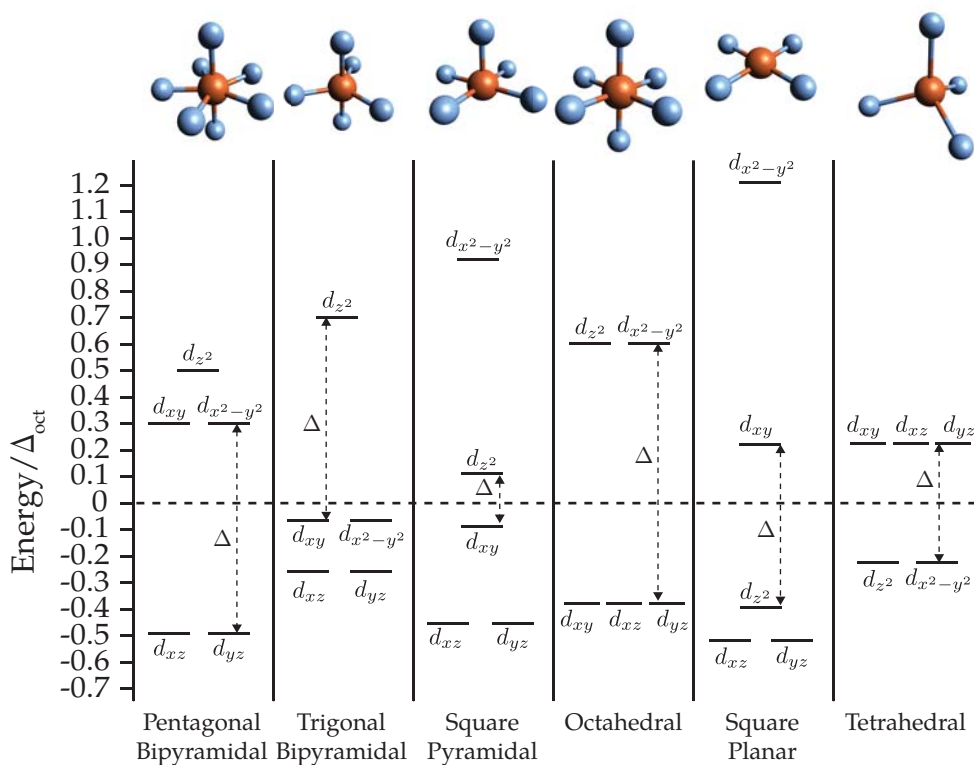


Figure 1.2: Splitting of the degeneracy in d orbitals by various geometries of crystal fields. The central metal atom is shown in orange, and ligands in light blue. The energy scale is normalized such that the splitting between octahedral levels is 1, with 0 representing the initial degenerate energy level of the d orbitals. Orbitals lying below the dotted line are stabilized, while those above are destabilized; the sum of the energy change of all orbitals is zero. The splitting strength Δ is labeled in each geometry.

ample, the metals and ligands which form the active site (together with their immediate surroundings) can be studied and modeled as a unit independent of the large framework of amino acids forming the bulk protein. Treatment of a group can be further simplified by methods which avoid the need to fully calculate the orbitals themselves, building them instead from perturbations of the base atomic case as in LCAO.

Crystal field theory (CFT) is another method to analyze highly ionic systems, such as complexes formed by the transition metals. First-row transition metal have atomic configurations that are filled through the 3s shell, so they participate in chemistry through their partially-filled 3d valence shell. In the atomic state, the five d orbitals are degenerate in energy due to the symmetric electric field of the nucleus. Introducing neighboring ligands to bond with the central metal atom lifts this degeneracy as the field is no longer spherically symmetric. Explicitly solv-

ing the Hamiltonian of this multi-atom system is computationally very expensive, but a very good approximate solution may be obtained by treating the neighboring atoms as point charges that modify the atomic d orbital energies. This is the basis for CFT. The modified orbital energies depend on the arrangement of the neighboring atoms, which may be characterized by the geometry of the ligands around the central metal atom as outlined in figure 1.2. The named structures in figure 1.2 are called coordination complexes.

The orbitals and energy levels in CFT are considered modified atomic orbitals and the bonding is considered ionic, so the electrons are fairly localized on either the metal or ligands. This allows assignment of formal oxidation states to both the metal and the ligands, with modifications of fractional oxidation state accounting for mixing of covalency. Aside from the formal oxidation state, different ligands result in different field strengths depending on their electronic structure, giving rise to a field strength parameter Dq (also called Δ). Combining the crystal field parameters with the Slater determinant from LCAO theory allows the computation and fitting of the orbital energy levels. Plotting these levels as a function of crystal field strength gives the Tanabe-Sugano diagram after the originators of this method as shown in figure 1.3.

1.1.1 Sample Applications

The first-row transition metals play important roles for many types of biological systems and inorganic coordination complexes. As these elements are filling their d shells, the bonds they form can take on a wide variety of parameters owing to the complexity of these orbitals. In the context of chemistry, these elements are usually not studied in their pure metallic form (which is more the realm of solid state physics), but instead are bound in coordination complexes or periodic structures. Other fields heavily involving the first-row transition metals are magnetic materials, dopants in solid-state materials, high-temperature superconductors (HTSs), mineralogy, catalysis, and astronomy.

Transition metals are central to the active sites in many proteins and biological systems and are essential for the continuation of life. A common example is the Fe heme present in hemoglobin and myoglobin, responsible for oxygen transport and storage for all vertebrates and many invertebrates. Aside from trying to understand biological molecules for their own sake, biomimetics is a field which bridges between biochemistry and chemical engineering. Biology offers many examples of unique and complicated compounds and enzymes which serve useful purposes. By studying and understanding the function of a biomolecule, a synthetic

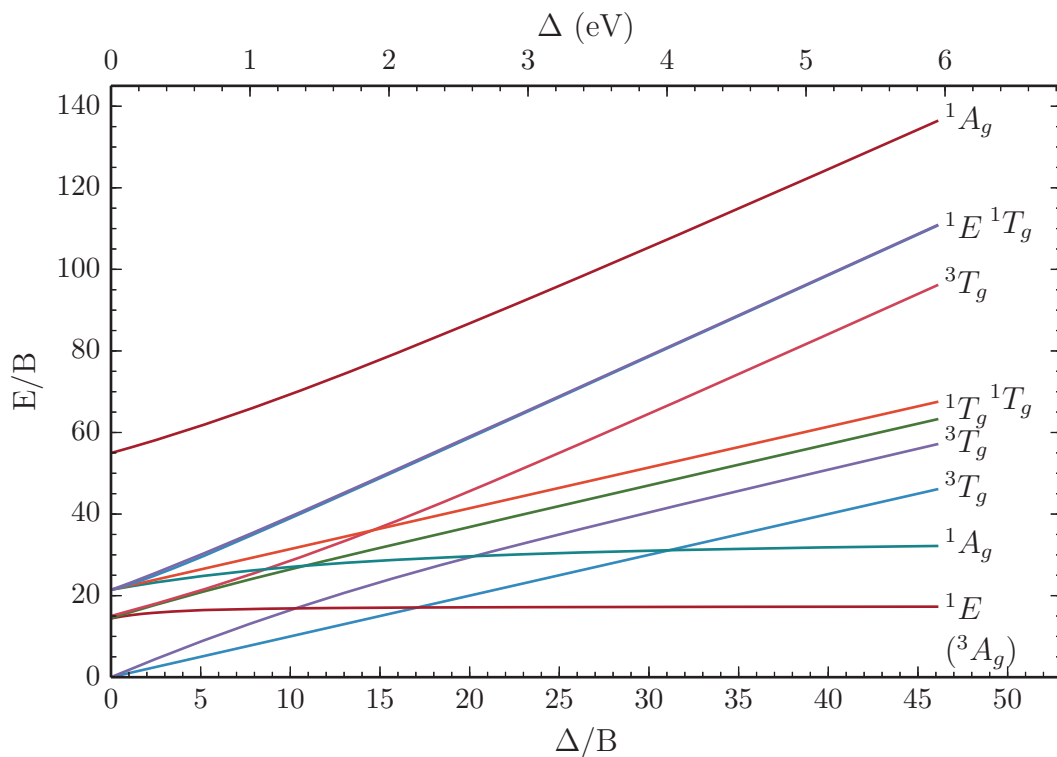


Figure 1.3: Tanabe-Sugano diagram for d⁸ transition metal. Y and lower x axes scaled by Racah parameter B, while the upper x axis is in eV for a typical value of B = 1000 cm⁻¹. States are labeled according to octahedral symmetry. The ³A_g level is at 0 across the plot [1, 2, 3].

compound might be found which adapts or mimics its features and extends them to new applications. Alternatively, biology can provide insight for ways to optimize the function of existing catalysts.

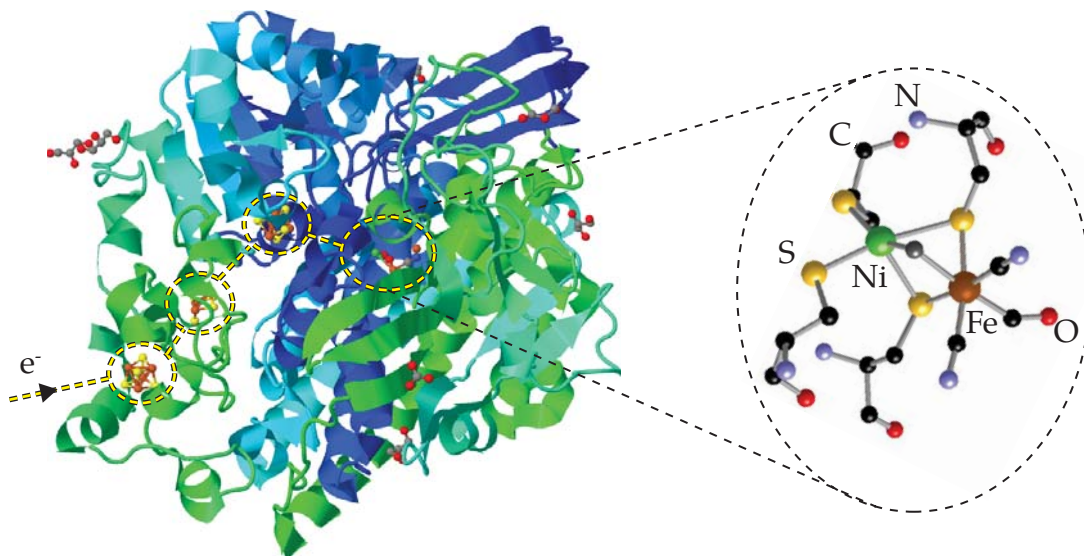


Figure 1.4: Structure of oxidized NiFe Hydrogenase from *Desulfovibrio fructosivorans*. Electrons are transported to the active site deep inside the enzyme by a series of Fe-S clusters. The path through these clusters to the active site is indicated by double black/yellow lines. An isolated view of the Ni-Fe active site is shown on the right, with sulfur ligands originating from nearby cysteines bridging between single Fe and Ni atoms. Structure generated using the Research Collaboratory for Structural Bioinformatics (RCSB) Protein Data Bank (PDB) [4], PDB ID: 1YQW [5].

1.2 X-ray Absorption Spectroscopy

XAS is the measurement of the x-ray absorption of a sample as a function of x-ray energy. It has a fairly recent history of application compared to spectroscopies of other bands, primarily because of the difficulty of measurements due to source brightness and detector limitations. While difficult, the technique has distinct advantages over other spectroscopies in certain scenarios due to its element-specificity. This makes possible the analysis of site-specific electronic structure measurements from the perspectives of the different elemental species involved.

In XAS, an absorption edge is the sudden increase in absorption coinciding with reaching the energy needed to excite or liberate a core electron from an inner shell of an atom. The series of edges labeled in figure 1.5 correspond to excitations of electrons from the levels labeled in figure 1.1. The K-edge is highest in energy and is the result of exciting a 1s electron. The one K-edge is followed by the three L-edges corresponding to the $L_{1,2,3}$ shells in figure 1.1, five M-edge, and so on. In principle there are as many edges as occupied shells to excite, but in practice the highest-lying edges can blend into the continuum and be very weak compared to other processes in the same energy band.

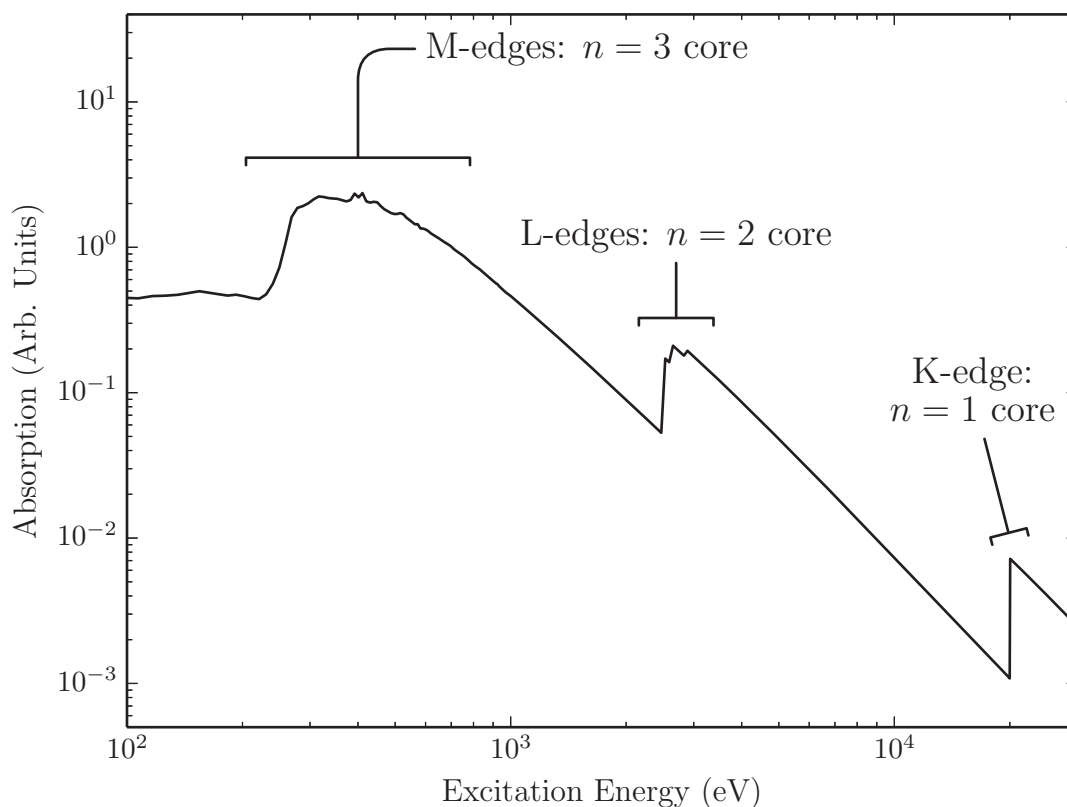


Figure 1.5: Long-range simulated example XAS in molybdenum calculated using the Lawrence Berkeley National Laboratory (LBNL) Center for X-ray Optics (CXRO) database [6]. This energy range covers the K-, L-, and M-edges (labeled). The single K-edge and three L-edges are visible, but the five M-edges are unresolved in the CXRO database.

1.2.1 XANES vs. EXAFS, Soft vs. Hard X-rays

XAS is divided into two general regions: x-ray absorption near-edge spectroscopy (XANES) and extended x-ray absorption fine structure (EXAFS). Each method focuses on a specific region of the absorption edge and probes different characteristics of the sample. XANES involves the excitation of core electrons into bound empty states, and provides information about the electronic states in a sample. EXAFS involves excitations of core electrons into higher-energy unbound states, which can subsequently be scattered by neighboring atoms and produce a characteristic interference pattern. EXAFS analysis deconvolves the oscillations occurring far after the main edge to determine the distance and type of atoms near the absorbing species.

The usefulness of the information to be gained from XANES depends on the nature of the edge measured. The edge position depends on the oxidation state of the probed element, while

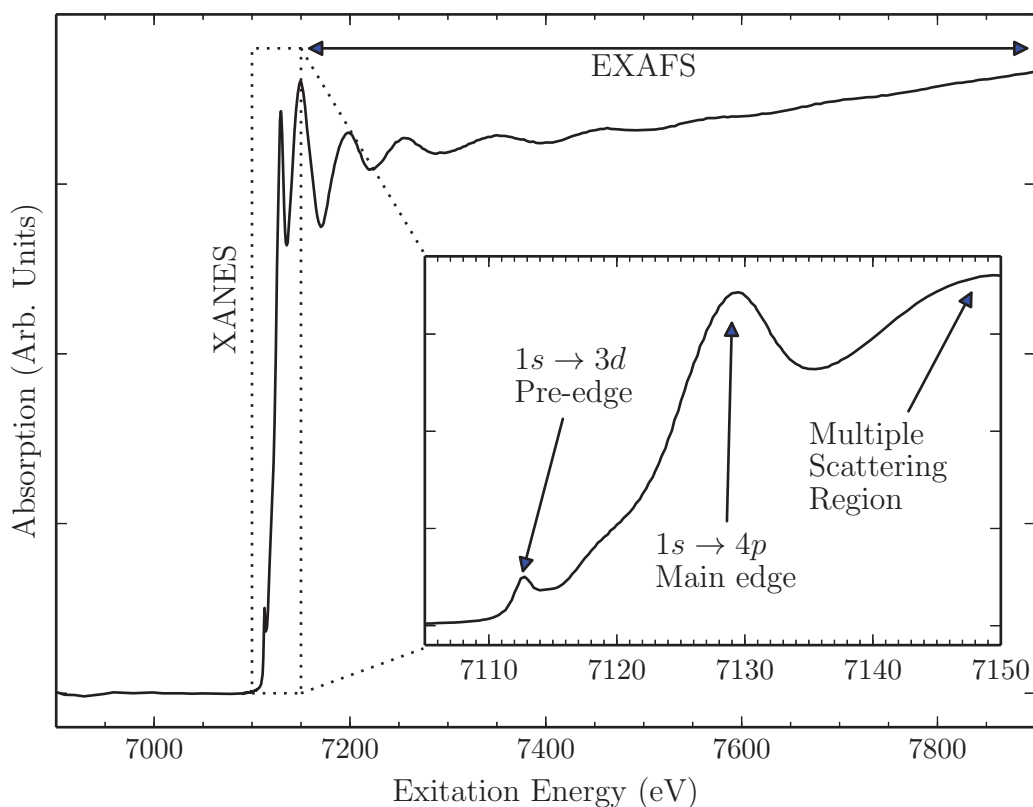


Figure 1.6: Fe K-edge XAS for illustration of common terminology. The EXAFS region starts after the main edge and extends for hundreds of eV in energy, while the XANES region comprises those features in the immediate neighborhood of the edge itself corresponding to bound- and semi-bound-state transitions. This sample demonstrates a weak pre-edge feature from forbidden $1s \rightarrow 3d$ transitions which become partially-allowed due in part to covalent mixing with ligand $2p$ orbitals.

the specific features such as peaks on the edge are due to unoccupied bound states. The dipole selection rules for linearly polarized x-rays are $\Delta J = +1, 0, -1$, $\Delta l = \pm 1$, and $\Delta s = 0$, and these rules apply to the transitions into bound states and determine which bound states appear on the edge. Therefore, the K-, L_1 and M_1 edge XANES features arise from s-p transitions; $L_{2,3}$ - and $M_{2,3}$ - XANES from p-d/s transitions; and $M_{4,5}$ features from d-f transitions. The most information may be derived from XANES transitions into partially filled (valence) shells, corresponding to K-edges for P-block elements, L-edges for transition metals, and M-edges for rare earth metals. Additionally, the higher-order edges have longer lifetimes resulting in narrower line-width from the uncertainty principle, $\Delta E \Delta t \geq \hbar/2$. This means that the edge and feature positions may be determined more precisely from the L- and M- edges than the K-edge, increasing the

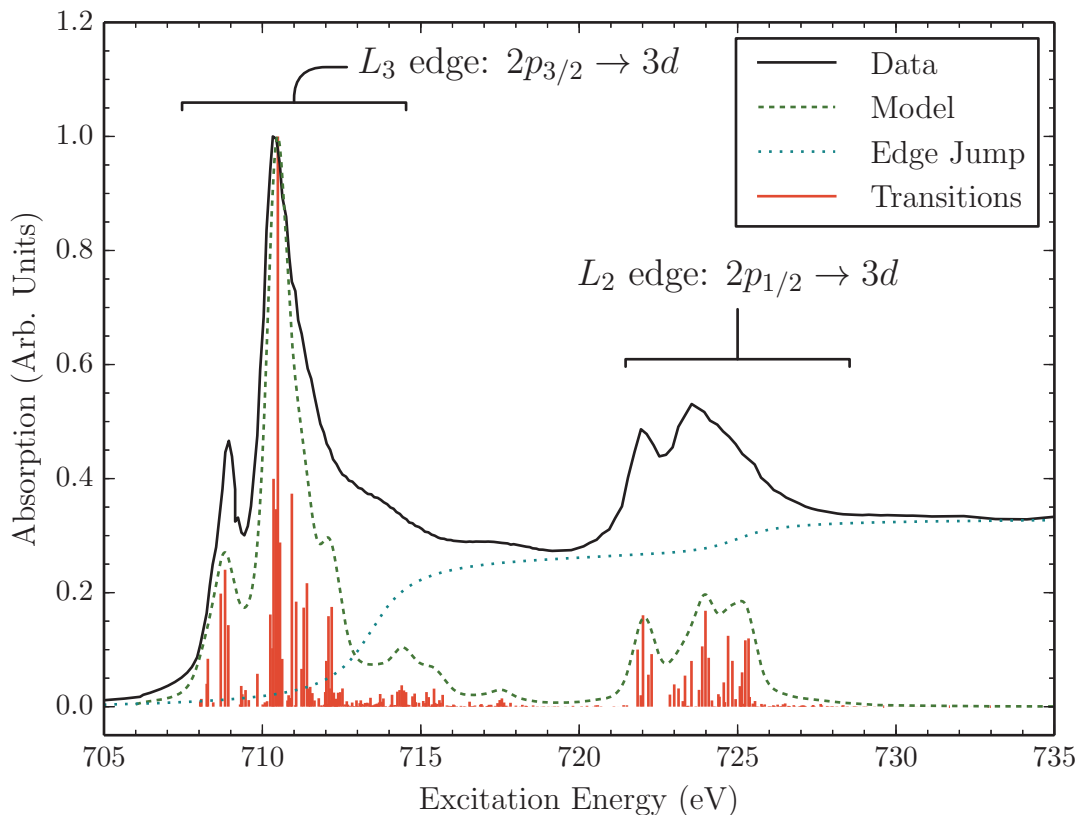


Figure 1.7: Measured Fe $L_{2,3}$ edges of Fe_2O_3 compared to components of a model. The total electron yield (TEY)-XAS is solid, compared to a charge transfer multiplets (CTM) model with O_h symmetry and $10Dq = 1.45$ eV [7]. Bound-state transitions are shown in orange, while their convolved spectrum is in dashed green. The edge jumps (dotted cyan) represent the ionization limits of the edges and contribute to the steps which the bound-state transitions lie upon. Compared to the K-edge, the L-edges typically have much stronger bound-state transitions compared to the edge strength. EXAFS is not typically performed on the $L_{2,3}$ edges since they lie too close in energy to the L_1 edge and each other to extract useful information.

sensitivity of these edges to oxidation state [8].

The absorption edges of different elements encompass a wide range in energy: C, Ni, and Mo have K-edges at 284, 8,333, and 20,000 eV respectively. The x-ray properties of materials, from the attenuation length, scattering coefficient, and interaction with optics, vary widely across this energy range. This affects the experimental conditions under which a sample must be measured, so that samples at energies below ≈ 3 keV must be measured in vacuum to prevent excessive absorption by the air or other ambient gas. The region below 1 keV contains many important edges, including K-edges of elements involved in organic chemistry such as C, N, and O; the L-edges of the top row transition metal elements such as Mn and Fe, and the

M-edges of rare-earth metals such as Gd and Eu. While XAS is more difficult to measure in the soft x-ray band, the wealth of information there makes it an important region of study. Entire synchrotrons such as the Swiss Light Source (SLS) and Advanced Light Source (ALS) have been optimized for the soft x-ray region.

1.2.2 Synchrotron Radiation

While infrared (IR) and ultraviolet/visible (UV/Vis) absorption spectroscopies have been practiced for decades using instrumentation that fits on a tabletop, XAS has only recently become practical for many samples due to the lack of bright, compact sources. A typical hard x-ray generator only produces at most $\approx 10^7$ photons, emitted into 2π or greater solid angle (uniformly into a half hemisphere). Collimating and monochromatizing such a source results in very low fluxes that require long integration times, even for concentrated samples. The primary market for this type of table-top x-ray source is for x-ray diffraction of concentrated, ordered samples.

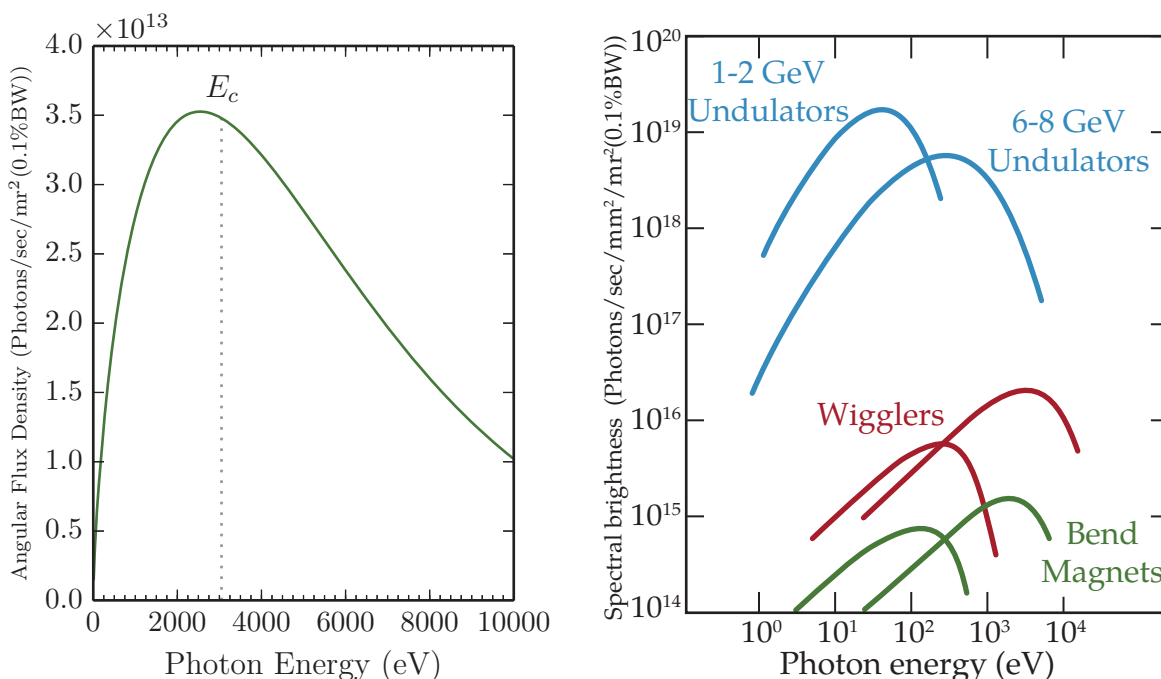


Figure 1.8: Typical brightness of different synchrotron radiation-generating structures. The left panel shows the power spectrum of a typical bend magnet at the ALS, with a critical energy indicated at ≈ 3.05 keV. The right panel shows typical spectral brightness of different types of structures, from lower (1-2 GeV) and higher (6-8 GeV) energy light sources [9].

The development of synchrotrons as light sources has been instrumental to the spread of XAS as a general analytical technique. First generation light sources from the mid-20th century were at the start operated parasitically off high-energy physics accelerators then developed into

dedicated storage rings [10]. The second generation sources from the 1970s onward increased brightness and decreased emittance and beam size over the first generation. The shift from second- to third-generation sources came with the development of insertion devices, periodic magnetic structures which increase brightness over bend magnets. Dedicated, high-brightness, low-emittance third-generation sources such as the ALS at LBNL or Advanced Photon Source (APS) at Argonne National Laboratory (ANL) are optimized for insertion devices and are now common throughout the world.

The three primary magnetic structures which produce synchrotron radiation are bend magnets, wigglers, and undulators. Of these, the bend magnet is the simplest and oldest concept. A beam of synchrotron light is produced when a relativistic electron beam is accelerated around a curve by a dipole magnet. Every synchrotron has a series of such magnets forming the storage ring, so they are present at all facilities by default. The x-ray beam generated by a bend magnet is produced tangential to the path of motion of the electron beam, with a broad energy spectrum peaking at a value determined by the beam energy and magnetic field strength. A common figure of merit is the critical energy, for which half the radiated power lies below and half above, giving the relation

$$E_c = \hbar\omega_c = \frac{3e\hbar B\gamma^2}{2m}, \quad (1.1)$$

where B is the field strength of the bend magnet, γ is the relativistic Lorentz contraction factor and e and m are the electron charge and mass, respectively.

Periodic structures were first developed in the late 1970s and gained wide adoption even on second-generation synchrotrons [11]. As their name suggests, periodic magnetic structures are composed of a series of alternating dipoles of strength B_0 and period λ_u , causing the electron beam to move through the device on a sinusoidal path (in the most basic case). The two types of devices are called “wigglers” and “undulators” depending on the strength and spacing of the magnets and hence the amplitude of the sinusoidal path. A primary parameter to characterize these periodic structures is the non-dimensional magnetic strength parameter

$$K \equiv \frac{eB_0\lambda_u}{2\pi mc}. \quad (1.2)$$

Wigglers have $K \gg 2$ and relatively few periods (of order 5-10), Undulators typically have $k \lesssim 1$ and many periods (from 30-100). Wigglers have an essentially broadband radiation spectrum, similar to but brighter than a bend magnet. They may be thought of as several bend

magnets in series, added together to increase flux. In undulators, the small excursion amplitude combined with the many periods causes constructive interference between the electron beam and the radiation from each period, producing emission that is highly peaked around a wavelength determined by the undulator parameters, along with odd-order harmonics. This is described by the undulator equation

$$\lambda = \frac{\lambda_u}{2n\gamma^2} \left(1 + \frac{K^2}{2} + \gamma^2\theta^2 \right), \quad (1.3)$$

with λ_u again being the period length of the undulator, θ the the angle of observation of the beam off the beam axis, and n being the harmonic number. The spectral width $\Delta\lambda$ of the peaks depend on the number of undulator periods N and is given by

$$\left(\frac{\Delta\lambda}{\lambda} \right)_n = \frac{1}{nN}. \quad (1.4)$$

To produce radiation of arbitrary wavelength requires changing the field strength or photon energy. As synchrotrons are multi-beamline facilities with permanent-magnet undulators, this is done in practice by changing the distance between the undulator jaws and the electron beam. Higher harmonics have decreased brightness over the first, but are still useful to extend the usable energy range of a single undulator by several times. While the total emitted power is less for an undulator than either bend magnets or wigglers, its spectral brightness is orders of magnitude higher as the flux is concentrated in narrower energy bands and smaller angles.

1.2.3 XAS Techniques: Transmission vs. EY vs. FY

The most straightforward way to measure the x-ray absorption cross-section is by transmission, the same method used for UV/Vis and IR absorption spectroscopy. According to the Beer-Lambert law, the transmission through a sample of thickness l is defined in terms of the incident photon intensity² I_0 and transmitted intensity I_1

$$T_E = \frac{I_1}{I_0} = e^{-\sigma_E l n}, \quad (1.5)$$

The other variables are the atomic density n and attenuation cross-section σ , which varies with energy. This leads to the definition of absorbance

$$A_E = \ln\left(\frac{1}{T_E}\right) = -\ln\left(\frac{I_1}{I_0}\right) \quad (1.6a)$$

$$A'_E = -\log_{10}\left(\frac{I_1}{I_0}\right), \quad (1.6b)$$

²See notation discussion later in this section (1.2.3).

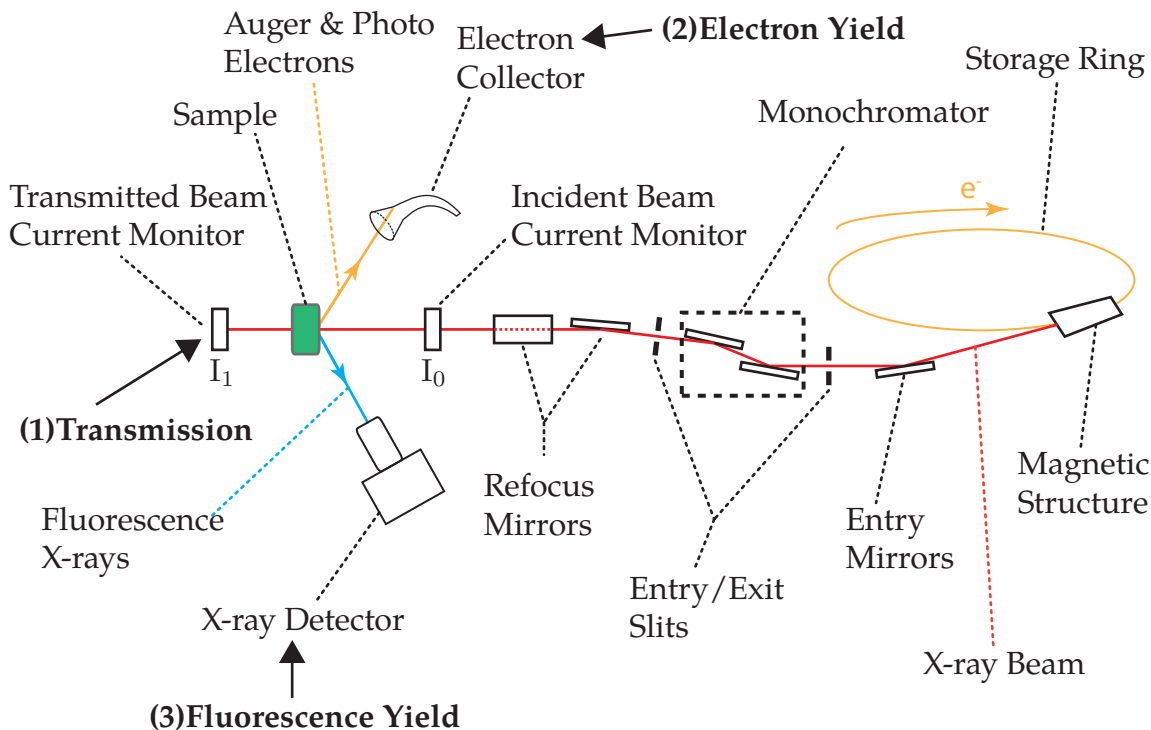


Figure 1.9: Schematic illustration of a typical synchrotron x-ray beamline configured for XAS. The storage ring carries an electron beam with energy in the GeV range. The electrons generate synchrotron radiation (x-rays) when passing through a magnetic structure, which may be either a bend magnet or a periodic magnetic structure (wiggler or undulator). The broadband x-ray beam passes through a series of optics to bend, focus, and monochromatize the final beam. The XAS measurement of the sample may then be taken in one of several ways: 1) Transmission; 2) Electron yield; 3) Fluorescence yield. The diagram depicts all three methods simultaneously.

with A_E being the absorbance at photon energy E and A'_E being the base-10 absorbance, and context determining which definition is used. Base-10 absorbance makes calculating fractional transmission easier to compute and compare, while natural-base absorbance is more directly related to the differential absorption process. Absorbance of unspecified base is typically base-10, so that a sample of 1 absorbance transmits 10% of incident light (versus $\approx 37\%$ for 1 natural-base absorbance) [12].

To measure the transmission spectrum requires measurements of both I_1 and I_0 . UV/Vis and other lower-energy bands typically use a beam splitter to measure both intensities simultaneously. X-rays, however, cannot be split easily or bent by more than a few degrees by grazing-incidence mirrors, so these measurements are typically performed separately, first with the sample in place in the beam, then again with the sample removed. As the beam intensity may fluctuate over time, the incident beam intensity must also be monitored to calibrate each mea-

surement of I to one another. The common term for this beam monitor is, unfortunately, also “ I_0 ”, so from this point onward the beam monitor will be named “ I_0 ” and the incident intensity (prior to entering the sample) will be “ I'_0 ”.

While transmission is the most direct measurement of the absorption coefficient, it is impractical for many types of samples in the x-ray band. Attenuation lengths range from nanometers to meters across the band, so samples need to be either very thin (below $1 \mu\text{m}$) or very thick (many cm). Additionally, transmission has poor signal-to-background sensitivity for dilute samples, whether thin films on a bulk substrate or dilute systems such as proteins in a matrix.

An alternative to transmission is to measure the decay products that result from x-ray absorption. After a photon is absorbed, the excited atom decays back to the ground state by one of several relaxation channels. Electrons in higher orbitals must release energy to fill the core hole, typically by either emitting a photon (fluorescence) or promoting another electron out of its initial orbital by the Auger process, as illustrated in figure 1.10. Due to the high energies involved (of order 0.1 - 10 keV) other processes such as phonon emission are vanishingly small. By making the assumption that the decay processes are directly and constantly proportional to the rate of absorption, the XAS may then be measured indirectly by monitoring the emission products.

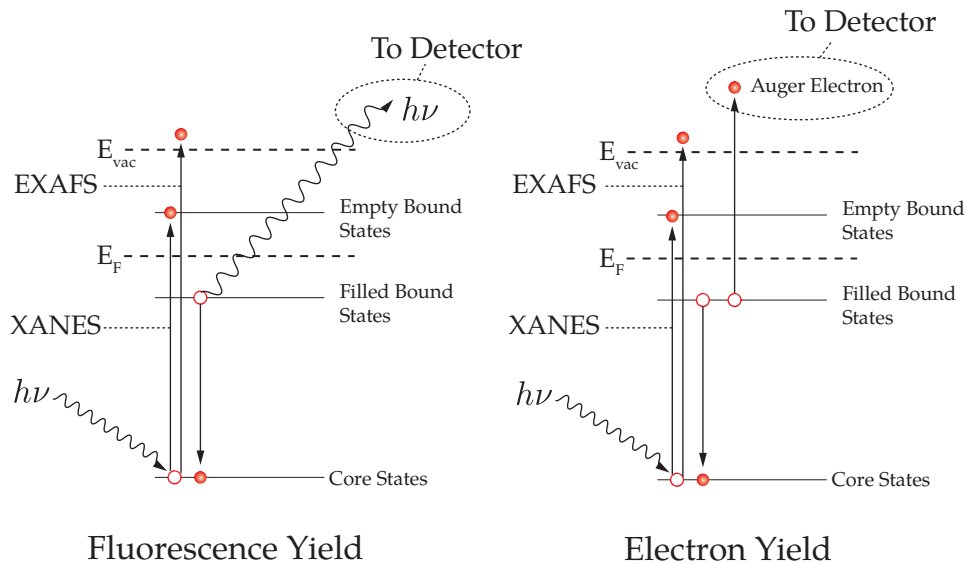


Figure 1.10: Mechanisms of TEY and PFY methods of measuring the XAS.

Measuring the XAS by collecting Auger electrons is called EY. TEY measures all electrons

emitted from the surface of the sample, which includes Auger and photo electrons, and electrons produced from other elements, while partial electron yield (PEY) uses an analyzer or gating apparatus to select only a portion of the emitted electrons to increase sensitivity. This technique is very surface-sensitive, as the escape depth of the electrons is only of order of 10s of nanometers [13]. The sample must be at least semi-conductive, otherwise charging of the sample can distort the spectrum. The sample must also be either in vacuum or placed inside some type of gas-ionization apparatus to collect the electrons, which restricts the sample applications further. Liquids, gases, and frozen solids are not typically measurable with TEY.

Similar to EY, FY measures photons as decay products from absorption events [14]. Like EY, FY is typically divided into the sub-categories of total fluorescence yield (TFY) and PFY depending on whether all fluorescence photons or only a subset are used to generate the XAS. An energy-resolving photon detector with a wide enough range can effectively measure both TFY and PFY at the same time. FY is much more bulk-sensitive than EY with a probe depth determined by sample attenuation length and the fluorescence photon escape depth, typically on the order of μm to mm depending on the sample and energy range.

Both EY and FY do not give a measure of σ_E directly and in practice it is not possible to measure absolute absorbance. This is unnecessary, however, for the types of information that is provided by the XAS as described in section 1.2.1. Each method may be measured independently and simultaneously depending on the sample parameters. Table 1.1 gives an overview of the parameters required by the different methods.

	Transmission	EY	FY
Sample Thickness	Thin	Thick/Any	Thick/Any
Background	High	Moderate	Low
Sensitivity	Bulk	Surface	Bulk
Sample Concentration	High	High	Dilute
Sample Phase	Any	Solid	Any

Table 1.1: Comparison between XAS measurement methods.

1.3 Motivation for Superconducting X-ray Detectors for PFY-XAS

PFY-XAS has been used for several decades to examine complicated systems in both the hard [15, 16] and soft [17, 18, 19] x-ray bands. Early measurements were typically made with ei-

ther energy-insensitive photodetectors with energy filtering, or more typically with energy-resolving, high-solid-angle detectors such as germanium or silicon SSDs. While these detectors have sufficed for many applications, two cases push the need for detectors with higher resolution without sacrificing efficiency.

1.3.1 Increased Sensitivity

Detection sensitivity is determined by the ability of a detector to separate weak signals from a large background. Many samples contain only small concentrations of the element of interest, such as the single Ni atom at the active site of the Hydrogenase protein in figure 1.4. The emission from the element of interest is much smaller than that from the other elements composing the sample, in this case oxygen, nitrogen, carbon, and other light elements.

Detector	Resolution ΔE_{FWHM}	Count Rate (counts/sec)	Efficiency $\eta\Omega/4\pi$	P/B Ratio
Ge (typical)	130 eV	3×10^5	0.1	50:1
Ge (best)	60 eV	3×10^4	3×10^{-2}	50:1
Ge (ideal)	40 eV	10^7	0.1	1000:1
STJ (typical)	8 eV	10^5	10^{-4}	200:1
STJ (best)	4 eV	10^6	10^{-3}	1000:1
STJ (ideal)	2 eV	10^7	10^{-2}	5000:1
Grating (typical)	0.5 eV	10^5	10^{-6}	200:1
Grating (best)	0.2 eV	10^6	10^{-5}	1000:1
Grating (ideal)	0.1 eV	10^6	10^{-3}	5000:1

Table 1.2: Comparison between ranges of performance and sensitivity of principle detector types for PFY-XAS at 500 eV.

Equation 1.7 calculates the PFY signal of a given detector. A sample is illuminated with a strong, monochromatic x-ray beam of energy E_0 with a flux of $I_0 = 10^{12}$ photons/sec, the measured number of counts N_x from element x at energy E_x over an acquisition time τ is given by

$$N_x = I_0\tau \frac{\mu_x(E_0)\epsilon_x}{\mu_{tot}(E_0) + \mu_{tot}(E_x)} \frac{\Omega}{4\pi} \eta. \quad (1.7)$$

Here η is the detector's quantum efficiency, μ_x and μ_{tot} are the absorption coefficients of the element and total sample at a given energy, ϵ_x is the element's fluorescence yield, and $\Omega/4\pi$ is the solid angle covered by the detector [15].

The detectors currently used most often for PFY-XAS are Si or Ge SSDs. High-purity germanium (HPGe) detectors have been in use for several decades due to the ease of manufacturing single-crystal germanium to high purity, but recent developments in silicon drift detectors have increased their popularity over HPGe for x-ray work. The Fano-limited resolution of an SSD is given by

$$\delta_{ssd}E = 2.355\sqrt{F\epsilon E_x}, \quad (1.8)$$

where F is the Fano factor for the material, ϵ is the energy required to generate an excitation, and E_x is the energy of the incident photon. For Si, $F = 0.1$ and $\epsilon = 3.62 \text{ eV}$. This resolution is derived from the normal distribution and represents the standard deviation of the peak observed from monochromatic photons.

Real detectors also experience electronic noise, which is added to the Fano-limited resolution to give

$$\delta E_{total} = \sqrt{\delta E_F^2 + \delta E_e^2}, \quad (1.9)$$

where δE_{total} is the total effective resolution. Current state-of-the-art Si drift detectors approach the Fano-limited resolution at energies above a few keV, with an electronic noise of 50 eV dominating at low energies. A sample SSD spectrum across the soft x-ray region is plotted in figure 1.11 compared to a Ta STJ detector. The resolution of the STJ at the 525 eV O K line is about 6 eV, while the SSD spectrum has a resolution of 60 eV at this energy.

Figure 1.11 demonstrates that Si SSD x-ray detectors can resolve many, but by no means all, x-ray emission lines from different elements. The problem increases for very weak lines in the neighborhood of much stronger neighboring lines, such as the weak Fe L emission at 705 eV close to the strong F K line at 676 eV. Samples like this require superconducting x-ray detectors for PFY-XAS analysis.

1.3.2 Issue: Non-proportionality of PFY to XAS

Along with the fundamental improvements to PFY-XAS that a higher-resolution detector offers, there are questions about the efficacy of PFY that have been renewed recently [20, 21, 22]. The main question is whether the signal measured by PFY is truly proportional to the XAS across all energies of the absorption edge. The basic assumption behind FY and EY XAS are that these rates are constant with energy and independent of initial and final states of the atom. This assumes the absorption and emission events are uncorrelated and independent.

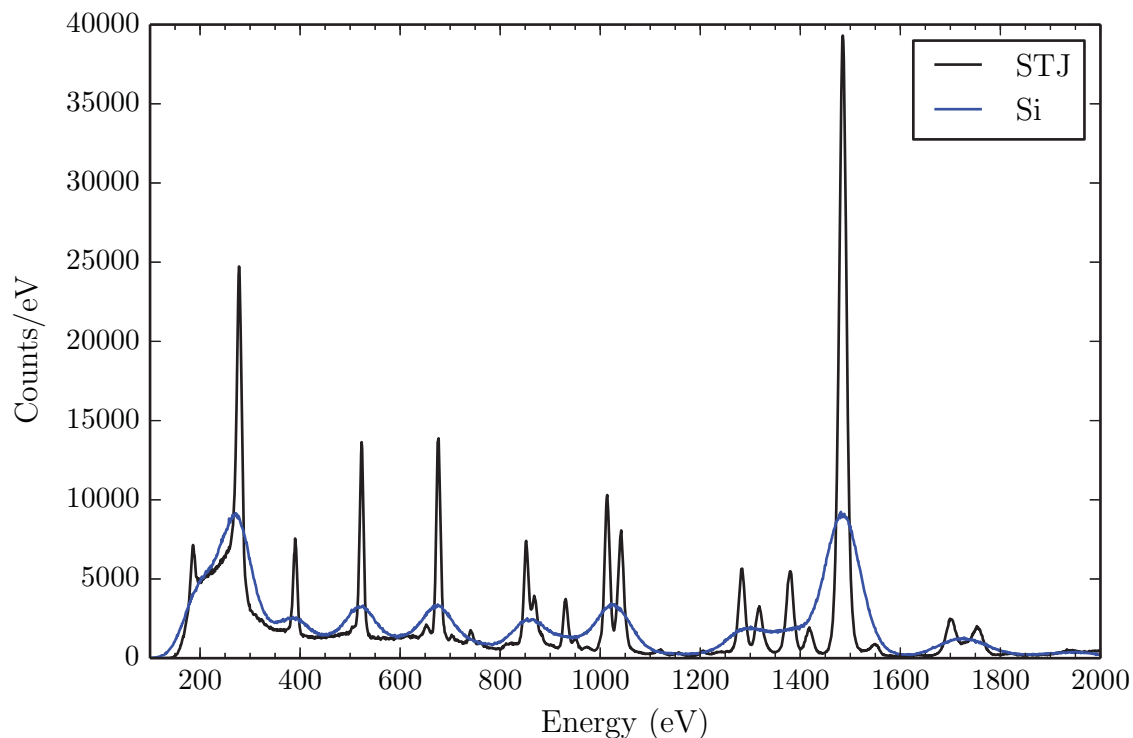


Figure 1.11: Multi-element emission spectrum recorded with STJ and simulated Si SSD. The Si detector can resolve bright, isolated lines, but groups of lines blend together into a single peak.

Since the transition metals have partially-filled d orbitals, L-edge XANES which probes p-d bound states is a powerful tool to understand their electronic structure and chemistry. Since the absorption edge position is characteristic of a given element, XAS can be used to pick out a single atom in a complex to localize the states probed. As outlined in section 1.2.3, there are several methods to measure the XAS depending on the form of the sample. The XAS is determined by Fermi's golden rule,

$$I_{XAS}(\omega, \vec{\epsilon}) \propto \sum_f \frac{\Gamma_f}{\pi} \frac{|\langle f | \vec{\epsilon} \cdot \vec{r} | i \rangle|^2}{(E_i + \omega - E_f)^2 + \Gamma_f^2}, \quad (1.10)$$

with ω and $\vec{\epsilon}$ being the energy and polarization of incident photons, $|i\rangle$ and $|f\rangle$ the initial and final states with energies E_i and E_f (and final state width Γ_f), and \vec{r} the position vector of the participating electron [22]. The observed L-edge XAS is not a direct probe of the electronic density of states (DOS), however, as the 3d valence states have significant overlap with the core wave functions including the 2p hole. This coupling between 2p and 3d gives rise to multiplet effects which split the d orbitals into many sub-levels [23]. So, the measured XAS intensity is not a true probe of the electronic DOS, but with the added information of an appropriate model

this information may be derived.

Transmission is not viable for many types of samples, including large molecules with a small fraction of the element of interest (such as proteins) or dilute samples such as dopants in a solid or chemicals in a solution. Instead, PFY may be used to separate the element of interest from a large background. The basis for PFY-XAS is the assumption that the measured fluorescence yield is directly proportional to the absorption coefficient of the sample, $I_{PFY} \propto I_{XAS}$, as the absorption of a photon creates a core hole which is then filled by the decay of a valence electron through the emission of a photon (fluorescence) or another electron (Auger).

This is a reasonable assumption for K-edges where the hole is buried deep in the 1s core and does not overlap significantly with the valence orbitals, but for the L-edges there is significant overlap between the e.g. 2p and 3d states. In this highly correlated case, the full FY-XAS then is described as a sum over all scattering pathways from the initial to final relaxed system, with the excited state treated as an intermediate, giving [20]

$$I_{PFY}(\omega, \vec{\epsilon}, \vec{\epsilon}') \propto \sum_f \left| \sum_n \sqrt{\frac{\Gamma_n}{\pi}} \frac{\langle f | \vec{\epsilon}'^* \cdot \vec{r} | n \rangle \langle n | \vec{\epsilon} \cdot \vec{r} | i \rangle}{E_i + \omega - E_n + i\Gamma_n} \right|^2. \quad (1.11)$$

The measured fluorescence intensity may then depend on the particular orbitals being filled by the creation of the core hole and is no longer proportional to the XAS as a function of energy. This is only true for decay pathways that originate in the 3d orbitals such as the L_α and L_β lines, while weaker satellites such as the L_ν and L_η should be unaffected [24, 25].

The STJ detector has high enough energy resolution that it can separate emission from these different lines and test whether they result in different XAS. Also importantly, the STJ has high enough efficiency to measure the PFY-XAS on very dilute samples in a reasonable amount of time. Aside from more efficient use of beam time, this is critical for sensitive samples such as biological proteins and catalytic systems which may undergo photochemistry with prolonged exposure to ionizing x-radiation. While a grating spectrometer would also have sufficient resolution to separate the different emission lines from a given element, the STJ detector has sensitivity several orders of magnitude higher than typical grating spectrometers to help collect photons from the weak L_ν and L_η lines and make this experiment practical. This dissertation aims to test predictions of non-proportionality for different forms of PFY-XAS using superconducting high-resolution x-ray detectors.

References

- [1] Y. Tanabe and S. Sugano, "On the Absorption Spectra of Complex Ions. I," *J. Phys. Soc. Japan*, vol. 9, no. 5, pp. 753–766, 1954. (page 6)
- [2] —, "On the Absorption Spectra of Complex Ions II," *J. Phys. Soc. Japan*, vol. 9, no. 5, pp. 766–779, 1954. (page 6)
- [3] —, "On the Absorption Spectra of Complex Ions, III The Calculation of the Crystalline Field Strength," *J. Phys. Soc. Japan*, vol. 11, no. 8, pp. 864–877, 1956. (page 6)
- [4] H. M. Berman, J. Westbrook, Z. Feng, G. Gilliland, T. N. Bhat, H. Weissig, I. N. Shindyalov, and P. E. Bourne, "The Protein Data Bank." *Nucleic Acids Res.*, vol. 28, no. 1, pp. 235–42, Jan. 2000. [Online]. Available: <http://www.pubmedcentral.nih.gov/articlerender.fcgi?artid=102472&tool=pmcentrez&rendertype=abstract> (page 7)
- [5] A. Volbeda, L. Martin, C. Cavazza, M. Matho, B. W. Faber, W. Roseboom, S. P. Albracht, E. Garcin, M. Rousset, and J. C. Fontecilla-Camps, "Structural differences between the ready and unready oxidized states of [NiFe] hydrogenases," *J. Inorg. Biochem.*, vol. 10, no. 3, pp. 239–249, 2005. (page 7)
- [6] CXRO, "Center for X-ray Optics: X-Ray Interactions with Matter," CXRO, 2014. [Online]. Available: http://henke.lbl.gov/optical_constants/ (page 8)
- [7] P. Kuiper, B. G. Searle, P. Rudolf, L. H. Tjeng, and C. T. Chen, "X-ray magnetic dichroism of antiferromagnet Fe₂O₃: The orientation of magnetic moments observed by Fe 2p x-ray absorption spectroscopy," *Phys. Rev. Lett.*, vol. 70, no. 10, pp. 1549–1552, Mar. 1993. [Online]. Available: <http://link.aps.org/doi/10.1103/PhysRevLett.70.1549> (page 10)
- [8] O. B. Drury, S. Friedrich, S. J. George, and S. P. Cramer, "The advantages of soft X-rays and cryogenic spectrometers for measuring chemical speciation by X-ray spectroscopy," *Nucl. Instruments Methods Phys. Res. Sect. A*, vol. 559, no. 2, pp. 728–730, 2006. (page 10)
- [9] D. Attwood, *Soft X-Rays and Extreme Ultraviolet Radiation: Principles and Applications*, 1st ed. New York, NY, USA: Cambridge University Press, 2007. (page 11)
- [10] G. C. Baldwin and D. W. Kerst, "Origin of synchrotron radiation," *Phys. Today*, vol. 28, no. 1, p. 9, 1975. [Online]. Available: <http://scitation.aip.org/content/aip/magazine/physicstoday/article/28/1/10.1063/1.3068762> (page 12)
- [11] H. Winick, G. Brown, K. Halbach, and J. Harris, "Wiggler and undulator magnets," *Phys. Today*, vol. 34, no. 5, p. 50, 1981. [Online]. Available: <http://scitation.aip.org/content/aip/magazine/physicstoday/article/34/5/10.1063/1.2914568> (page 12)
- [12] A. D. McNaught and A. Wilkinson, *IUPAC. Compendium of Chemical Terminology, 2nd ed. (the "Gold Book")*. WileyBlackwell; 2nd Revised edition edition, Aug. 1997. [Online]. Available: <http://goldbook.iupac.org/> (page 14)
- [13] F. M. F. de Groot, "X-ray absorption and dichroism of transition metals and their compounds," *J. Electron Spectros. Relat. Phenomena*, vol. 67, no. 4, pp. 529–622, 1994. (page 16)

- [14] S. Eisebitt, T. Böske, J. E. Rubensson, and W. Eberhardt, "Determination of absorption coefficients for concentrated samples by fluorescence detection," *Phys. Rev. B*, vol. 47, no. 21, pp. 103–109, 1993. (page 16)
- [15] J. Jaclevic, J. A. Kirby, M. P. Klein, A. S. Robertson, G. S. Brown, and P. Eisenberger, "Fluorescence Detection of EXAFS: Sensitivity Enhancement for Dilute Species and Thin Films," *Solid State Commun.*, vol. 23, no. 3, pp. 679–682, 1977. (page 16, 17)
- [16] G. N. George, S. P. Cramer, T. G. Frey, and R. C. Prince, "X-Ray Absorption Spectroscopy of Oriented Cytochrome Oxidase," *Biochem. Biophys. Acta*, vol. 1142, pp. 240–252, 1993. (page 16)
- [17] S. J. George, M. D. Lowery, E. I. Solomon, and S. P. Cramer, "Copper L-Edge Spectral Studies - A Direct Experimental Probe of the Ground-State Covalency in the Blue Copper Site in Plastocyanin," *J. Am. Chem. Soc.*, vol. 115, no. 7, pp. 2968–2969, 1993. (page 16)
- [18] S. Mitra-Kirtley, J. van Elp, G. Peng, B. G. Searle, Y. H. Huang, M. K. Johnson, Z. H. Zhou, M. W. W. Adams, M. J. Maroney, and S. P. Cramer, "Electronic Structure and Symmetry in Nickel L-Edge X-ray Absorption Spectroscopy : Application to a Nickel Protein," *J. Am. Chem. Soc.*, vol. 116, pp. 1918–1923, 1994. (page 16)
- [19] P. Glatzel, L. Jacquemet, U. Bergmann, F. M. F. DeGroot, and S. P. Cramer, "Site-Selective EXAFS in Mixed-Valent Compounds Using High Resolution Fluorescence Spectroscopy: A Study of Fe in Prussian Blue," *Inorg. Chem.*, vol. 41, no. 12, pp. 3121–3127, 2002. (page 16)
- [20] R. Kurian, K. Kunnus, P. Wernet, S. M. Butorin, P. Glatzel, and F. M. F. de Groot, "Intrinsic deviations in fluorescence yield detected x-ray absorption spectroscopy: the case of the transition metal L_{2,3} edges." *J. Phys. Condens. Matter*, vol. 24, no. 45, p. 452201, Nov. 2012. [Online]. Available: <http://www.ncbi.nlm.nih.gov/pubmed/23060535> (page 18, 20)
- [21] A. Föhlisch, F. M. F. de Groot, M. Odelius, S. Techert, and P. Wernet, "Comment on 'State-Dependent Electron Delocalization Dynamics at the Solute-Solvent Interface: Soft-X-ray Absorption Spectroscopy and Ab Initio Calculations'," *Phys. Rev. Lett.*, vol. 112, no. 12, p. 129302, Mar. 2014. [Online]. Available: <http://link.aps.org/doi/10.1103/PhysRevLett.112.129302> (page 18)
- [22] R. J. Green, D. Peak, A. J. Achkar, J. S. Tse, A. Moewes, D. G. Hawthorn, and T. Z. Regier, "Comment on 'State-Dependent Electron Delocalization Dynamics at the Solute-Solvent Interface: Soft-X-Ray Absorption Spectroscopy and Ab initio Calculations'," *Phys. Rev. Lett.*, vol. 112, no. 12, p. 129301, Mar. 2014. [Online]. Available: <http://link.aps.org/doi/10.1103/PhysRevLett.112.129301> (page 18, 19)
- [23] F. M. F. de Groot, "Multiplet effects in X-ray spectroscopy," *Coord. Chem. Rev.*, vol. 249, no. 1-2, pp. 31–63, Jan. 2005. [Online]. Available: <http://linkinghub.elsevier.com/retrieve/pii/S0010854504000670> (page 19)
- [24] F. M. F. de Groot, M.-A. A. Arrio, P. Sainctavit, C. T. Chen, F. M. F. D. Groot, C. Cartier, D. M. Cristallographie, U. Paris, and P. Jussieu, "Distortions of X-Ray absorption spectra measured with fluorescence yield," *Phys. B*, vol. 208-209, pp. 84–86, 1995. (page 20)

- [25] P. S. Miedema, P. Wernet, and A. Föhlisch, "State-dependent fluorescence yields through the core-valence Coulomb exchange parameter," *Phys. Rev. A*, vol. 89, no. 5, p. 052507, May 2014. [Online]. Available: <http://link.aps.org/doi/10.1103/PhysRevA.89.052507> (page 20)

Chapter 2

Superconducting Tunnel Junctions

Superconductors are so-named because they exhibit zero resistance below a certain temperature called the material's critical temperature, T_c . Superconductivity is due to the fact that a portion of the conduction-band electrons near the Fermi level pair up into coherent packets called Cooper pairs, creating a gap in energy between the highest-energy filled electronic state and the lowest-energy unoccupied state. This energy gap means there is a minimum energy required to create an excitation in the superconductor to break a Cooper pair. When two superconductors are separated by a thin insulator, a tunnel junction is formed that can be used as an x-ray detector. When the two sides of the junction are voltage-biased relative to one another and an energetic photon is absorbed in one of the superconducting electrodes, free excess charges are generated in proportion to the x-ray energy. The excess charges tunnel across the barrier and create a current proportional to the incident photon's energy. This chapter discusses the theoretical background of superconducting x-ray detectors and factors affecting their resolution and performance. It also discusses the development of Ta-based STJ x-ray detector arrays at STAR Cryoelectronics.

2.1 Superconductivity

A perfect conductor is a material with zero electrical resistance. A phase transition into a state with this property was observed for the first time in mercury by Heike Kamerlingh Onnes in 1911 [1]. After more materials were found to have a transition to this zero-resistance state, Meissner and Ochsenfeld discovered in 1933 that they also share another surprising property: any magnetic field applied to the material as it goes through the superconducting transition is expelled from the material, so that the magnetic flux through it is zero [2]. This result is not

expected from a mere perfect conductor. In fact, a superconductor is a phase of matter distinct from the metallic solid phase characterized by the two essential properties:

- Zero resistance (superconductivity)
- Expulsion of magnetic fields (Meissner effect)

Prior to the development of the microscopic theory of superconductivity by Bardeen, Cooper, and Schrieffer (BCS) in 1957 [3], superconductors were described macroscopically by the phenomenological London equations

$$\Lambda \frac{\partial \vec{J}_S}{\partial t} = \vec{E} \quad (2.1a)$$

$$\Lambda (\nabla \times \vec{J}_S) + \vec{B} = 0, \quad (2.1b)$$

with $\Lambda = m/n_S e^2$ determined by the mass m , charge e , and number density n_S of superconducting electrons. Equation 2.1a describes how an electric field continues to accelerate the current in the absence of an electrical resistance, which implies that for stationary currents there is no electric field inside a superconductor. Equation 2.1b shows how the current flowing in the superconductor is determined by the magnetic field. Using Ampère's law $(\nabla \times \vec{B}) = \mu_0 \vec{J}_S$ to substitute for \vec{J}_S in equation 2.1b gives the relation

$$\nabla^2 \vec{B} = \frac{\mu_0 n_S e^2}{m} \vec{B}. \quad (2.2)$$

Applying appropriate boundary conditions of an external field B_0 at the surface of a superconductor leads to solutions of the form

$$B_z = B_0 e^{\pm y/\lambda}, \quad (2.3)$$

with the z -component lying along the surface of the superconductor and y pointing into the surface along the surface normal. The parameter λ is called the London penetration depth and is given by:

$$\lambda = \sqrt{\frac{m}{\mu_0 n_S e^2}}. \quad (2.4)$$

The direct result of this solution is the exponentially decaying magnetic field inside the superconductor over the length scale λ . Any external magnetic field gives rise to a surface current which cancels the field from penetrating the bulk of the superconductor. This describes the

Meissner effect. Most elemental superconductors are driven normal by magnetic fields above a critical value H_c . However, for certain so-called type-II superconductors, it is energetically favorable to let external fields penetrate the superconductor and drive certain regions normal. Each of the regions contains quantized magnetic flux of magnitude $\phi_0 = 2 \times 10^{-15} \text{ Tm}^2$, and ϕ_0 is called the magnetic flux quantum.

The London equations correctly describe the relations between current, magnetic, and electric fields in a superconductor and complement Maxwell's equations. However, they do not provide a mechanism underlying the superconducting state. This was provided by the theory of Bardeen, Cooper, and Schrieffer (BCS) in 1957.

In a normal (non-superconducting) metal, the valence electrons move freely through the metal and can be thought of as a collective charge sea bound by the physical boundaries of the metal. This is called a free electron gas due to the independence of the electrons from their originating atoms. The states of this gas are still affected by the atomic lattice and characterized by the Bloch functions $U(\vec{r})$ to give electronic wave functions of the form:

$$\Psi_{\vec{k}} = U(\vec{r})e^{i\vec{k}\cdot\vec{r}} \quad (2.5)$$

which depends on the wave vector \vec{k} of the electron and its position \vec{r} . Due to Fermi statistics, each of these states may hold two electrons, one with spin up and one with spin down, so that at zero temperature all states up to the Fermi energy E_F are filled. The Fermi energy defines a surface in k -space, with all allowed E_k values occupied up to E_F . At finite temperatures, electrons may become excited above E_F to carry energy as shown on the left in figure 2.1. This gives rise to the electronic specific heat c_V^e which increases linearly with temperature.

Vibrations of the atomic lattice are also important for the BCS theory of superconductivity. Vibrations of the lattice are quantized due to the finite degrees of freedom of the atomic lattice, which means that they may be treated as a form of particle termed a "phonon". Phonons are not true particles, but exhibit many of the same properties such as well-defined momentum and the ability to scatter with other particles. Their properties are determined by the lattice parameters and are quantized by a wave vector \vec{q} which is bound by a maximum value $q_D^{\vec{}}$ called the Debye wave number. Phonons have their own associated specific heat c_V^L , which dominates at temperatures above a few Kelvin before converging asymptotically to a maximum at $3Nk_B$.

The first indication about the mechanism of superconductivity came in 1950, when it was observed that different isotopes of the same element have different critical temperature T_c [4, 5].

T_c scales inversely with the isotope mass, suggesting that phonons were involved in the underlying mechanism of superconductivity. The BCS theory describing this interaction between phonons and electrons provides the first microscopic model underlying superconductivity in low-temperature superconductors. If one electron with wavevector \vec{k}_1 travels through the metal, it attracts positively charged ions to its path and thereby polarizes the lattice. Another electron with wavevector \vec{k}_2 is attracted to this polarization, and the attraction is maximized for $\vec{k}_2 = -\vec{k}_1$. This attractive potential results in pairing of electrons characterized by $[\vec{k}_1, \vec{k}_2]$. The \vec{k} values lie within a narrow energy band of $\hbar\omega_D$ around E_F .

For a given pair $[\vec{k}_1, \vec{k}_2]$, which may be more conveniently characterized by the combined the center of mass (COM) wavevector \vec{k} and position vectors $[\vec{r}_1, \vec{r}_2]$, the wave function can be expressed as

$$\Phi_k = \exp[i\vec{k} \cdot (\vec{r}_1 - \vec{r}_2)]. \quad (2.6)$$

The set of wavefunctions is complete, so that a stationary state may be defined as a linear combination of pairs

$$\Psi = \sum_{\vec{k}} a_{\vec{k}} \exp[i\vec{k} \cdot (\vec{r}_1 - \vec{r}_2)]. \quad (2.7)$$

A wave packet constructed this way from paired electrons of opposite \vec{k} is called a Cooper pair. This ordering into a packet sets the scale for the range of coherence among pairs, their wavelengths, and velocities. The coherence range may be thought of as the “size” of a Cooper pair, and is given by the Pippard coherence length

$$\xi_0 = 0.18\hbar v_F / k_B T_c, \quad (2.8)$$

which is typically of the order 10s of nm [3]. The electron velocity v_F at the Fermi energy varies among superconductors similarly to T_c . Cooper pairs in close proximity exhibit strong phase coherence, so that the entire ensemble of Cooper pairs may be thought of as a fluid represented by an average function $|\Psi(\vec{r})|$. If there is net momentum of the fluid, the pair phase $\theta(\vec{r})$ will exhibit a gradient leading to the general form for the ensemble wave function

$$\Psi = |\Psi(\vec{r})| e^{i\theta(\vec{r})}. \quad (2.9)$$

While a normal metal has a partially-filled, continuous conduction band, a superconductor is characterized by a gap of energy 2Δ between the Cooper pairs and the lowest unoccupied single-electron levels. As shown in figure 2.1, the conduction band electrons in a normal metal

fill states up to the Fermi level E_F and may be excited by any increment of energy. Upon transition to the superconducting state, there is a gap of magnitude Δ between E_F and the lowest unoccupied single-electron state that corresponds to the binding energy of a Cooper pair. In the semiconductor representation of superconductors, Cooper pairs are shown in the middle of the gap at the Fermi energy E_F , with the gap symmetric around E_F .

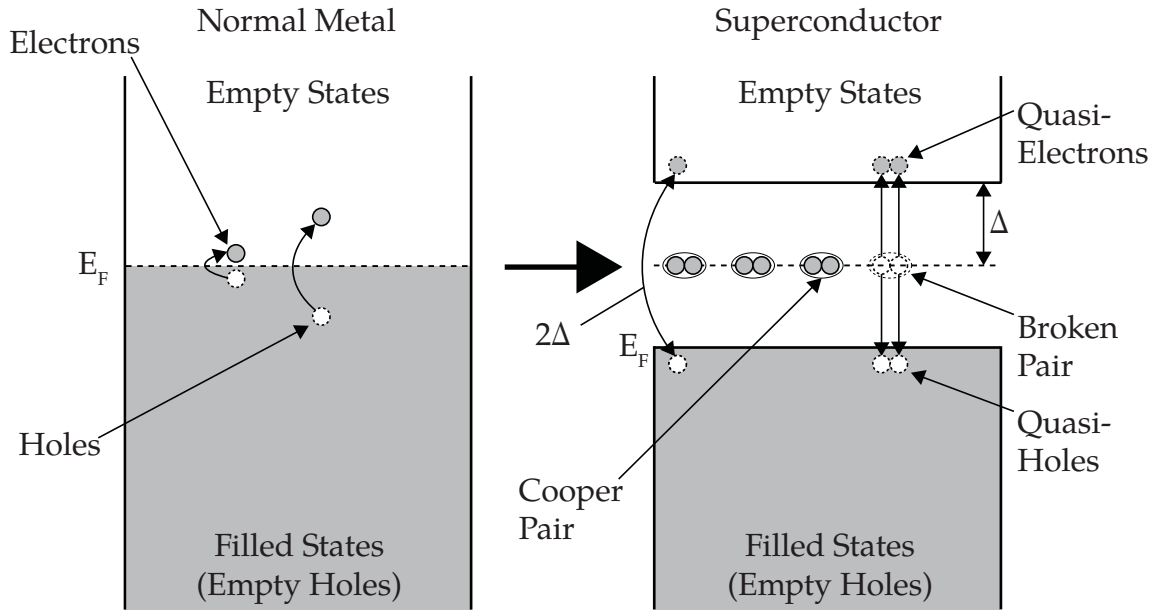


Figure 2.1: Formation of Cooper pairs creates an energy gap at the Fermi energy in the transition from the normal metal to the superconducting state.

Because superconductors have a gap in the density of states, excitations have a threshold energy of 2Δ . Cooper pairs are broken to create two excitations called quasiparticles (qps) as shown on the right panel of figure 2.1. The “quasi” is due to the correlated nature of particles in a superconductor, where many-body effects dominate over single particle effects so that an excitation is not seen as a single particle but as a change in occupancy of the group.¹ Excitations close to the gap have electron-like or hole-like properties, similar to a quantum superposition which may take on either role probabilistically. Further from the gap, excitations become more definitely hole- or electron-like.

The gap parameter Δ is not constant with temperature, but increases with decreasing temperature along with the condensation of electrons into Cooper pairs. Its value is indirectly defined through an integral over the probabilities of pair occupancies [6]. This leads to a tempera-

¹Phonons are quasiparticles as well as they are collective excitations of the atomic lattice.

ture dependence of the gap parameter Δ , as shown in figure 2.2. At temperatures below $\approx 0.3T_c$ the gap is within 1% of the value at $T = 0$ K. As the temperature increases towards T_c , the gap decreases to zero.

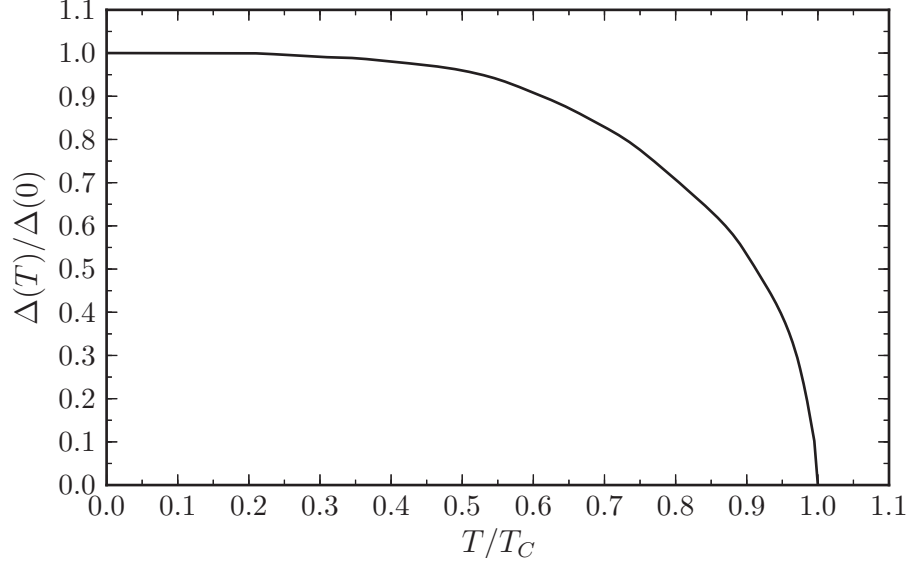


Figure 2.2: Temperature dependence of the superconductor gap parameter Δ . Units are normalized in temperature to T_c and in energy to the gap size at $T = 0$ K [7].

Not shown in figure 2.1 is the difference between the normal metal and superconductor DOSs about the Fermi level and gap, respectively. A normal metal has a DOS N_n that is a function of excitation energy E as $N_n(E) \propto \sqrt{E}$. At zero T, all states below E_F are filled, and N_n may essentially be taken as a constant for energies close to E_F . The DOS in a superconductor follows the relation

$$N_s(E) = \frac{N_n(E_F)E}{\sqrt{(E^2 - \Delta^2)}}. \quad (2.10)$$

This causes the DOSs for both electron-like and hole-like quasiparticles on either side of the gap to diverge at the gap Δ , and converge to the normal metal DOS further away from the gap. The shape of N_s is depicted schematically in figure 2.3 in section 2.1.1.

2.1.1 Tunnel Junctions

A tunnel junction is a physical arrangement where a very thin insulating potential barrier separates two conductive regions. Charge carriers are classically forbidden inside this barrier, but may transit it through quantum-mechanical tunneling. Tunnel junctions may be formed from any combination of normal conductors, superconductors, or semiconductors. Here we will focus on three types:

1. normal-insulator-normal (NIN)
2. superconductor-insulator-normal (SIN)
3. superconductor-insulator-superconductor (SIS)

The names describe the arrangement of the layers composing the junction, *e.g.* a superconductor-insulator-normal (SIN) junction consists of a superconducting region separated from a normal region by an insulating barrier. A schematic diagram of an superconductor-insulator-superconductor (SIS) junction showing the energy levels and DOSs is shown in figure 2.3. This figure is drawn according to the semiconductor-representation and shows the divergent qp DOSs at $E = \pm\Delta$, the population of excited quasiparticles on both sides of the gap, and the offset eV between the two superconducting regions from an applied bias voltage. For SIN or normal-insulator-normal (NIN) junctions, either or both sides may be replaced by a normal metal with a constant DOS.

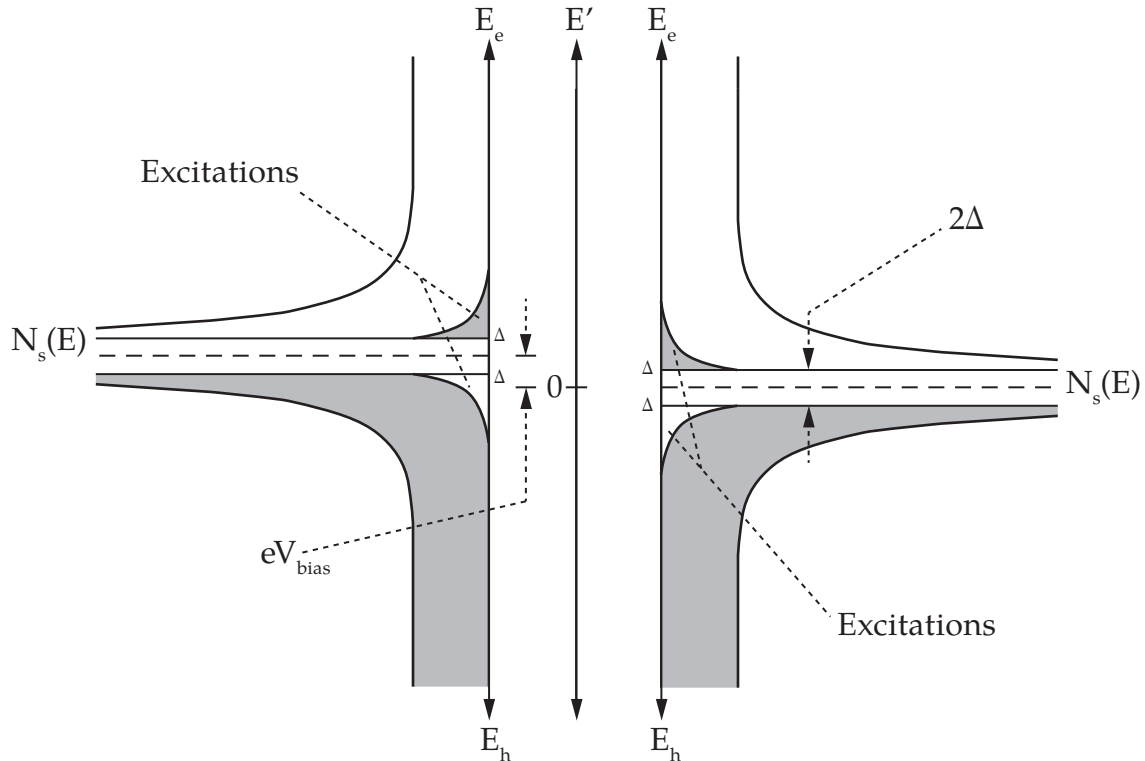


Figure 2.3: Diagram of the density of states in an SIS junction as a function of energy for two identical superconductors of gap Δ . The junction is biased at a voltage V_{bias} that results in an energy offset eV_{bias} between the electrodes. The junction is shown at nonzero temperature, causing the presence of excitations above the gaps. Filled states are shaded gray.

In all junctions, tunneling occurs whenever filled states on one side of the barrier face empty states on the other side of the barrier. Applying a bias voltage eV to the junction changes the relative energy of the two sides, and results in a tunneling current I such that

$$I(V) = \int N_1(E' - eV)N_2(E')(f(E' - eV) - f(E'))dE', \quad (2.11)$$

where $N(E)$ is the density of states in the junction electrodes and $f(E)$ is the Fermi function that determines occupancy,

$$f(E) = \frac{1}{e^{E/k_B T} + 1}. \quad (2.12)$$

The integral limits in equation 2.11 are set by the energy range over which tunneling can occur. Equation 2.11 allows the computation of the tunneling current I as a function of applied voltage, a relationship that is important to the electronic characteristics of a tunnel junction.

NIN junctions behave like resistors with a conductance set by the tunnel barrier thickness and the junction area. An NIN junction with conductance G_n then has a relationship between current I_{nn} and voltage bias V following

$$I_{nn} = G_n V. \quad (2.13)$$

This is due to the fact that the normal metal DOS is essentially constant near the Fermi level, so biasing the junction causes a linearly increasing overlap between occupied and empty states available for tunneling. For SIN junctions, there are initially no available states for tunneling at low bias voltages due to the superconducting gap. The onset of current at $V_{bias} = eV$ is discontinuous and directly yields the form of the DOS of the superconductor. For $T = 0$ K, this has the form

$$I_{ns} = \begin{cases} 0 & eV \leq \Delta \\ (G_n/e)\sqrt{(eV)^2 - \Delta^2} & eV > \Delta \end{cases}. \quad (2.14)$$

For $T \neq 0$ K the case is more complicated as equation 2.11 has to be solved numerically.

For an SIS junction with two superconductors of gap parameters Δ_1 and Δ_2 , equation 2.11 is again not solvable analytically. For $T = 0$ K, there will be zero current up to the gap voltage, then a discontinuous onset of current at $I = (\Delta_1 + \Delta_2)/e$. At nonzero temperature, excitations occupy states on both hole-like and electron-like sides of the barrier and cause a finite tunneling current below the gap. The complete integral that describes the I-V relationship in an SIS junction is

given by [6]

$$I_{ss} = \frac{G_n}{e} \int_{-\infty}^{\infty} \frac{|E' - eV|}{[(eV - E')^2 - \Delta_1^2]^{1/2}} \frac{|E'|}{[E'^2 - \Delta_2^2]^{1/2}} [f(E' - eV) - f(E')] dE', \quad (2.15)$$

where $f(E)$ is the Fermi function given by equation 2.12 and G_n is the normal state conductance. The sub-gap current then depends on temperature through both the excitations brought about by $f(E)$, and the changing gap parameter which has a temperature dependence shown in figure 2.2. The I-V curve displays a relationship with temperature illustrated in figure 2.4.

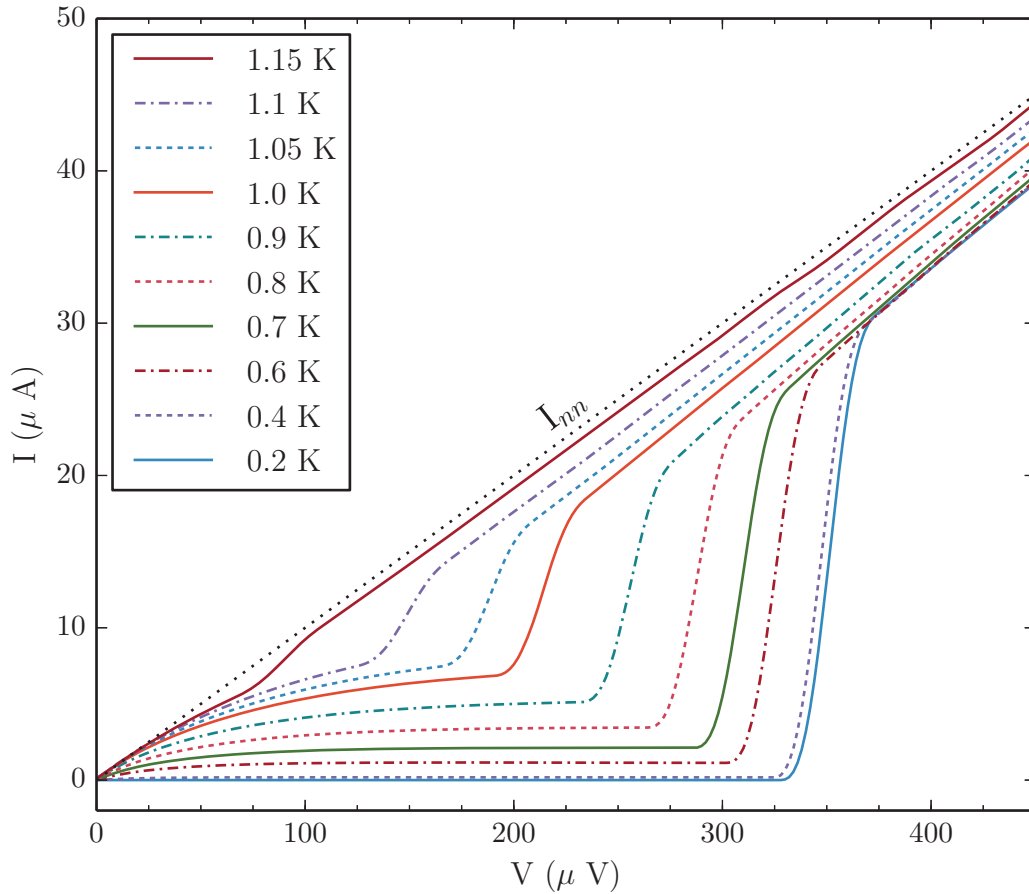


Figure 2.4: Simulated current through an aluminum SIS junction as a function of bias voltage at multiple temperatures, computed using equation 2.15.

The junction modeled in figure 2.4 is aluminum on both sides, with a T_c of 1.175 K and a gap parameter of $\Delta_{Al} = 0.17$ mV. Significantly below T_c , the I-V curve displays near-zero current below the gap, and a sudden increase of current near the gap at $340 \mu\text{V} = 2\Delta_{Al}/e$. As the temperature is increased to near T_c , the gap energy decreases while current increases at bias

points below the gap due to thermal excitations of quasiparticles. For voltages $V \gg 2\Delta_{Al}/e$, the current approaches I_{nn} , the normal state tunneling current.

2.2 SIS Tunnel Junctions as Photon Detectors

SIS tunnel junctions can be used as high-resolution x-ray detectors due to the fact that energy absorption in one of the electrodes creates excess quasiparticles and a subsequent increase in tunneling current that is proportional to the x-ray energy. This use as photon detectors was first proposed in the early 1980s [8] and forms the basis for this dissertation.

2.2.1 Mechanism

A photon may be absorbed in a material in several ways depending on its energy. Low-energy photons below the ionization potential of any atoms in the material scatter off the electron clouds of the lattice atoms and lose energy through inelastic processes, such as exciting electronic transitions for optical phonons or vibrational transitions for IR photons. Higher-energy photons ionize one or more lattice atoms to generate photoelectrons. In either case, the energy of the incident photon is eventually distributed among phonons after the high-energy excitations have relaxed. In a superconductor, these excess phonons then break Cooper pairs and generate quasiparticles above the gap in excess of the equilibrium state. These quasiparticles initially have an energy distribution that depends on the DOS and the partitioning of the incident photon energy among the different decay paths. Quasiparticles at energies $> 3\Delta$ can scatter down and emit phonons with energies $> 2\Delta$, which can break additional Cooper pairs. So, after the initial photon absorption in the superconductor, the energy is distributed into a population of quasiparticle excitations on one side of the STJ due to the breaking of Cooper pairs. These processes of pair breaking and down-scattering continue until all phonons with energy $> 2\Delta$ have been absorbed by Cooper pairs and all quasiparticles have scattered below an energy of 3Δ . Monte Carlo simulations show that at the end of the relaxation process, $\approx 60\%$ of the incident x-ray energy is converted into excess quasiparticles, and $\approx 40\%$ into phonons [8, 9]. The average energy to create an excess quasiparticle is therefore $\epsilon \simeq 1.7\Delta$.

If a voltage bias is applied across the junction, these excess quasiparticles will preferentially tunnel across the barrier to the counter-electrode and transfer a net charge across the junction that is detectable as a current pulse. The typical charge for *e.g.* a 1 keV photon absorbed in a superconductor with $\Delta \approx 1$ meV is of order 10^6 quasiparticles. If they tunnel exactly once,

they would generate a current pulse with a time constant determined by the the barrier transmissivity. Fortunately, the nature of quasiparticles as group excitations gives rise to a cycling phenomenon which can enhance the tunneling current [10]. There are several processes highlighted in figure 2.5 that contribute to the primary tunneling current, termed forward tunneling (FT), reverse tunneling (RT), and backtunneling (BT) respectively.

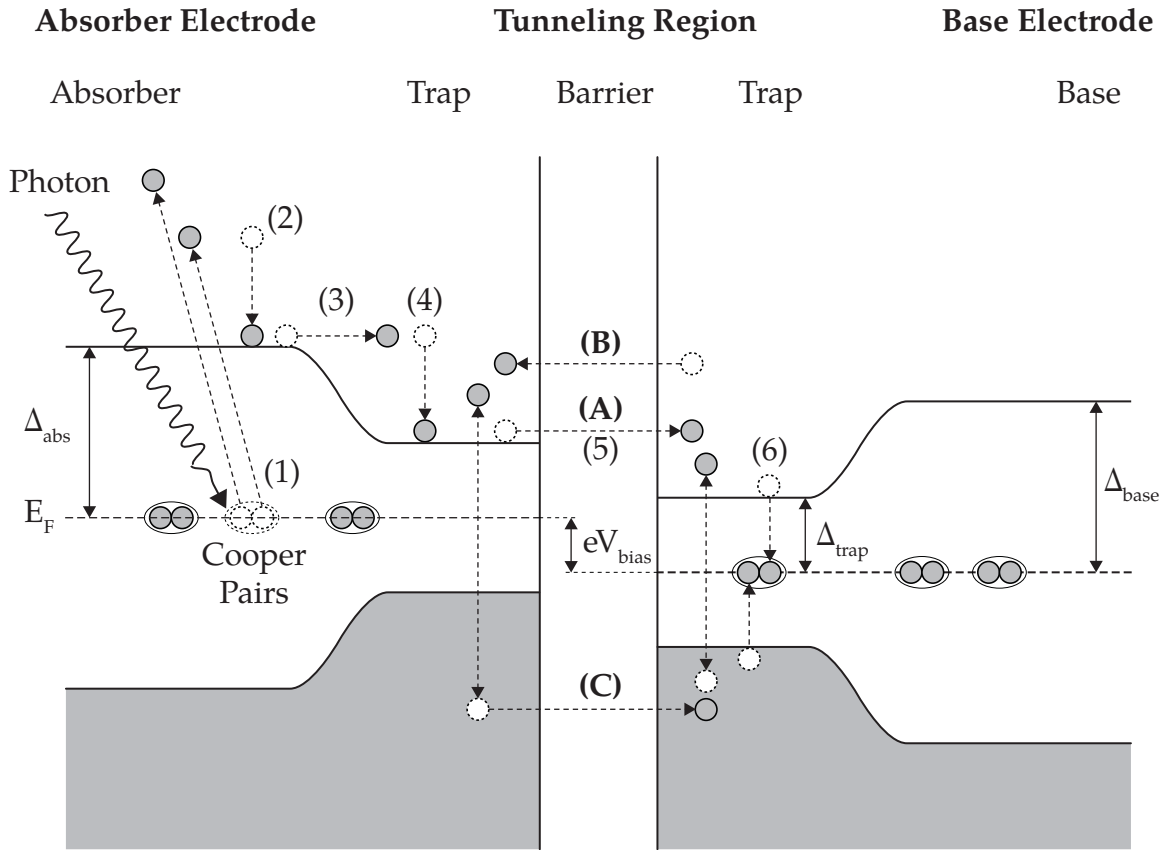


Figure 2.5: Operating principle of an STJ as photon detector. The junction is biased by a voltage V_{bias} , which results in an energy offset between the two sides by eV_{bias} . A photon is absorbed in the top layer, breaking Cooper pairs and generating excess quasiparticles above the gap (1). These excess qps thermalize down to just above the gap by emitting phonons (2) and transition to the lower-gap trap region (3) where they scatter again down to the gap and become confined near the barrier (4). There they tunnel (5) to the base electrode and recombine into Cooper pairs (6). This entire process is called direct tunneling (DT) and is labeled as (A). Quasiparticles in the base electrode may also tunnel against the bias if they are high enough above the gap, a process called reverse tunneling (RT) and labeled as (B). As qps are an expression of a many-body system, occupancy of a electron-like state above the gap partially implies occupancy of a hole-like state below the gap. This may be filled by tunneling of an electron below the gap as noted in process (C), termed backtunneling (BT). This in turn implies the occupancy of an electron-like state above the gap in the absorber trap, which may itself tunnel again. Backtunneling may occur many times for each qp generated by the photon.

Forward tunneling occurs when a quasi-electron tunnels with the bias from the higher-potential absorber electrode to the lower-potential base electrode. Reverse tunneling occurs when a quasi-electron tunnels against the bias, which subtracts from the net charge. Reverse tunneling (RT) is substantially decreased by increasing the junction bias as the rate of both forward tunneling (FT) and RT depend on the DOS on either side of the junction to tunnel from and into, and that the qps injected into the counter-electrode well above Δ are more likely to scatter down than to reverse-tunnel. The process of backtunneling is a phenomenological result of the many-body nature of quasiparticle excitations and is key to charge amplification. This process arises from the fact that quasiparticles have both electron-like and hole-like character, and can convert from an electron into a hole through a process called branch-mixing. So, a quasi-electron above the gap in the base electrode can turn into a quasi-hole on that side of the barrier, and the quasi-hole can tunnel back across the barrier thereby transferring charge across the barrier in the same direction as the forward-tunneling process. This quasi-hole now present on the absorber-side of the barrier may then tunnel back across as a quasi-electron, and so on for many cycles. While counter-intuitive in a classical sense, this process is very real for the coherent many-body system in a superconductor and has been confirmed experimentally [10].

To increase this multiple-tunneling amplification further, the junction is engineered to trap the excited quasiparticles in a region close to the gap in order to decrease the tunneling time constant τ_t and increase the probability of multiple-tunneling. This is accomplished by depositing a thin layer of lower-gap superconductor between the electrodes and the tunnel barrier. The lower-gap superconductor interacts with the electrodes through the proximity effect, which causes a continuous transition of the gap parameter through a region between two different superconductors. For a device with Ta electrodes as developed in this work, a good choice for the trap is Al as it has a small gap than Ta with a T_c of ≈ 1.3 K, well below that of Ta. This is illustrated in figure 2.5 by the two different gap sizes near the barrier with a wide transition from the Ta gap value into the Al trap region. Devices with a trap region can amplify the initial charge by 10-100 times, with typical amplification in the range of 20-30 times.

2.2.2 Resolution

The energy resolution attainable with STJ detectors is affected by several factors. In general, these factors may be divided into intrinsic and extrinsic contributions. Intrinsic contributions

are due to phenomena in the device itself that affect the conversion of incident photon energy into charge, while extrinsic factors come from the components used to measure the charge and provide correct operating conditions for the device. The intrinsic resolution, E_i , is itself dependent on several factors [11] and may be written as

$$\delta E_i = \sqrt{\delta E_{Fano}^2 + \delta E_{tun}^2 + \delta E_{part}^2 + \delta E_{geom}^2}. \quad (2.16)$$

The first term in equation 2.16 is the Fano-limited resolution from the charge-generation process, E_{Fano} . This is the same type of term that governs *e.g.* SSDs, gas proportional counters, or any detector where the photon energy is distributed among charge carriers with finite energies. The Gaussian energy resolution is then

$$\delta E_{Fano}(E_x) = 2.355\sqrt{F\epsilon_q E_x}, \quad (2.17)$$

with F being the material-dependent Fano factor, ϵ_q the energy required to create a quasiparticle, and E_x the energy of the absorbed x-ray [8]. For Ta, $F \approx 0.2$ and $\epsilon_q \approx 1.7\Delta$, which is greater than $\epsilon_q = \Delta$ due to losses to phonons that are either too low in energy or diffuse out of the superconductor before they may break a Cooper pair. The limiting energy resolution at 500 eV is then

$$\delta E_{Fano}(500 \text{ eV}) \approx 0.81 \text{ eV} \quad (2.18)$$

for Ta with $\Delta = 0.7 \text{ meV}$ at an x-ray energy of 500 eV. This is the fundamental physical limit that could be achieved if all other factors can be suppressed.

The next terms in 2.16 are due to the noise added by the multiple-tunneling process, termed the tunneling noise δE_{tun} and the partitioning noise δE_{part} . The tunneling noise is due to variance in the number of times a qp will tunnel before recombining, and is given by [10]

$$\delta E_{tun} = 1 + \frac{1}{\langle n \rangle}, \quad (2.19)$$

where $\langle n \rangle$ is the average number of times a qp tunnels. This parameter is then dependent on the thickness and effectiveness of the trap region, and the time for qps to recombine into Cooper pairs.

Partitioning noise δE_{part} is due to the randomness of electron- or hole-like state occupancy coupled with the fact that only qps at an energy at least eV_{bias} above the energy gap can reverse-tunnel against the bias. It is essentially a quantum mechanical by-product of the multiple pathways that are available for a quasiparticle at energy $E > \Delta + eV_{bias}$, whether to tunnel as a

quasi-electron or back-tunnel as a quasi-hole for example. The expression for this noise has been derived as

$$\delta E_{part} = 2e\sqrt{N_0\gamma_{av}(1-\gamma_{av})}, \quad (2.20)$$

where γ_{av} is the average fraction of quasiparticles that tunnel as holes and N_0 the total number of qps participating in the process [12]. γ_{av} is a function of the junction bias, as it depends on the fraction of qps above $\Delta + eV_{bias}$ in the electrodes, which causes the partitioning noise to primarily affect low-bias operation and having very little effect on higher-bias operation. The three terms δE_{fanor} , δE_{tun} , and δE_{part} are commonly combined into an overall term for the statistical processes underlying the charge generation process δE_{stat} , which when expressed in terms of the full width at half maximum (FWHM) may be condensed to the form [13]

$$\delta E_{stat}^{FWHM}(E_x) = 2.355\sqrt{\epsilon_q E_x (F + 1 + \frac{1}{\langle n \rangle})}. \quad (2.21)$$

The last term in equation 2.16 δE_{geom} is a lump term which covers several factors arising from the size and shape of the device and its interfaces. Another factor is phonon diffusion out of the device before breaking Cooper pairs. Phonons may be lost via several channels: into the substrate, through the edges of the device, and into non-superconducting contaminants on the surface. Edge losses also cause the responsivity to vary with position, with regions close to the edge having a reduced responsivity [14]. For square devices, the impact of edge losses scales inversely with device size, since the perimeter increases linearly while area increases quadratically as the edge size is increased. These factors are all very specific to the particular device and do not have an analytical form. However, they do scale regularly with photon energy E_x so that

$$\delta E_{geom} \propto E_x, \quad (2.22)$$

which causes δE_{geom} to dominate at high energy.

The factors mentioned previously which are not considered intrinsic to the device itself are the electronic noise δE_{elec} and the bias noise δE_{bias} . The bias noise is due to the stability of the circuit to hold a particular bias during data acquisition. Stability issues may also arise when several pixels share a common ground, as is common in many array designs. Bias noise is negligible in our current preamplifiers, which have a stability $< \pm 1\mu V$ over several hours, but it still is mentioned here as a consideration in the overall development of STJs as high-resolution detectors. The electronic noise, however, is always a finite component which does not change

with with photon energy E_x . This is noise due to intrinsic noise in the preamplifier components, as well as coupling of ambient radio frequency (RF) radiation into the amplification circuits. The latter may be decreased by shielding of the electronics, while the former is improved through careful analog and digital circuit design. Section 3.2 gives an overview of the specific amplifiers used with this particular STJ detector system.

Combining the intrinsic and extrinsic contributions in quadrature and neglecting bias noise results in the overall expression for device resolution

$$\begin{aligned} \delta E_{tot} &= \sqrt{\epsilon_q E (F + 1 + \frac{1}{\langle n \rangle} + \gamma) + \delta E_{elec}^2 + \delta E_{geom}^2} \\ &\Downarrow \\ \delta E_{tot} &= \sqrt{\delta E_i^2 + \delta E_{elec}^2}. \end{aligned} \tag{2.23}$$

2.2.3 Operation considerations

Among the physical requirements and considerations that must be addressed to operate STJs as a photon detector, the first most obvious consideration is temperature. These devices must be superconducting, which includes the lower-gap trap regions adjacent to the barrier. Table 2.1 lists the T_c and gap parameter of several superconductors of interest for STJ development. Due to the proximity effect and thinness of the layers, the trapping regions will have a higher T_c than their bulk material value.

Element	T_c (K)	2Δ (meV)
Nb	9.25	3.05
Ta	4.47	1.4
Al	1.175	0.34
Sn	3.722	1.15
Pb	7.196	2.73

Table 2.1: Properties of selected superconducting elements [15].

Although the entire junction may be superconducting below the transition temperature of the trapping regions, this is not sufficient to operate as a photon detector. Firstly, as demonstrated in figure 2.2, the gap parameter changes rapidly in the neighborhood of T_c and does not stabilize until $T \lesssim 0.3T_c$. As the number of quasiparticles generated by an absorbed photon is dependent on the size of the gap, this means that the measured pulse height for a given photon

energy changes with T close to T_c . Theoretically this could be accounted for by careful calibration of pulse height to temperature were it not for a second issue: background current from thermal excitations. The population of excitations above and below the gap as depicted in figure 2.3 is generated by phonons breaking Cooper pairs. The temperature must be low enough to “freeze out” all phonons with energies $> 2\Delta$ that may break Cooper pairs. The I-V curves in figure 2.4 demonstrate how the sub-gap current increases as the temperature approaches T_c . Large currents contribute shot noise $\propto \sqrt{I}$ that degrades resolution and eventually overwhelms the pulses generated by photons. In practice, the junction needs to be operated at temperatures $\lesssim 0.1T_c$ to achieve high resolution with stable pulse heights and minimal current noise.

Another important consideration concerns the presence of magnetic field as the device passes through T_c . As discussed at the end of section 2.1, type-II superconductors experience penetration of magnetic field in the form of a lattice of flux vortices where the material is driven normal. While a theoretical type-I superconductor will expel all applied flux by the Meissner effect as it passes through T_c , type-II superconductors, which include thin films of some type-I materials, do not behave this way. Instead, any field penetrating the sample during the transition is locked into place into a static lattice of flux vortices that persists even when all external fields are removed. A superconductor in this state is said to contain “trapped flux”. Any trapped flux in the junction creates small regions of SIN or NIN junctions, which increase the leakage current and degrade performance. Photon-detecting device geometries are typically of high aspect ratio with a total thickness $\lesssim 1 \mu\text{m}$ but edges of order $100 \mu\text{m}$, while flux vortex size is 10’s of nm. Therefore only the normal component of the magnetic field typically generates trapped flux with the vortices normal to the plane of the detector. Nb is a type-II superconductor, and while bulk Ta is type-I, it becomes type-II when deposited as a thin film. Therefore it is critical that Ta-based devices are well-shielded magnetically to fields normal to the surface plane of the devices as they pass through T_c .

While section 2.1.1 described the I-V curves in terms of tunneling of quasiparticles, there is another phenomenon which contributes to the tunneling current. This is the direct tunneling of Cooper pairs through the barrier mentioned in section 2.2.1. Described by Josephson in 1962 [16], this phenomenon is so important that SIS junctions are commonly called “Josephson junctions”, and the effect the Josephson effect. The first form of the Josephson effect, called the direct current (dc) Josephson effect, is a result of the phase coherence of $\theta(\vec{r})$ across junctions smaller

than the Cooper pair coherence length ξ_0 . The phases are offset by a difference ϕ , leading to a zero-field current density

$$J_{dc} = J_c \sin\phi = \frac{\pi}{4} \frac{(2\Delta)}{R_N}, \quad (2.24)$$

which has an amplitude J_c called the critical current density that depends on the gap parameter, junction area, temperature, and normal-state conductance R_N . Since spatial variations of the phase difference ϕ depend on the parallel component of an applied magnetic field [17], the current I_{dc} has a periodic relationship with the applied magnetic field, which follows the relation

$$I_{dc}(\Phi) = I_{dc}(0) \left| \frac{\sin(\pi\Phi/\Phi_0)}{(\pi\Phi/\Phi_0)} \right|. \quad (2.25)$$

Here Φ is the flux applied to the junction and Φ_0 the flux quantum. This results in an $I(\Phi)$ curve as plotted in figure 2.6. While we want to avoid any applied fields as the junction passes through T_c , after the device is cold we need to apply a magnetic field parallel to the device plane to suppress I_{dc} . The exact field strength depends on the geometry of the device, including the barrier thickness, length and width dimensions. Typical field values are on the order of 100 Gauss. As we still require the magnetic field to be minimized as the devices transit T_c , this requires an electromagnet in the vicinity of the detector chip. This magnet must lie inside of any magnetic shielding in place around the devices.

In addition to the dc Josephson effect, there exists an alternating current (ac) Josephson effect due to pair tunneling between Fermi levels separated by a voltage V . This creates an ac current at a frequency $f = 2eV/h \approx 0.5 \text{ GHz}/\mu\text{V}$. Since the wavelength of this ac Josephson effect is commensurate with the dimensions of the junction, it creates resonant modes called Fiske modes that produce current peaks in the I-V curve at voltages [18]

$$V_n = n\pi \frac{\hbar\nu_{ph}}{2eL}. \quad (2.26)$$

Here ν_{ph} is the resonance frequency of the resonator cavity formed by the junction and L is the length along a given dimension. A rectangular junction will have Fiske modes along each length dimension. Fiske modes also have a $\sin(\Phi)/\Phi$ dependence like the dc Josephson current, so applying a magnetic field will largely suppress these modes [19]. It is never possible to completely suppress all Fiske mode resonances in all detectors of an STJ array simultaneously, but it is still desirable to suppress the magnitude of the currents produced by the Fiske modes. This provides bias stability and helps prevent the bias from latching onto a Fiske mode when

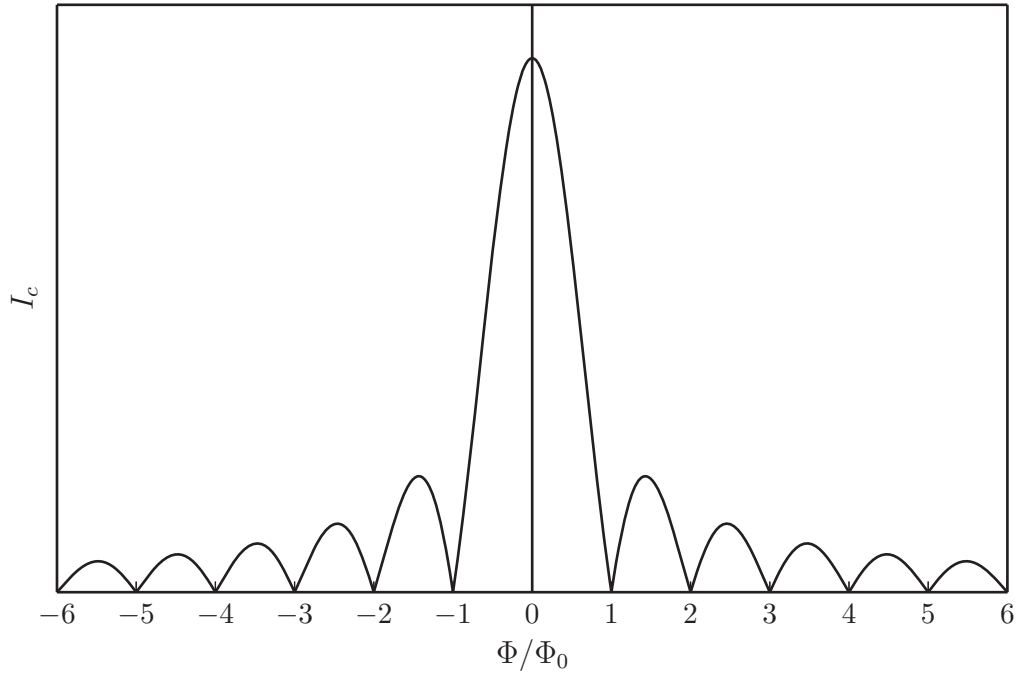


Figure 2.6: Maximum zero-voltage current vs. flux density in an SIS junction according to equation (2.25).

the junction is in an active state after absorbing a photon. Since the two dimensions of a rectangular junction are independent, the suppressing field should be applied along the diagonal so that each dimension experiences a component of the field. This sets the proper orientation of the devices to the detector magnets.

2.3 Device Fabrication

Tunnel junctions for photon detection are fabricated using the general methods of photolithographic thin film fabrication used in micro-electronic manufacturing. The process steps, including the order of layer deposition and etching, depend upon the composition of the layers and lead layouts. As described in section 2.1.1, a tunnel junction is formed when two superconductors are separated by a thin insulating layer acting as a tunnel barrier. For photon-detecting STJs, the top and bottom layers should be of the same material so that the qp recombination lifetimes and DOSs are the same. The top layer is called the absorber since that is the desired region where photons are to be absorbed. The smaller-gap material on either side of the tunnel barrier is the trap region.

The Ta-based process used for the STJ x-ray detectors in this dissertation is adapted from a

commercial Nb/Al process developed at STAR Cryoelectronics for superconducting quantum interference devices (SQUIDs). While Ta offers higher quantum efficiency and better limiting resolution than Nb due to its smaller gap parameter Δ_{Ta} , it can grow in two different solid phases which presents a challenge not present with Nb. The desired phase is body-centered cubic (bcc) or α -Ta phase with a comparably high $T_c \approx 4.4$ K, while thin films formed on certain substrates can generate tetragonal Ta or β -Ta [20, 21] with $T_c \approx 0.5$ K. Bulk Ta is entirely α -phase, and thin films are often mixed-states α and β , with the exact properties of β -Ta varying widely. What is known is that its transition temperature T_c is well below 1 K, leading to a much smaller Δ than α -Ta or Al. The formation of mixed α/β phases is strongly dependent upon the deposition conditions, so it is undesirable in a controlled process producing uniform, homogeneous films. A base layer of pure β -Ta is possible but undesirable in this application as it would have no trap region and hence no multiple-tunneling amplification.²

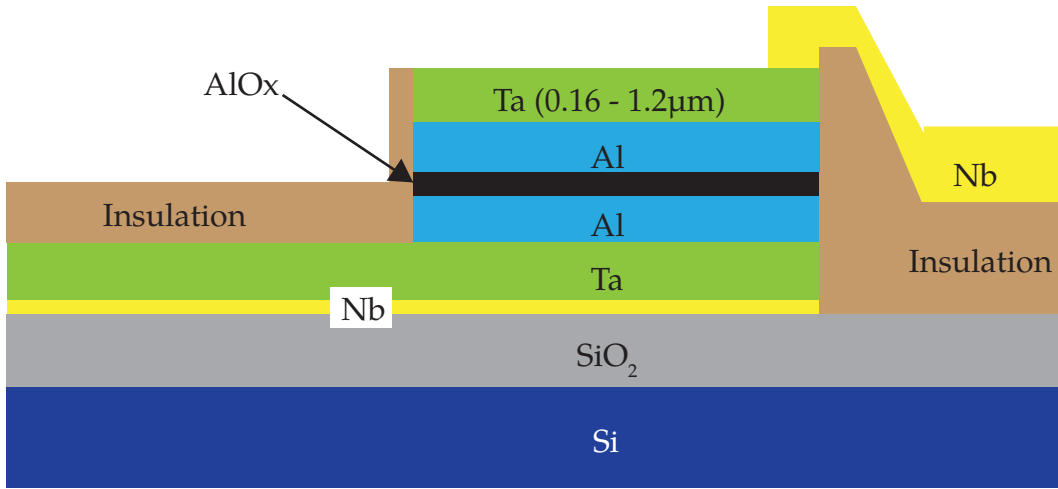


Figure 2.7: Cross-sectional schematic of STJ device: a thin layer of Nb is deposited to seed the α -phase growth of Ta in the bottom layer. The Al-aluminum oxide (AlOx)-Al trilayer is deposited in a single vacuum cycle along with the base and top Ta. The feature labeled “insulation” may be fabricated from different materials, including polymer or anodized oxide. The top traces are of Nb to prevent qp diffusion from the device into the leads.

The starting point of any micro-fabrication process is the substrate. Past STJ devices for photon detection have been produced on silicon [13, 22] and sapphire [23, 24, 25] single-crystal wafers. Silicon is easy to handle (etch and cut) and cheap, while sapphire is more thermally conductive. The substrate choice then depends largely on the process development. Our devices

²Pure β -Ta base layer devices may have other applications though, as eliminating the multiple-tunneling effect could produce devices with shorter pulse decay times (and hence faster pulses/greater photon flux potential) at the cost of decreased pulse height.

are fabricated on an Si substrate, as it adapts processes developed for commercial production of Nb-based SQUIDs and will scale well to larger production runs of STJ chips. A disadvantage to Si and SiO₂ is that it tends to favor the formation of β -Ta when Ta is deposited directly onto their surfaces. To overcome this, a thin layer (≈ 5 nm) of Nb is deposited initially onto the wafer surface. The bcc Nb subsequently seeds the growth of the correct α -Ta [26]. Since $\Delta_{Nb} > \Delta_{Ta}$ and the layer is very thin compared to the Ta base layer, this does not affect the function of the device.

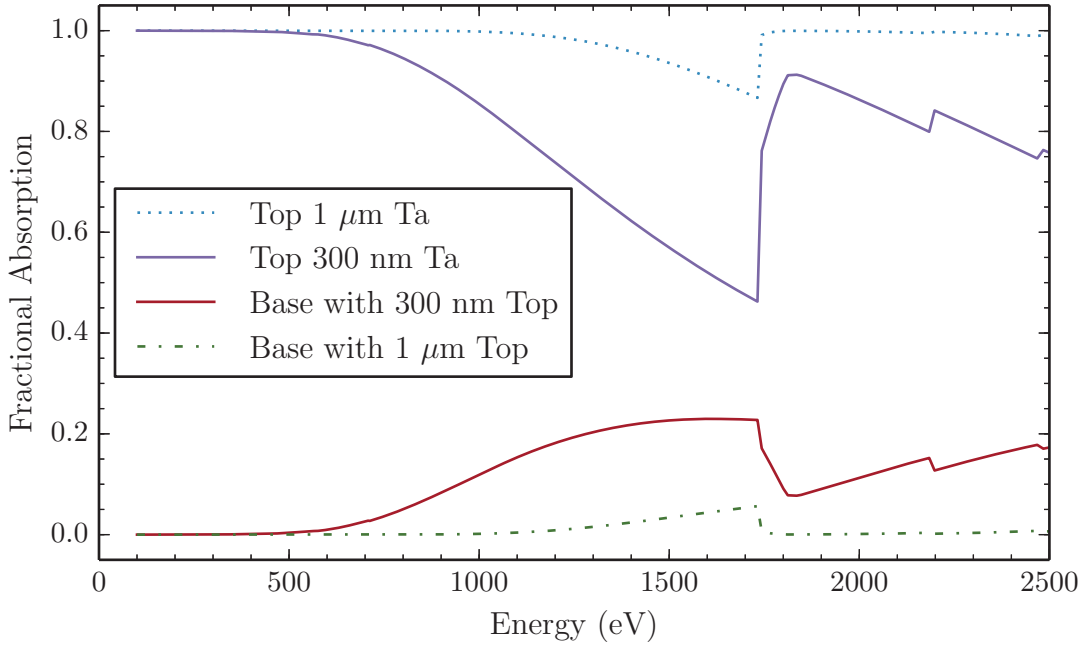


Figure 2.8: Fractional absorption of photons in top and bottom layers of Ta STJ devices as a function of photon energy for two different absorber thicknesses. Top and bottom layers include contributions from the 50 nm-thick Al trap regions. The Ta base layer is 265 nm thick, and does not absorb all photons that make it through the top layer. Those passing through the base and into the substrate are thrown away.

The heart of the process is the formation of a uniform, quality tunnel barrier. It should be thin enough to have a high tunneling probability without suffering from pinhole defects. Any microscopic holes in the barrier will lead to a shorted (dead) junction. Uniformity is also important to prevent geometric deviations from affecting the resolution too greatly.³ The most common barrier choice is Al₂O₃ (commonly called AlOx) due to ruggedness and ease of deposition control and purity. In addition, a reliable AlOx tunneling barrier process has been

³While other affects from the edge regions and surfaces dominate the geometric contribution to the resolution, surely we want barrier variance to play as small a role as possible.

developed previously as part of the Nb/AlO_x/Nb trilayer, a foundation of SQUID fabrication. An added bonus for our needs is that Al is an excellent material for the trap region, as it has a smaller gap than Ta but its T_c is not too low. The fabrication of the barrier is then a matter of depositing a layer of Al, oxidizing its surface, and covering that oxide layer with another Al trap film. The barrier thickness also affects the leakage current I_L and critical current I_c : both I_L and I_c decrease with barrier thickness. Normalizing I_c to the area to give the critical current density J_c , which then can be used as a parameter to characterize junctions independent of size. The range of J_c that gives good performance for radiation detection is generally 50 - 500 A/cm² [27], and for our devices we aim for $J_c \approx 150$ A/cm². This gives a barrier thickness of ≈ 10 nm, with ≈ 50 nm-thick Al traps on either side.

The base Ta layer thickness is 265 nm for all devices, while the top Ta layer thickness is variable. To increase absorption probability in the top layer it is desirable to make it as thick as possible, illustrated by the differential layer absorption plotted in figure 2.8. However, increasing the film thickness can negatively affect device performance by increasing δE_{geom} . The greater volume of thick films leads to more total lattice defects and imperfections, and the increased area of the edge interface around the device perimeter increases qp losses. There may also be strain in the film from mismatched lattice parameters at the interface with the Al layer and edges. In very thin films this strain is fairly even through the thickness of the film, but as the thickness is increased a strain gradient begins to form between the trap interface and the upper portion of the layer. This can distort the gap parameter and greatly impact performance. Addressing these problems is a matter of tuning the fabrication process for a given film thickness to achieve neutral strain, minimal defects, and uniform and controlled edge profiles [21]. For this project, devices with high resolution have been fabricated with up to 300 nm-thick absorbers, while 500 nm-thick absorbers have demonstrated lower but acceptable resolution. Absorbers of 1 μ m thickness are improving as well.

Device fabrication is performed on 4 inch diameter 0.5 mm thick silicon wafers. The mask layout has multiple arrangements of STJ devices, including 112-pixel array chips, two different configurations of 36-pixel array chips, and test chips with multiple pixel sizes and shapes for device characterization. The arrays are in the center of the wafer, with test chips on two sides to track variation across the wafer. Figure 2.9 is a rendering of the wafer layout showing all the mask layers. One wafer produces 12 112-pixel arrays and 16 of the standard square 36-pixel

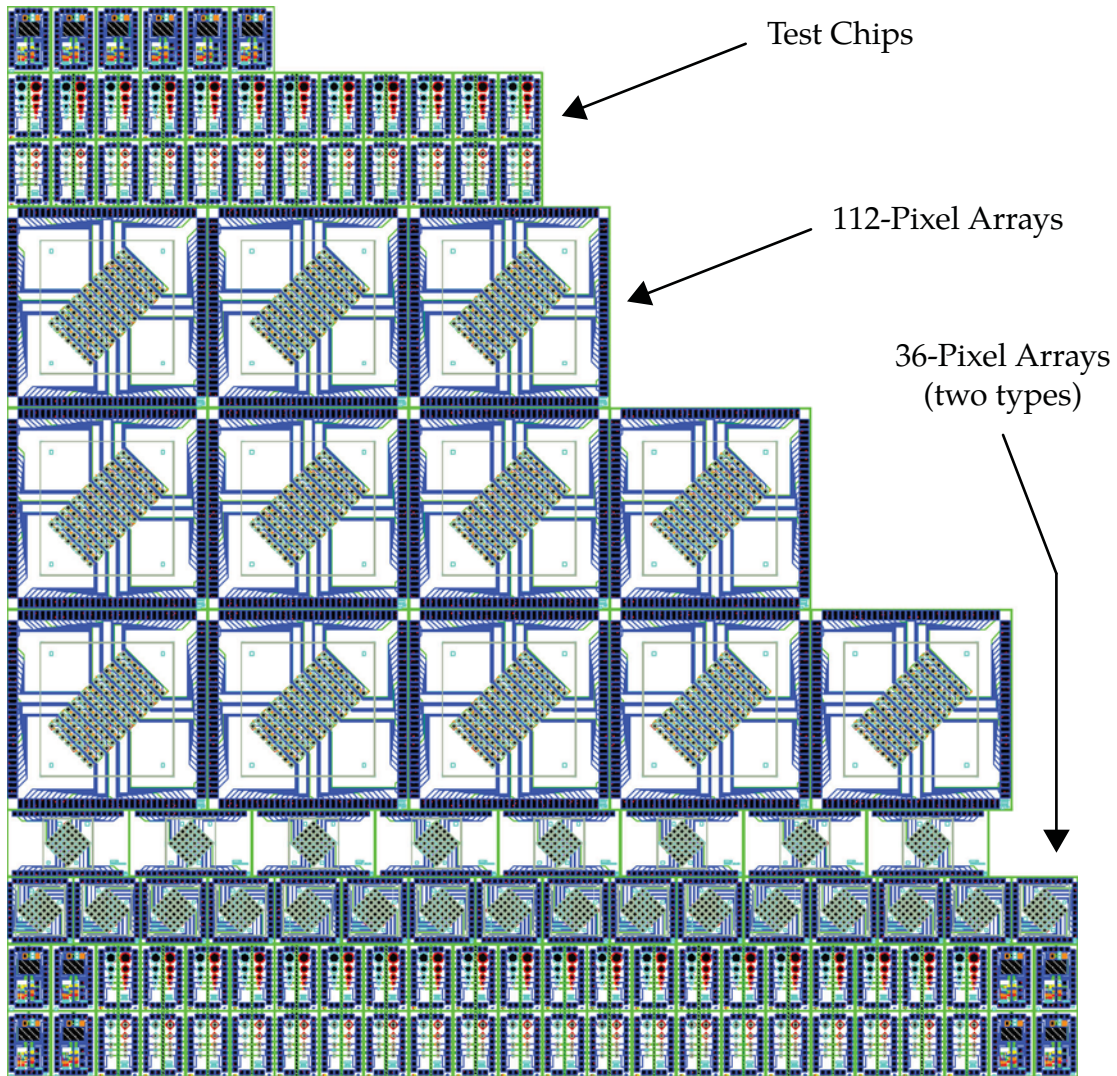


Figure 2.9: Rendering of die pattern used to fabricate STJ devices on a 4-inch silicon wafer.

arrays. A photo of a finished 36-pixel array chip is shown in figure 2.10.

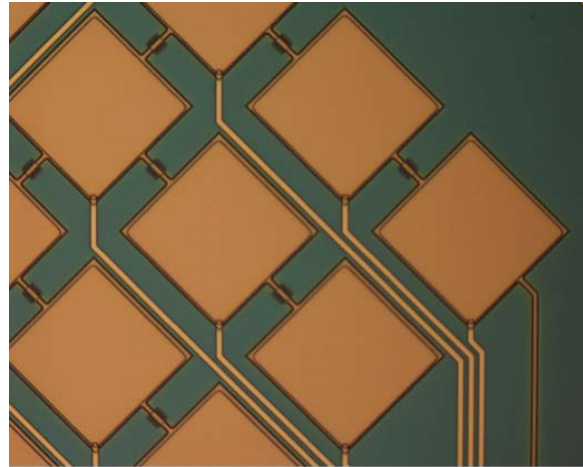
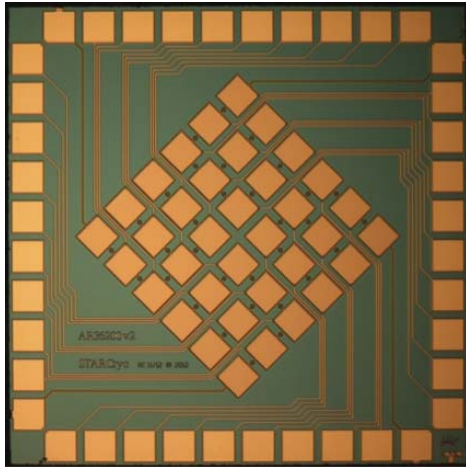


Figure 2.10: Photo of STAR Cryoelectronics 36-pixel array chip. The configuration is a 6×6 square array, with 4 quadrants of 9 pixels each sharing a common ground. Each quadrant along with its ground is routed to one row of bond pads at the chip edge, for 40 total bond pads and wires.

References

- [1] H. K. Onnes, "No Title," *Comm. Phys. Lab. Univ. Leiden*, vol. 29, 1911. (page 24)
- [2] W. Meissner and R. Ochsenfeld, "Ein neuer Effekt bei Eintritt der Supraleitfähigkeit," *Naturwissenschaften*, vol. September, pp. 787–788, 1933. (page 24)
- [3] J. Bardeen, L. N. Cooper, and J. R. Schrieffer, "Theory of Superconductivity," *Phys. Rev.*, vol. 108, no. 5, pp. 1175–1204, 1957. (page 25, 27)
- [4] C. A. Reynolds, B. Serin, W. H. Wright, and L. B. Nesbitt, "Superconductivity of Isotopes of Mercury," *Phys. Rev.*, vol. 78, p. 487, 1950. (page 26)
- [5] E. Maxwell, "Isotope Effect in the Superconductivity of Mercury," *Phys. Rev.*, vol. 78, p. 477, 1950. (page 26)
- [6] T. V. Duzer and C. W. Turner, *Principles of Superconductive Devices and Circuits, (Second Ed.)*. Upper Saddle River, NJ, USA: Prentice Hall PTR, 1999. (page 28, 32)
- [7] I. Giaever and K. Megerle, "Study of Superconductors by Electron Tunneling," *Phys. Rev.*, vol. 122, no. 4, pp. 1101–1111, 1961. (page 29)
- [8] M. Kurakado, "Possibility of High Resolution Detectors using Superconducting Tunnel Junctions," *Nucl. Instruments Methods*, vol. 196, pp. 275–277, 1982. (page 33, 36)
- [9] N. Rando, A. Peacock, A. van Dordrecht, C. Foden, R. Engelhardt, B. G. Taylor, P. Gare, J. Lumley, and C. Pereira, "The Properties of Niobium Superconducting Tunneling Junctions As X-ray Detectors," *Nucl. Instruments Methods*, vol. 313, no. 1-2, pp. 173–195, 1992. (page 33)
- [10] C. A. Mears, S. E. Labov, and A. T. Barfknecht, "Energy-resolving superconducting x-ray detectors with charge amplification due to multiple quasiparticle tunneling," *Appl. Phys. Lett.*, vol. 63, no. 21, pp. 2961–2963, 1993. (page 34, 35, 36)
- [11] K. Segall, C. Wilson, L. Frunzio, L. Li, S. Friedrich, M. C. Gaidis, D. E. Prober, A. E. Szymkowiak, and S. H. Moseley, "Noise mechanisms in superconducting tunnel-junction detectors," *Appl. Phys. Lett.*, vol. 76, no. 26, pp. 3998–4000, 2000. (page 36)
- [12] K. Segall and D. Prober, "Quantum partition noise in a superconducting tunnel junction," *Phys. Rev. B*, vol. 64, no. 18, p. 180508, Oct. 2001. [Online]. Available: <http://link.aps.org/doi/10.1103/PhysRevB.64.180508> (page 37)
- [13] S. Friedrich, J. B. LeGrand, L. J. Hiller, J. Kipp, M. Frank, S. E. Labov, S. P. Cramer, and A. T. Barfknecht, "High-Resolution Tunnel Junction Extreme Ultraviolet Detectors Limited by Quasiparticle Counting Statistics," *IEEE Trans. Appl. Supercond.*, vol. 9, no. 2, pp. 3330–3333, 1999. (page 37, 42)
- [14] R. Cristiano, E. Esposito, L. Frunzio, C. Nappi, G. Ammendola, L. Parlato, G. Pepe, H. Kraus, and P. Walko, "Quasiparticle diffusion, edge losses, and back-tunneling in superconducting tunnel junctions under x-ray irradiation," *J. Appl. Phys.*, vol. 86, no. 8, p.

- 4580, 1999. [Online]. Available: <http://scitation.aip.org/content/aip/journal/jap/86/8/10.1063/1.371406> (page 37)
- [15] B. W. Roberts, "Survey of Superconductive Materials and Critical Evaluation of Selected Properties," *J. Phys. Chem. Ref. Data*, vol. 5, no. 3, pp. 581–821, 1978. (page 38)
- [16] B. D. Josephson, "Possible New Effects in Superconductive Tunnelling," *Phys. Lett.*, vol. 1, no. 7, pp. 251–253, 1962. (page 39)
- [17] R. L. Peterson, "Sidelob Suppression in Small Josephson Junctions," *Cryogenics (Guildf)*, vol. 31, p. 132, 1991. (page 40)
- [18] M. D. Fiske, "Temperature and Magnetic Field Dependences of the Josephson Tunneling Current," *Rev. Mod. Phys.*, vol. 36, pp. 221–222, 1964. (page 40)
- [19] S. Friedrich, M. F. Cunningham, M. Frank, S. E. Labov, A. T. Barfknecht, and S. P. Cramer, "Fiske modes in superconducting tunnel junction detectors," *Nucl. Instruments Methods Phys. Res. Sect. A*, vol. 444, no. 1-2, pp. 151–155, 2000. (page 40)
- [20] M. Zhang, Y. Zhang, P. Rack, M. Miller, and T. Nieh, "Nanocrystalline tetragonal tantalum thin films," *Scr. Mater.*, vol. 57, no. 11, pp. 1032–1035, Dec. 2007. [Online]. Available: <http://linkinghub.elsevier.com/retrieve/pii/S1359646207005477> (page 42)
- [21] L. A. Clevenger, A. Mutscheller, J. M. E. Harper, C. Cabral, and K. Barmak, "The relationship between deposition conditions, the beta to alpha phase transformation, and stress relaxation in tantalum thin films," *J. Appl. Phys.*, vol. 72, no. 10, p. 4918, 1992. [Online]. Available: <http://scitation.aip.org/content/aip/journal/jap/72/10/10.1063/1.352059> (page 42, 44)
- [22] J. B. le Grand, C. A. Mears, L. J. Hiller, M. Frank, S. E. Labov, H. Netel, D. Chow, S. Friedrich, M. A. Lindeman, and a. T. Barfknecht, "A superconducting tunnel junction x-ray detector with performance limited by statistical effects," *Appl. Phys. Lett.*, vol. 73, no. 9, p. 1295, 1998. [Online]. Available: <http://scitation.aip.org/content/aip/journal/apl/73/9/10.1063/1.122372> (page 42)
- [23] P. Verhoeve, N. Rando, a. Peacock, a. van Dordrecht, a. Poelaert, and D. Goldie, "Superconducting tunnel junctions as photon counting detectors in the infrared to the ultraviolet," *IEEE Trans. Applied Supercond.*, vol. 7, no. 2, pp. 3359–3362, Jun. 1997. [Online]. Available: <http://ieeexplore.ieee.org/lpdocs/epic03/wrapper.htm?arnumber=622090> (page 42)
- [24] R. den Hartog, a. Kozorezov, J. Wigmore, D. Martin, P. Verhoeve, a. Peacock, a. Poelaert, and G. Brammertz, "Quasiparticle diffusion and the energy resolution of superconducting tunneling junctions as photon detectors. II. Experiment," *Phys. Rev. B*, vol. 66, no. 9, p. 094511, Sep. 2002. [Online]. Available: <http://link.aps.org/doi/10.1103/PhysRevB.66.094511> (page 42)
- [25] C. Jorel, P. Feautrier, and J.-C. Villégier, "Tantalum STJ for Photon Counting Detectors," *IEEE Trans. Applied Supercond.*, vol. 15, no. 2, pp. 587–590, 2005. (page 42)

- [26] D. W. Face and D. E. Prober, "Nucleation of body-centered-cubic tantalum films with a thin niobium underlayer," *J. Vac. Sci. Technol. A Vacuum, Surfaces, Film.*, vol. 5, no. 6, p. 3408, Nov. 1987. [Online]. Available: <http://scitation.aip.org/content/avs/journal/jvsta/5/6/10.1116/1.574203> (page 43)
- [27] K. Joosse, H. Nakagawa, H. Akoh, S. Takada, K. Maehata, and K. Ishibashi, "Effect of the Critical Current Density and the Junction Size on the Leakage Current of Nb / Al - AlO_x / Nb Superconducting Tunnel Junctions for Radiation Detection," *Jpn. J. Appl. Phys.*, vol. 35, no. 5A, pp. 2633–2637, 1996. (page 44)

Chapter 3

Cryostat Design

This chapter discusses the design and implementation of a liquid-cryogen-free cryostat that enables STJ detector operation at a synchrotron light source. For highest sensitivity in XAS experiments, the cryostat is designed to maximize solid angle while maintaining an energy resolution better than 10 eV FWHM. Since the largest junctions that achieve acceptable resolution are on the order of 200 μm per side, arrays are needed to achieve good collection solid angle. Our Ta-based STJs require temperatures below ≈ 300 mK to operate, and XAS requires a cryostat that can insert them into an end station as close to the sample as possible while maintaining low temperatures for long periods. This chapter discusses the design and construction of an adiabatic demagnetization refrigerator (ADR) with a liquid-cryogen-free pulse-tube cryocooler pre-cooling to 3 K and a 42 cm cold finger capable of operating chips with up to 112 STJ pixels at 100 mK. It also describes the preamplifier to read out STJ signals and the development of a new, compact, digitally-controlled 32-channel preamplifier by XIA LLC to allow operation of STJ arrays.

3.1 Cryogenic Development

The design requirements for the cryostat are to hold temperatures below 0.3 K for as long as possible, and the devices themselves must be well-shielded from d radiation to prevent heating. In addition, the detector array must be held on a cold finger that can be inserted into an end station for maximum solid angle coverage without exceeding the count rate capabilities of the detectors. Finally, automation and user-friendliness are very desirable.

The thermal load onto the detector cold stage at temperature T comes from both the mechanical support and thermal radiation from outer, warmer surroundings. The radiative thermal

load onto the inner stages may be approximated by the Stefan-Boltzmann law,

$$\begin{aligned}\frac{P}{A} &= \epsilon\sigma T^4 \\ \sigma &= \frac{2\pi^5 k^4}{15c^2 h^3} \approx 5.6703 \times 10^{-8} \text{ W/m}^2\text{K}^4.\end{aligned}\tag{3.1}$$

The emissivity ϵ is a property of the material surface, with $\epsilon = 1$ being an ideal radiative black-body. This relates the radiative power density of a body directly to its temperature. This relation also works in reverse when considering the radiative heat load onto a body from its warmer surroundings, which can be expressed as

$$\frac{P}{A} = \epsilon\sigma(T_S^4 - T^4),\tag{3.2}$$

where T_S is the temperature of the surroundings, and the object is at temperature T .

Since available cooling power is scarce at very low temperatures, typical cryostats are made with multiple cold stages. Outer, warmer stages with greater cooling power shield the inner, colder stages from thermal radiation. A common method is to use liquid cryogenics such as nitrogen at 77 K and helium at 4.2 K in reservoirs to cool outer and inner stages of the cryostat, respectively. An alternate approach is to use a helium gas closed-cycle refrigerator, often called a cryocooler, to replace the liquid reservoirs. While initially more costly and complex than liquid cryostats, closed-cycle refrigerators are easy to operate and may remain cold indefinitely with little attention. These dry cryostats are also gaining popularity as liquid helium is becoming more scarce and expensive, and as they require less training and associated hazards to operate.¹

Whether using liquid cryogenics or a cryogen-free system, additional cooling is needed to get the STJ chips below 0.3 K. Two types of sub-K cryostat which have been used for low-temperature detectors are helium dilution refrigerators and magnetic refrigerators. The former has the advantage of long hold time, at the tradeoff of increased complexity, size, and cost. Magnetic coolers, while requiring periodic regeneration to operate at a given temperature set-point, still have an excellent duty cycle for small loads like detector chips. Both types need other cooling mechanisms to reach a nominal starting temperature before the magnetic or dilution refrigerator may begin cooling below 1 K. To accomplish the goals outlined above, we have adapted an existing cryogen-free adiabatic demagnetization refrigerator (ADR) cryostat with features to support STJ arrays optimized for spectroscopy.

¹The term ‘‘Push-button cryostat’’ speaks to the simplicity of operating a cryocooler system.

3.1.1 Overall Structure

The base cryostat is the STAR Cryoelectronics DRC-100. This cryostat is built around a modified PT-407 pulse-tube cryocooler from Cryomech, Inc. This cooler has two cold stages, an upper stage rated at 25 W cooling power at 55 K, and a lower stage 0.7 W power at 4.2 K [1]. These are nominal values, and the actual base temperatures are typically lower depending on the thermal load. The upper stage can attain a base temperature of 30 K when unloaded while the lower stage may reach 2.3 K [2]. Based on typical operating parameters in the DRC-100 design, are typically referred to as the “60 K” and “3 K” stage, respectively. This type of pulse-tube cooler has a remote rotary valve which may be mounted with a flexible high-pressure line away from the main cold head. This is desirable for sensitive applications, since the rotary valve is the main source of vibration and may be isolated.

The outermost shell of the cryostat serves as mechanical support for all internal components, and as a vacuum chamber to thermally isolate them from the environment. High vacuum is necessary to prevent gaseous thermal conduction to the cold stages from the outer shell, which will be at the same temperature as the room in which the cryostat is operated, nominally 295 K. The vacuum shell is rectangular in cross-section to minimize the footprint. It is composed primarily of four parts: the top plate, upper and lower housings, and the base plate. All parts are machined from 6061-T6 aluminum alloy, and nickel plated to provide a highly-conductive, oxide-free surface. Each joint has two glands, with an inner groove retaining a viton o-ring to seal the vacuum and an outer groove for Spira-Shield electromagnetic interference (EMI) shielding [3]. All ports and vacuum-sealing surfaces have this double-groove arrangement to prevent stray EMI from entering the cryostat. The upper vacuum shell has a port to attach the pump-purge assembly, which includes a micro-Pirani pressure gauge and multiple valves.

The top plate assembly includes feedthroughs for the ADR heat switch drive-shaft and main connector plate. All wiring connections into the vacuum are carried on the connector plate, made from gold-plated brass or stainless steel depending on the application. Also connected to the top plate is the hitch plate assembly, which provides a lift point to suspend the cryostat from its service stand as well as protecting the pulse tube. Routine maintenance is performed by hanging the cryostat from the hitch plate and dropping the vacuum shells and radiation shields off the bottom.

The pulse tube cryocooler is mounted on the top plate of the vacuum shell, with its two cold

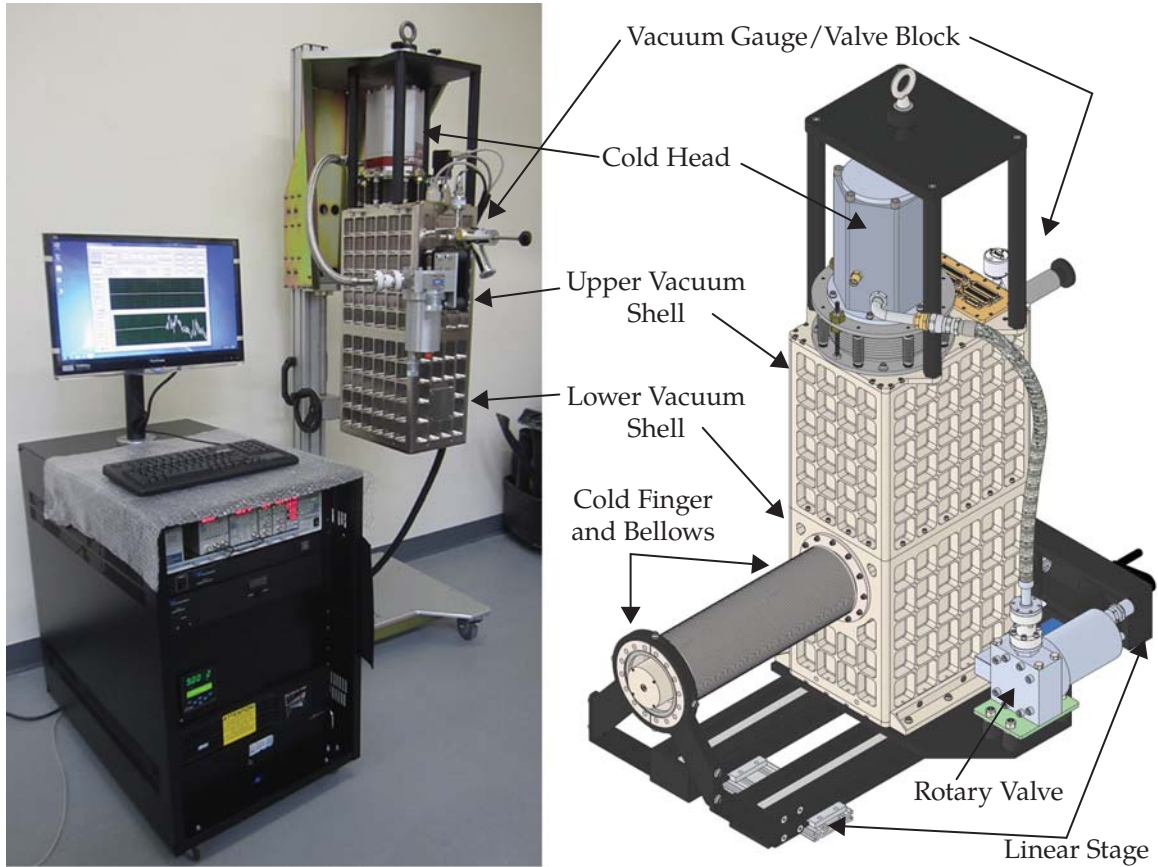


Figure 3.1: Overview of the DRC-100-based ADR cryostat. Left panel: A completed and operating DRC-100 cryostat hanging from its service stand. The mobile rack holds the control computer and electronics including thermometry, ADR magnet power supply, and pressure monitor. The control software logs all cryostat parameters and controls the ADR regeneration and control cycle. Right panel: Rendering of the external structure of the STJ cryostat, including the cold finger and linear translation stage. The rotary valve is moved from the upper rear of the vacuum shell to the linear stage plate to make room for the preamplifier electronics box described in section 3.2 (not pictured).

stages extending downward into the vacuum chamber. The pulse tube is not rigidly mounted to any part of the cryostat in order to decouple vibrations from its ≈ 2 Hz operating cycle. Instead, it is mounted to the top of the chamber on a sprung vacuum bellows. The bellows has adjustable stop nuts so that it may float free under vacuum but has minimal movement when brought up to atmosphere. Inside the cryostat, the pulse tube cold stages are thermally linked to the cryostat cold stages with flexible oxygen-free high-conductivity (OFHC) copper braid assemblies. These assemblies are laser-welded under vacuum, followed by vacuum annealing to maximize thermal conductivity while remaining flexible. While the braids allow the pulse tube ≈ 1 cm of motion, it is preferable for movement to be minimized after installation to maintain

the annealed state of the braids.

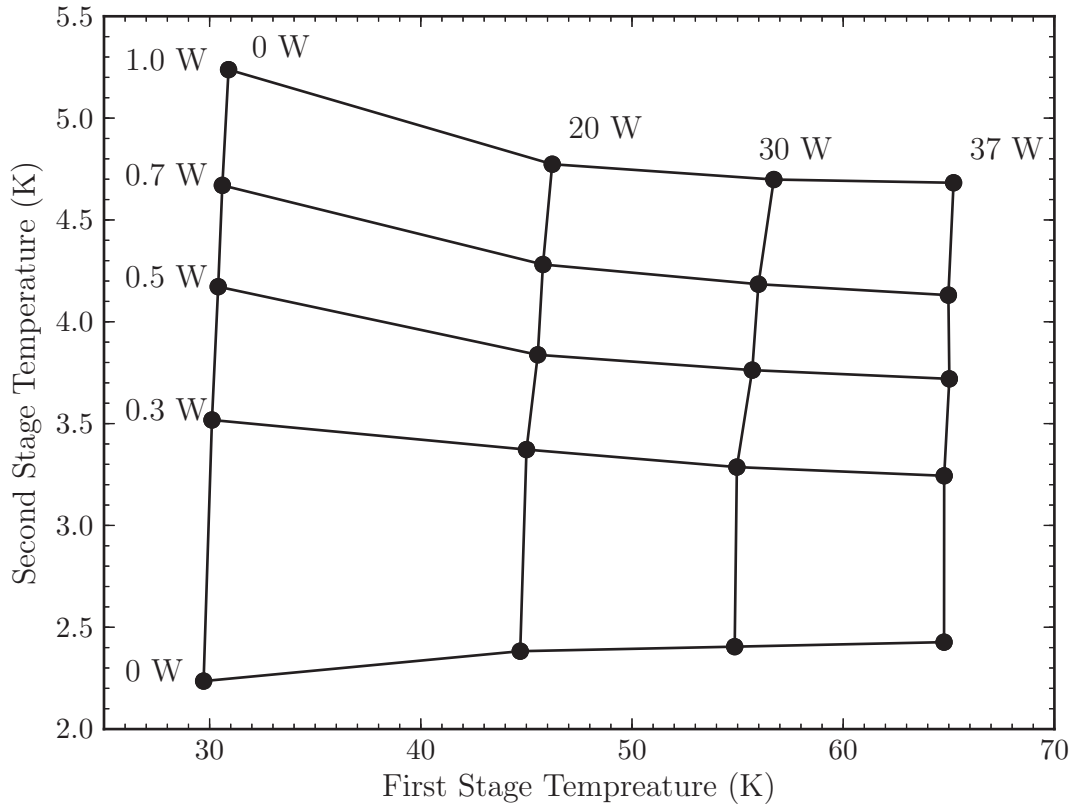


Figure 3.2: Capacity curve for the Cryomech PT-407 pulse tube [2]. The temperature of each stage is partially related to the load on the other stage.

Unlike the DRC-100 pictured in figure 3.1, the STJ will not be operated hanging from a service stand or stationary on a lab bench. When installed to an analysis chamber it must be possible to isolate the cryostat from the chamber vacuum with a gate valve, but during operation the end of the cold finger must be right up near the sample. This means it must be mounted to a linear translation stage. The cryostat rides on a parallel-drive manual stage from Velmex, Inc. The bottom of the lower vacuum shell is attached to an interface plate which bolts to the slide carriages. An insulating acetal sheet and standoff washers are used between the case and carriage plate as it must be electrically isolated from the main vacuum chamber to prevent ground loops. A custom snout vacuum bellows gives approximately 275 mm total travel. The base flange of the snout bellows is also electrically insulated from the cryostat case with a Viton sheet. The chamber end of the bellows has a rotatable 100-mm Conflat ultra-high vacuum (UHV) flange, which is supported from the linear slide by two-way adjustable bracket assembly.

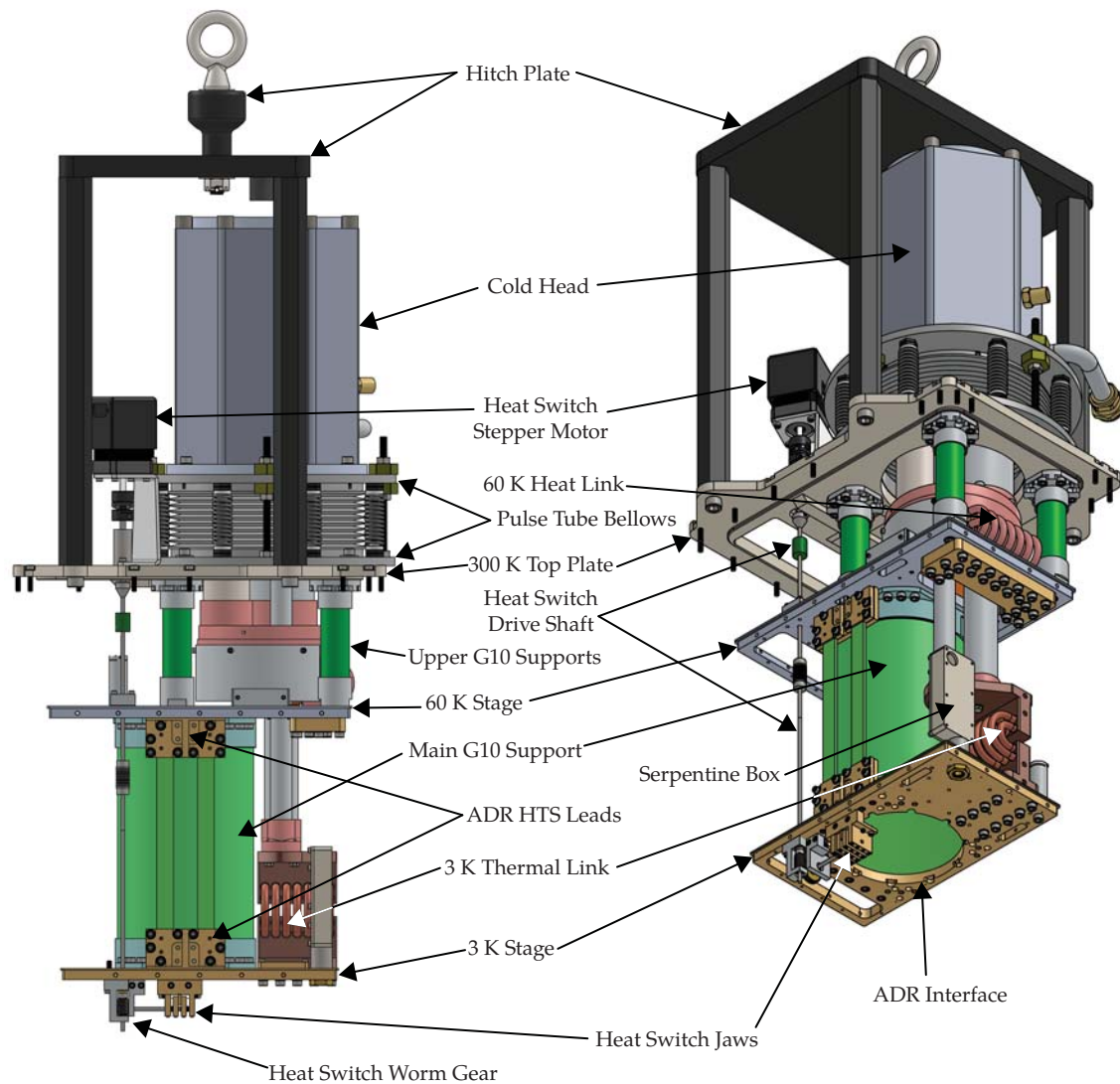


Figure 3.3: Internal components of the primary cryostat structure side view and isometric view. The ADR HTS leads are pictured installed but without copper or superconducting leads attached. The 300 K connector plate and feedthrough plates on the 60 K and 3 K stages are also absent. Notable features are the heat switch drivetrain and the open space inside the main G-10 support where the ADR assembly is inserted.

The cryostat internals are suspended from the top plate by insulating standoffs. G-10 fiberglass is one of the strongest and least thermally conductive structural materials through the cryogenic temperature range and is used as the insulator between stages. The 6061 Al 60 K stage is attached to the top plate by four small standoffs, and the OFHC 3 K stage is in turn suspended from the 60 K plate by one large G-10 tube which also surrounds the ADR mag-

net assembly. Radiation shields of nickel-plated 3003 aluminum alloy attach to each stage and surround the lower-temperature inner stages. Light-tightness of the radiation shields and all feedthroughs is essential to minimize radiative load onto each successive inner stage. To allow unhindered pumping to high vacuum, each stage therefore has a baffled assembly to allow gas movement while rejecting light. The 60 K stage has a simple baffle collar surrounding the descending pulse tube, while the 3 K stage has a machined “serpentine box” which is coated on the inside with a light-absorbing coating. Any wiring or other links that are routed to inner cold stages are heat sunk along the way to each successive stage. This includes the ADR heat switch, thermometry, signal looms, and magnet power leads.

The conductive heat load onto each stage via the structural members and other components would require finite elements analysis (FEA) to model accurately, but for a rough estimate we may use the simplified formula

$$P = k_{avg} A \frac{T_h - T_c}{d} \quad (3.3)$$

with the power in watts P depending on the average thermal conductivity k_{avg} in the temperature range between T_h and T_c , cross-sectional area A , and length d of the conducting member, between the higher T_h and lower T_c temperatures. As the thermal conductivity of most materials changes greatly over the cryogenic temperature range, we replace k with its average over the range of interest, calculated by

$$k_{avg} = \frac{1}{T_h - T_c} \int_{T_c}^{T_h} k(T) dT. \quad (3.4)$$

Other components and connections involving the ADR are discussed in section 3.1.2. At the 3 K and colder stages, all parts carrying a thermal load are fabricated from OFHC copper and gold-plated. While polished copper may have better emissivity and contact conductivity than gold, it degrades over time from surface oxidation so gold-plated surfaces are preferred for long part life. Some structural parts at 3 K are fabricated from unplated 6061 Al since they are surrounded by shielding at 3 K and have no thermal role. Table 3.1 lists estimates of the heat loads onto each main stage from different sources. The heat load onto the 60 K stage is dominated by radiation from the room-temperature vacuum shield, and the heat load onto the 3 K stage by the mechanical support of the G-10 posts.

Onto 60 K Stage (from 300 K)	
Heat Source	Power (mW)
G-10 Supports	780
Radiative	22,600
Heat Switch	50
Wiring	530
Total	$\approx 24,000$
Onto 3 K Stage (from 60 K)	
Heat Source	Power (mW)
G-10 Support	83
Radiative	12
Heat Switch	15
Wiring	7
ADR power leads	6
Total	123

Table 3.1: Heat loads onto the main stages of the cryostat from different sources. These estimates are for the base DRC-100 cryostat without cold finger assembly. The radiative loads are estimated using 3.2 with appropriate emissivities for the exposed surfaces from [4]. Conduction along various members is approximated using equation 3.3. Average thermal conductivities are calculated using data from [5, 6, 7, 8, 9, 10, 11] with equation 3.4.

3.1.2 ADR

The ADR is the heart of the cryostat that allows sub-K operation. Essentially it operates by magnetizing a paramagnetic material with a superconducting “ADR-magnet”, transferring the heat of magnetization into a thermal bath at 3 K through a closed heat switch, then decoupling the paramagnet from the bath by opening the heat switch and ramping the \mathbf{B} -field to zero. The concept of magnetic cooling single-stage ADRs has existed for some time [12, 13], but these require bath temperatures below 2 K to operate well due to the finite cooling power available from the paramagnet. The two-stage ADR developed around 1990 allows operation with a bath above 2 K by introducing a high-heat capacity intermediate guard stage between the bath and the detector cold stage to intercept the heat load from warmer stages [14]. Because of the final temperatures reached by each stage, they are referred to as the “1 K” and “50 mK” stages.

The primary components of an ADR are 1) a paramagnet to cool the cold stage, which is mounted in such a way to thermally isolate it from its surroundings; 2) an electromagnet to

magnetize the paramagnet; and 3) a heat switch that can controllably couple and decouple the paramagnet from a cold bath. An ADR is operated through a magnetic cycle illustrated in figure 3.4 which consists of four phases:

1. Magnetization of paramagnet
2. Dwell
3. Demagnetization of paramagnet
4. Temperature control or free phase

The starting point prior to magnetization has the heat switch closed to thermally anchor the paramagnet to the cold bath, which is 4.2 K for liquid helium cryostats and typically between 2.8-3.5 K for our DRC-100-based dry cryostats. With the switch still closed, a magnetic field is gradually ramped into the electromagnet to align the spins in the paramagnet which reduces entropy (path A, figure 3.4). This is done slowly to prevent eddy current heating and to allow the heat generated from the reduction in entropy to be bled into the thermal bath. Once full field strength is reached, the system is held in that state to allow all excess heat out to the bath until thermal equilibrium is reached (Dwell phase). The heat switch is opened to thermally isolate the paramagnet, and the field is ramped out of the electromagnet (path C). The energy required to increase the disorder of the spins comes from the thermal energy of the paramagnet and anything connected to it, causing it to cool as the field is removed. If operating in temperature control mode, the field is reduced until the target temperature is reached, then slowly ramped out under proportional-integral-derivative (PID) control to maintain temperature along path D' until the field reaches zero. Since STJs only require temperature below a certain threshold, they may also be run in free phase with the field completely removed and the temperature allowed to slowly drift up from the base temperature along path D. This reduces the complexity of the control electronics as well as the danger from stray magnetic field on the STJ devices. Once the temperature has risen above operating parameters, the heat switch is closed and the cycle restarts. The process along paths A through C is called a regeneration cycle.

The cryostat used in this dissertation uses two different paramagnets and two separate cold stages. Both are mounted inside one magnet, with the control focus on the colder 50 mK stage. Each of the two cold stages can be divided into a mechanical structure and a thermal structure.

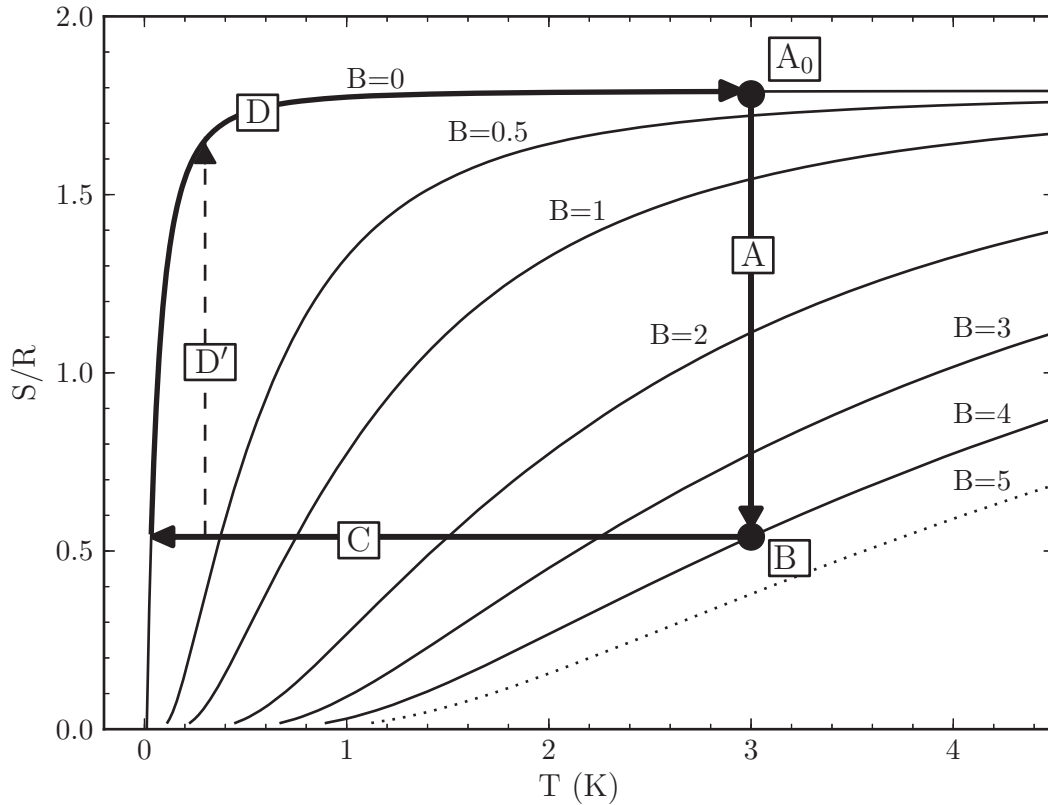


Figure 3.4: Entropy of ferric ammonium alum (FAA) vs. temperature in a magnetic field. The entropy is normalized to the universal gas constant R , with curves vs. temperature at indicated applied magnetic field B from 0 to 4 T, with the dotted $B = 5$ T curve shown for reference to wet cryostats. An ADR cycle starts at a base temperature on the $B = 0$ T curve at the point marked A_0 . The magnetic field is ramped up slowly so the FAA magnetizes isothermally along path A. The final field at point B is held for a time to allow all excess heat to diffuse into the thermal bath. The FAA is decoupled from the bath and demagnetized along path C. For non-regulated operation the field is completely removed, reaching a final base temperature where path C intersects the $B = 0$ T curve and gradually warming along path D. If temperature regulation is desired, some residual field is left in the magnet and removed with the aid of a PID controller to follow path D' . Curves generated from thermodynamic data from [15] and [16]

The mechanical structure supports and thermally isolates each stage from one another and from the rest of the cryostat. The thermal structure is the actual portion of the stage that holds the paramagnet and cools the load. The thermal structure is made from OFHC copper rods, with each stage having a horizontal and a connected vertical rod. These rods are suspended by a series of puck assemblies threaded with Kevlar string, which has a very high ratio of strength to thermal conductivity. The 1 K stage is suspended from the 3 K base puck, and the 50 mK stage is in turn suspended from the 1 K stage, allowing each stage to be thermally isolated

while maintaining mechanical rigidity. The arrangement of the puck components is illustrated in figure 3.5. Unlike most materials, Kevlar actually elongates slightly as it is cooled from room temperature, so each component of the puck is made from a different material so that differential contraction between the parts increases the tension on the Kevlar. The outer puck frame is machined from 6061 aluminum, the 1 K mount from Ti-6-4 alloy, and the 50 mK mount from brass. When cooled, the Ti contracts the least and the brass the most. The Ti mounts also have a clamp section made from OFHC copper, since copper rods would shrink and loosen inside a clamp made of Ti. There are two versions of the puck assembly, one full-thickness version which is installed on the top position inside the magnet shield, and three low-profile versions with reduced-height 4 K puck frames to free up room for accessories.

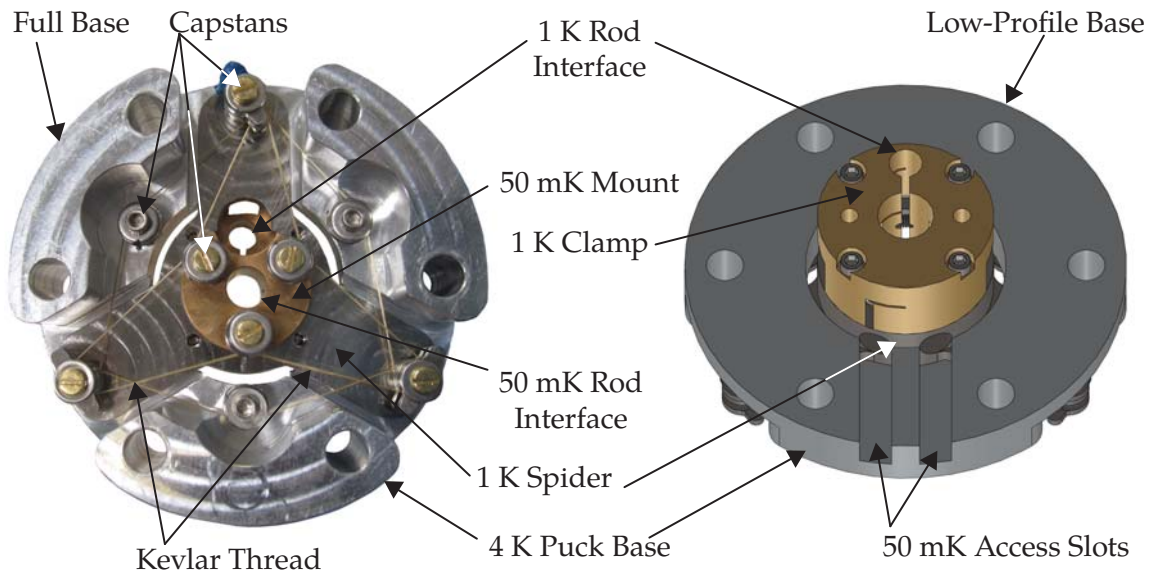


Figure 3.5: ADR suspension puck components. The left view is a photo of an assembled full-thickness puck to illustrate the routing of the Kevlar threads. The right view is a model rendering of a low-profile puck from a rear oblique view to show the separate copper 1 K rod clamp attached to the Ti 1 K mount. The parts marked as “Interface” are where the 1 K and 50 mK rods pass through and are clamped to the puck.

As annotated in figure 3.6, each rod is supported by two pucks and linked with a connector block to form the rigid assembly. The ADR U-frame along with the pucks and ADR baseplate form the mechanical support structure. The three pucks outside of the magnet have aluminum puck covers to protect the Kevlar thread. Each stage also has thermometer blocks for semiconductor-type ruthenium oxide (RuOx) thermometers, and thermal links to the heat switch to allow each stage to be connected or disconnected from the 3 K stage as needed for the

magnetization cycle. The heat switch itself is not shown in figure 3.6, but the components are visible in figure 3.3. The mechanical heat switch has a set of OFHC Cu jaws driven by a worm gear on a shaft that passes up to the 300 K top plate. A stepper motor outside the vacuum chamber is coupled through to the shaft by a ferrifluidic feedthrough. The jaws clamp onto the ADR heat link paddles along with a link on the 3 K plate, forming a thermally conductive path when closed. Opening the switch releases the jaws and removes the conductive path. The thermal continuity is checked by wires connected to the 1 K and 50 mK thermometer blocks. When the switch is closed, the inner stages are electrically connected to the cryostat case which may be confirmed with a multimeter. The open switch state naturally shows as an open circuit on both touch wires.

The cooling power is provided by paramagnetic materials inside a superconducting magnet, visible in the upper portions of figure 3.6. The 1 K stage in this ADR design uses gadolinium gallium garnet (GGG) with the chemical formula $\text{Gd}_3\text{Ga}_5\text{O}_{12}$. It has a total spin of $\frac{7}{2}$ but exists in the form of a spin-liquid without a well-defined magnetic ground state [17]. Its ordering temperature is ≈ 0.7 K and it has a large heat capacity while being fairly thermally conductive. It is used as a heat sink for wiring between 3 K and the FAA stage. The gadolinium gallium garnet (GGG) is purchased commercially in single-crystal form and machined to its final shape, yielding a 144 g crystal with one surface polished to $0.2 \mu\text{m}$ average roughness to provide good thermal contact. Without thermal load, this material can reach ≈ 400 mK but since it is used as a thermal block in this cryostat it typically reaches 800-900 mK.

The primary 50 mK stage is cooled by a pill of hydrated ammonium iron(III) sulfate dodecahydrate salt with a chemical formula of $\text{Fe}(\text{NH}_4)(\text{SO}_4)_2 \times 12\text{H}_2\text{O}$, more commonly called ferric ammonium alum (FAA). The ground state of the Fe(III) ion is ${}^6\text{S}_{\frac{5}{2}}$. Hydration is important to prevent spin ordering between adjacent iron sites, so the salt pill must be grown slowly, and can not be exposed to vacuum or temperatures exceeding its breakdown temperature $\approx 40^\circ\text{C}$. To protect it from vacuum, the salt pill is grown inside a stainless steel can which is sealed after growth. Since FAA is also a poor thermal conductor, a fan-like array of pure gold wires extend from the base of the can throughout the salt pill. Gold and stainless steel are necessary as the FAA is very corrosive and would oxidize copper. The total weight of the FAA salt pill is ≈ 52 g. The rod supporting the pill passes through a hole cut in the center of the GGG crystal without touching it.

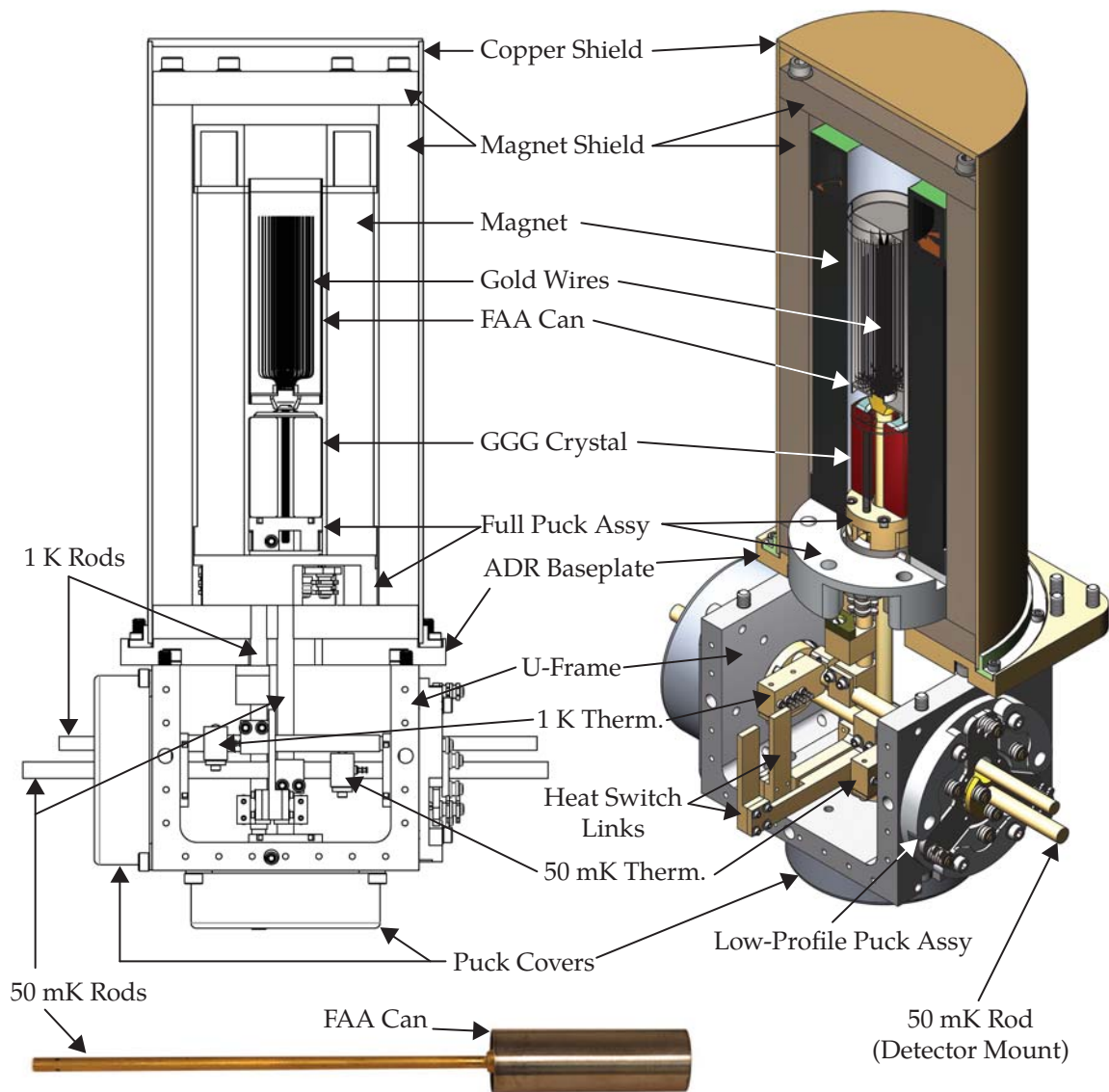


Figure 3.6: Cutaway views of the ADR assembly in a standard configuration. The copper shield, magnet shield, magnet, and ADR baseplate have been cut away, as well as the GGG and FAA paramagnets. Two of the low-profile pucks mounted to the U-frame have covers, while the third uncovered puck is where the superpuck is installed (see section 3.1.3). The single full-thickness puck assembly mounted inside the magnet shield is upside-down compared to the other three pucks, with the GGG crystal mounted directly to the 1K rod clamp. The whole pictured ADR assembly is built as pictured and mounted to the underside of the 3 K stage baseplate. The magnet is mounted to the face of the thicker puck, with the magnet shield base sandwiched between the puck and the ADR baseplate. Not shown is a channel for the magnet leads along the copper shield and through the top of the magnet shield. The parts labeled “1 K Therm.” and “50 mK Therm.” are the thermometer blocks for attaching RuOx thermometers and leads.

The two paramagnets are suspended inside the bore of a superconducting magnet which applies the field for the magnetization cycle. This magnet design has an operating field of 4 T at 8 A DC current. While many ADR designs in liquid He cryostats use a 5 or 6 T magnet, the lower starting temperature of this dry system allows a smaller magnet to reach the same or better base temperature as evident from figure 3.4. The low current needs also allow smaller copper leads from 300 K to 60 K. The magnet leads between the 60 K and 3 K stages are made from high- T_c $\text{Ba}_2\text{Sr}_2\text{Ca}_1\text{Cu}_2\text{O}_8$ (BSCCO) strips mounted in G-10 fiberglass supports. This reduces the thermal load onto the 3 K stage both from the wires themselves and from ohmic heating when a current is applied. All leads from 3K to the magnet are low- T_c multifilament superconducting NbTi magnet wire. Installed in the top cover of the magnet are a Si diode thermometer and a cernox resistive temperature detector (RTD) thermometer to monitor the magnet temperature for quench prevention². The RTD is not sensitive to magnetic fields but has variable calibration, while the diode has stable calibration while being unusable in magnetic fields. So, the diode is used to calibrate the RTD prior to running the first regeneration cycle. Surrounding the ADR magnet is a thick magnetic shield of vanadium permendur³ to minimize flux outside the magnet. This material has among the highest saturation limits at ≈ 2.3 T through a wide temperature range [18]. Vanadium permendur is a relatively poor conductor and cannot be plated, so a copper heat sink shield surrounds the magnetic shield to cool it and protect it from its surroundings (as the top of the magnet shield lies just below the 60 K stage).

3.1.3 Cold Finger

The cryostat so far described will achieve a base temperature of around 50 mK but needs adaptation to function as a detector for XAS. The STJ array chip must be positioned as close to the XAS sample as possible to maximize solid angle for collection of photons. A cold finger assembly with the detector chip on the end is therefore necessary to allow insertion of the detector chip into the analysis chamber. The heat load onto the detector stage and other stages must be minimized as well, requiring that several nested layers are needed to shield the internals from thermal radiation. The assembly has outer radiation shields extending from the 60 K and 3 K stages, and an innermost detector rod connected to the ADR 50 mK stage that holds the STJ chip. The outer shields are referred to as the 60 K and 3 K snout shields. The ends of the cold fin-

²Quenching a superconducting magnet occurs when the entire magnet rapidly goes normal from the superconducting state, generating heat and risking damage to the magnet.

³Composition: 49% Fe 49% Co 2 % V by atomic fraction.

ger must be able to admit x-ray photons to the detector chip while rejecting lower-energy light to minimize radiative heating of the detector stage. This requires several IR-blocking filters at multiple temperatures to prevent radiative loading of the stages . The size of the cold finger is designed around the 112-pixel array chip and carrier, which sets the minimum size inside the 3 K snout shield. A 36-pixel carrier is also compatible.

The 60 K snout is made from Ni-plated 6061 aluminum alloy to save weight. A can-shaped magnetic shield of CO-NETIC alloy from Magnetic Shield Corp. fits over the end of the 60 K snout to protect the detector chip. The 60 K snout shield mounts directly to the lower 60 K radiation shield, while the inner 3 K snout shield is mounted to a support member extending from the ADR frame. This support is called the superpuck because it replaces one of the puck covers over the Kevlar suspension puck and is made from 6061 aluminum. An OFHC copper baffle ring mounts to the end of the superpuck to block light from passing through the hole in the 3 K lower radiation shield. This baffle ring is the mount point for the 3 K snout. A braided copper heat link clamped between the 3 K stage plate and a the baffle ring provides the main cooling pathway for the 3 K snout. Two IR filters in a carrier assembly are placed on the end of the 3 K snout shield while the 60 K magnet shield has a 12 mm hole to pass photons. The 3 K snout shield itself is gold-plated OFHC copper, with flat sections at the end to mount the detector magnet coils and a detachable endcap for accessing the detector chip.

The STJ detector magnets are in the form of a split pair of coils installed on the outside of the 3 K snout shield. The windings are multi-filament NbTi in Cu matrix from Supercon, Inc.⁴ This wire is wrapped around a bobbin allowing for approximately 1800 turns per coil. The bobbin itself is rectangular in cross-section to save axial space at the end of the cold finger. While this shape and the separation of the coils is non-ideal for field strength and uniformity compared to typical Helmholtz coil design, it functions well in this setting. As the devices only require an in-plane field of order 3 mT, the current needs are small. Additionally, field expulsion from superconducting regions of the STJs renders them unaffected by out-of-plane fields provided they are small. The bobbins are made from gold-plated OFHC copper and have a rounded edge profile to add room between their corners and the surrounding 60 K snout shield.

⁴The specific wire used is type 56S53, with 56 30 μm -diameter filaments in the copper matrix, with an overall wire diameter of 0.33 mm including formvar insulation.

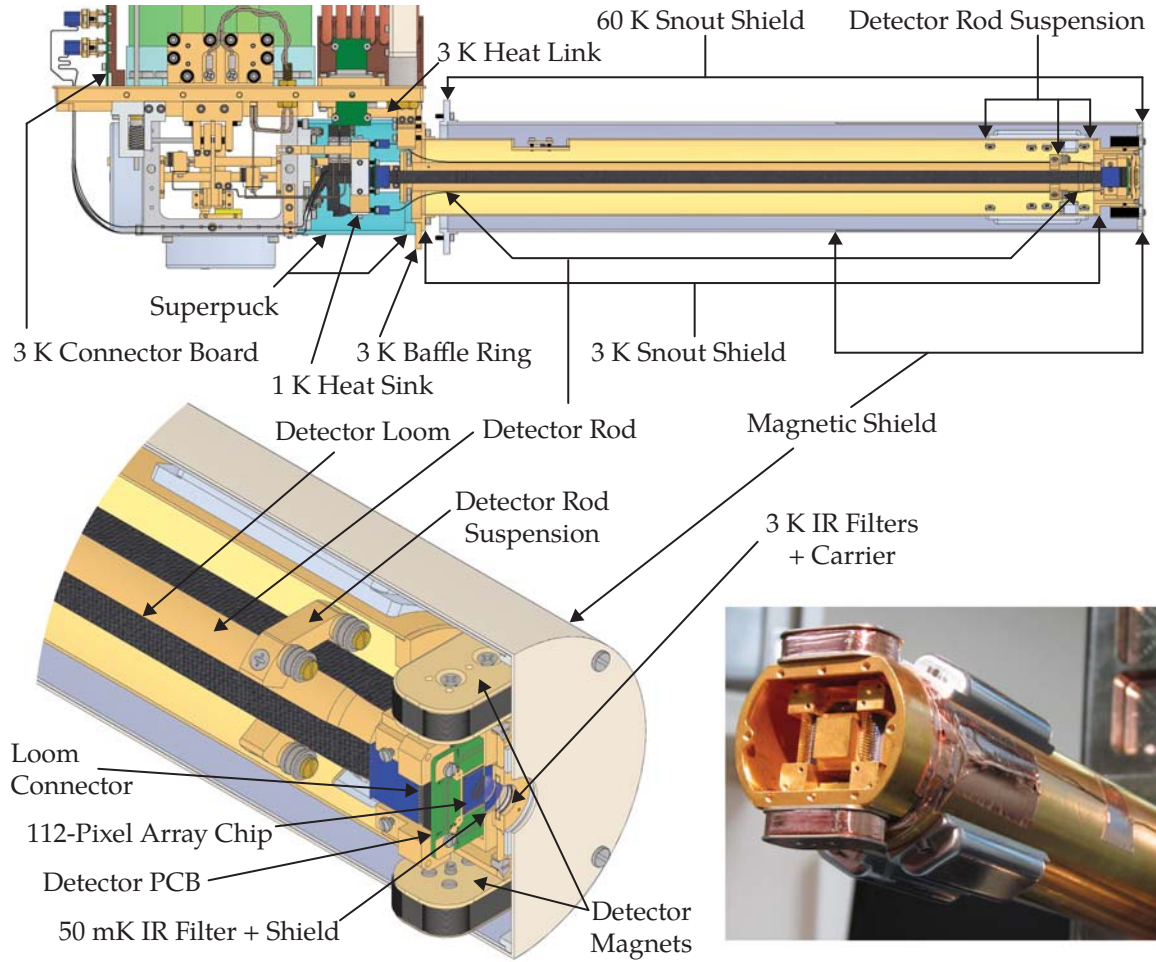


Figure 3.7: Cutaway vies of the overall version I cold finger assembly installed on the ADR. The 60 K snout shield in the upper view mounts to the lower 60 K radiation shield which is not shown, so it appears to float in space here. The lower right photo taken during cold finger assembly shows the detector rod installed with suspension inside the 3 K snout shield. The detector chip, 3 K end cap, and 60 K snout shield assembly are not installed in the photo.

In designing the IR filters, we consider the Planck radiation formula for a blackbody

$$S(\lambda) = \frac{2hc^2}{\lambda^5} \frac{1}{e^{hc/\lambda kT} - 1}, \quad (3.5)$$

with the radiated power density $S(\lambda)$ in units of $W/sr\ m^3$. The m^{-3} is composed of an area component in m^2 from the area of the emitting body, and a wavelength component in meters. For other measurements, a more convenient unit is $W/sr\ m^2\ nm$, which re-scales equation 3.5 by 1000: $S(\lambda_{nm}) = S(\lambda_m)/1000$. Figure 3.8 shows the shape of this distribution for room temperature (295 K) and 60 K. The room T emission peaks around $10\ \mu m$, which is in the mid-IR band, while the 60 K radiation is vanishingly small in comparison and peaks at much longer

wavelength. So, the most important band to filter out is between roughly 5 - 30 μm .

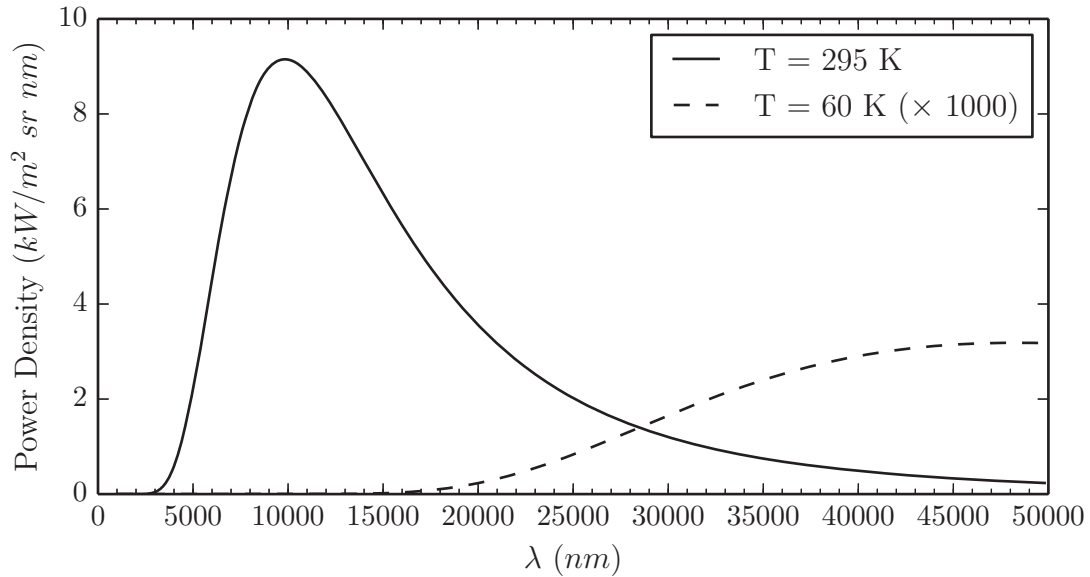


Figure 3.8: Power emitted by blackbodies at room temperature and 60 K. The 60 K spectrum has been multiplied by 1000 to make it visible on the same plot as the room T spectrum.

The requirements for the IR filters are reasonable transparency to soft x-rays, opacity to optical and lower-energy photons, and good thermal anchoring so that the middle of the filter is not significantly higher temperature than the rest of the shield. A common choice for this energy band is a polymer film coated with a thin layer of aluminum [19, 20]. The polymer backing provides mechanical support allowing for very thin Al films, while the Al film is the primary blocker of low-energy photons. STAR Cryoelectronics has developed a microfabrication process to produce such filters in-house. The filters consist of a polyimide (Kapton) film deposited onto a 0.2 μm Si substrate which is then coated with an Al film. A center circular opening is etched from the backside of the substrate, and the frame size is determined by patterning and etching through all layers. The filter may be made in an arbitrary shape by patterning, with the polymer/Al film freely suspended over the central opening on a Si frame. The current design for this spectrometer is circular, with an outer diameter (OD) of 10 mm and an inner open window of 6.35 mm diameter and films with 350 nm polyimide and 100 nm aluminum. Aluminum is chosen because its low atomic number makes it relatively transparent to low-energy x-rays compared to other metals. This design was initially made for a 1800 eV target energy, which means the Al film is somewhat thick for operating at or below 500 eV. Future runs of 60 and 20 nm Al will be optimized for lower-energy XAS as discussed in chapter 6.

At the heart of the cold finger assembly is the detector rod which carries the array chip. This design accommodates either 36- or 112-pixel chips on a printed circuit board (PCB) mount board. The signal and ground wires are carried from the chip by 2 or 4 woven superconducting wire looms with 32 wires each. The looms are manufactured to specification by Tekdata Interconnect Systems and have nylon thread interwoven with the wires for mechanical support. The end of the detector rod must serve multiple functions. The detector carrier board mounts directly to the end for thermal contact. The design specifications required all components of the cold finger be demountable while the vacuum shell and internal shields are installed, so the chip board and looms are connectorized using adapted micro PCB headers. The rod end has clamps that retain the ends of the detector looms while thermally anchoring them at 50 mK. Finally, to prevent stray leakage radiation from reaching the STJs, a chip cover with an IR filter is installed immediately in front of the detector. The chip cover completely covers the chip carrier and has extra radiation blocks that extend back over the looms to the loom clamps. The base of the rod is clamped directly to the ADR 50 mK horizontal rod around the area shown in figure 3.6 as "Detector Mount". Since the rod must be installable through the snout port, it has a joint where it may be detached from its clamp base.

The detector wiring path must travel from 50 mK at the chip to the 300 K top plate which requires good heat sinking at each cold stage to minimize the heat load. The looms also must be detachable at the base of the rod while also being heat-sunk to the 1 K stage between the detector rod and the 3 K stage. This is accomplished by a heat sink block with more clamped connectorized looms. Another set of looms travels from the 1 K block through the 3 K baseplate to the a breakout PCB mounted to the 3 K stage. This board reroutes the signals and grounds from the 32-wire looms into the correct ordering for the 78-wire looms which travel through the 60 K stage to the 300 K top plate.

Since the detector rod supporting 112 pixels is quite heavy with a center of mass many cm from its mount point to the ADR rod, it is significantly deflected if unsupported. The solution to this problem is a supplementary suspension between the 3 K snout shield and the detector rod. The requirements for this suspension are stringent, as all the cold finger components must be installed sequentially through the snout port and there is finite space between the 3 K and 60 K snout shields for components. Like the ADR pucks, this suspension uses tensioned Kevlar thread. Unlike the pucks, it only fully restricts motion along one degree of freedom (vertically).

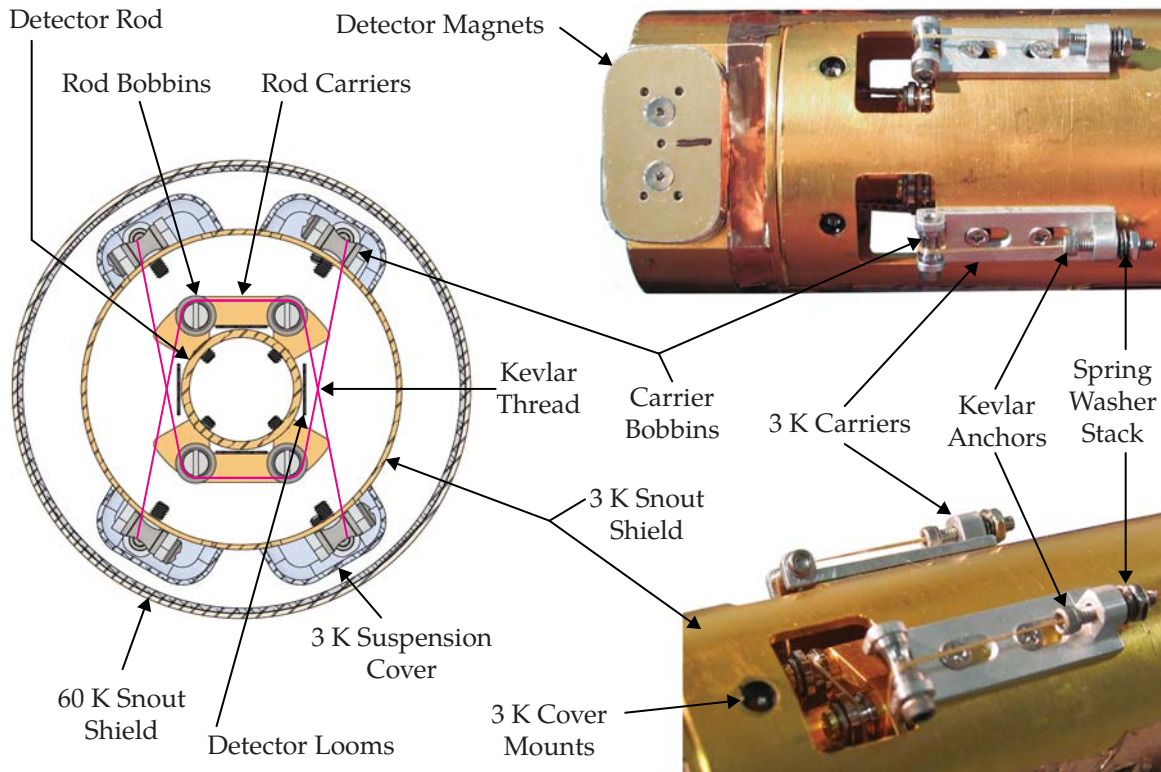


Figure 3.9: Views of the detector rod suspension design. The left figure shows a cross-sectional view of the nested shields and detector rod forming the cold finger assembly. The position of the suspension components in relation to the snout shields is visible, with the routing of the Kevlar thread shown in magenta. The photos on the right show the suspension installed without the protective covers. The installed 3 K covers are visible in the lower right photo in figure 3.7.

Without the benefit of differential contraction of components to counteract Kevlar elongation, it also needs to be tensioned with a spring mechanism to apply a preload.

The design of the suspension is illustrated in figure 3.9. The four carrier assemblies on the outside of the 3 K snout shield anchor the Kevlar thread assemblies, which pass over stainless steel bobbins through access holes in the 3 K snout. The two thread assemblies pull upwards and downwards on the detector rod to hold it firmly in the center of the bore. Each thread assembly is fabricated by threading a length of Kevlar through two center-drilled 2-56 machine screws and bonding it in place with Stycast epoxy. This is performed in a jig that places tension on the Kevlar while the epoxy sets so that it does not break free when tension is applied later during installation. The thread assemblies are tensioned by a nut with a stack of Belleville spring washers against the carrier assembly. Low-profile covers shown in figure 3.7 protect the components and cover up the holes in the 3 K snout shield. The first generation covers were

made from 6061 aluminum alloy for cost and weight savings but their performance was very poor. Second generation covers are gold-plated OFHC copper.

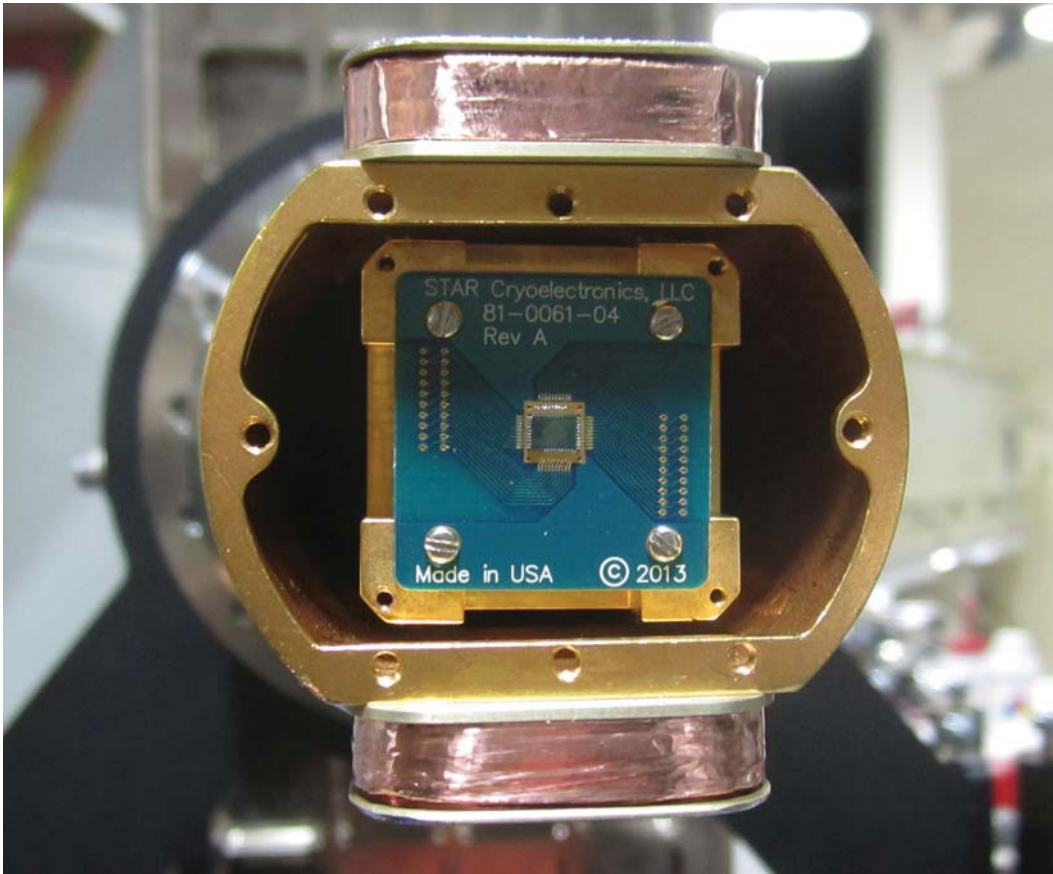


Figure 3.10: Photo of a 36-pixel chip installed onto the standard detector rod with end caps removed.

The cold finger assembly adds heat load to each associated cold stage. Estimates of the load added by each cold finger component are provided in table 3.2. Under the assumption that the 3 K snout shield is truly at 3 K, the load onto the FAA stage is dominated by the detector looms and rod suspension.

Radiative Load	Power (mW)
60 K Snout Shield	5200
3 K Snout Shield	2
Detector Rod Loads	Power (nW)
Radiative	3
Suspension	135
Wiring Looms (36-pixel)	180
Wiring Looms (112-pixel)	360

Table 3.2: Heat loads onto the stages of the cryostat from addition of cold finger. Calculated using same methods and data as table 3.1. Note detector rod loads are in nW.

3.2 Electronics

The requirements for the preamplifier electronics are to maintain a stable voltage bias across the detectors and to amplify the current pulses to levels measurable by downstream electronics without broadening the energy resolution of the detector. This can be accomplished with a dc-coupled current-sensitive preamplifier with a low-noise field effect transistor (FET) input. Since the preamplifier interacts directly with the devices, it should be considered as part of the overall detector system rather than post-processing electronics.

A simplified schematic of a current-sensitive transimpedance preamplifier is shown in figure 3.11. The STJ device is represented by the dotted box and is modeled by its dynamic resistance R_{dyn} in parallel with a capacitance C_{STJ} . X-ray induced signals are represented by a current source I_x . The bias is applied to the non-inverting input of the op-amp by varying the voltage V_{BIAS} , so that the feedback keeps the voltage of the inverting input at the same level. The output voltage is given by the total current through the STJ times the feedback resistor R_F , or $V_{out} = R_F I_x$. The value of the feedback resistor $R_F = 1M\Omega$ is chosen by a trade-off between gain and Johnson noise.

3.2.1 LLNL Preamplifiers

This preamplifier currently in use at Lawrence Livermore National Laboratory (LLNL) was initially developed at Yale University (figure 3.12) [21]. The amplifier is centered around an AMPTEK A-250 pre-amplifier with a low-noise 2SK146 input FET. Feedback is provided through $R_F = 1 M\Omega$ (R_{23} in figure 3.12) and a small feedback capacitor $C_F = 1$ pF is added for stability. Since dc-coupling the STJ is not compatible with a constant FET bias current, a

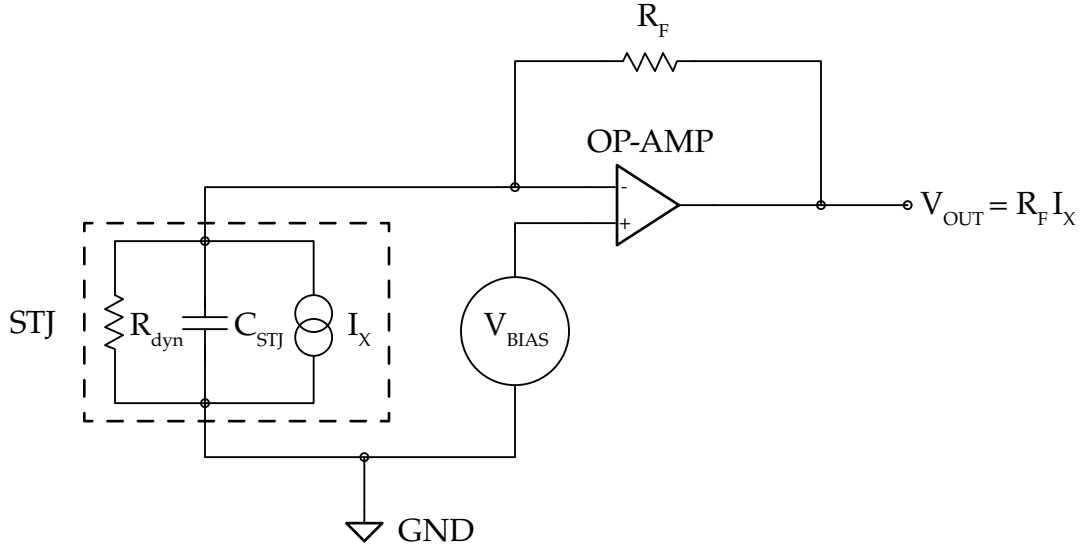


Figure 3.11: Operating principle of a current-sensitive transimpedance amplifier. The STJ is modeled by its dynamic resistance R_{dyn} , capacitance C_{STJ} , and signal current I_x . The bias is applied through the op-amp by varying V_{BIAS} , while the output voltage is given by $R_F I_x$.

secondary feedback loop (U_{11} and U_{12} in figure 3.12) senses the STJ voltage and adjusts the FET bias current through R_{25} to be compatible with the desired STJ bias. The potentiometer R1 operates on pin 3 of U_{12} of the nulling stage to adjust the bias voltage on the STJ.

The preamplifier is fabricated on a 100 mm-wide 3U Eurocard-type board, with control switches on the front panel and a 96-pin connector on the back to attach to a suitable backplane. The LLNL test cryostat (section 4.1) is set up to use these preamplifiers with battery power for low-noise measurements. Here the preamplifier has an electronic noise of ≈ 2 eV FWHM, which is used as a baseline to evaluate the performance of other preamplifiers.

A housing designed to hold 10 LLNL-type preamplifiers to operate on the cryogen-free cryostat is shown in figure 3.13. The input is a 78-pin connector carrying 32 channels that is directly compatible with the output connectors of the cryostat top plate. The connector is attached to a PCB backplane that distributes input signals to the preamplifiers through a jumper board to allow selection of any 10 channels from the input 32. Power may be supplied through a supply located in the bottom compartment of the housing, or from a 3-pin LEMO connector selectable by a switch on the back of the housing. The I-V outputs of the preamplifiers are run through a multi-pole switch board at the bottom of the rack to output BNC connectors on the front of the housing. Signal outputs from the preamplifiers are connected to a row of BNC connectors on the back panel of the housing.

3.2.2 XIA Preamplifiers

A parallel project by our collaborators at XIA LLC is to develop a new, compact STJ preamplifier. The limitations of the LLNL preamplifier for reading out detector arrays are its size (160 cm²), its cost (\$1000/preamp), and its manual operation. The goal of the Small Business Innovation Research (SBIR)-funded project is to develop market-ready, fully computer-controlled, compact and affordable arrays of preamplifiers optimized for STJ detectors [22].

The XIA preamplifier is conceptually similar to the older LLNL preamplifier, in that it is also current-sensitive with a low-noise FET at its input and a secondary feedback loop to allow dc coupling to the STJ. However, to lower the cost, the expensive A250 op-amp is replaced by a simple FET circuit [23], and inexpensive surface-mount components are used. This also allows reducing the footprint per preamplifier to < 10 cm², so that 32 preamplifiers can be placed on a single 3U Eurocard board, 16 on each side (figure 3.15). Finally, the manual bias is replaced by a digital-to-analog converter (DAC) so that the preamplifier can be computer controlled. To reduce crosstalk and interference from the digital circuitry, all digital components are located on a separate 32-channel 3U board. A schematic of the XIA readout is shown in figure 3.14.

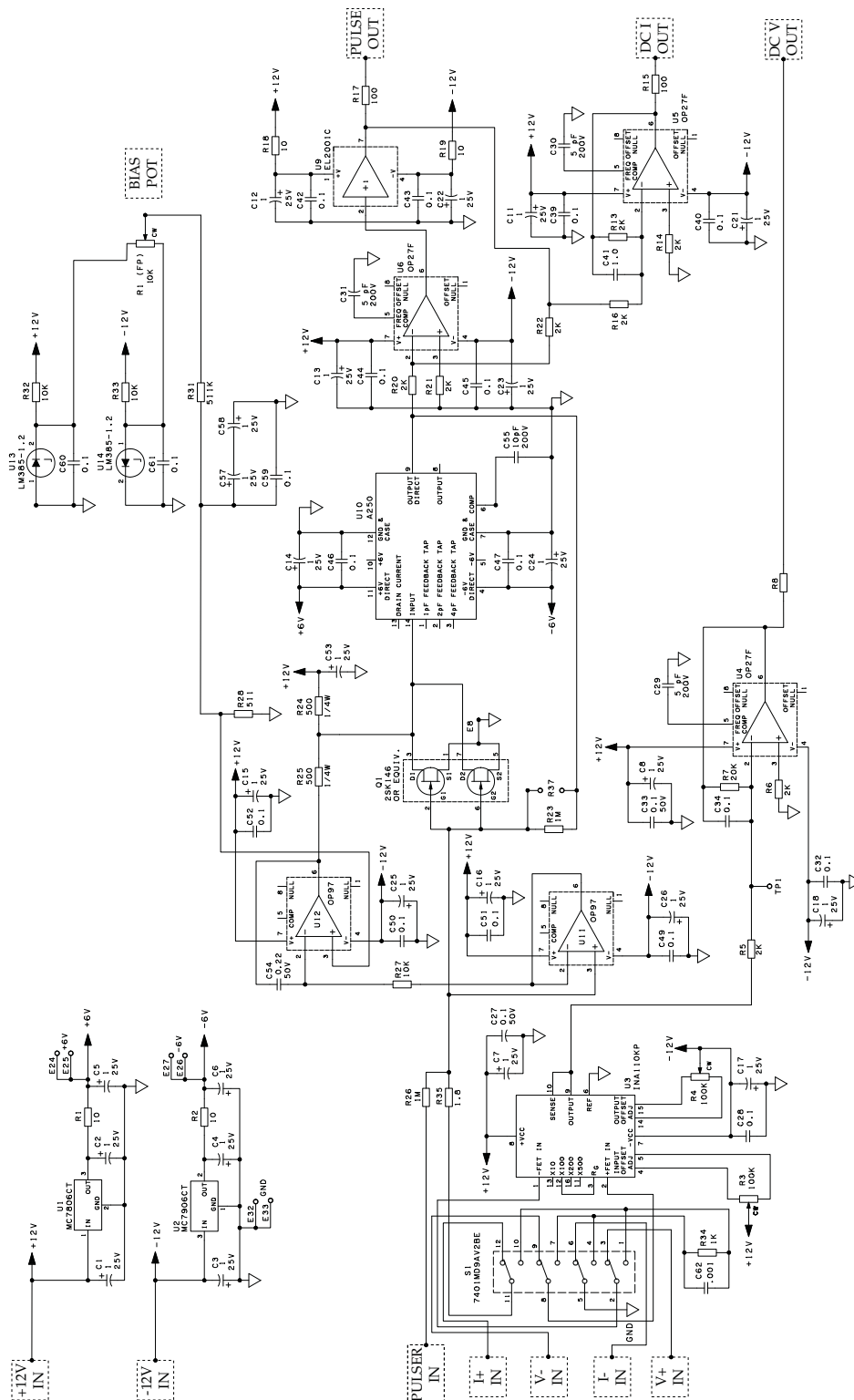


Figure 3.12: Simplified LLNL preamplifier circuit diagram. Major inputs and outputs (dotted boxes) enter the circuit on a 96-pin backplane connector, and the bias potentiometer R_1 is mounted to the front panel of the card.

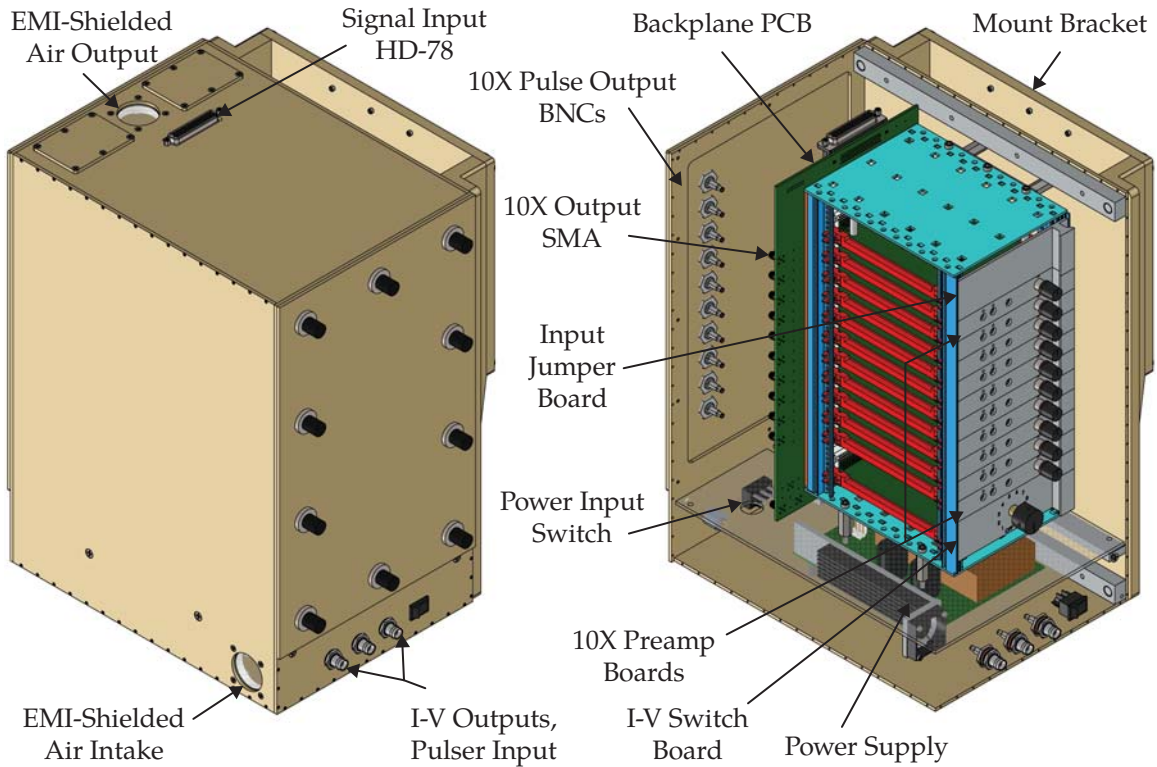


Figure 3.13: Preamplifier housing for 10-card rack of LLNL preamplifiers.

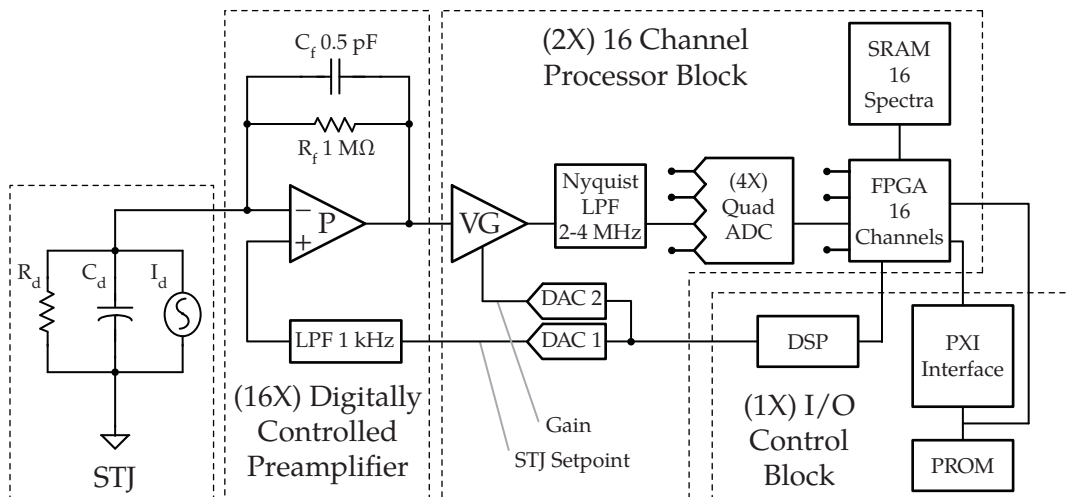


Figure 3.14: Diagram of primary components of XIA preamplifier.

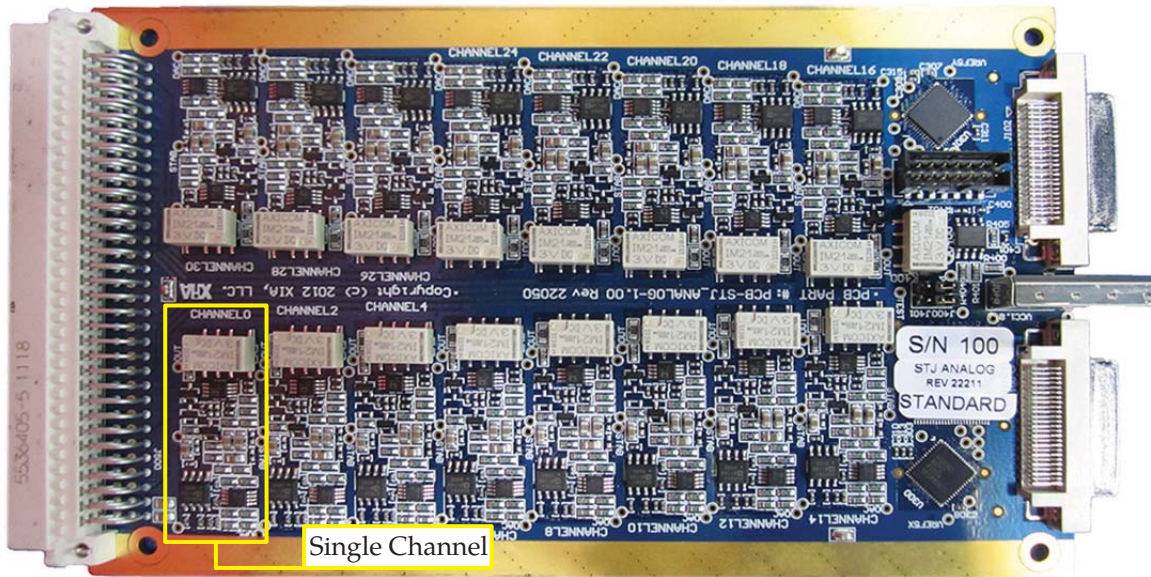


Figure 3.15: Photograph of prototype 32-channel STJ preamplifier from XIA LLC. This PCB holds 32 independent STJ preamplifiers on a single 3U Eurocard board, 16 on the front side and 16 on the back side.

References

- [1] Cryomech Inc., “Cryorefrigerator Specification Sheet: PT407 with CP2870 PT-407,” 2013. [Online]. Available: http://www.cryomech.com/specificationsheet/PT407_CP2800_ss.pdf (page 52)
- [2] —, “PT407 Cryorefrigerator Capacity Curve,” 2007. [Online]. Available: http://www.cryomech.com/capacitycurve/PT407_CP2800_cc.pdf (page 52, 54)
- [3] Spira Manufacturing Corporation, “Spira Shield Specification Sheet,” 2014. (page 52)
- [4] S. White, R. Simon, and G. Petencin, “Electronics Division Internal Report No. 323: On Radiation Loading in Cryogenic Dewars and Emissivity Measurements for Radiation Shield Materials,” National Radio Astronomy Observatory Green Bank, West Virginia, Tech. Rep., 2011. (page 57)
- [5] M. Barucci, E. Olivieri, E. Pasca, L. Risegari, and G. Ventura, “Thermal conductivity of Torlon between 4.2 and 300K,” *Cryogenics (Guildf.)*, vol. 45, no. 4, pp. 295–299, Apr. 2005. [Online]. Available: <http://linkinghub.elsevier.com/retrieve/pii/S0011227505000032> (page 57)
- [6] S. Castellazzi, M. Cimberle, C. Ferdeghini, E. Giannini, G. Grasso, D. Marrè, M. Putti, and A. Siri, “Thermal conductivity of a BSCCO(2223) c-oriented tape: a discussion on the origin of the peak,” *Phys. C Supercond.*, vol. 273, no. 3-4, pp. 314–322, Jan. 1997. [Online]. Available: <http://linkinghub.elsevier.com/retrieve/pii/S0921453496006399> (page 57)
- [7] N. J. Simon, E. S. Drexler, and R. P. Reed, *Properties of Copper and Copper Alloys at Cryogenic Temperatures, NIST Monograph 177*. Gaithersburg, MD: NIST Monographies, 1992. (page 57)
- [8] R. O. Pohl, X. Liu, and E. Thompson, “Low-temperature thermal conductivity and acoustic attenuation in amorphous solids,” *Rev. Mod. Phys.*, vol. 74, no. October, pp. 991–1013, 2002. (page 57)
- [9] E. D. Marquardt, J. P. Le, and R. Radebaugh, “Cryogenic Material Properties Database,” in *Cryocoolers 11*. Kluwer Academic Publishers, 2001, pp. 681–687. (page 57)
- [10] A. L. Woodcraft, G. Ventura, V. Martelli, and W. S. Holland, “Thermal conductance at millikelvin temperatures of woven ribbon cable with phosphor-bronze clad superconducting wires,” *Cryogenics (Guildf.)*, vol. 50, no. 8, pp. 465–468, Aug. 2010. [Online]. Available: <http://linkinghub.elsevier.com/retrieve/pii/S0011227510001220> (page 57)
- [11] J. Tuttle, E. Canavan, and M. DiPirro, “Thermal and Electrical Conductivity Measurements of CDA 510 Phosphor Bronze,” *AIP Conf. Proc.*, vol. 55, p. 1219, 2010. (page 57)
- [12] W. F. Giauque and D. P. MacDougall, “Attainment of Temperatures Below 1 Degree Absolute by Demagnetization of $Gd_2(SO_4)_3 \cdot 8H_2O$, url = <http://link.aps.org/doi/10.1103/PhysRev.43.768>, volume = 43, year = 1933,” *Phys. Rev.*, no. 9, p. 768, May. (page 57)

- [13] C. V. Heer, C. B. Barnes, and J. G. Daunt, "The Design and Operation of a Magnetic Refrigerator for Maintaining Temperatures below 1°K," *Rev. Sci. Instrum.*, vol. 25, no. 11, p. 1088, 1954. [Online]. Available: <http://scitation.aip.org/content/aip/journal/rsi/25/11/10.1063/1.1770944> (page 57)
- [14] C. Hagmann and P. Richards, "Two-stage magnetic refrigerator for astronomical applications with reservoir temperatures above 4 K," *Cryogenics (Guildf.)*, vol. 34, no. 3, pp. 221–226, Mar. 1994. [Online]. Available: <http://linkinghub.elsevier.com/retrieve/pii/0011227594901724> (page 57)
- [15] J. R. Hull and R. a. Hull, "Tables of Thermodynamic Functions of Paramagnetic Substances and Harmonic Oscillators," *J. Chem. Phys.*, vol. 9, no. 6, p. 465, 1941. [Online]. Available: <http://scitation.aip.org/content/aip/journal/jcp/9/6/10.1063/1.1750936> (page 59)
- [16] A. H. Cooke, "The Establishment of the Absolute Scale of Temperature below 1° k." *Proc. Phys. Soc.*, vol. 62, no. 5, p. 19, 1949. (page 59)
- [17] O. Petrenko, D. Paul, C. Ritter, T. Zeiske, and M. Yethiraj, "Magnetic frustration and order in gadolinium gallium garnet," *Phys. B Condens. Matter*, vol. 266, no. 1-2, pp. 41–48, May 1999. [Online]. Available: <http://linkinghub.elsevier.com/retrieve/pii/S0921452698014902> (page 61)
- [18] C. T. Corporation, "Hiperco 50A Alloy," 2005. [Online]. Available: <http://cartech.ides.com/datasheet.aspx?E=199> (page 63)
- [19] N. Rando, P. Verhoeve, P. Gondoin, B. Collaudin, J. Verveer, M. Bavdaz, and A. Peacock, "IR Filters for High Responsivity Cryogenic Detectors," *Nucl. Instruments Methods Phys. Res. Sect. A*, vol. 444, pp. 457–460, 2000. (page 66)
- [20] a. Hoshino, K. Shinozaki, Y. Ishisaki, T. Ohashi, K. Tanaka, T. Mihara, and Y. Tawara, "Evaluation of the IR-UV blocking filters for ADR with a TES microcalorimeter," *Nucl. Instruments Methods Phys. Res. Sect. A Accel. Spectrometers, Detect. Assoc. Equip.*, vol. 559, no. 2, pp. 471–473, Apr. 2006. [Online]. Available: <http://linkinghub.elsevier.com/retrieve/pii/S0168900205025015> (page 66)
- [21] S. Friedrich, K. Segall, M. C. Gaidis, C. M. Wilson, D. E. Prober, P. J. Kindlmann, A. E. Szymkowiak, and S. H. Moseley, "Single Photon Imaging X-ray Spectrometers Using Low Noise Current Preamplifiers with dc Voltage Bias," *IEEE Trans. Appl. Supercond.*, vol. 7, no. 2, pp. 3383–3.386, 1997. (page 70)
- [22] W. K. Warburton, J. Harris, M. H. Carpenter, L. Fabris, and S. Friedrich, "Preamplifier development for superconducting tunnel junction array X-ray detector electronics," *IEEE Nucl. Sci. Symp. Med. Imaging Conf.*, vol. 1, pp. 742–748, Oct. 2010. [Online]. Available: <http://ieeexplore.ieee.org/lpdocs/epic03/wrapper.htm?arnumber=5873857> (page 72)
- [23] L. Fabris, N. W. Madden, and H. Yaver, "A fast , compact solution for low noise charge preamplifiers," *Nucl. Instruments Methods Phys. Res. Sect. A*, vol. 424, no. October 1998, pp. 0–6, 1999. (page 72)

Chapter 4

Spectrometer Performance

This chapter discusses the performance of our STJ x-ray detectors, the readout electronics, and the new cryostat for STJ operation at the synchrotron. Prototype chips with different sizes and geometries were initially tested at LLNL and at the LBNL ALS to optimize detector fabrication, and to measure the resolution as a function of detector size and photon energy. This chapter also discusses the performance of the cryogen-free cryostat, including its ADR performance, IR-blocking windows, and snout detector magnet. Finally, the x-ray response of a 36-pixel detector array operated in the cryogen-free ADR and read out with the XIA electronics is discussed in preparation for the XAS measurements of chapter 5.

4.1 STJ Device Characterization

In the first phase of this project, a new generation of Ta-based STJ x-ray detectors was developed and characterized in an ADR at LLNL. Chips with multiple pixel sizes were tested to characterize the geometric factors contributing to the energy resolution and to evaluate the performance of a particular fabrication run.

The “wet” LLNL cryostat has liquid nitrogen and helium reservoirs for pre-cooling to 4 K, and a two-stage ADR with FAA and GGG to cool to a base temperature < 0.1 K. The maximum field of the ADR magnet is 5 T, higher than the STAR cryostat’s 4 T, because it starts the ADR cycle from a higher temperature of 4.2 K. To shield the STJ detectors from external magnetic fields, the ADR magnet is surrounded by a vanadium permendur shield, and the STJ mount stage has an additional magnetic shield fabricated from cryoperm[®]10. The STJ mount is located in the center of the cryostat below the ADR instead of on the end of a snout. The detector mount has positions for three copper holders in the center of the solenoid (figure 4.1), of which one

holder can be illuminated by x-rays from outside the cryostat, and the other two positions are used to measure I-V curves. Three IR-blocking filters, one at 77 K and two at 4.2 K, protect the illuminated devices from thermal radiation. The ADR is operated in the unregulated mode, with a base temperature below 0.1 K. The detector mount lies inside a superconducting solenoid to apply a magnetic field on order of several to tens of mT to suppress the dc-Josephson current and Fiske mode resonances. The solenoid was measured with a Hall probe outside the cryostat with low currents to find its current-field relationship of approximately 0.05 mT/mA, so that a typical operating current of 150 mA results in a field of 7.5 mT.

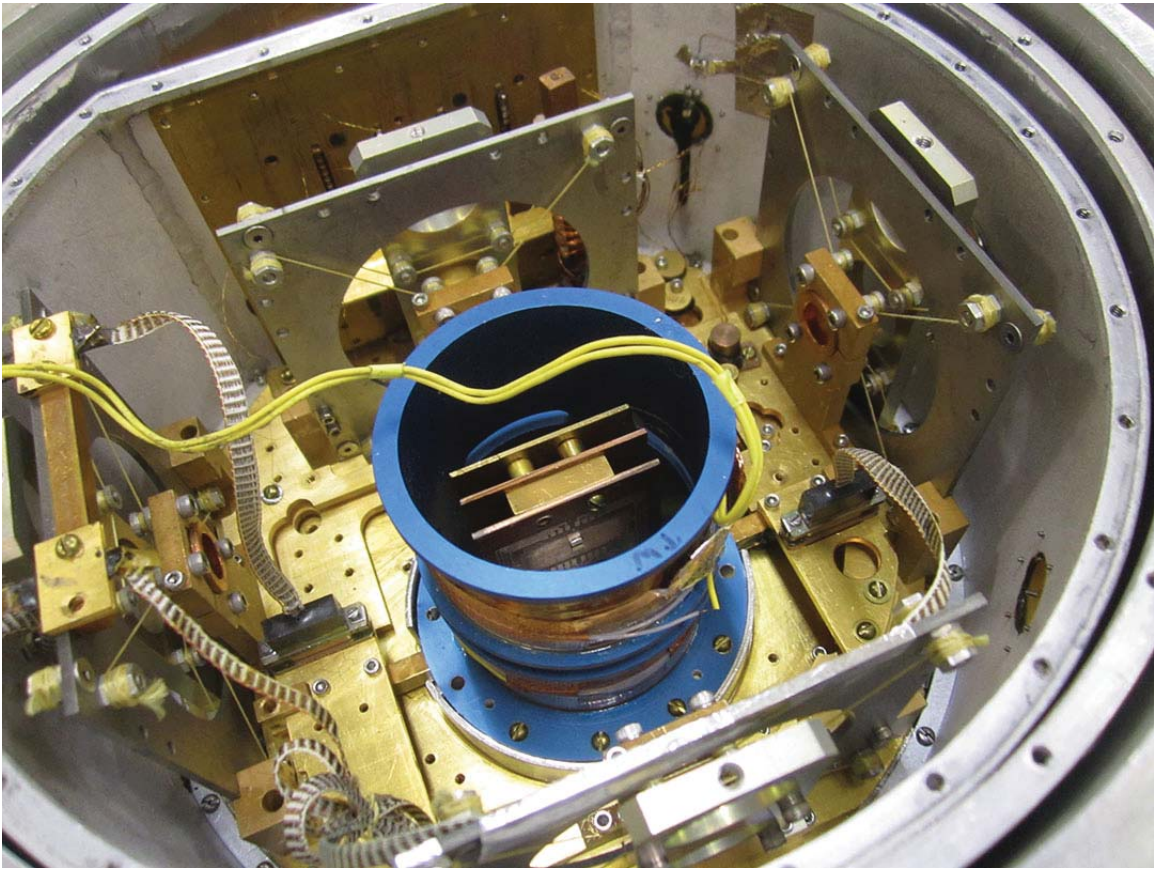


Figure 4.1: Photo of the internal cold stages of the LLNL test cryostat. The magnetic shield protecting the test stage is removed so that the solenoid coil and three detector mounts are visible.

To assess the quality of a certain STJ fabrication run, we initially measure STJ I-V curves. Ideal characteristics are high dynamic resistance below the gap to reduce the influence of FET noise, low leakage current for low shot noise, and regions along the I-V curve free from Fiske modes where the device may be biased stably. A typical I-V curve for a $208 \times 208 \mu\text{m}$ detector from

a 36-pixel array is shown in figure 4.2. The Fiske modes are not visible in the I-V curve due to suppression by the magnetic field, but their position and influence on the signal can still be seen as peaks in the more sensitive noise curve (dotted line). The large noise peak at 0 V is due to the dc Josephson current, which though reduced in current still has a large effect on the device noise. The dynamic resistance R_{dyn} is defined by the relation

$$R_{dyn} = \left(\frac{dI}{dV} \right)^{-1} \quad (4.1)$$

and can be approximated by the inverse of the slope in a given region. A good threshold for minimum R_{dyn} is $\approx 1 \text{ k}\Omega$, so this particular device with $R_{dyn} \approx 2.1 \text{ k}\Omega$ below $150 \text{ }\mu\text{V}$ is a good functional device. The gaps between Fiske modes are good regions to stably bias the junction. The detectors may be operated with currents as low as 50 mA in the detector solenoid, although operating right at this threshold is not very stable so typical magnet currents of around 150 mA ($\approx 7.5 \text{ mT}$) are used during device characterization.

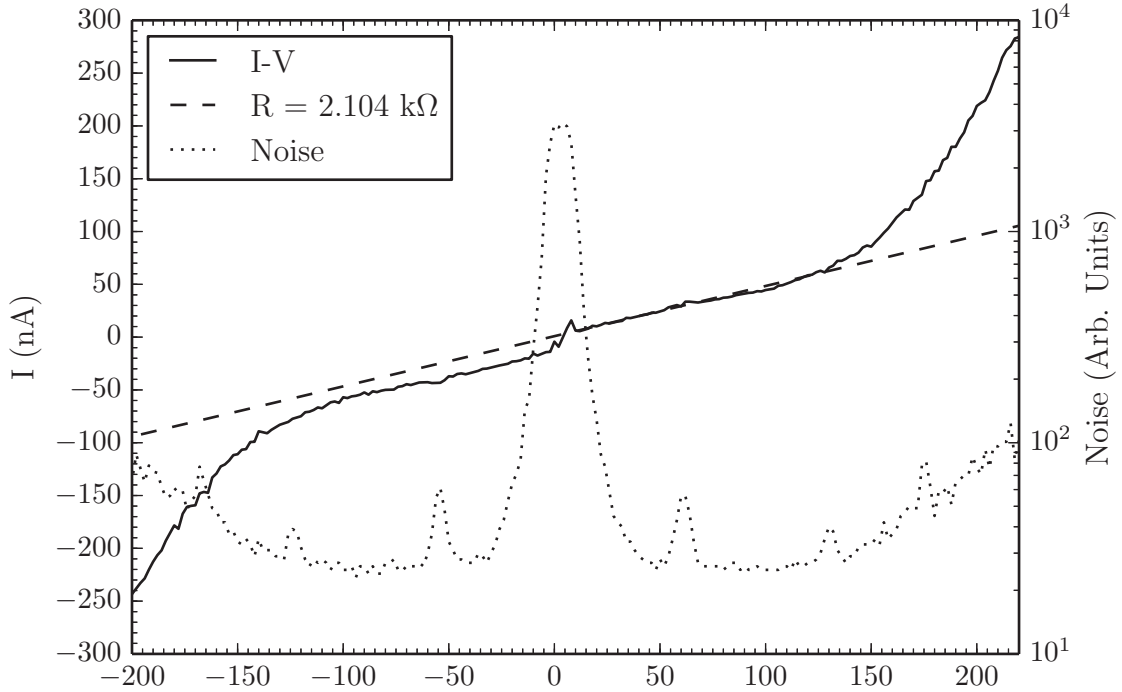


Figure 4.2: I-V Curve of a typical $208 \times 208 \text{ }\mu\text{m}$ STJ pixel, measured with XIA electronics.

For illumination with x-ray photons, the cryostat is connected to a two-stage (Henke-type) x-ray generator. A primary electron beam from a hot filament generates broadband

Bremsstrahlung radiation from a W/Ta target, which in turn illuminates a secondary stage with multiple targets of various composition. This allows the generation of characteristic x-ray emission from the different elements composing the secondary targets. Compared to a single-stage (Manson-type) x-ray generator, which accelerates the electron beam directly onto the sample target, the Henke generator has very little background Bremsstrahlung radiation at the expense of lower photon flux. This is desirable to determine the resolution of the detectors at characteristic emission energies.

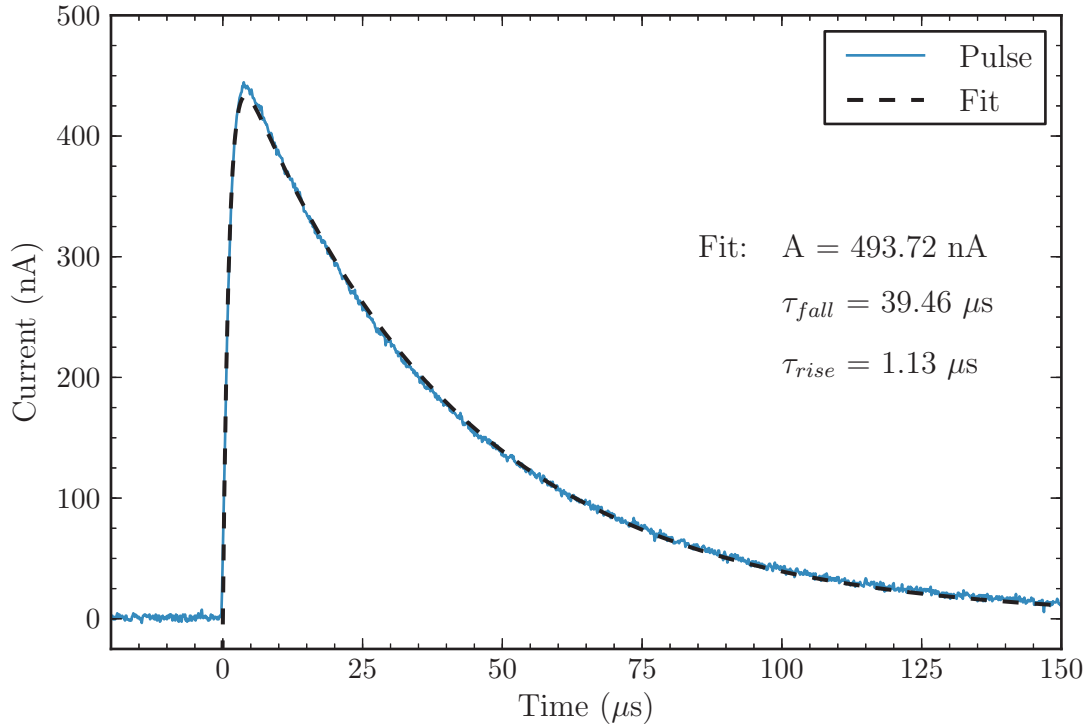


Figure 4.3: A typical STJ output pulse from XIA preamplifier. This pulse is from the Al K line at 1.486 keV. The fitted pulse follows equation 4.2. The decay time τ_{fall} is directly related to the quasiparticle recombination time.

Absorption of a photon generates a voltage pulse at the output of the preamplifier, which may be observed directly with an oscilloscope or fed into a digitizer or pulse height analyzer. A typical pulse from the aluminum K_β line at 1557 eV is shown in figure 4.3. The pulse is fitted to an equation of the form

$$I(t) = A(e^{-\frac{t}{\tau_{fall}}})(1 - e^{-\frac{t}{\tau_{rise}}}). \quad (4.2)$$

The decay time τ_{fall} is a direct measure of the quasiparticle lifetime, while the rise time is determined by the time it takes quasiparticles to become trapped in the Al films near the tunnel

barrier. This in turn is affected by the location where the photon was absorbed. The highest resolution is achieved for x-ray absorption in the top electrode, but events may also originate in the base electrode, leads, or silicon substrate. Photons absorbed in the top electrode have the shortest rise time as the generated qps may be trapped into the Al and tunnel immediately, while events from other locations have longer rise times because quasiparticles or phonons have to diffuse to the trap first.

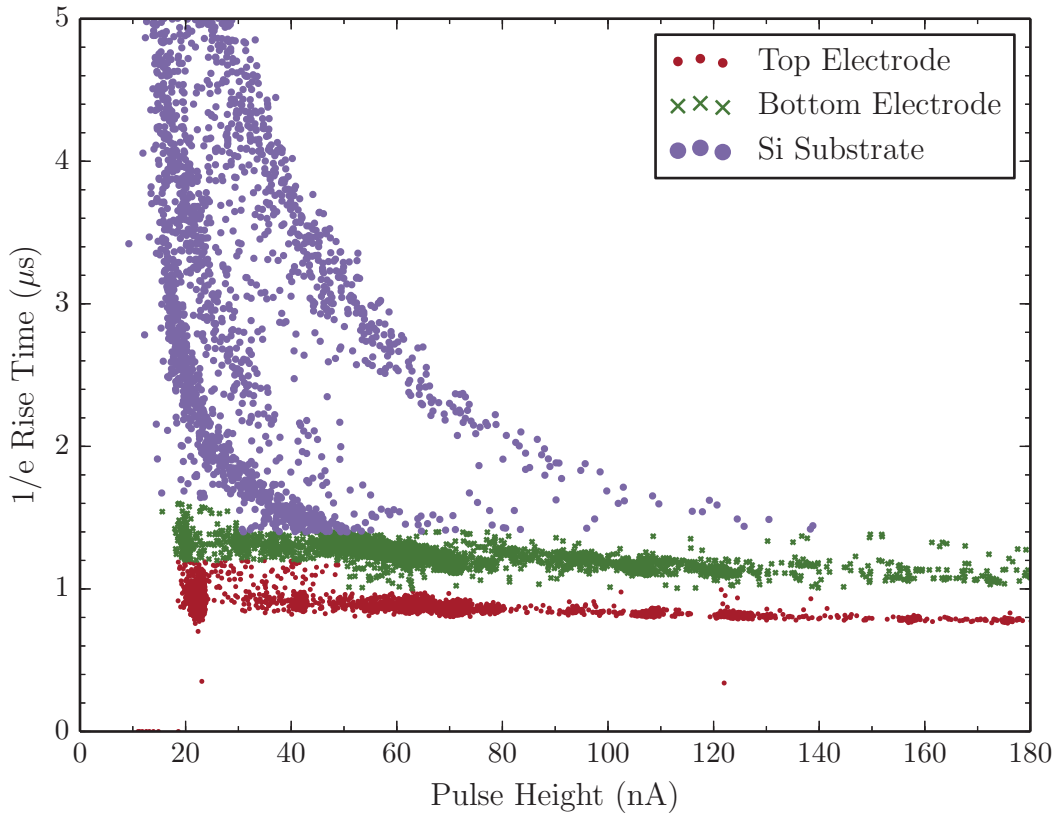


Figure 4.4: Sorting pulses by rise time vs. pulse height allows discrimination between events that originate in the top vs. bottom electrodes and other locations. The events shown here were acquired using the LLNL preamps with a $138 \mu\text{m}$ test device, and the gain is different for the XIA pulse shown in figure 4.3 for a $208 \mu\text{m}$ device.

Sorting the events by pulse height and rise time therefore allows clear separation between events from different absorption locations (figure 4.4). Substrate events do not show any structure in energy and contribute a low-energy spectral background. Binning the events from the top and base electrodes into separate spectra (figure 4.5) shows several important differences between them. The base electrode spectrum is much weaker than the top, since only high-

energy photons that are transmitted through the top absorber contribute. Events from the base electrode are also offset in energy from those in the top electrode, which can lead to a line splitting artifact that can affect spectral purity at higher energies. Achieving the highest energy resolution and best spectral purity therefore requires pulse discrimination based on rise time differences to only select events originating in the top electrode. The data presented in figure 4.4 were acquired with LLNL preamplifiers, digitized and recorded to disk for subsequent off-line pulse processing. At this time, the XIA electronics do not have this capability, but it is under development for implementation in field-programmable gate arrays.

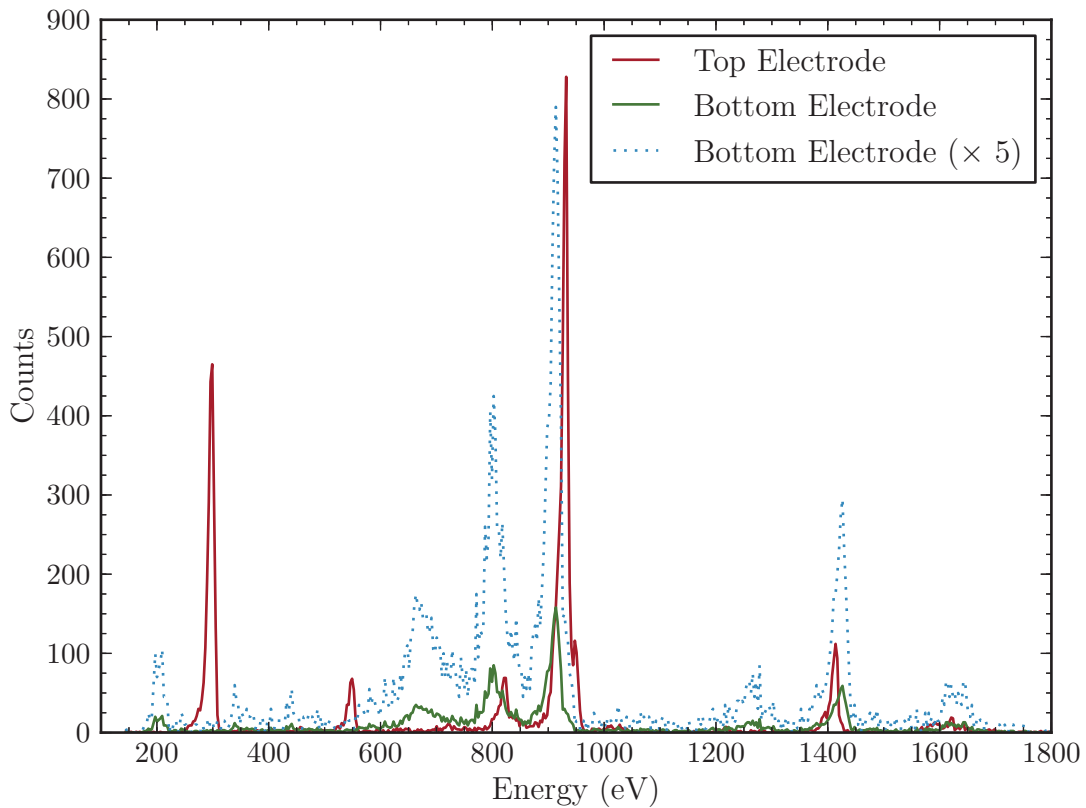


Figure 4.5: Spectrum of top and bottom electrode events sliced from the data in figure 4.4, with pulse heights calibrated to the Cu L_{α} line at 929.7 eV.

The next parameter to characterize is the detector responsivity, i.e. the amount of charge generated by a photon per energy. Higher responsivity is essential for highest energy resolution for constant noise. The responsivity varies with device bias due to the changes in tunneling probability due to the DOSs on either side of the junction (see figure 2.3). Typically, the responsivity will have a maximum at some bias point below the gap, then decrease towards the gap as

fewer states are available to tunnel into. Figure 4.6 shows the responsivity vs. bias for several device sizes from 67 to 284 μm on each edge. The noise curves are plotted rather than I-V curves to better illustrate the locations of Fiske mode resonances. The devices are illuminated with aluminum K_α and K_β photons at 1486 and 1557 eV, and the average pulse height is normalized to 1 keV and is used as the measure of responsivity. All devices show maximum responsivity in the neighborhood of $V_{bias} = 100 \mu\text{V}$ which is the optimum bias point. Except for the smallest device with edges of 67 μm , the devices have similar responsivities, suggesting that the contribution of the STJ edges to the quasiparticle lifetime is not very strong since it no longer affects devices above $\approx 100 \mu\text{m}$.

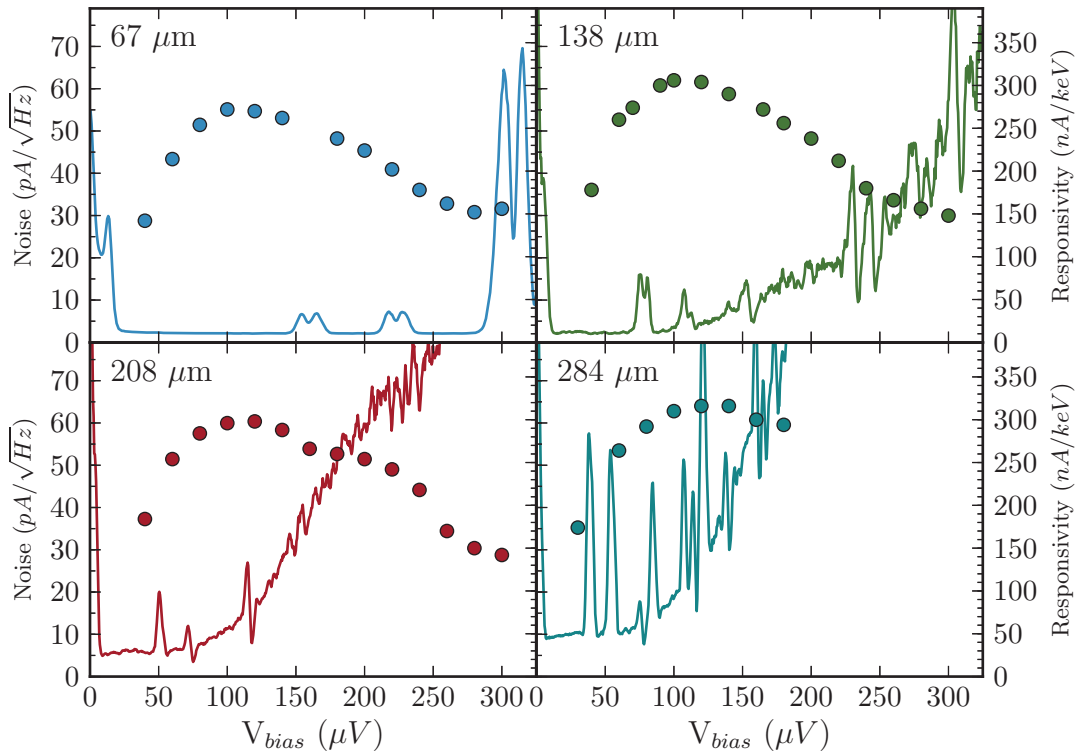


Figure 4.6: Responsivity vs. V_{bias} for STJs of different sizes. Noise curves (solid lines) are plotted to the left-hand scale in $\text{pA}/\sqrt{\text{Hz}}$, while responsivities (markers) are plotted to the right-hand scale in nA/keV .

4.2 Spectral Response

The energy resolution ΔE_{FWHM} of an STJ detector is a combination of statistical, electronic, and geometric factors adding in quadrature,

$$\Delta E_{FWHM} = \sqrt{\Delta E_{stat}^2 + \Delta E_{geom}^2 + \Delta E_{elec}^2}, \quad (4.3)$$

with E_{stat} given by

$$\Delta E_{stat} = 2.355 \sqrt{\epsilon_q E_x (F + 1 + 1/\langle n \rangle)}. \quad (4.4)$$

To assess the relative magnitude of the different contributions to the line broadening, we have measured the spectral response of four STJ detectors with different sizes to x-rays from a metal oxide target in the Henke tube. Figure 4.7 shows the energy resolution of the four detectors at the O K line at 525 eV, as extracted from a Gaussian fit to the centroid of the line. The $(138\mu\text{m})^2$ STJ has the highest energy resolution of 4.8 eV FWHM, while the resolution degrades for the smaller $(67\mu\text{m})^2$ as well as for the larger detectors. Increased spatial inhomogeneities, device capacitance, and ΔE_{elec} can account for the reduced resolution for the larger devices. The reduced energy resolution of the smaller detector is likely due to the increased influence of quasiparticle loss at the junction edges, which increases geometric inhomogeneities ΔE_{geom} , but plays less of a role in large STJs. This is consistent with the increased low-energy shoulder in the response of the $(67\mu\text{m})^2$, which is also due to edge losses.

Surprisingly, in all four STJs the O K line has a higher energy resolution than the lower-energy C K and B K lines at 277 and 186 eV, respectively. The width of these lines is consistently and reproducibly > 10 eV FWHM. Since none of the noise contributions in equations 4.3 and 4.4 increase at low energies, this suggests that the source line width contributes significantly to the observed broadening, most likely due to the width of the conduction band from which the electron relaxes that produces the measured x-ray.

To accurately characterize the energy resolution therefore requires a truly monochromatic, tunable x-ray source, such as a synchrotron beam line with a source energy width < 0.5 eV. For this measurement, the detector chip is installed in the LLNL cryostat at the end of ALS beam line 6.3.1 on a movable stage so that the beam can be directed onto the correct device. A micrometer stage in front of the cryostat window holds several precision pinhole filters of 20 - 100 μm diameter to illuminate mostly the center of one device and reduce artifacts from photons absorbed at the detector edges, substrate, and wiring. The storage ring was operating in two-bunch mode, which has $\approx 20 \times$ reduced flux over the normal operating mode to help ensure the count rate does not saturate the device. When the beam line is tuned to a particular energy E_x , higher orders from the grating monochromator are also present at intervals of nE_x . Figure 4.8 shows the measured spectrum from a single 208 μm detector illuminated directly by ALS beam line 6.3.1. Fitting a Gaussian to the first order peak as shown in the inset of figure 4.8

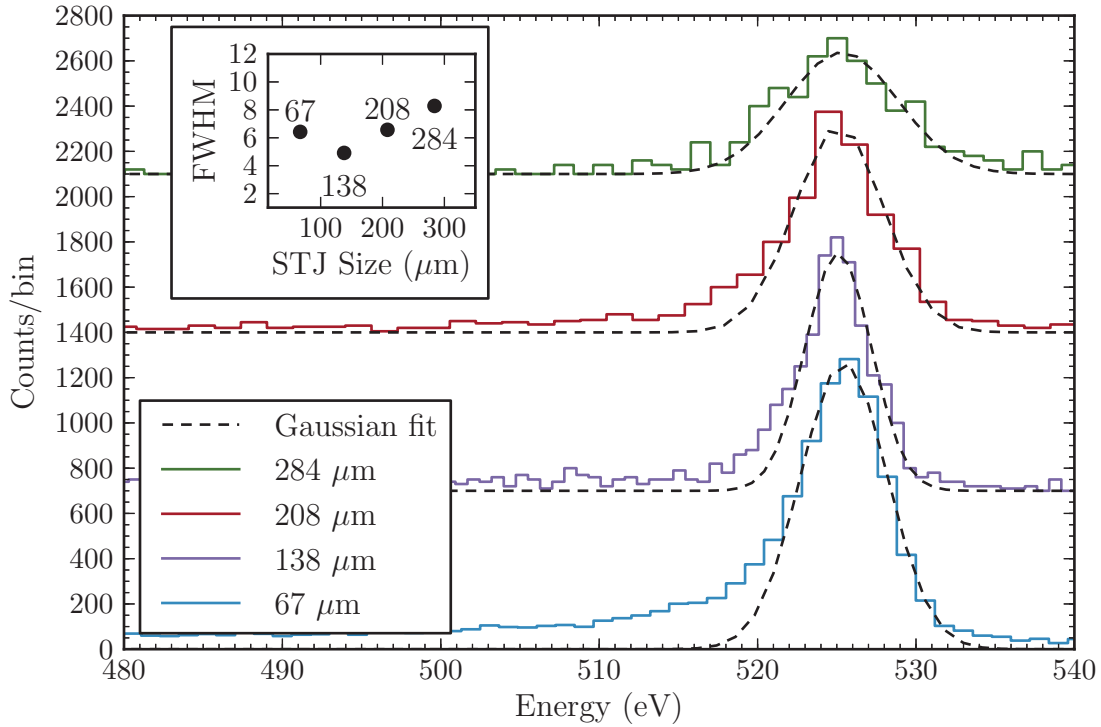


Figure 4.7: Spectra and fitted resolution of the O K line for four STJ device sizes. The inset shows the FWHM of the fitted Gaussian functions at 525 eV.

gives the device resolution of 2.5 eV FWHM at 250 eV.

To measure the electronic noise, a function generator injects narrow-width pulses at regular intervals during the measurement. The size of the pulses is chosen so they lie outside the range of the x-ray pulse heights, typically at a higher energy. This gives a direct measure of the electronic noise ΔE_{elec} introduced by the preamplifier. Figure 4.9 shows the results of direct illumination measurements across the range from 200 - 850 eV. The theoretical resolution is calculated using equation 4.4. Subtracting the constant electronic noise of ≈ 1.92 eV and the beam line source resolution (not shown) from the measured resolution in quadrature gives the intrinsic resolution. Note that the intrinsic energy resolution is lower than the statistical limit according to equation 4.3. This is due to the fact that most of the tunneling noise that accounts for the term $(1 + 1/\langle n \rangle)$ affects mostly the end of the pulse. Since these spectra were measured with a shaping time of $10 \mu s$ (which is shorter than the pulse decay time), the full effect of the tunneling noise is not yet observable [1]. The fact that this effect of reduced statistical noise is observable underscores the high quality of the STJ x-ray detectors.

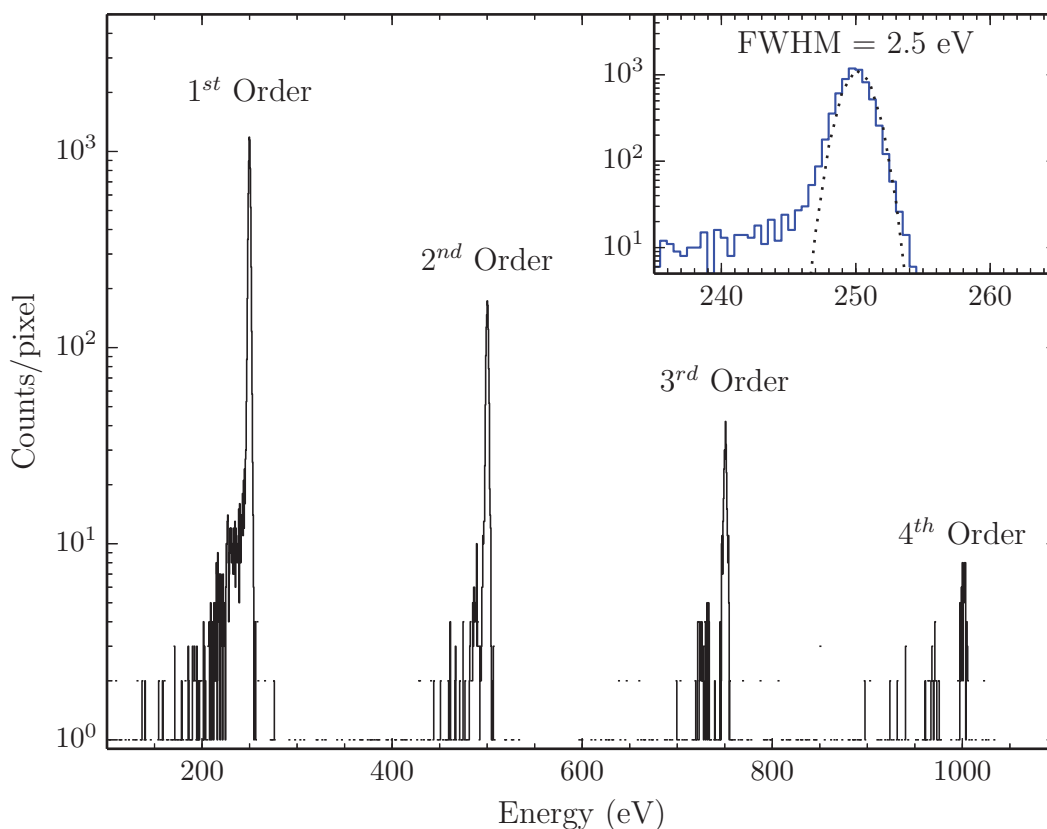


Figure 4.8: Direct synchrotron illumination spectrum from a 208 μm STJ.

4.2.1 Count Rate

For high-sensitivity XAS at bright synchrotron light sources, it is essential that the detector can be operated at high count rates. Each independent x-ray pulse has a finite decay time (figure 4.3), and at count rates below ≈ 1000 cts/sec/pixel each pulse is likely well-separated from other pulses in time. As the rate is increased, so is the likelihood that a new pulse will be triggered before the detector has completely decayed back to the quiescent state from the previous pulse, a condition called pulse pile-up. Modern pulse analysis systems, such as the XIA analyzer used for this detector, have algorithms to handle the separation of pulses from pileup and the recovery of each individual event. However, these algorithms never perfectly account for pile-up. As a result, the resolution at very high count rates does degrade despite of the pile-up filtering.

To measure this effect in our Ta STJs, the full cryogen-free ADR was installed at an offline vacuum chamber at the ALS equipped with a Manson-type x-ray generator. This generator has

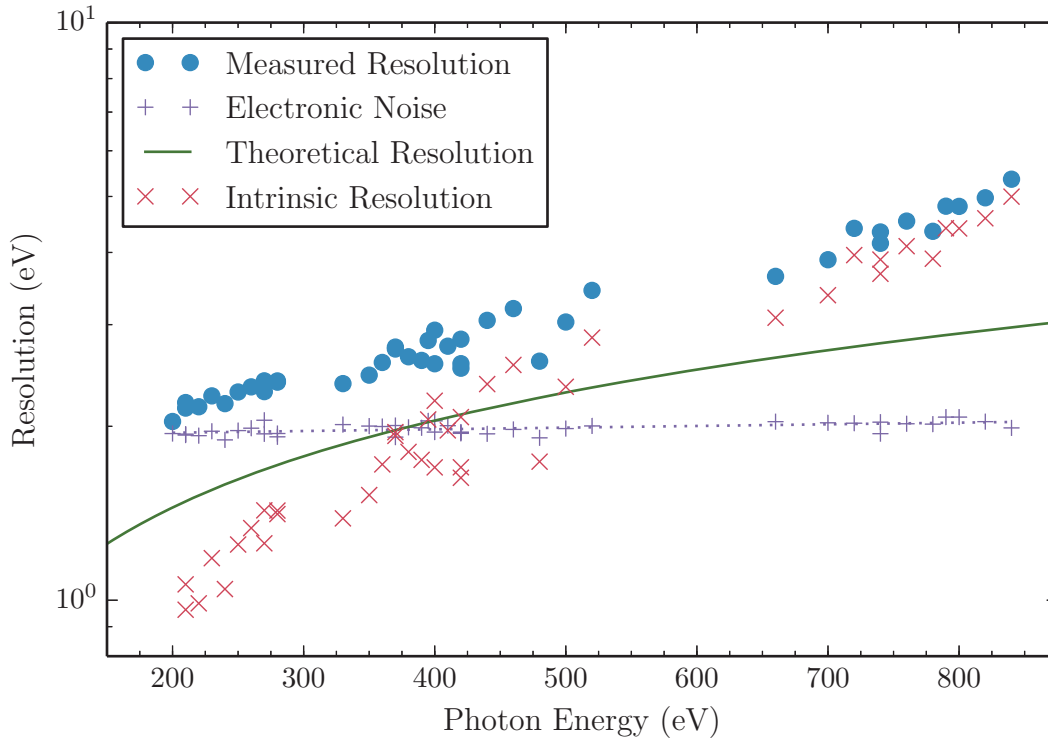


Figure 4.9: Measurement of energy resolution as a function of energy for a $208 \mu\text{m}$ STJ by direct illumination at the synchrotron. The measurement beamline resolving power is around 1000 and therefore negligible.

only a single target, which is excited by an electron beam from a hot filament. The resulting spectrum has a broad Bremsstrahlung background, but has the advantage that it may be driven at high photon flux. The STJ detector cold finger is inserted fully into the vacuum chamber close to the generator to achieve the highest count rates. Figure 4.10 shows the energy resolution at 525 eV for different count rates from an FeO target excited with a 1 keV electron beam. The lower x-axis shows the count rate per pixel while the upper x-axis shows the equivalent count rate for a full 112-pixel array. The resolution extracted from a Gaussian is fit to the O K line as in other measurements. At the lowest rate, the energy resolution of 8.5 eV FWHM is significantly reduced from the values measured by direct illumination at beam line 6.3.1 due to the source line width. It is roughly constant up to 1000 counts/s per pixel, then increases as the rate approaches 10,000 counts/s per pixel. The maximum tested rate is ≈ 12 kcts/sec/pixel, as that is the limit of the x-ray generator. While the resolution at that rate is reduced to ≈ 25 eV FWHM, this would still be very useful for many samples that do not have extremely closely spaced lines, especially compared to the ≈ 90 eV resolution expected from a silicon drift detector in this en-

ergy range. The combination of high resolution (compared to Si drift detectors), high-efficiency (compared to grating analyzers), and high speed (compared to microcalorimeters) makes STJ x-ray detectors well-suited for XAS with soft x-rays.

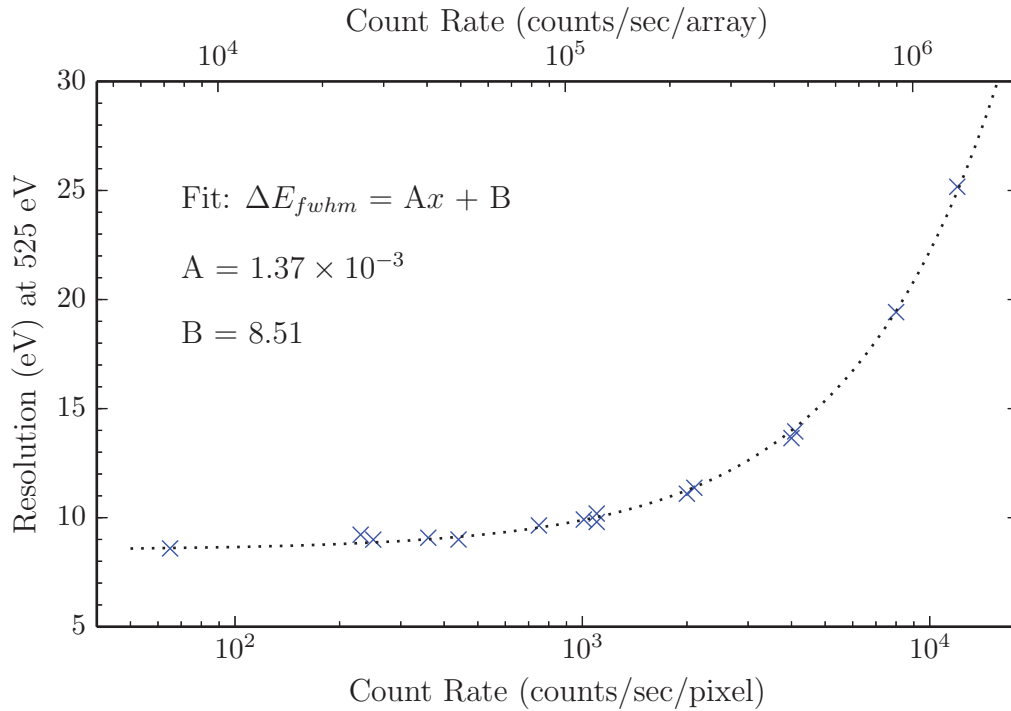


Figure 4.10: Energy resolution of the O K line at 525 eV as a function of count rate. The spectra were acquired with the XIA preamp from an FeO target in a Manson-type x-ray generator.

4.2.2 Homogeneity

To test the homogeneity of different detector pixels in an STJ array, we acquired x-ray emission spectra with multiple pixels of an array simultaneously from a mixed-element source. This test was performed at LLNL, with one of the copper detector holders modified to accept a 36-pixel array later to be installed in the dry ADR cryostat for XAS. A mixed target for the Henke x-ray source was prepared with powdered $\text{Fe}_7(\text{CN})_{18}$, NiF_2 , and MnO on an aluminum holder to provide a multitude of low-energy x-ray lines.

The STJs were biased and spectra were acquired simultaneously with the 32-channel XIA preamplifier board. Figure 4.11 shows spectra from 26 of the pixels, with each successive spectrum offset by 200 counts so that they are all visible. The response of the pixels is extremely uniform across the array, and the resolution is uniformly high. The O K line is fit to a Gaussian

as before, and the resulting distribution of energy resolutions is binned into the histogram (see inset). The majority of the pixels in this measurement have a resolution between 8 and 10 eV. The spectra show no evidence of cross-talk or other degradation by biasing and operating the entire array simultaneously. The summed spectrum of the 26 pixels is shown in figure 4.12 on a log scale to highlight lines from trace elements. Since the XIA pulse height analysis system does not yet have the ability to separate the top- and bottom-layer events by rise time discrimination, the spectrum shows the line-splitting artifacts at higher energies. At this resolution, the minor emission lines such as the $L_{\nu,\eta}$ lines of Ni, Mn, and Fe are weak but clearly separable from the primary L lines. This implies that the performance of the array is sufficient for synchrotron XAS where the spectrum is measured by gating on either the $L_{\alpha,\beta}$ or the $L_{\nu,\eta}$ emission from a transition metal sample.

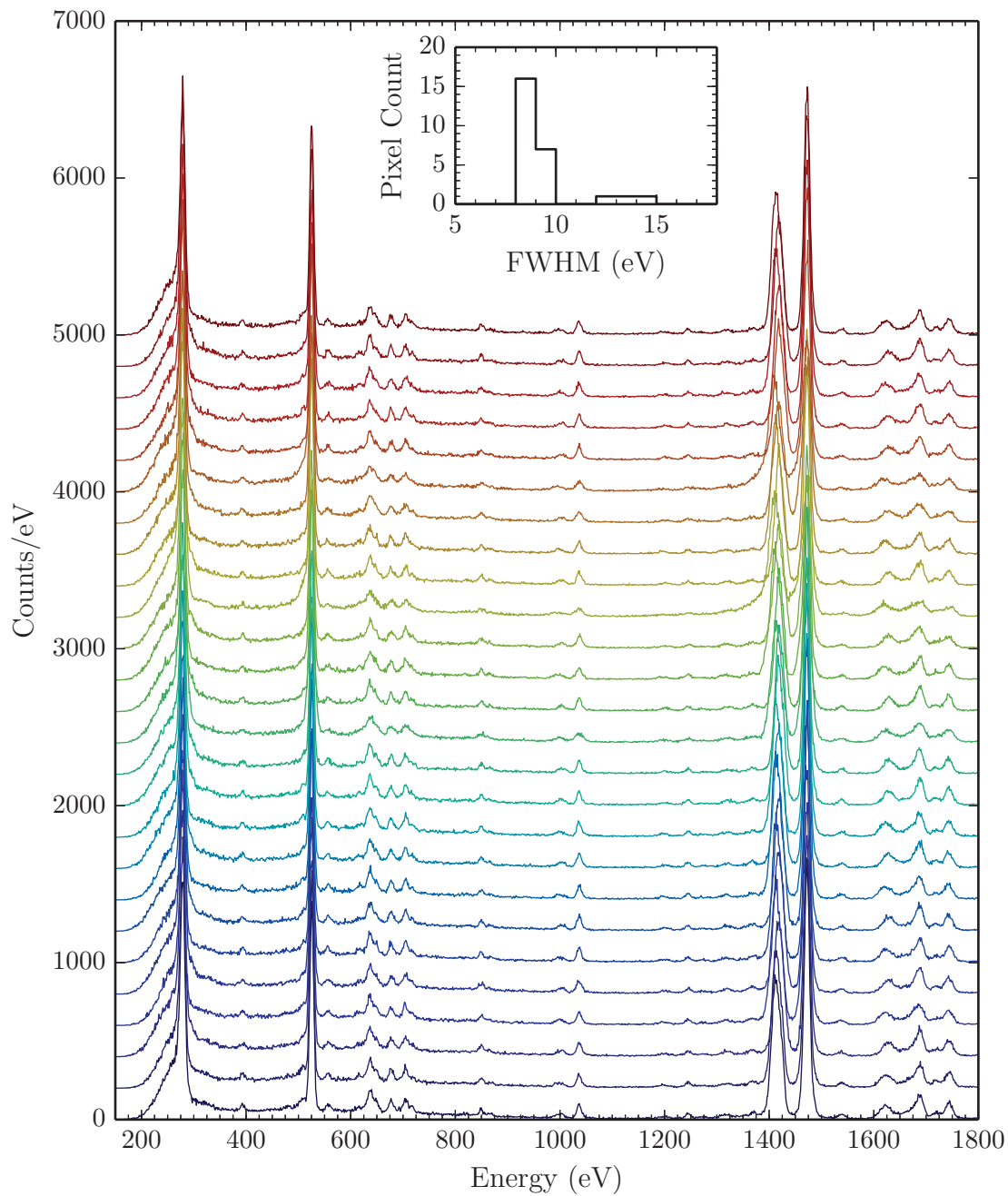


Figure 4.11: Simultaneous emission spectrum from 36-pixel array of a mixed-target, using XIA electronics. Each spectrum is sequentially offset by 200 counts. The plot in the top center of the image is a histogram of pixel resolution at the O K line at 525 eV.

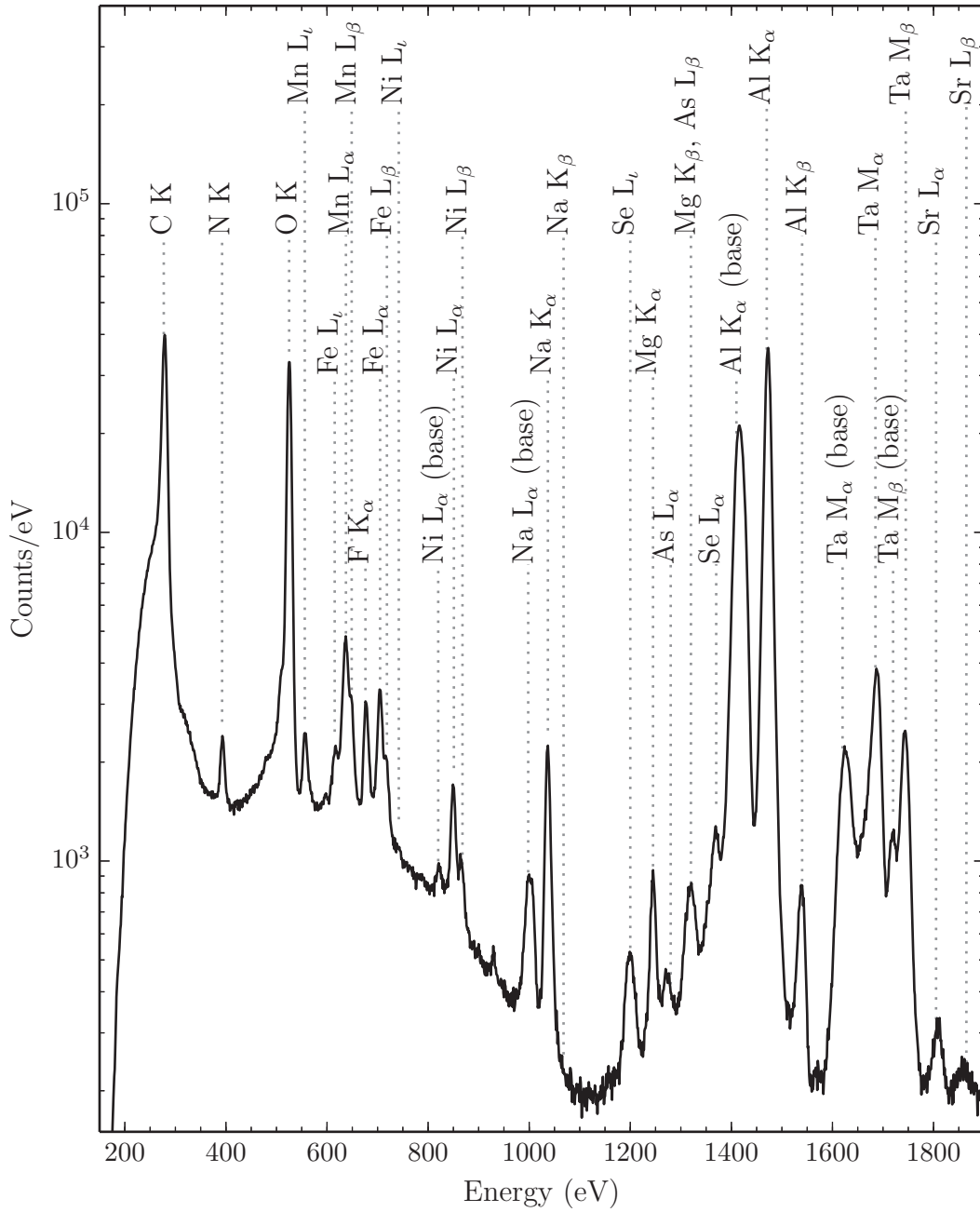


Figure 4.12: Summed spectrum emission spectrum from all pixels in 4.11. Resolvable lines from elements have been labeled. At higher energies, base layer events become visible as lower-energy lines split from their parent lines labeled “(base)”.

4.3 Dry ADR Performance

The cryogen-free ADR cryostat is prepared for cool-down similar to traditional wet cryostats, in that it must be initially evacuated to a pressure below 1 mTorr. If the cold finger is installed, this must be done slowly to prevent rapid pressure variations from damaging the IR filters on the ends of the snout shields, with a target pump-down rate is below about 0.5 %/second. The Pirani block includes a needle valve for throttling the pump, or a more accurate dosing valve such as the Pfeiffer EVN 116. Throttling is only necessary above 500 mTorr, at which point the vacuum pump is connected directly to the cryostat through the main seal-off valve. Once the pressure is below 1 mTorr, the cool-down is started by turning on the compressor. This may be done on the control panel software, and if the computer is networked and accessible via remote desktop software, it can be done remotely from anywhere with internet access. The heat switch must be closed during cooling so that the GGG and FAA stages are not thermally isolated.

The cooling time depends on the thermal mass of the installed components, most of which is from the ADR magnet and its magnetic shield. The cold finger also adds a sizable load. Figure 4.13 shows the typical cool-down time of the full version 1 STJ cryostat with the cold finger installed. The 60 K and 3 K stage temperatures are measured at the cold head interface with the thermal links, and the temperature at the end of 3 K snout shield is measured with a bare diode at the detector magnet coil. A sharp increase in the cooling rate of the 3 K stages occurs after ≈ 13 hours into the cool-down due to rapidly increasing thermal conductivity of the components at low temperature. This transfers more power into the 3 K stage, increasing the total system load and increasing in the 60 K stage temperature according to Fig. 3.2. The cryostat reaches a stable base temperature about 16 hours after starting the pulse tube compressor.

Note that the end of the 3 K snout shield is several K higher than the base of the cold head. This is a result partly of the bare diode thermometer not being perfectly heat sunk to the shield, and partly reflects a temperature gradient between the base and the end of the snout. The ADR cycle can be started once the cryostat temperatures have equilibrated after about 16 hours. Safety checks include testing that the heat switch opens and closes without issues, and that the ADR magnet and leads are superconducting. The control software also has built-in safety measures to prevent damage such as quench monitoring and control and temperature limits during regeneration. Additionally, the software parameters include the magnet inductance and residual resistance which are used to calculate the current ramp rate. If the observed rate as a

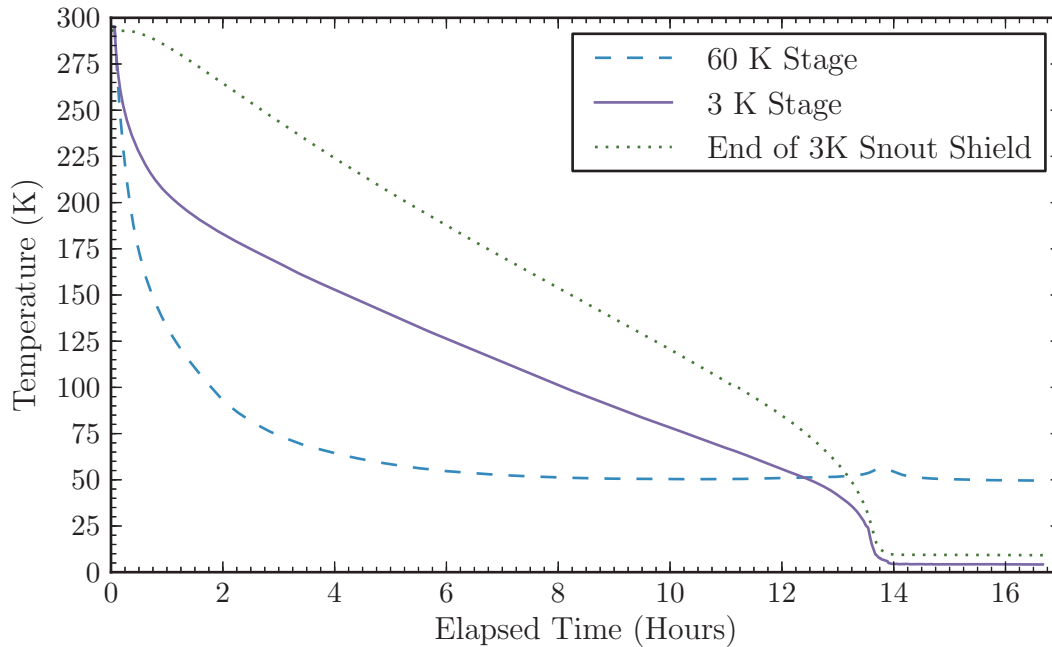


Figure 4.13: Cool-down rate of the STJ cryostat with cold finger installed.

function of voltage is outside the setpoint, the software aborts the regeneration cycle and ramps the current down to zero. While this level of caution is not necessary for wet ADR cryostats, this cryostat does not have the large reservoir of liquid cryogenes to sink the heat from a magnet quench, so it is best to avoid quenching to prevent costly damage. The calibration of the magnet RTD is also checked before the first regeneration cycle since cooling from room temperature and recalibrated if necessary.

The ADR cycle proceeds by ramping the current to a maximum of 8 A corresponding to a field of 4 T, holding it there for a set time to allow the temperature to stabilize, and ramping it back down after the heat switch is opened to thermally isolate the GGG and FAA stages. The time taken for each cycle may be set in the software, with typical values ranging from 10 to 30 minutes per segment depending on how much thermal mass each stage is carrying. Figure 4.14 shows the temperature of the magnet and the various stages of the ADR through a typical regeneration cycle with 20 minute segments. Since the T_c of the NbTi magnet windings is above 9 K, there is a large safety margin in this cycle against quenching.

The FAA and GGG stages heat up during the ramp-up segment due to the energy of ordering their magnetic moments. Ramping the field up slowly limits the heating of the GGG and FAA stages, while ramping down slowly is also preferable to prevent eddy current heating

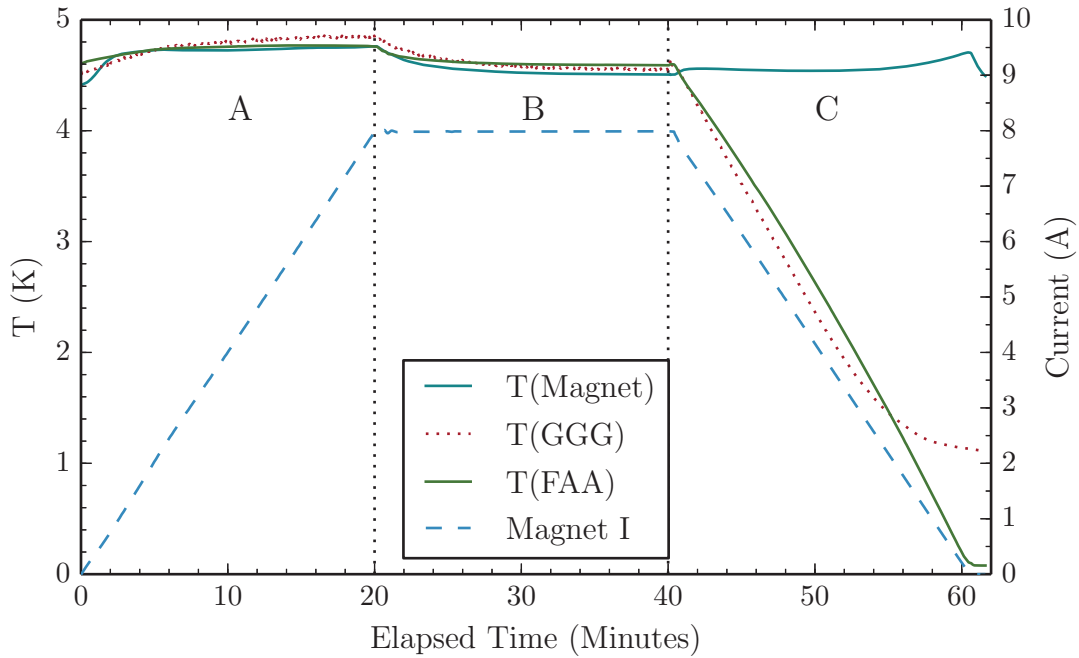


Figure 4.14: Temperatures of the ADR cold stages during the regeneration cycle with cold finger installed. The portions of the cycle labeled A, B, and C correspond to the segments labeled in Fig. 3.4, and the heat switch is opened between B and C at 40 minutes elapsed time. The y-axes are split for magnet current and thermometer temperature.

in the metal components of those stages. Each stage warms slightly as the field is ramped up, but stabilizes in temperature as the heat of magnetization is removed through the heat switch. The heat switch is opened before ramp-down to cool the GGG and FAA stages to their final temperatures of 1 K and 70 mK, respectively. The FAA reaches its lowest temperature almost immediately following the ramp-down, but the GGG has a higher heat capacity and is therefore slower to equilibrate and cools for a time after the end of the cycle.

Once the ADR regeneration cycle is complete the magnet current is completely at 0 A and the cold stages reach their coldest temperatures. If the ADR is left idle, the FAA and GGG stages will slowly warm, which is acceptable for STJ operation as the temperature does not need to be constant but only need below ≈ 0.3 K. The ADR may also be set to run in temperature regulation mode which maintains a small field in the magnet to control the temperature on the FAA stage. The software is coupled to a Stanford Research Systems SIM960 PID controller to maintain the FAA temperature at the setpoint with better than $10 \mu\text{K}$ deviation. This is preferable to unregulated operation as it increases the cooling power of the FAA stage. Figure 4.15 shows the temperature evolution during a regulation cycle with the snouts installed. While this is below

the desired hold time for this system, it is still acceptable for STJs, with 8.5 hours regulation time and 9.5 hours below 300 mK. The ADR performance is dominated by the high thermal radiation load from the warm 60 K snout shield as described earlier, and will be improved in future re-designs of the cold finger.

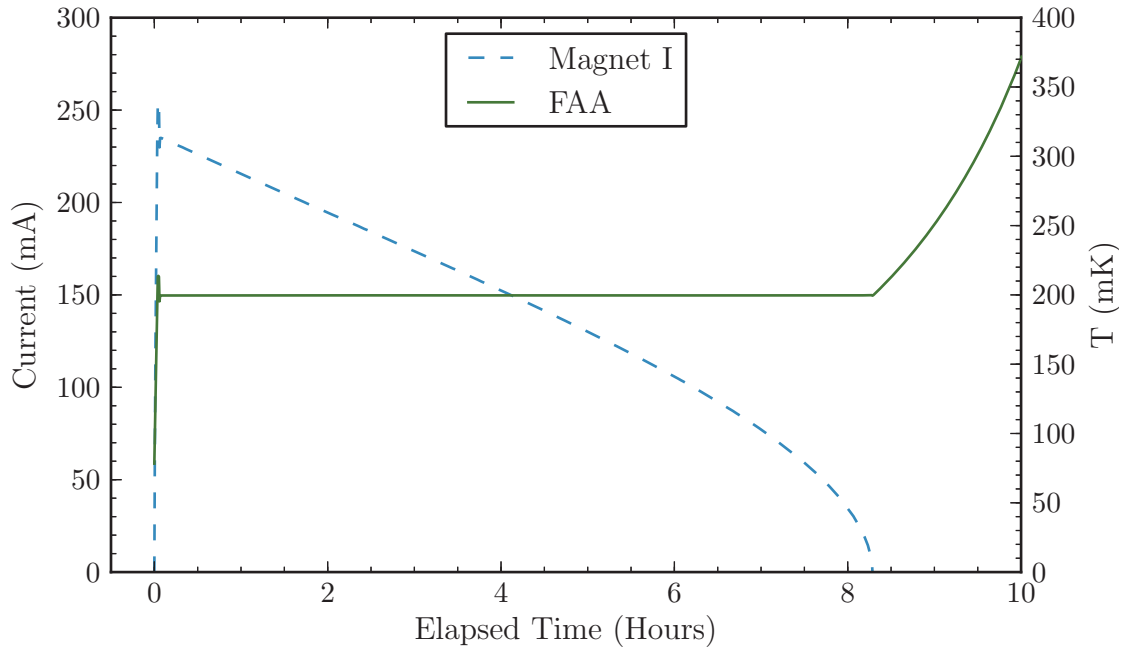


Figure 4.15: Operation of the ADR in temperature regulation mode after a regeneration cycle. The temperature of the FAA stage is set to 200 mK. Once the magnet current is ramped down to zero after ≈ 8.5 hours hold time, the FAA temperature begins to rise.

4.3.1 IR-Blocking Windows

To operate STJ detectors at a temperature < 0.3 K within centimeters of a sample at room temperature, three IR filters are installed at the end of the cold finger. The filters consist of 100 nm of aluminum backed by 350 nm of polyimide film for mechanical support. The aluminum film is the primary blocker of low-energy light, and as an excellent thermal conductor it keeps the suspended film cold.

To characterize the performance of the filters, their absorption is measured on two different spectrometers covering the mid-IR and UV/Vis ranges. The IR measurements were performed with a commercial Bruker Vertex 70v Fourier-transform infrared (FTIR) spectrometer, covering the range from 2500 to 20000 nm. While this range only covers the main portion of the blackbody spectrum at room temperature, this measurement helps set bounds on the expected

absorbance and can be extrapolated to longer wavelengths. Figure 4.16 shows the measurement of a standard IR-blocking filter. The spectrometer sensitivity falls off above an absorbance of 2, becoming highly nonlinear before approaching the measurement limit of an absorbance of 6. So, any data above an absorbance of 2 are considered less meaningful, and many points register at the threshold of 6 absorbances, which means the detector measured no signal. This spectrum indicates the transmission is well below the sensitivity of the instrument and sets a lower bound for the filter absorbance in the IR band indicated by the dashed line in figure 4.16. The actual absorbance is almost certainly much higher.

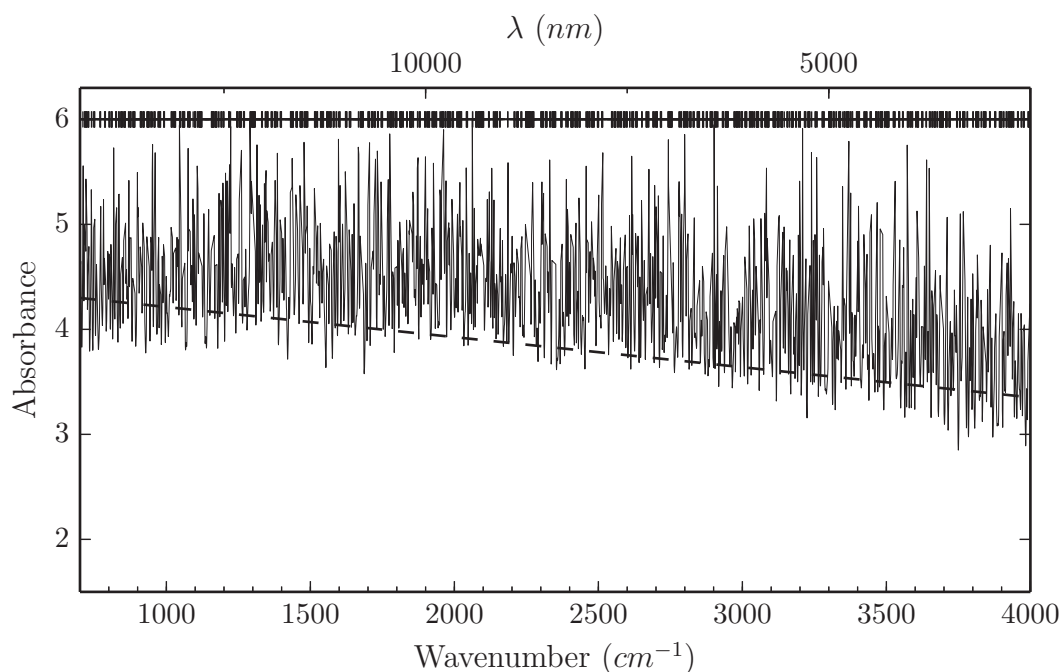


Figure 4.16: Mid-IR band absorption of one snout IR filter. Data points which registered some non-zero value are plotted in black, while points which register as 6 absorbances (or no measurement) are plotted as crosses at Abs = 6. The dashed line is the fitted boundary value used in figure 4.18.

UV/Vis measurements were performed in a similar manner on a commercial Agilent Cary 60 spectrometer. The results are plotted in 4.17, which has a similar fraction of high-absorbance points, with points at 10 absorbances corresponding to zero counts and indicating that the measured transmission is below the sensitivity of the instrument. The region between 240 nm and 300 nm is likely due to constructive interference in the aluminum layer, allowing slightly more photons through in that band.

These measurements of absorption are rough at best, but help to set bounds on the expected

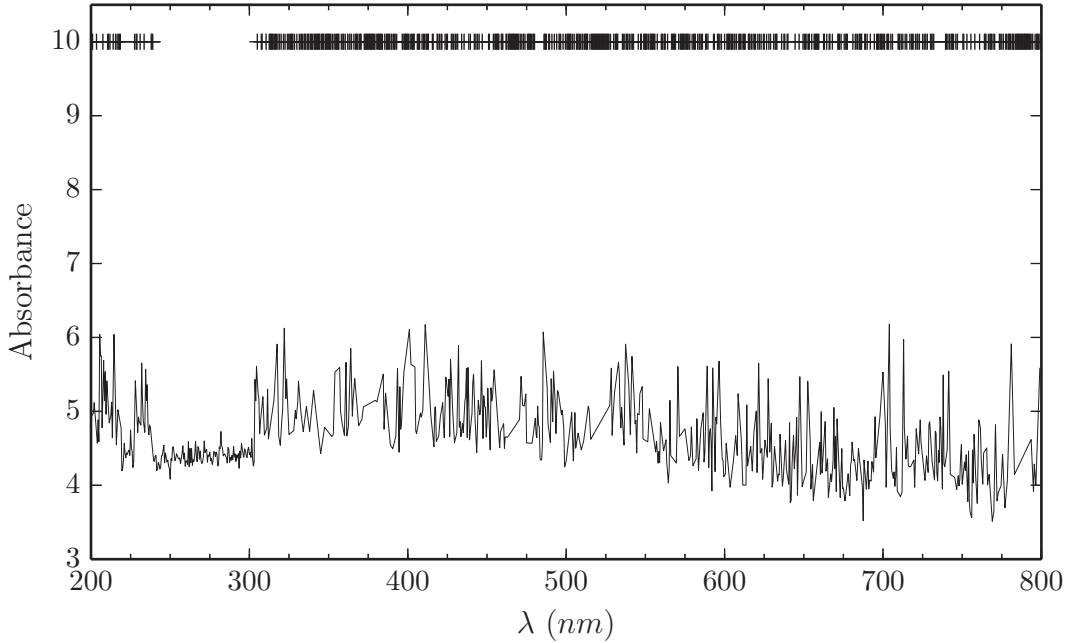


Figure 4.17: UV/Vis absorption of one snout IR filter. Data points which registered some non-zero value are plotted in black, while points which register no measurement are plotted as crosses at an absorbance of 10.

radiative load onto the detector stage. In most cases, the cryostat will be operated in a vacuum chamber at room temperature, so the power spectrum from a 295 K blackbody (figure 3.8) is appropriate for calculating the thermal load. The power S_1 through one filter of base-10 absorbance A when illuminated by a source of power S_0 follows the relation

$$S_1 = S_0 \times 10^{-A}. \quad (4.5)$$

For multiple filters the absorbance adds, so $S_2 = S_0 \times 10^{-2A}$ and $S_3 = S_0 \times 10^{-3A}$. Using the fitted boundary line in figure 4.16 yields an upper limit for the transmitted power. These results are plotted in figure 4.18. The line corresponding to 2 filters in figure 4.18 is numerically integrated to calculate expected power through the IR filters on to the 50 mK stage. The calculation is performed for 2 filters as these are what sets the radiative load onto the detector stage, and the third filter attached detector stage does not affect its load. The outermost 6.35 mm open window sets the aperture, yielding a cone of approximate inner angle $\theta = 28^\circ$ and a solid angle $\Omega \approx 0.75$ sr. The illuminated region on the FAA stage has a radius of ≈ 4.5 mm giving an area of 64 mm^2 . This results in ≈ 20 nW maximum radiative power onto the FAA stage from room temperature blackbody radiation through the filters, about $7 \times$ greater than the load from the

surrounding 3 K snout shield, assuming this shield is, in fact, at 3 K. If the filters are more effective by 1 absorbance unit, the power drops to 0.2 nW and is negligible compared to even the radiative loading from the surrounding 3 K snout shield. Since this is very likely the case, we may conclude the IR filters are effective at shielding the STJ detector chip from IR radiation.

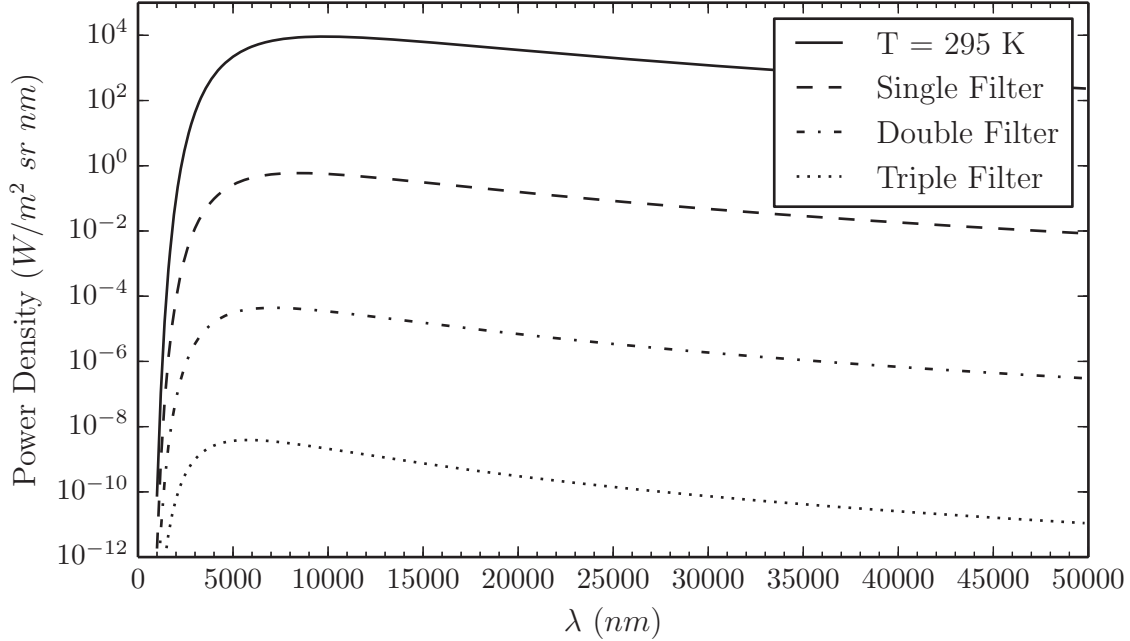


Figure 4.18: Power from a blackbody at 295K transmitted through one, two, or three IR filters.

On the opposite end of the spectrum, the filters should be as transparent as possible to x-rays above ≈ 100 eV. This was measured directly at beam line 4.0.2 at the ALS while the ring was operating in 2-bunch mode. While the beam line flux is reduced by a factor of ≈ 15 in 2-bunch mode compared to standard operations, it still has adequate flux in the sub-keV region. The region above ≈ 1200 eV is increasingly noisy due to the limited flux available from the 5th harmonic at beam line 4.0.2, but is still useful to characterize the filters. Figure 4.19 shows the measured absorption vs. energy for a single filter to bring out the edge detail at low energies. The prominent C, N, and O edges are from the Kapton (polyimide) support layer, while the Al K edge is visible around 1,575 eV. The model is generated using the ALS CXRO database [2], with $0.1 \mu\text{m}$ Al on a $0.35 \mu\text{m}$ Kapton film. The model matches the observed transmission except for right at the absorption edges where bound-state transitions dominate to create near-edge structure that is not included in the CXRO database.

As in the IR measurements, the multiple filters add linearly in absorbance. The transmission

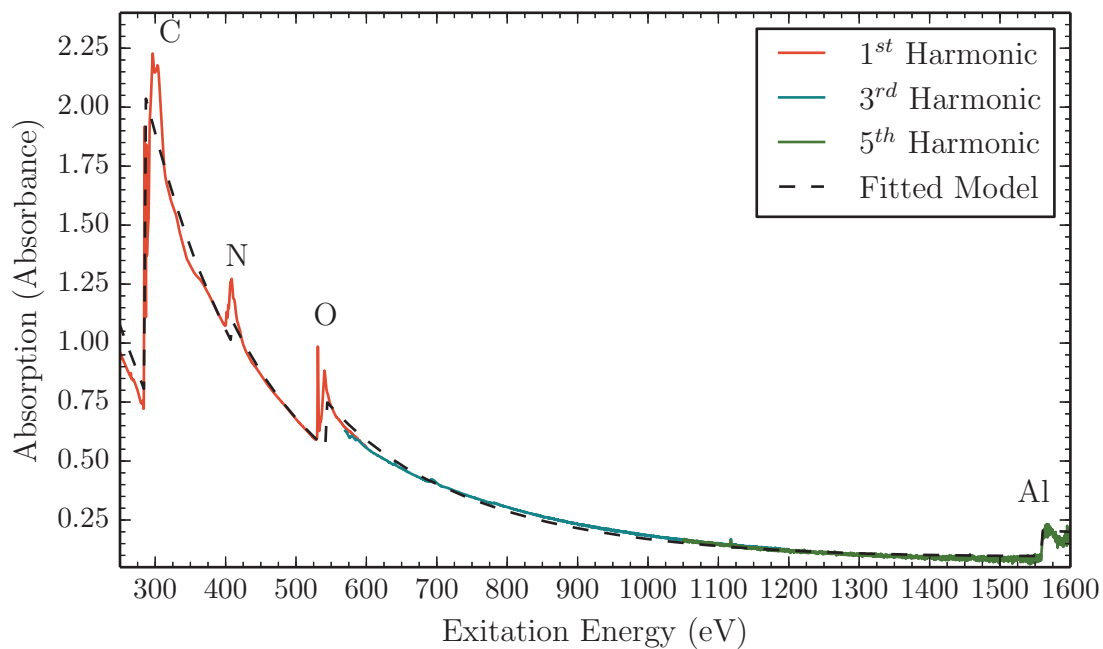


Figure 4.19: Measured x-ray absorbance of a version 1 IR filter. Data were collected on ALS beam line 4.0.2 in transmission mode. The energy range is covered by three harmonics of the beam line and two different gratings; data from each harmonic is plotted separately.

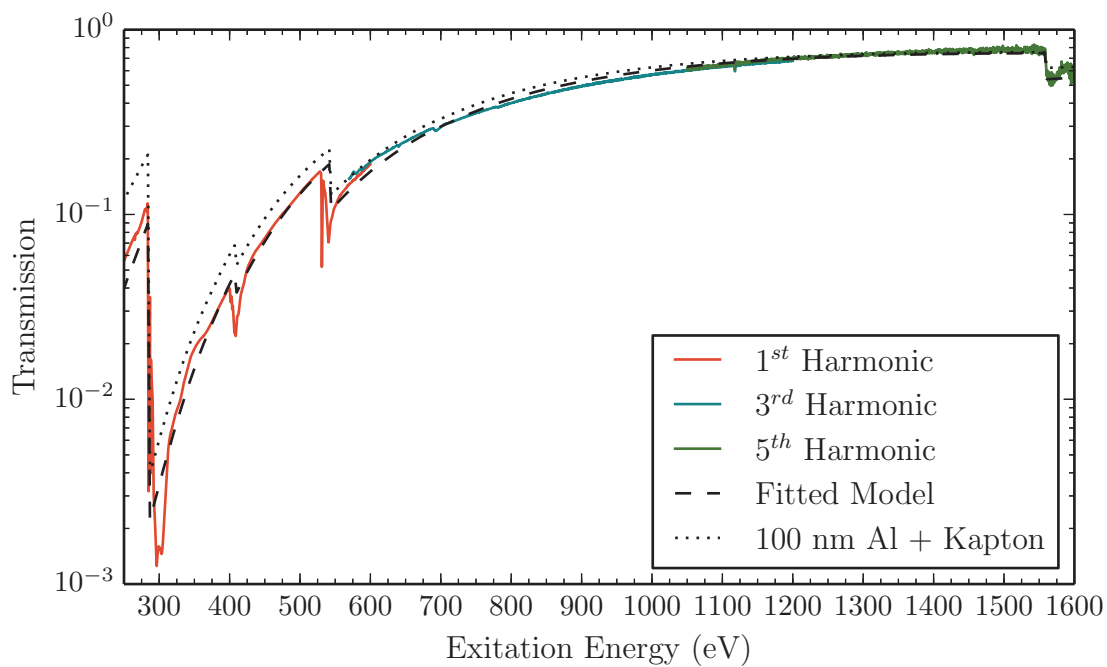


Figure 4.20: Soft x-ray band transmission of a stack of 3 IR filters as installed in the STJ snout assembly.

T is related to base-10 absorbance A by

$$T = \log_{10}(-A). \quad (4.6)$$

Figure 4.20 shows the transmission of the 3-filter stack, which is the fraction of incident photon flux that will reach the detector chip behind all three filters. The edge features are the same ones labeled in figure 4.19. While acceptable for work above the O K edge, the $< 10\%$ transmission below that edge may be limiting for difficult experiments. Future windows may reduce the Al thickness to 20 nm and the polyimide thickness to 200 nm for increased transmission.

4.3.2 Detector Magnets

The performance of the STJ detector is also affected by the detector magnet coil pair at the end of the cold finger. This pair of magnets is attached to the outer face of the 3 K snout shield at a distance of ≈ 2 cm from the detector chip. The magnets must be superconducting to prevent ohmic heating from loading the cold finger, and must apply a field along the plane of the detector chip of $\gtrsim 3$ mT. To approximate the expected field in the center of the coil from approximately 1800 turns of wire per coil, the magnet is modeled as a solenoid of length $2l$ and inner/outer diameters a and b . The field in the center of the a solenoid as a function of overall current density J is given by [3]

$$B_0 = JaF(\alpha, \beta) \quad (4.7)$$

with $\alpha = b/a$, $\beta = l/a$, and the function $F(\alpha\beta)$ is defined by

$$F(\alpha, \beta) = \mu_0\beta \ln\left(\frac{\alpha + (\alpha^2 + \beta^2)^{1/2}}{1 + (1 + \beta^2)^{1/2}}\right). \quad (4.8)$$

To approximate the coil as a solenoid, we use values of $2l = 6.5$ mm, $a = 2.3$ mm, and $b = 10$ mm. The overall current density is the total current circulating around the cross-sectional area of the magnet of $\approx 3.6 \times 10^{-5}$ m², giving a current density of approximately 2.8×10^7 A/m². The value of F with these parameters is 6.48×10^{-7} T·m/A. Rewriting equation 4.7 into a form that relates the central field to input current I for this magnet with n turns gives

$$B_0(I) = aF(\alpha, \beta) \left(\frac{nI}{l(b-a)} \right). \quad (4.9)$$

For the above values, $B_0 = 145$ mT/A, in the center of the magnet. Away from the center but still on the symmetry axis of the coil, the field is calculated by dividing the coil into two sections

offset by the distance from the center z , giving $\beta_1 = (l - z)/a$ and $\beta_2 = (l + z)/a$. This adjusts equation 4.7 so that it becomes

$$B_0 = \frac{1}{2}Ja[F(\alpha, \beta_1) + F(\alpha, \beta_2)]. \quad (4.10)$$

The center of the STJ chip is about 20 mm from the magnet, giving an approximate field vs. applied current of 7 mT/A. Since there are two magnet coils adding together, this field is doubled to 14 mT/A. From these approximations, we expect to be able to operate the STJ with a current above 200 mA.

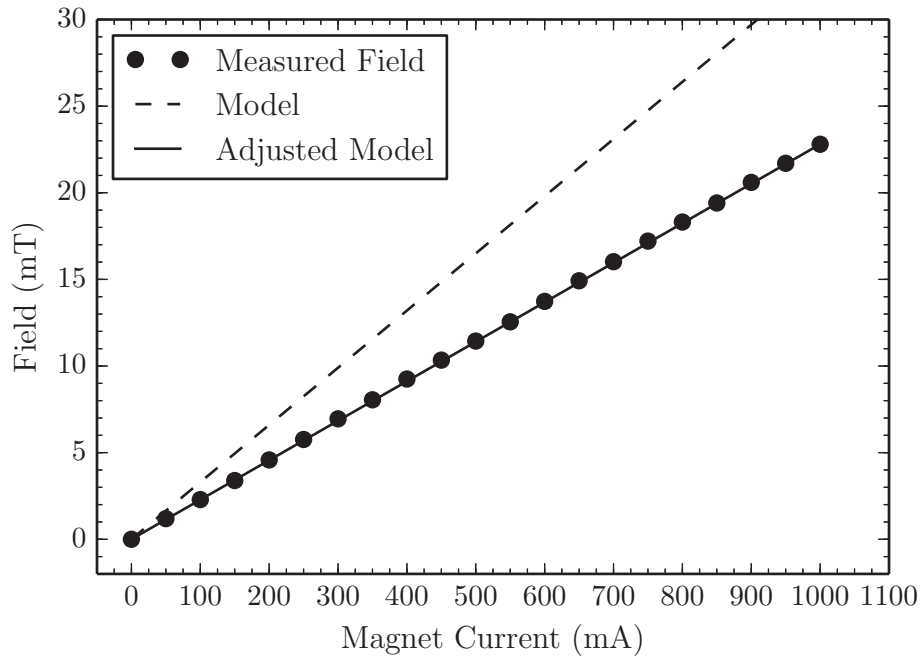


Figure 4.21: Magnetic field strength of the first generation STJ detector magnet 10 mm outside the coil. The models are calculated from equation 4.10

To test whether the actual field performance from these magnets is close to the design, a single coil was installed clamped directly onto the 3 K stage with a Lakeshore HGCT-3020 transverse Hall effect sensor positioned close to one face. This hall sensor is specifically designed to operate at cryogenic temperatures with minimal error. The hall sensor was positioned approximately 10 mm from the face of the magnet. The measured field vs. current applied to the magnet is plotted in figure 4.21. This is lower than the expected current (dashed line), which is not unexpected given the approximations of the calculations. Since the field response is very linear, the model can be adjusted by a factor of 0.7 to fit the data (4.21). With this scaling, the

field at the detector position is 9 mT/A for the magnet pair, which means the STJ should operate well at a magnet current of ≈ 0.3 A.

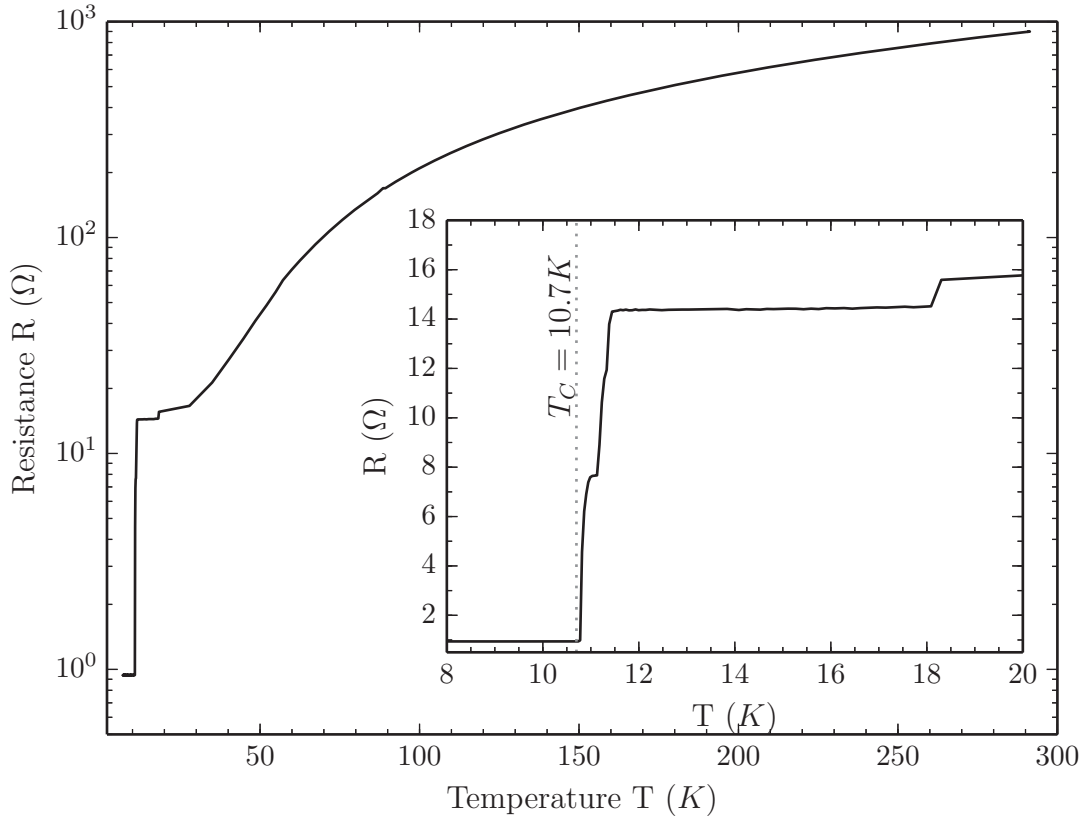


Figure 4.22: Resistance of the snout magnet coil assembly as a function of measured temperature.

The second test of the detector magnets is to confirm that they superconduct when installed at the end of the 3 K snout shield. The resistance measurement is a 2-wire measurements that includes the lead resistance of the normal-conducting leads at high temperature and thus has a residual resistance of $\approx 0.9 \Omega$. Several steps in the $R(T)$ curve below 20 K correspond to separate segments of the leads becoming superconducting. The data were taken from a first-generation magnet with aluminum bobbins, which were designed conservatively to require as little current as possible. Their performance shows that future magnets can be comfortably decreased in size and still handle the increased current. As shown in figure 4.22, the magnets become fully superconducting when the measured temperature at end of the 3K snout passes 10.7 K. The discrepancy between the observed T_c and the true NbTi T_c of 9.2 K is due to the non-ideal thermal contact of the bare diode thermometer, so that the measured temperature is higher

than the true temperature at the end of the snout. This is confirmed by the observation that the magnets have been operated without quenching up to nominal temperatures as high as 9.8 K.

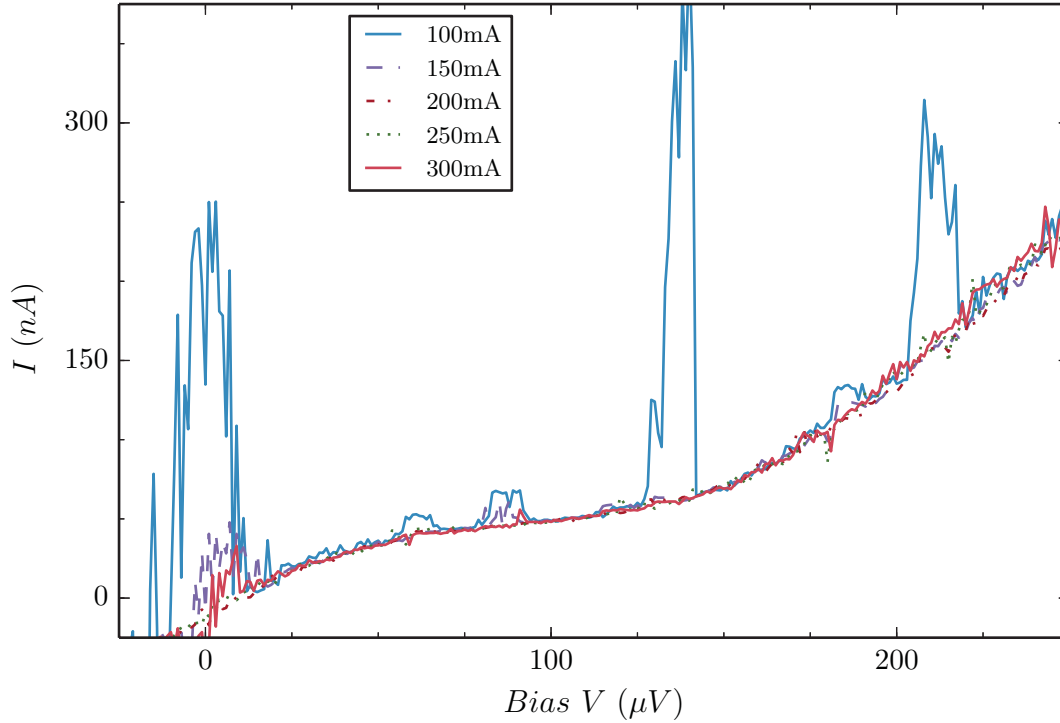


Figure 4.23: $I(V)$ curves for a single STJ at indicated currents applied to the detector magnet coils.

The final test of the detector magnets is to install an STJ array chip at the end of the cold finger and measure the device $I-V$ curves to establish stable operating fields. Figure 4.23 shows how the $I-V$ curve of a single pixel responds to various currents applied to the magnets. At low fields, the noise from the dc Josephson current and the Fiske mode resonances at ≈ 120 and $\approx 210 \mu V$ are clearly visible. As the magnet current is increased, not all Fiske modes disappear at equal rates, but beyond a threshold value they are all suppressed. While the Fiske modes and dc Josephson current are reduced significantly by a current of 200 mA corresponding to an estimated 2 mT from both coils, this still does not give the desired operating stability. The noise curves in figure 4.24 show that the influence of Fiske modes on preamplifier noise is still present at ≈ 200 mA, but no longer at 300 mA. One reason for this better-than-expected performance is the influence of the high-permeability magnetic shield on the 60 K snout shield that concentrates the field lines at the detector chip.

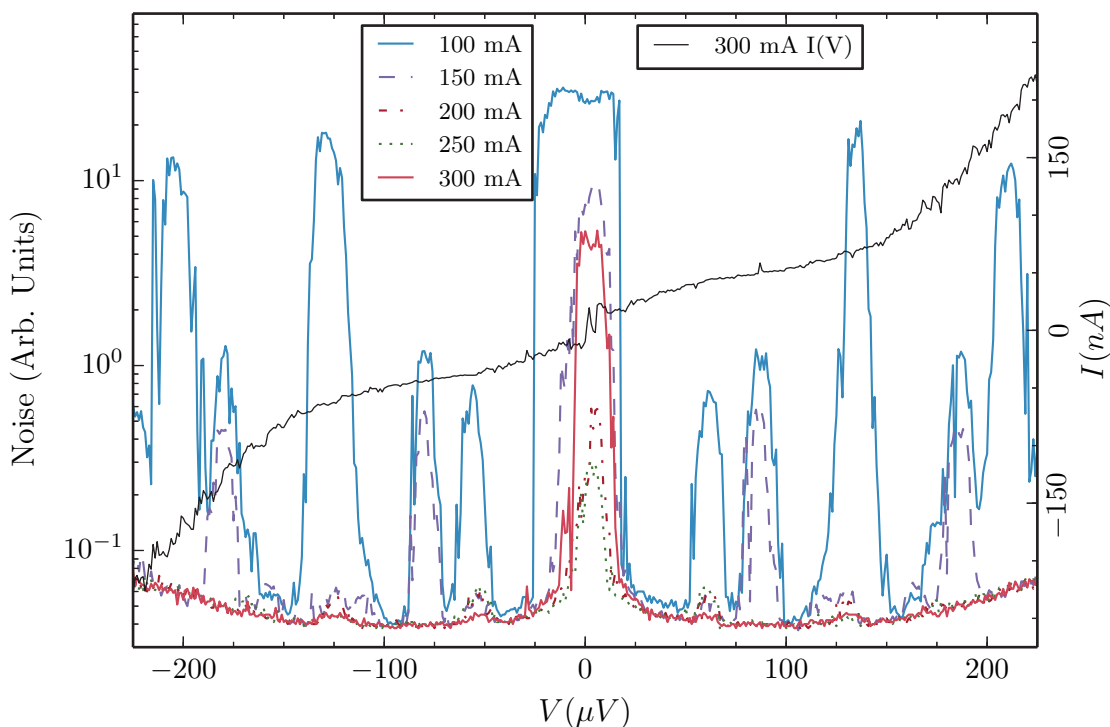


Figure 4.24: Noise curves for a single STJ at indicated currents applied to the detector magnet coils. The $I(V)$ curve at the full field of 300 mA is plotted in black for reference.

4.4 XAS Setup

For PFY-XAS at a synchrotron beamline in the soft x-ray band, the cryostat is attached directly to a Conflat flange of a sample analysis endstation so that it shares the UHV vacuum space. A manual gate valve allows the detector to be isolated from the chamber for installation and removal, and to protect the detector from potential vacuum fluctuations during sample changes. The optimum orientation for XAS aligns the detector cold finger with the polarization of the incident x-ray beam to suppress elastic scattering. This is typically at 90° relative to the beam for for linearly-polarized bend magnet and undulator beam lines.

During measurement the detector is inserted fully into the analysis chamber to maximize the solid angle for photon collection. The pulse height analyzer (PHA) and acquisition electronics must be linked to the beam line control software to control timing of the data collection. The beamline control software operates the monochromator, slits, and sample stage to set the desired x-ray beam energy and resolution. The process of measuring an absorption spectrum by PFY involves stepping the beam line energy through a series of excitation energies, collecting

full emission spectra at each energy. Only the fluorescence from the element of interest is used as a measure of the absorption. Best practices indicate that samples needing long acquisition times for good counting statistics should be analyzed in multiple XAS scans and subsequently averaged to prevent data corruption from artifacts, dropped beam, or other sources. The acquisition time required at each beam line energy point depends on the fluorescence flux from the sample and the collection efficiency, but typically ranges from 5 seconds to many minutes per energy, acquired over many sequential scans.

Once the ADR is cycled and the cryostat is at operating temperature with current applied to the detector magnets, the STJ detectors are set-up using the XIA control software. Figure 4.26 shows the software window with the bias control panel active, which is used to set the bias voltages and the preamplifier gains. A separate pulse analysis panel is used to configure pulse shaping times and gain offsets, and a PHA panel is used to collect emission spectra. The PHA panel is useful for diagnostics, but is not used for collecting XAS spectra.

Figure 4.27 shows the I-V curves for 24 pixels while installed at beamline 6.3.1, confirming that the noise performance in a beam line environment is similar to the offline measurements in a laboratory. The leakage currents are quite uniform across the array. The Fiske modes are more visible in some pixels than in others due to small variations in device geometry across the array. However, these pixels have very similar x-ray spectra to those without visible Fiske mode resonances.

The full array performance is assessed by illuminating a mixed-element target at a fixed x-ray beam energy that is high enough to excite most elements of the sample. Figure 4.28 shows the summed emission spectrum of a stainless steel target from the entire array. The resolution at the O K line at 525 eV is ≈ 8 eV, matching the performance of the array in the LLNL test cryostat. Since the XIA PHA software does not yet have the ability to discriminate pulse height rise time, the spectrum does display some base-layer artifacts at higher energies as well as the substrate artifact around 800 eV. The Fe and Ni lines are much stronger than the Cr and O lines due to both to the choice of excitation x-ray energy (for Ni) and their larger fractional makeup of the sample (for Fe). The $L_{\nu,\eta}$ emission from the metals is clearly visible and separable from the other lines. This means that the instrument performance is sufficient to gate on either the $L_{\alpha,\beta}$ or the $L_{\nu,\eta}$ lines of a transition metal element in fluorescence-detected XAS experiments.

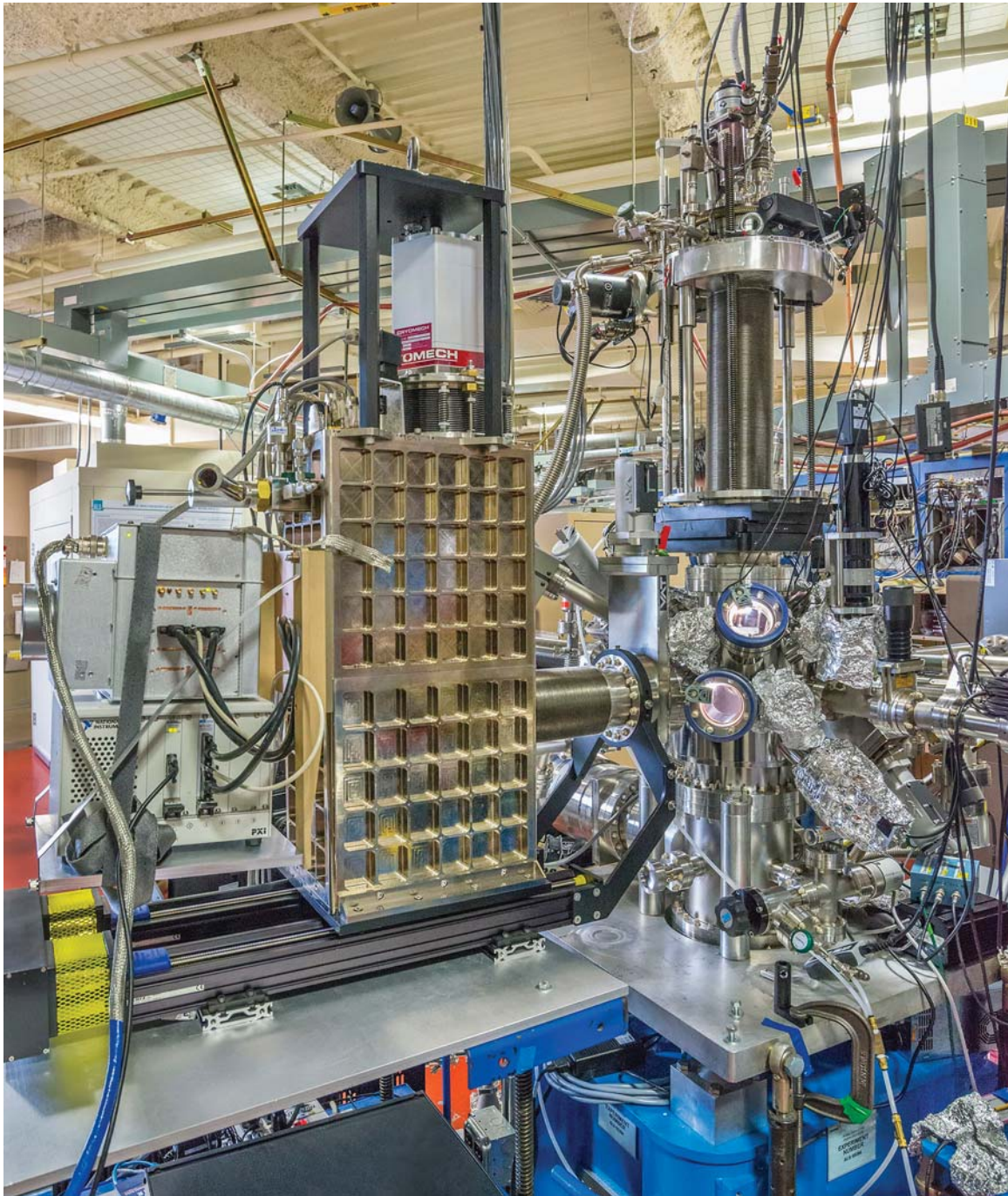


Figure 4.25: STJ detector installed at the experiment endstation on beam line 6.3.1 at the Advanced Light Source (ALS). The detector is fully inserted into the sample chamber for measurement. The x-ray beam enters the chamber from the right side of the photo.

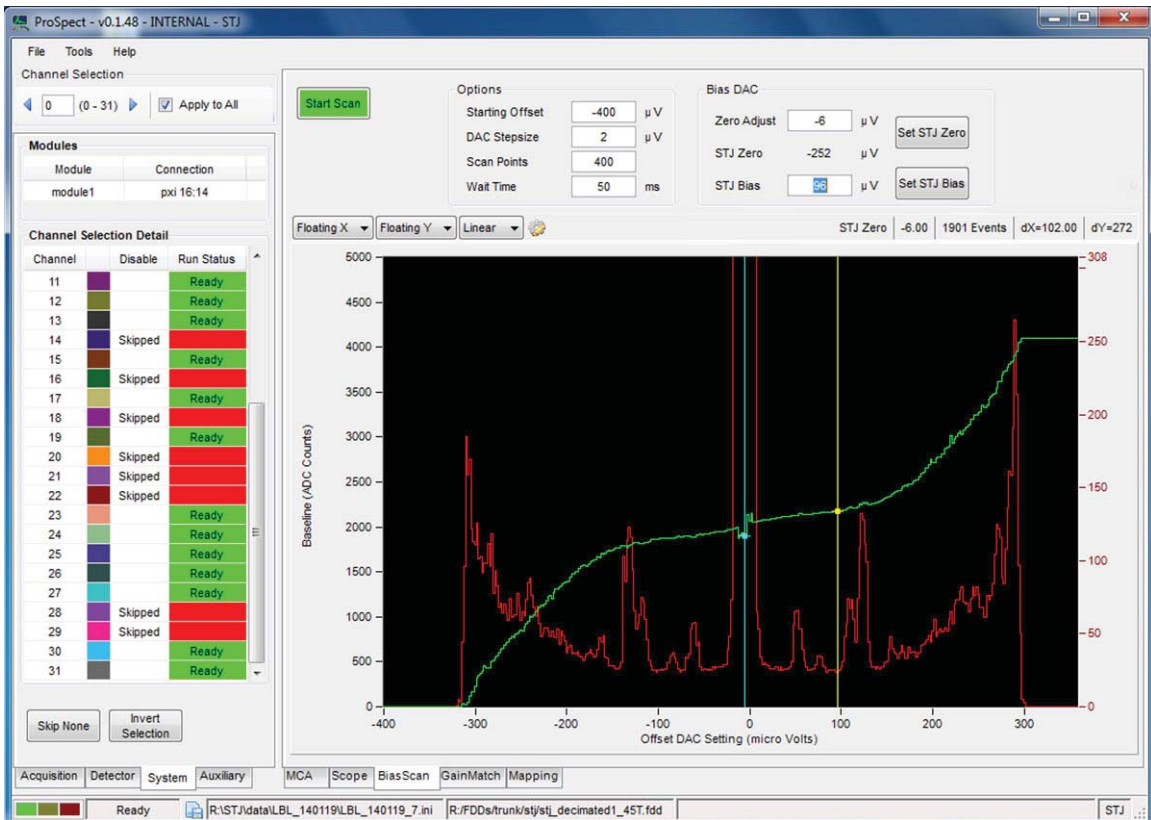


Figure 4.26: XIA STJ control software. This window shows the bias control panel. The main plot shows I-V (green) and noise (red) curves from one pixel selected from the list in the left frame. Vertical cursors show the zero and bias set-points for this pixel.

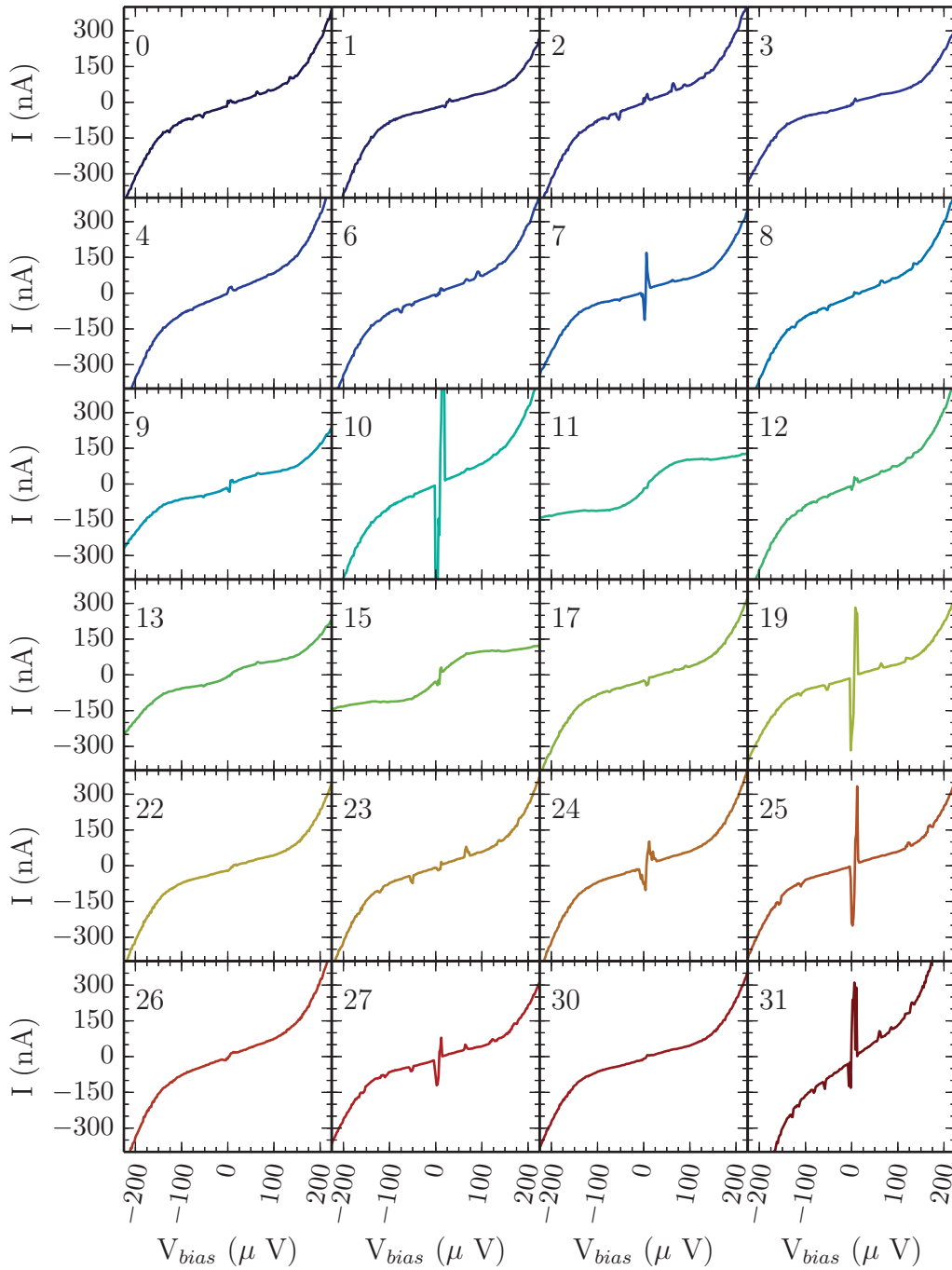


Figure 4.27: I(V) Curves for 24 operating pixels of the 36-pixel array installed at ALS beam line 6.3.1. The detector magnet current is 300 mA.

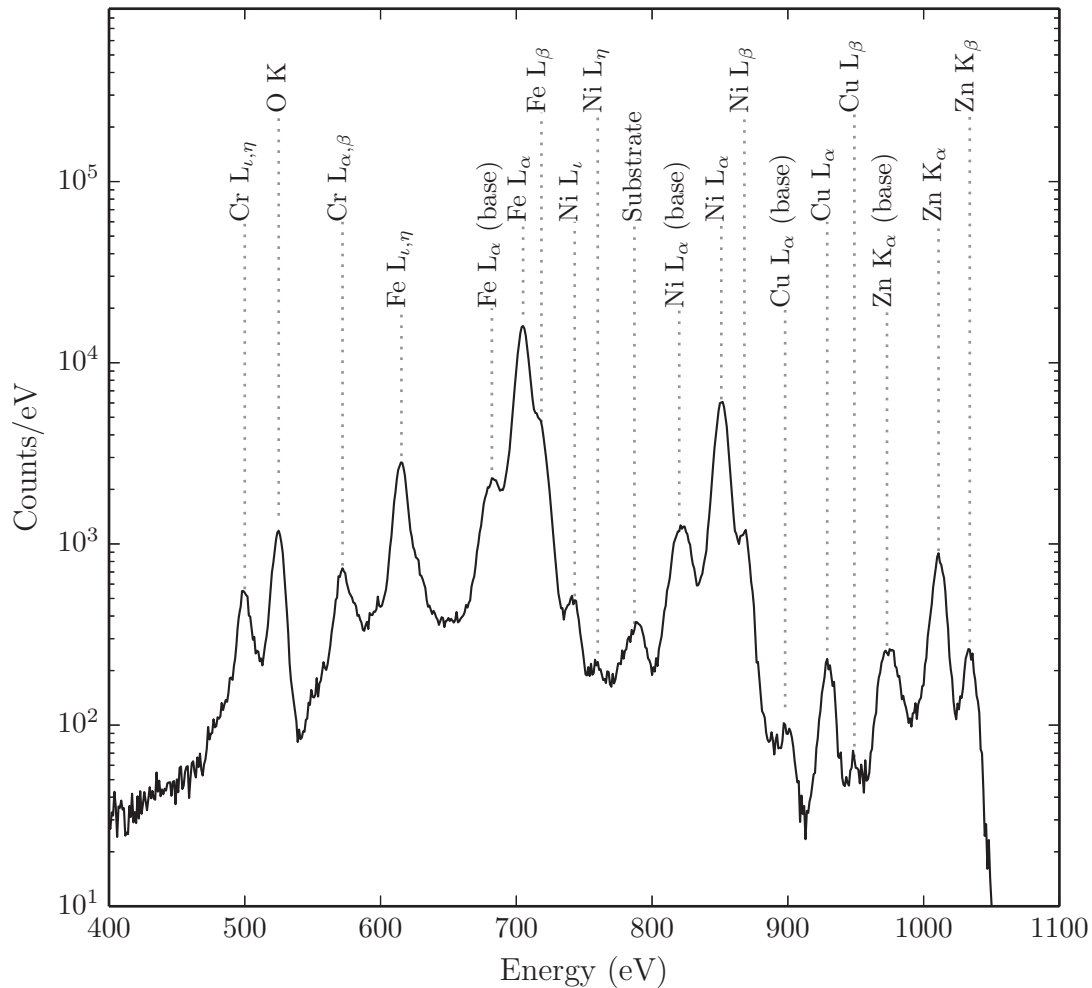


Figure 4.28: Combined emission spectrum from the 36-pixel array at ALS beam line 6.3.1. The target is a fragment of AISI 304 stainless steel excited with an x-ray beam energy of 900 eV.

References

- [1] L. J. Hiller, M. L. van den Berg, and S. E. Labov, "Multiple-tunneling noise in superconducting tunnel junctions from partial current integration," *Appl. Phys. Lett.*, vol. 79, no. 26, p. 4441, 2001. [Online]. Available: <http://scitation.aip.org/content/aip/journal/apl/79/26/10.1063/1.1428618> (page 86)
- [2] CXRO, "Center for X-ray Optics: X-Ray Interactions with Matter," CXRO, 2014. [Online]. Available: http://henke.lbl.gov/optical_constants/ (page 99)
- [3] M. N. Wilson, *Superconducting Magnets*, ser. Monographs on Cryogenics. Clarendon Press, 1986. [Online]. Available: <http://books.google.com/books?id=Z51mCRITaxkC> (page 101)

Chapter 5

Application

This chapter describes an experimental study examining whether PFY-XAS as currently performed at most synchrotrons provides an accurate measure of the absorption spectrum of dilute metal complexes. This work requires the high resolution and sensitivity of the STJ spectrometer and could not have been performed with conventional Si- or Ge-based x-ray detectors.

As detailed in chapter 1, measurement of XAS by PFY with energy-resolving detectors has long been commonplace for synchrotron studies of dilute materials. These measurements rely upon the assumption that the intensity of the x-ray fluorescence is directly proportional to the XAS for all incident x-ray energies. While this is probably largely true for K-edge XAS measured using the K emission lines, for L-edge measurements, recent theoretical predictions suggest that the L-edge XAS of transition metals with large field splitting will be distorted when measured by fluorescence yield. This is due to the lack of independence between the absorption and emission events, which causes the emission process to be highly correlated with the absorption process. The particular bound state that the core electron is excited into affects the transition probabilities of decay from $3d \rightarrow 2p$ shells, which correspond to the L_α and L_β emission lines. In effect, these emission lines are no longer spectators of the absorption process, but actively participate in and are affected by the excitation of the core electron into bound states. However, the emission from filled orbitals that do not participate in the absorption process should remain unaffected. For first-row transition metal L-edges, these are the $3s \rightarrow 2p$ transitions corresponding to the L_i and L_η lines.

Hence, the first goal of this work is to show whether the XAS is in fact distorted when measured with PFY. This requires the preparations of samples that are thin enough for transmission measurements, yet dilute enough for PFY, which in turn requires development of novel sample

fabrication techniques. The second goal of this work is to address whether PFY-XAS using the L_{ν} and L_{η} emission lines instead of the $L_{\alpha,\beta}$ lines can in fact provide a more accurate measure of the absorption. The final goal of this work is to assess using charge transfer multiplets (CTM) calculations whether significant information is in fact lost through any distortion of the XAS using L_{α} and/or L_{β} lines for the PFY, or whether appropriate analysis still reveals metal ligand fields, spin-states, and other derived information. It is important to emphasize that the high resolution and efficiency of STJ detectors is essential for these experiments, both to separate the different emission lines as well as to measure the weak signal from dilute, thin film samples.

5.1 Sample Preparation

The goal of this experiment is to determine whether there is a difference between the PFY-XAS and the true XAS for transition metal L-edges as measured in transmission mode. This deviation is correlated with the strength of the crystal field at the metal atom and will be larger in compounds with strong fields. The choice of system to study is guided by several requirements. It should have a strong crystal field to emphasize the effect. The true XAS must be measured to compare against the PFY- and TEY-XAS, which means the sample must be compatible with transmission XAS. It also must be possible to produce dilute and uniform solutions of the sample to prevent self-absorption when measuring the PFY-XAS. Ideally the sample used for PFY measurements is identical to the transmission sample to rule out chemical environment from changing the spectrum rather than the desired PFY deviation. These are very stringent requirements and require the development of new methods of sample preparation and measurement.

Transmission measurements in the soft x-ray region are far less common than transmission measurements in the hard x-ray region due to the very short attenuation lengths of most materials below 1 keV. The sample must be uniform to prevent pinholes from saturating the signal with background noise, and very thin, of order 1 μm thick, to be partially transparent to the x-ray photons. However, most samples for soft x-ray transmission are very concentrated and so are unsuitable for PFY-XAS free from density-dependent distortions. The transmission sample must therefore be dissolved in an inert, low-Z matrix to achieve the desired concentration while being transmissive enough for transmission measurements. We have chosen commercially available photoresist, a polymer used in microelectronic fabrication that may be spun onto a substrate in repeatable manner to produce thin films of controlled, uniform thickness. The AZ 1500 family of photoresists are available in a range of viscosities, allowing a range of

film thicknesses depending on the spin speed as shown in table 5.1 [1]. These thicknesses are in the μm range, which is the target range for soft x-ray transmission measurements.

Spin speed (rpm)	2000	3000	4000	5000	6000
AZ 1505	0.71	.58	0.50	0.45	0.41
AZ 1512HS	1.70	1.39	1.20	1.07	0.98
AZ 1514H	1.98	1.62	1.40	1.25	1.14
AZ 1518, AZ 1518HS	2.55	2.08	1.80	1.61	1.47
AZ 1529	4.10	3.35	2.90	2.59	2.37

Table 5.1: Film thickness as a function of spin speed of photoresists in the AZ-1500 family [2]. Thickness is in μm .

The next step with this choice of substrate is to identify candidate metal compounds to dissolve in it to produce homogeneous films. The principal solvent is propylene glycol monomethyl ether acetate (PGMEA) along with other volatile organic compounds (VOCs), so the sample should be soluble in organic solvents. A good candidate class is the metal-acetylacetonate (acac) series of compounds, which are commercially available for most first-row transition metals and therefore allows a systematic study of XAS for different cases of line separation. In addition, as shown in figure 5.1, metal-acetylacetonate (acac) compounds typically feature a central metal atom coordinated with bidentate acac ligands via the oxygen atoms, giving them a strong crystal field splitting. The methyl groups on the outside of the acac ligands make them soluble in many organic solvents, and they are commercially available for all the first-row transition metals. The attenuation length of selected metal-acac samples is shown in figure 5.2, which indicates that the pure form is unsuitable for either transmission or PFY-XAS and must be dissolved in the photoresist matrix to appropriate concentrations.

The photoresist/metal-acac transmission samples must be fabricated as thin, uniform films on a substrate which is also transmissive to x-rays in the soft x-ray region. Silicon nitride (SiN) is a common choice of substrate for this type of experiment. It has an attenuation length less than $1 \mu\text{m}$ below 1 keV, but is strong enough to fabricate into free-standing films with thicknesses of order 100 nm so that it is reasonably transmissive. The SiN substrates used for these samples is supplied by Norcada, Inc. on silicon frames with an open window etched in the center. The SiN thickness is 200 nm with a square window 1.5 mm per side in a 5 mm square Si frame. To fabricate thin film samples, the windows are secured to a glass microscope slide and installed

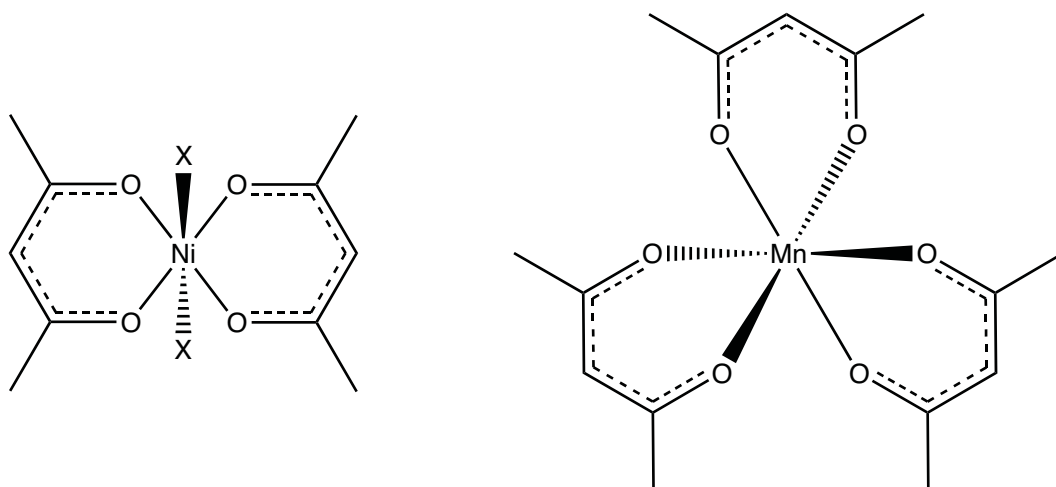


Figure 5.1: Diagrams of $\text{M}(\text{II})(\text{acac})_2$ $\text{M}(\text{III})(\text{acac})_3$ compounds of Ni and Mn. The Ni(II) compound is depicted in its monomeric solvated state with Xs denoting solvating molecules.

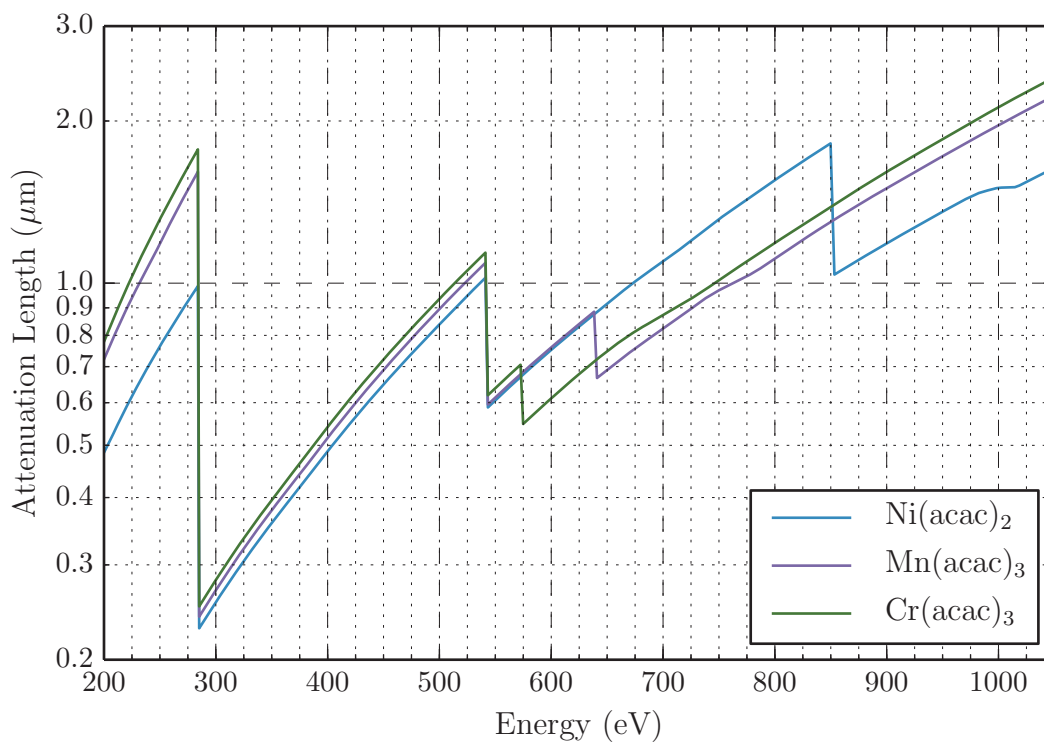


Figure 5.2: Soft x-ray attenuation lengths of metal-acac samples under study [3].

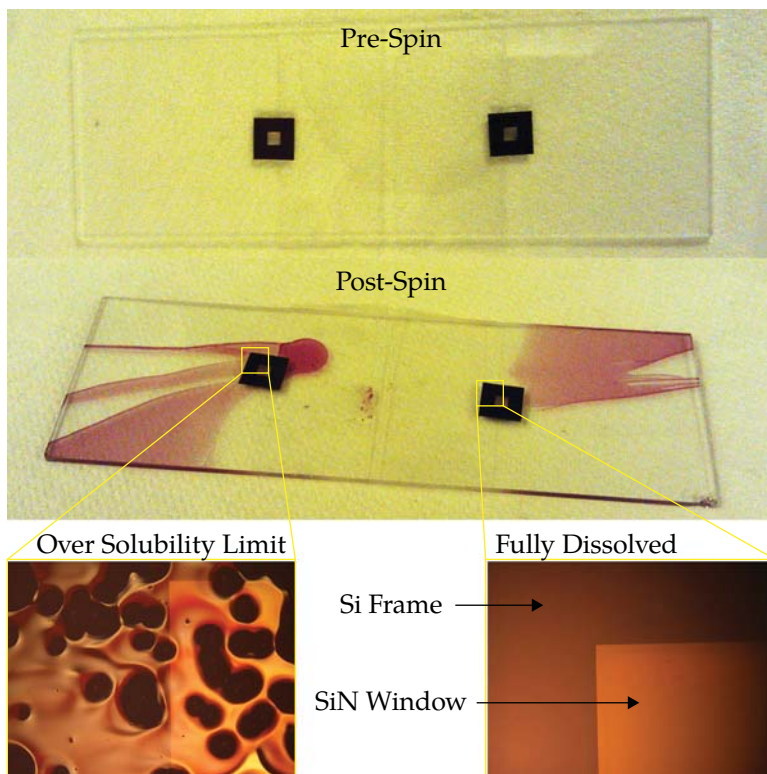


Figure 5.3: Method for producing transmission sample films on SiN membrane windows using AZ 1500-series photoresist. Bottom views through microscope show the difference between a sample with undissolved particles and one that is fully dissolved in the photoresist film.

to the vacuum chuck of a photoresist spinner. Drops of photoresist with dissolved sample are applied to the substrates before turning on the spinner for 10 seconds. Figure 5.3 shows two windows on a slide before and after spinning with resist. The samples are set aside to air-dry, avoiding the soft-bake step of typical resist applications so as not to harm the dissolved compounds.

The specific resist chosen for sample fabrication is AZ 1518 spun at 4000 rpm, with a nominal film thickness of $1.80 \mu\text{m}$ according to table 5.1 [2]. The metal-acac samples have varying levels of solubility in the resist. Attempting to dissolve amounts over the solubility limit of a particular compound results in leftover solid particles in the film. This is not critical for the transmission measurement inasmuch as the low dissolved concentration results in a poor signal to background ratio, but it is undesirable for PFY measurements as the particles are much larger than the sample attenuation length and will result in self-absorption artifacts in the spectrum. Adding small amounts of acetone when mixing the sample into the resist greatly increases the solubility of the metal-acac samples, with the tradeoff of a thinner film from the lowered vis-

cosity of the photoresist. The increase in signal due to increased concentration is stronger than the signal loss due to the thinner film, allowing transmission measurements with reasonable statistics to be measured.

Different metal-acac compounds from the first-row transition metals were tested with this technique, though only some were found to be sufficiently soluble in photoresist. The best candidates were Ni(acac)₂, Fe(acac)₃, Mn(acac)₃, and Cr(acac)₃. The Fe(acac)₃, though soluble in the photoresist initially, was found to be unstable over time with exposure to x-rays and so was not used to study PFY-XAS shifts. The Mn(acac)₃ was also found to decompose to Mn(II) from the starting state of Mn(III), but this occurred in the process of dissolving it in the photoresist, and the resulting metal/photoresist matrix was found to be stable over the course of exposure to x-rays.

5.1.1 Sample Characterization

After dissolving the metal-acac compound in acetone and photoresist and letting the spun-on sample dry, its thickness and concentration were measured by transmission XAS and UV/Vis spectroscopy. Figure 5.4 shows the XAS of standard thickness photoresist versus photoresist thinned with a measured quantity of acetone. These spectra cover the N and O K edges as these are common elements of the organic polymer resist. As the resist is predominantly carbon, the C K edge is too strong to measure in transmission, completely blacking out at the C K edge. The addition of approximately 15% acetone by volume to the photoresist results in a film approximately 0.4 times as thick as the standard, or around 0.75 μm . This measurement serves to approximate the thickness of the resulting films with metal-acac samples dissolved with the aid of acetone.

The weights of sample, photoresist, and solvents are tracked during preparation of the transmission samples. The exact amounts used vary according to the solubility of the metal-acac compound, but typical values are 5-7 g (4.5-6.5 mL) photoresist, 50-200 mg sample, and 200-500 mg (0.2 - .6 mL) solvent. The concentration of the sample in the liquid resist may be calculated prior to deposition, but after curing a large fraction of the VOCs evaporate and the polymer cross-links to a matrix and changes its density. The sample concentration in the prepared films must therefore be measured directly with UV/Vis spectroscopy. To extract concentration data from the isolated metal-acac UV/Vis requires knowing the extinction coefficient of the compound at its characteristic absorption bands. According to the Beer-Lambert law, the absorp-

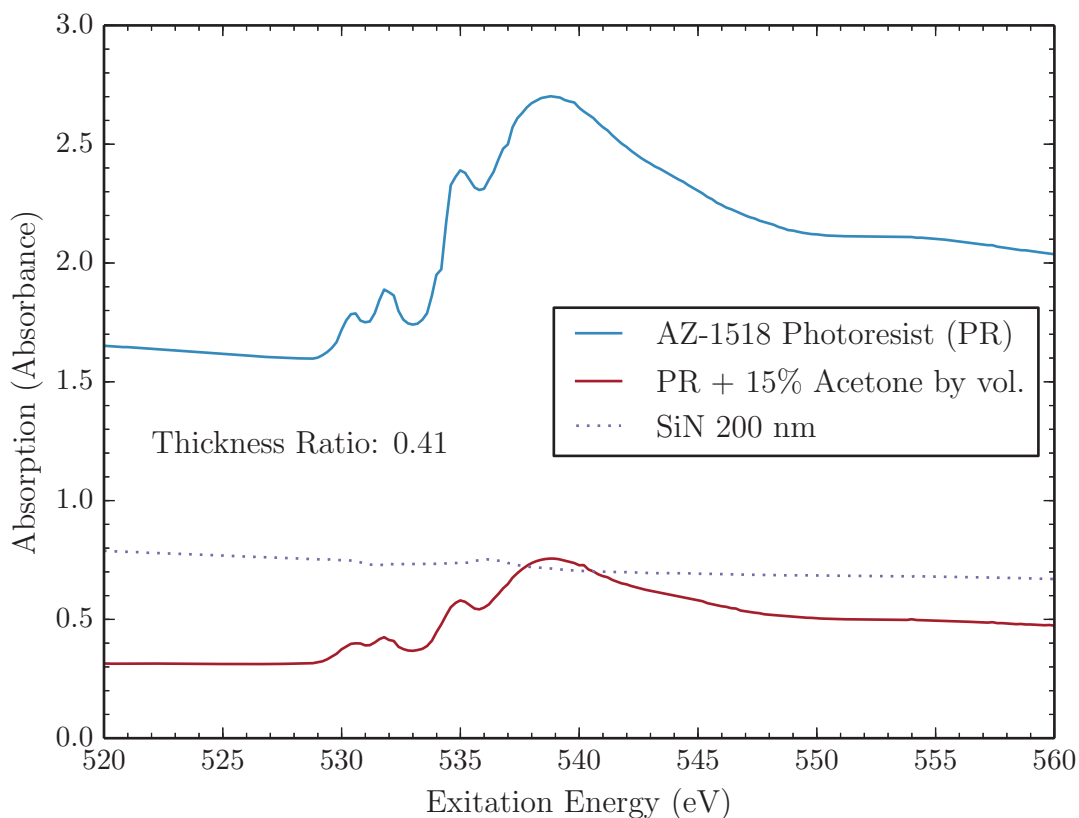


Figure 5.4: XAS of films of AZ 1518 photoresist (PR) comparing the standard specification to photoresist thinned with acetone, plotted in units of base-e absorbance.

tion at a wavelength λ is a product of the extinction coefficient σ_{λ} , the path length through the sample l , and the sample concentration c :

$$A = \sigma_{\lambda}lc. \quad (5.1)$$

Samples of varying concentration of metal-acac are prepared by dissolving in acetone and measured in a sample cuvette of known path length. UV/Vis spectra for $\text{Ni}(\text{acac})_2$ are shown in the top panel of figure 5.5, while $\text{Mn}(\text{acac})_3$ is shown in figure 5.6. From these spectra, prominent absorption bands are identified to fit for the extinction coefficient as in the bottom panels of figures 5.5 and 5.5.

To measure the concentration of dissolved metal-acac sample in the prepared transmission samples, calibration samples are spun onto sapphire discs with an aliquot of the mother solution that used for the SIN transmission samples. Sapphire is transparent to UV/Vis photons down to ≈ 300 nm and is a suitable substrate for UV/Vis measurements. The UV/Vis spectra of

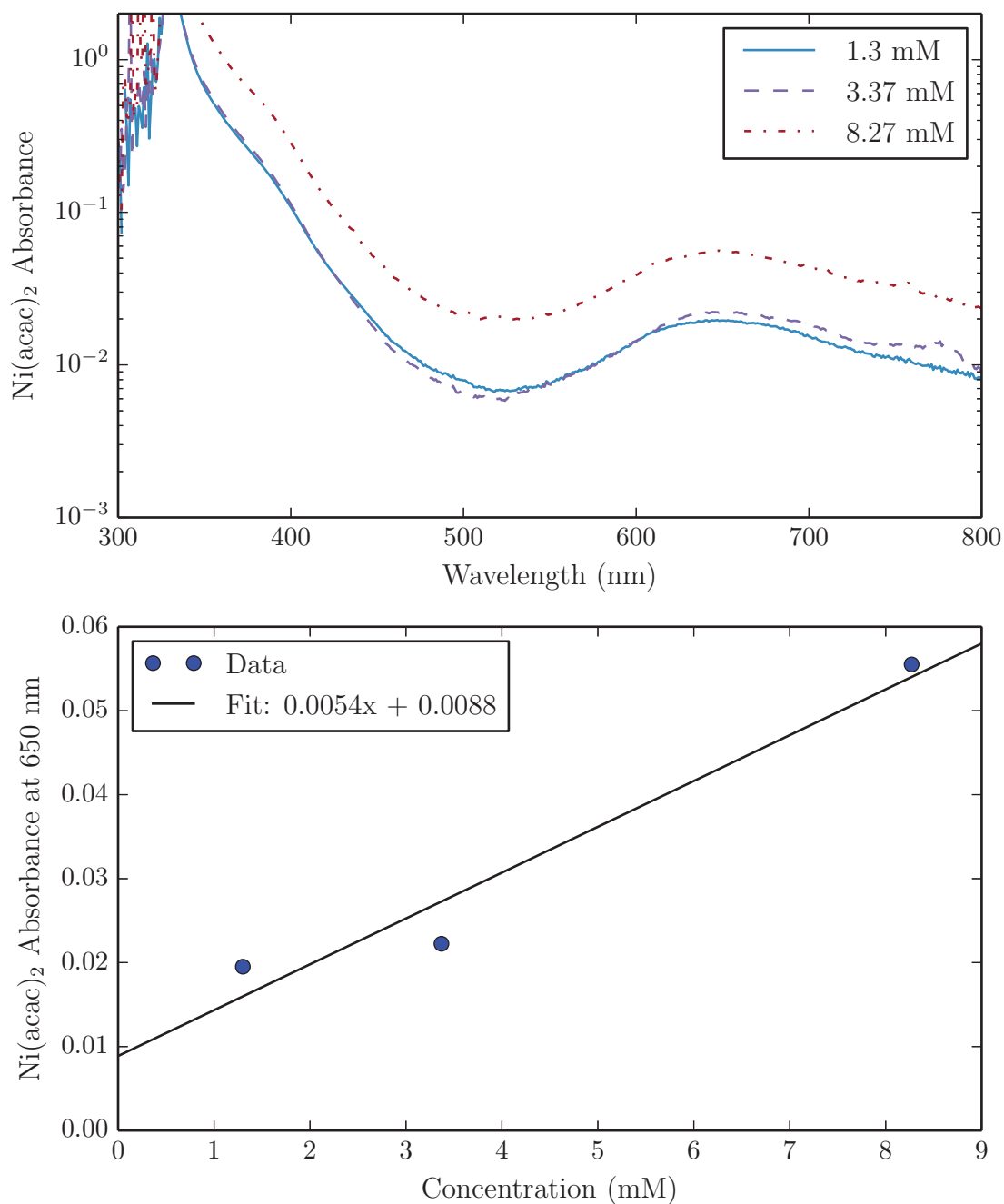


Figure 5.5: Top panel: UV/Vis absorption spectra of Ni(acac)_2 dissolved in acetone at indicated concentrations. Bottom panel: extinction coefficient of Ni(acac)_2 determined from UV/Vis absorption spectrum peak at 650 nm.

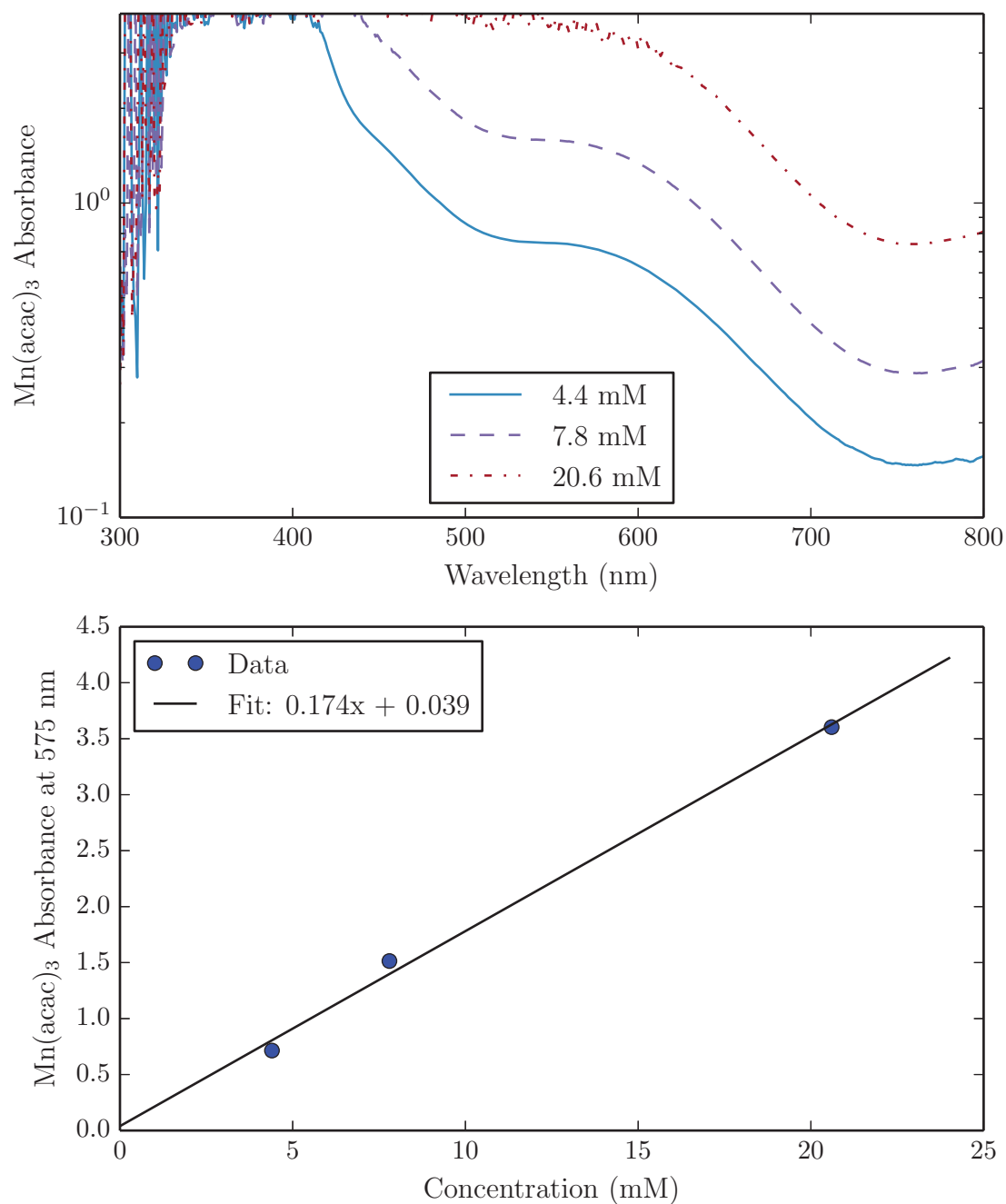


Figure 5.6: Top panel: UV/Vis absorption spectrum of $\text{Mn}(\text{acac})_3$ dissolved in acetone. Bottom panel: extinction coefficient of $\text{Mn}(\text{acac})_3$ determined from UV/Vis absorption spectrum peak at 575 nm.

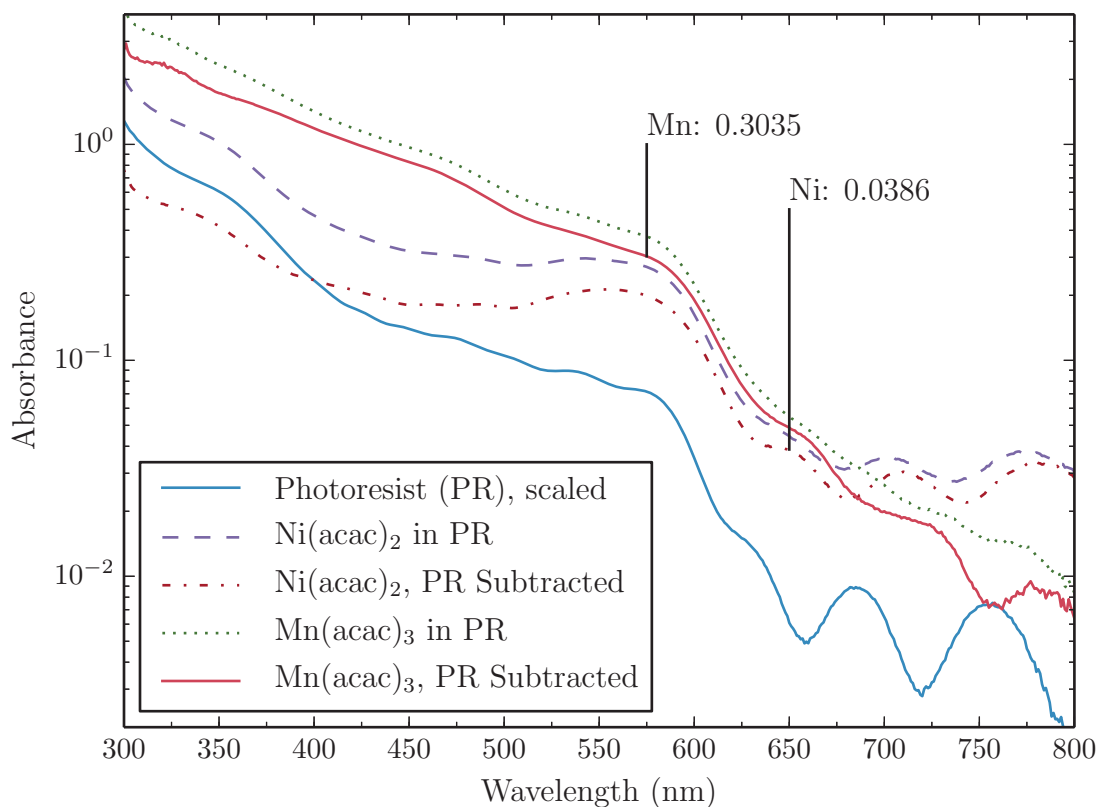


Figure 5.7: UV/Vis absorption spectrum of $\text{Mn}(\text{acac})_3$ and $\text{Ni}(\text{acac})_2$ dissolved in photoresist. The metal-acac samples are spun onto sapphire disks. Subtracting the photoresist background spectrum gives the spectra for the dissolved metal-acac samples.

$\text{Mn}(\text{acac})_3$ and $\text{Ni}(\text{acac})_2$ samples in photoresist are shown in figure 5.7. Standard, undiluted AZ 1518 photoresist is also spun onto discs so its contribution to the UV/Vis spectrum may be measured and subtracted from the mixed samples to give the remaining metal-acac spectra dissolved in the film, as seen in figure 5.7. From the extinction coefficient fits in figures 5.5 and 5.6, this gives concentrations of 5.5 mM for $\text{Ni}(\text{acac})_2$ and 1.5 mM for $\text{Mn}(\text{acac})_3$. Both concentrations are practical for PFY-XAS as they are dilute enough to prevent self-absorption while being concentrated enough to detect a signal from the species of interest.

5.2 Experimental Setup

X-ray absorption spectra of prepared metal/photoresist film samples were measured at the LBNL ALS. Transmission, TEY, and silicon drift detector (SDD) PFY data were measured on beam line 4.0.2, a beamline equipped with an elliptically polarizing undulator (EPU) and

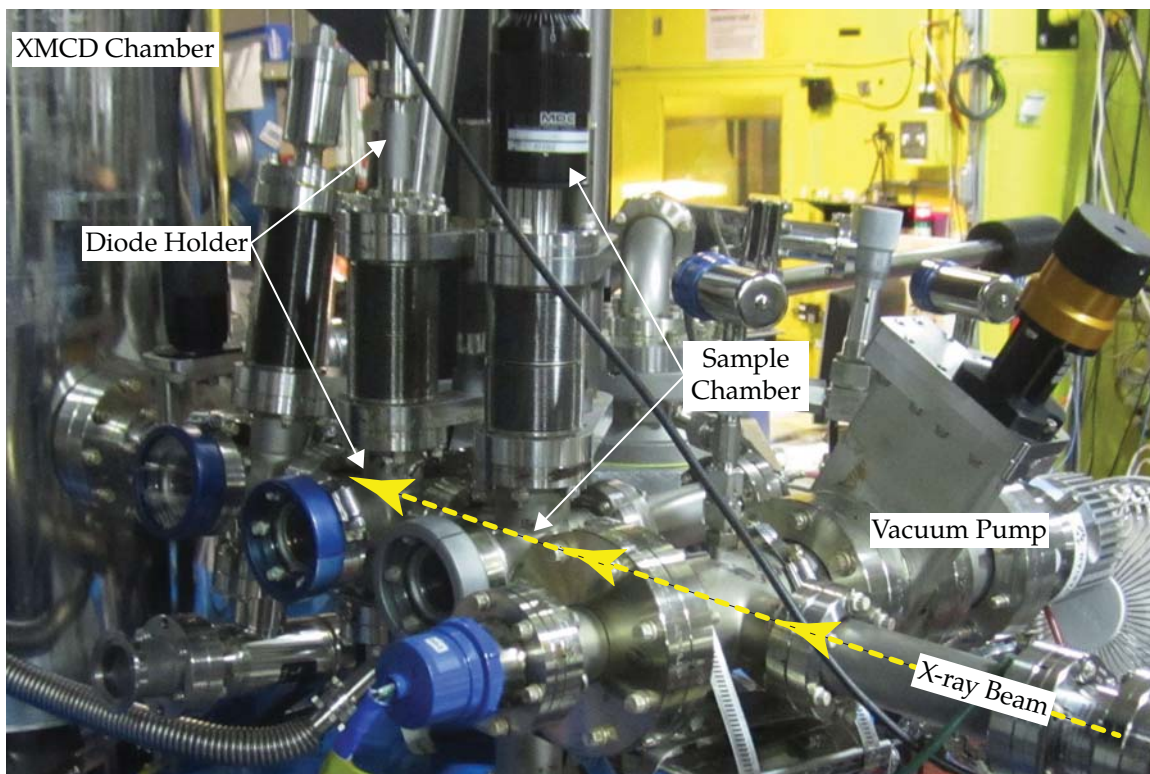


Figure 5.8: Photo of the transmission sample chamber installed on ALS beam line 4.0.2. The six-way crosses for the transmission diode and sample holder with manipulators are labeled. The beam enters the chamber from the right of the photo, passing through the transmission samples to be measured by the diode in the back position.

variable-included angle, plane grating monochromator that produces over 1×10^{12} photons/sec/0.1% BW between 200 and 1,200 eV [4]. The resolving power of the beamline depends on the monochromator slit settings. The measurements of these samples were made with entrance/exit slits both set at $40 \mu\text{m}$, yielding a maximum resolving power $E/\Delta E$ of approximately 5000 around 700 eV [5].

A small transmission sample chamber was assembled from two 2.75-inch six-way vacuum crosses and installed in between two endstation chambers on the beamline to hold the SiN samples. A sample finger made from aluminum alloy was machined with a series of holes spaced to allow close packing of the transmission samples alternating between the front and back sides. The finger is installed on a rotary-linear combination manipulator with a PTFE insulating sheet to decouple it electrically from the vacuum chamber. A wire connects the bottom of the finger to a vacuum electrical feedthrough to allow sample current measurements in sample drain mode. The manipulator is installed to a 4-inch Z-stage for greater range of motion, allowing 18

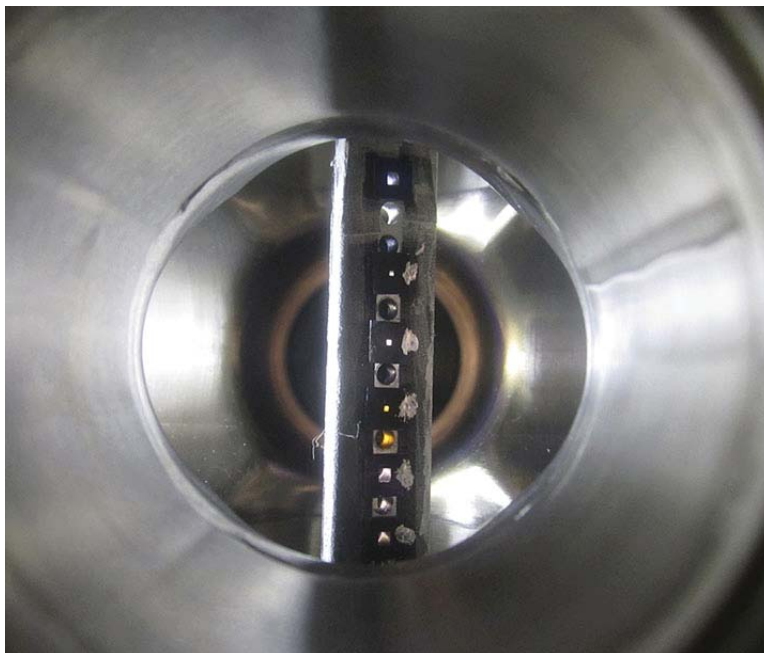


Figure 5.9: Photo of the transmission sample holder installed on ALS beam line 4.0.2. The holder is turned towards the viewport to show the SiN windows, but during measurement it is rotated normal to the x-ray beam, which enters the chamber from the right of the photo.

transmission samples to be installed to the finger, with space above and below the transmission section for powdered TEY samples. A Photonis Channeltron CEM 4868 detector is installed to one of the spare ports on the six-way cross to measure TEY in emission mode. The rear six-way cross has a Si photodiode on a movable finger for transmission measurements. The transmission chamber set-up on beam line 4.0.2 is shown in figure 5.8, while a close-up of the sample finger loaded with samples is shown in figure 5.9. Downstream from the temporary transmission chamber setup is a large chamber for x-ray magnetic circular dichroism (XMCD) measurements with a 6 T superconducting magnet, partially visible in the background of figure 5.8. This magnet was not used for these experiments; instead, the chamber was used to measure PFY-XAS with a single-element Vortex-EM SDD attached to a port at 90° from the incident x-ray beam. This chamber has a position for removable copper sample holders that may be inserted through a sample load lock. After transmission measurements were made in the transmission chamber, the samples were inserted into the XMCD chamber to measure with the SDD.

The incident beam intensity is measured by drain current from a fine gold mesh grid placed in the beam ahead of the sample. As noted in section 1.2.3, this incident intensity is not equivalent to the Beer-Lambert law I_0 , even though this is the common name given to this mea-

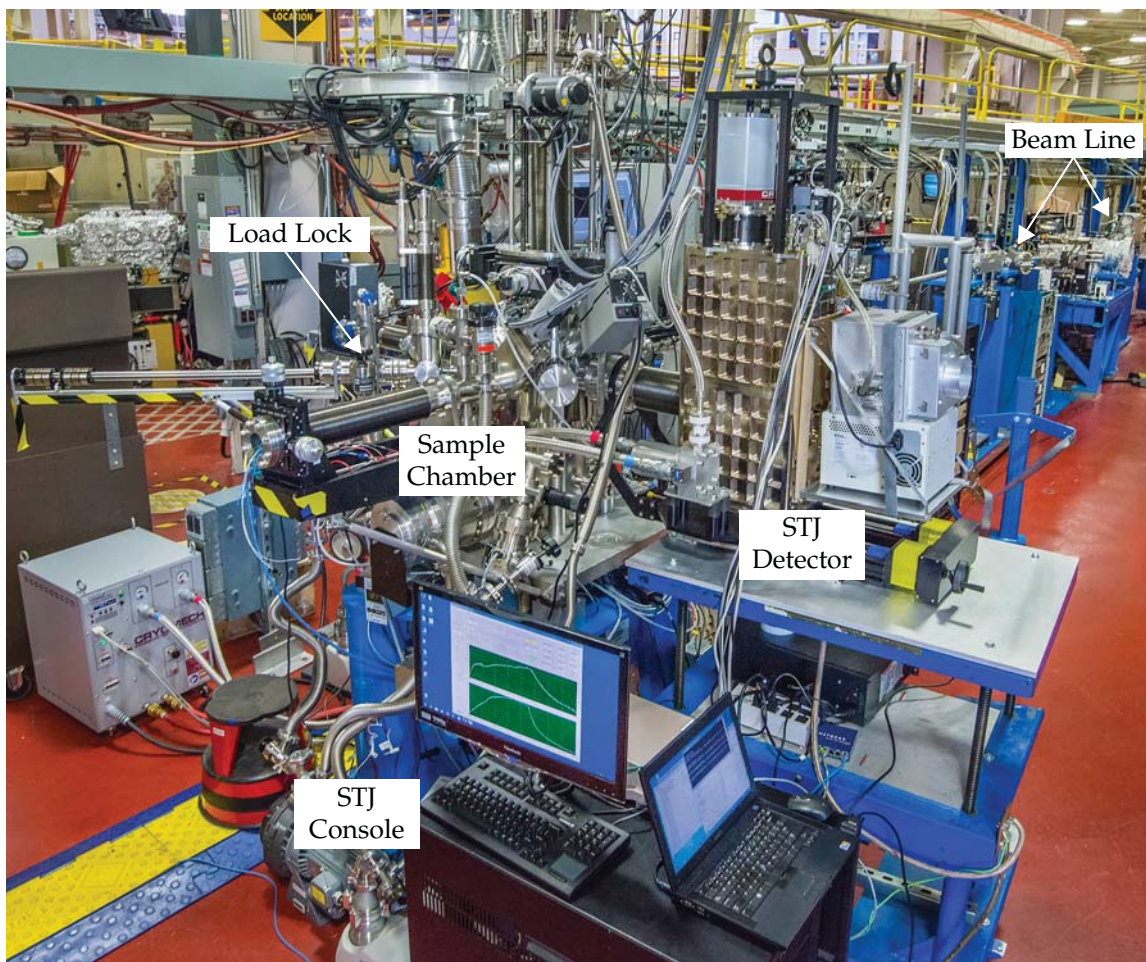


Figure 5.10: STJ detector installed to the experiment endstation on ALS beam line 6.3.1. The detector control console is in the foreground. The detector is inserted fully into the sample chamber for measurement. This photo is taken from the rear of the beam line looking toward the ALS storage ring in the background. The long transfer arm on the left is used to introduce samples into the chamber from the load lock.

surement. The I_0 term used for the remainder of this chapter will refer to the incident beam intensity.

The PFY-XAS measurements with the STJ detector were performed at the ALS beam line 6.3.1. This is a bend magnet beam line with a Hettrick-Underwood type variable-line-spacing plane grating monochromator. The photon flux depends on the grating used and exit slit settings, ranging from 2×10^9 to 1×10^{11} photons/sec/0.1% BW between 200 and 2,000 eV [6]. The maximum resolving power $E/\Delta E$ of the beam line is about 2000. This beam line does not have the same performance of beam line 4.0.2, but the endstation on 4.0.2 is not compatible with the STJ detector at this time.

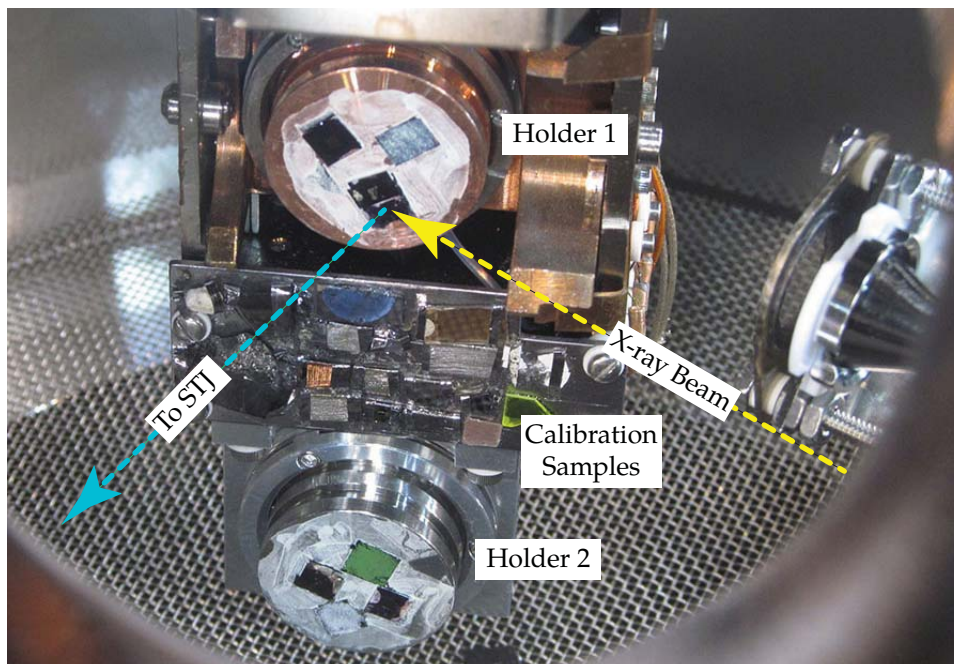


Figure 5.11: Photo of the sample finger loaded with two sample holders for PFY measurements on ALS beam line 6.3.1, viewed from above through a window port. The STJ detector snout is withdrawn in this photo; during measurements, the snout is inserted until it is nearly touching the sample holders. The beam enters the chamber from the lower right, and the STJ detector is inserted from the lower left. A Channeltron for TEY measurements of the calibration samples is visible on the right.

The STJ detector installed to one of the endstation chambers on beam line 6.3.1 is shown in figure 5.10. The chamber is equipped with a sample finger on a computer-controlled rotatable X-Y-Z stage. The samples are loaded onto removable sample holders made that are inserted into the chamber through a load lock. This allows many samples to be measured in one beam time without breaking vacuum. The detector is attached to a 6-inch port on the chamber at 90° from the x-ray beam. This orientation is chosen to suppress the elastic scatter of the incident x-ray beam, as the detector is oriented normal to the beam polarization. The sample holders are made from either stainless steel or copper, the choice depending on the elements that are measured in the sample. Two sample holders loaded with metal/photoresist samples on SiN windows are shown in the chamber in figure 5.11. The upper holder in the photo has Ni-acac/photoresist films and a calibration sample of powdered NiF₂ pressed into carbon tape, while the lower holder has Mn- and Cr-acac films with calibration samples of Mn and Cr oxides. The middle position has a variety of solid calibration standards permanently installed. As in the transmission measurements, a gold mesh grid upstream of the samples measures the incident beam

intensity. The metal/photoresist samples shown in this photo are from the same batch that was measured in transmission on beam line 4.0.2, allowing consistent and direct, quantitative comparison between the PFY and transmission XAS.

As these measurements are carried out at two separate beamlines over the course of several beam times, accurate energy calibration is necessary. The calibration of different beam lines often differ by up to several eV, and the calibration may drift over the several days of beam time. The calibration samples are stable and well-characterized samples, preferably with very sharp features that allow calibration to < 0.1 eV absolute. Ni, Mn and Cr measurements were calibrated with NiF_2 , MnF_2 , and Cr_2O_3 respectively. The calibration samples are measured at the start of the beam time and at regular intervals every few hours to track any calibration drift.

5.3 Metal-acac XAS

5.3.1 $\text{Ni}(\text{acac})_2$

Nickel is an important metal to the functioning of many biological and chemical systems and so has been the subject of considerable study in the soft x-ray band [7, 8, 9, 10]. The shifts in edge position and relative intensities of the L_3/L_2 edges allow analysis of the oxidation and spin state of the nickel site in coordination compounds [11, 12]. Because of the emphasis on branching ratio between the L_3/L_2 edges, it is very important to be able to measure the correct intensities of the edge features without distortion.

The transmission measurements recorded on beam line 4.0.2 were analyzed according to the steps laid out in figure 5.12. Dividing the diode intensity by I_0 and inverting the result (to show absorbance instead of transmittance) results in the spectrum labeled “Total Absorbance” in figure 5.12. The XAS from the Ni is superimposed on the bulk absorbance of the remainder of the sample, which causes the decreasing overall absorption with energy. Since the PFY-XAS has high background rejection and will isolate only the absorption from the Ni, the background must be removed from the transmission spectrum for an accurate comparison. A polynomial fit to the pre-edge approximates the effect of the background absorbance, and when subtracted from the total transmission spectrum gives the final Ni XAS spectrum labeled as “Net Absorbance” in figure 5.12. This procedure is repeated for each scan of the sample. The Ni-acac/photoresist transmission sample was measured a total of four scans, and the scans are averaged together to give the final transmission XAS for $\text{Ni}(\text{acac})_2$.

While a complete transmission measurement requires calibrating the I_0 intensity with the

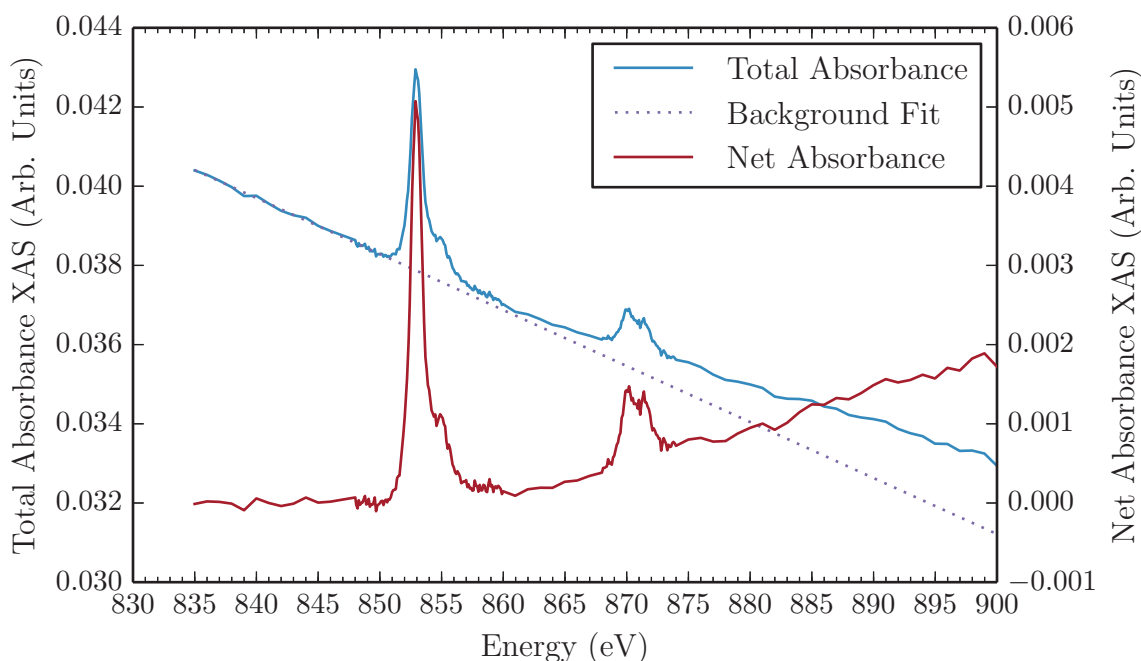


Figure 5.12: Analysis method for transmission XAS data. The absorption of other elements in the sample generates the sloped background on top of which is the measured Ni absorption edge. Subtracting a polynomial fit to the background gives the net Ni XAS.

direct beam on the diode in order to yield absolute absorbance measurement, this is not necessary in this experiment because the TEY and PFY spectra will not be possible to calibrate to absolute absorbance. Since the goal is to compare the relative intensities of the bound state transitions, normalizing to the peak height is appropriate.

The transmission XAS is the baseline or “true” XAS to compare the different measurement methods.

The summed emission spectra in figure 5.13 are normalized to the total exposure time in each region. The O K and Cu L peaks are very constant throughout the measurement, indicating that sample does not have significant self-absorption and the Ni concentration is at an acceptable level for PFY-XAS. Furthermore, the detector response is very stable over the measurement period over whole energy band surrounding the element of interest.

The XAS spectra shown in figure 5.14 are normalized to the L_3 peak height. Another common method is to normalize to the post- L_2 edge height, but as these spectra have varying levels of statistical noise and background subtraction effects, normalizing with this method distorts the relative L_3 and L_2 peak heights. This is sensible as the post-edge heights between the L_3 and L_2 edges and beyond the L_2 edge are not bound-state transitions and so should not be affected

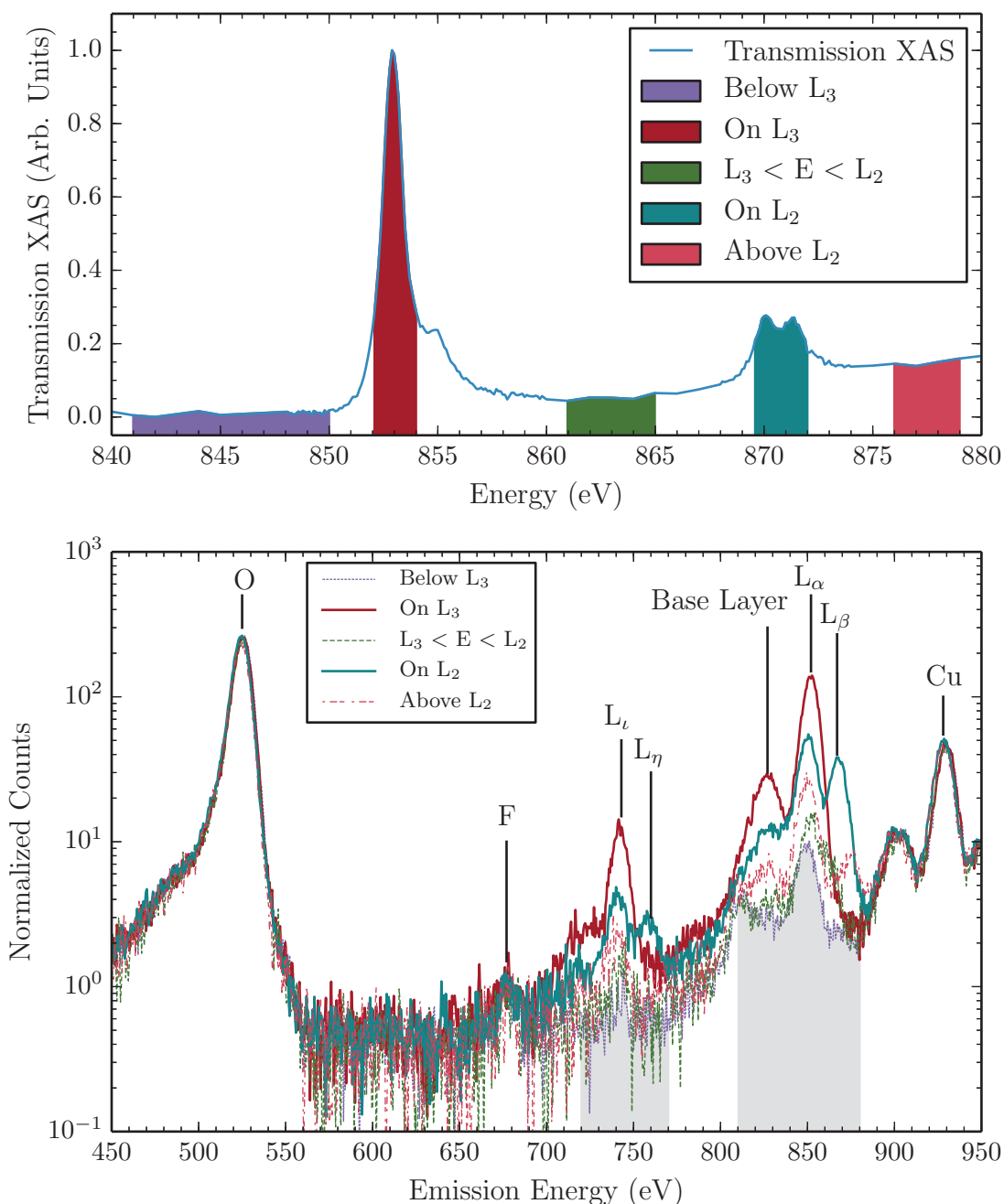


Figure 5.13: Top panel: transmission XAS of Ni(acac)₂ in photoresist with five regions corresponding to pre-, mid-, and post-edge (regions 1 and 5), on top of the L₃ and L₂ edges (regions 2 and 4). Lower panel: Emission spectra recorded with the STJ detector of Ni(acac)₂ during PFY-XAS scans on ALS beam line 6.3.1. Each spectrum summed over the XAS regions indicated in the top panel in order to compare the sample fluorescence across the absorption edge. Lines labeled L_x are from Ni, while other elements are indicated by their L_α or K positions. The shaded regions under the emission spectra correspond to the extraction regions used for PFY-XAS in figure 5.14.

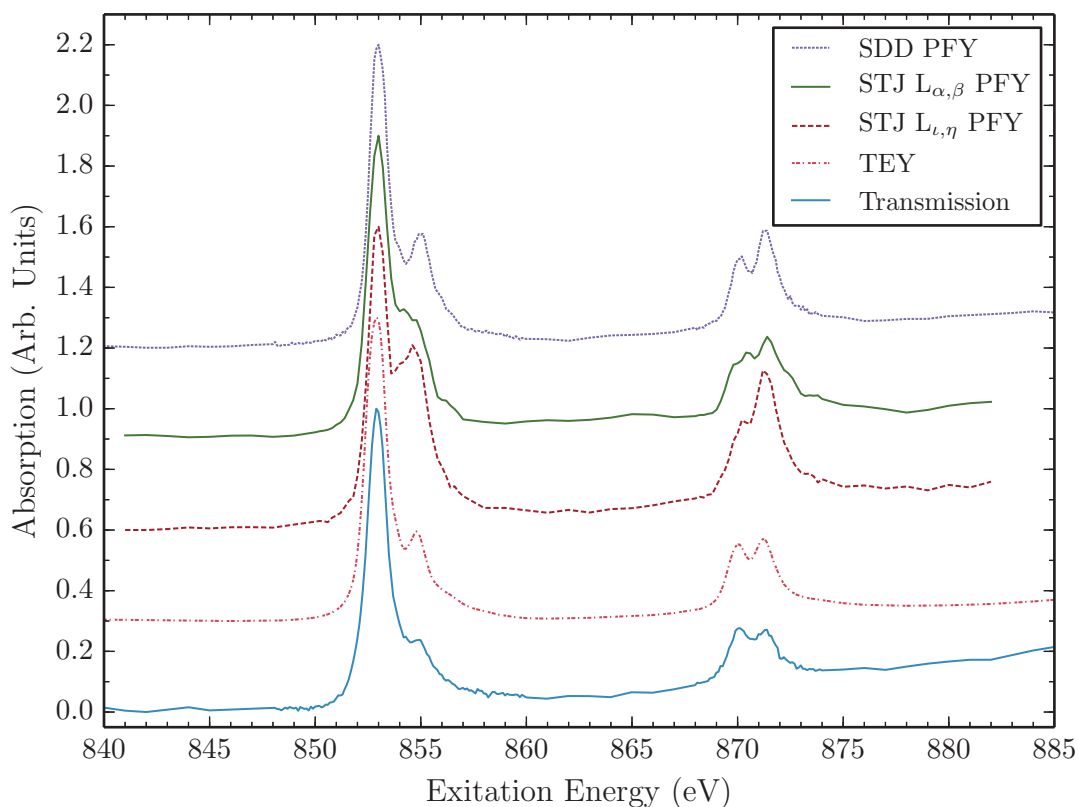


Figure 5.14: PFY-XAS of Ni(acac)₂ in photoresist measured with the STJ with separate extraction regions for the $L_{\alpha,\beta}$ and $L_{\iota,\eta}$ lines.

by bound-state deviations in fluorescence yield. The spectra in figure 5.14 are offset for clarity, and include the summed transmission and TEY XAS, PFY-XAS measured with the Vortex SDD (all measured on beam line 4.0.2), and PFY-XAS measured with the STJ detector on beam line 6.3.1 with two different extraction windows capturing the Ni $L_{\alpha,\beta}$ and $L_{\iota,\eta}$ emission respectively.

The STJ data were acquired over 5 scans, each taking about 30 minutes to complete with a per-point integration time of 10 seconds. To maximize the resolution of the 6.3.1 XAS data, the beam line monochromator slits were set to $5 \mu\text{m}$, corresponding to the maximum resolving power of about $2000 E/\Delta E$. The tradeoff to achieving high resolution is that the beam line flux is decreased substantially, to order 10^9 photons/sec. The per-pixel count rate measured by the STJ detector was approximately 30 counts/sec/pixel, which is very slow for this detector but was set by the low beam line flux. Measurements made during a previous beam time at 6.3.1 with $60 \mu\text{m}$ slits showed greatly increased count rates, but the resulting energy resolution of the beamline was too poor to resolve the different bound-state transitions at the edges. The STJ

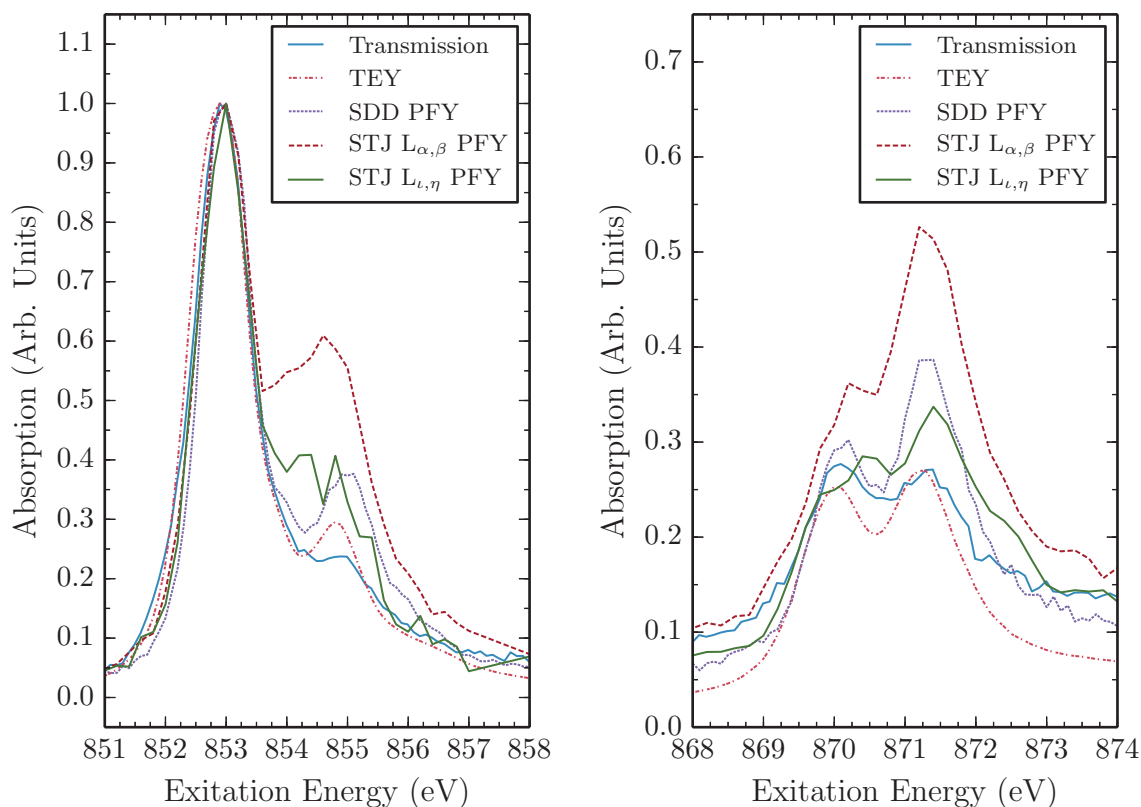


Figure 5.15: Close-up views of the L_3 and L_2 regions of figure 5.14.

detector would greatly benefit from a brighter beam line due to its high count-rate capabilities and high resolution.

Figure 5.15 shows zoomed-in views of the L_3 and L_2 edge regions. These data highlight the differences between the methods. Especially important is the difference between the $L_{\iota,\eta}$ and $L_{\alpha,\beta}$ STJ data, since they come from the same source data and are measured simultaneously. The bound-state transitions at 854.8 and 871.4 eV are enhanced in the PFY data, especially in the STJ $L_{\alpha,\beta}$ data that only includes emission from those lines. The 110 eV resolution of the SDD detector does not allow it to resolve these lines, so the PFY-XAS measured with the SDD is a combination of the $L_{\alpha,\beta}$ and $L_{\iota,\eta}$ emission. The $L_{\iota,\eta}$ XAS spectrum does not fully coincide with the transmission data at 854.8 eV, but this is likely due to the resolution of the beam line combined with statistical noise.

Figure 5.16 compares the $\text{Ni}(\text{acac})_2$ x-ray emission spectroscopy (XES) measured with the STJ detector and the SDD, which has a resolution of approximately 110 eV in this range. While

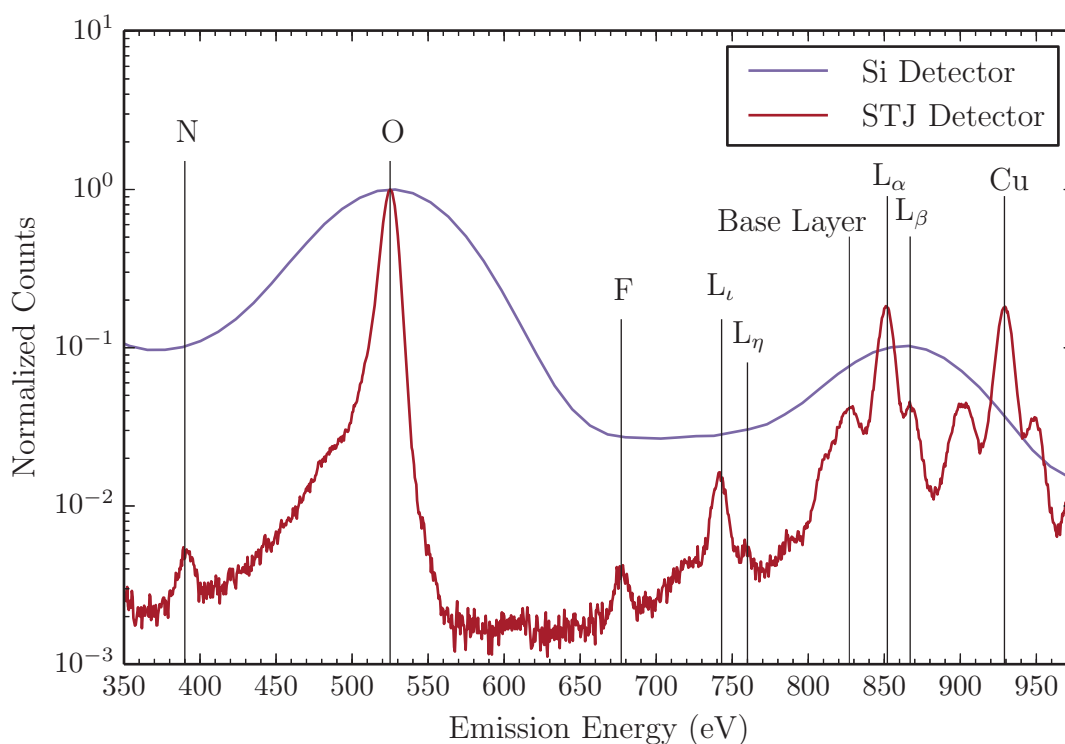


Figure 5.16: Comparison between measured fluorescence spectra of $\text{Ni}(\text{acac})_2$ in photoresist from STJ and Si drift detectors. The spectra are summed over the whole XAS scan and so will show all features highlighted in figure 5.13 simultaneously. Both spectra are normalized to the O K line intensity. Lines labeled L_x are from Ni, while other elements are indicated by their L_α or K positions.

the Ni L and O K peaks are separable in the SDD data, the Ni peak is blended with the Cu background of the sample holder, increasing the background at that peak. The baseline noise is also three orders of magnitude higher in the SDD than the STJ, so while this fairly concentrated sample on a bright beamline is measurable with the SDD in PFY mode, the detection threshold will be higher than the STJ for very dilute samples or those with bright, adjacent lines such as Co or Cu for Ni spectra. The STJ also has the capability to detect the weaker $L_{\iota,\eta}$ lines, which are below the detection threshold for the SDD even without intermediate lines in the middle of the Ni spectrum. While solid state detectors perform increasingly well for PFY-XAS as the energy is increased, they are still fundamentally limited by the noise threshold and selectivity in samples with many emission lines.

5.3.2 Mn(acac)₃

Manganese is another transition metal which is central to the function of important enzymes, including photosystem II which is integral to photosynthesis. As with the Ni(acac)₂ data, the Mn(acac)₃ transmission samples were measured on the beam line 4.0.2 at the ALS. The analysis method for a single scan is presented in figure 5.17, where as before a polynomial must be fit to the background to extract the XAS due only to the Mn L-edges. The spectrum labeled “Total Absorbance” is derived from the measured diode signal (transmitted through the sample) divided by the beam line I₀ monitor and inverted to give absorption. The Mn-acac/photoresist transmission sample was measured a total of five scans, and the scans are averaged together to give the final transmission XAS for Mn(acac)₂. This single spectrum is not normalized; as with the Ni data, the multiple scans are normalized to the L₃ peak intensity after summing together.

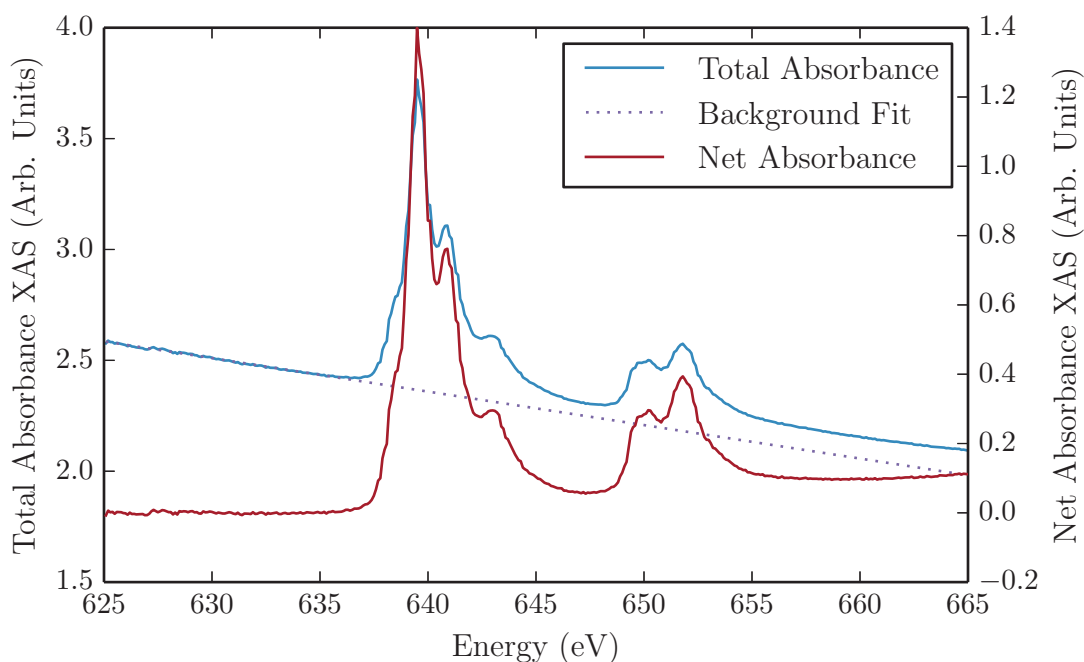


Figure 5.17: Process of analyzing Mn(acac)₃ transmission XAS from raw beamline data. The absorption of other elements in the sample generates the sloped background on top of which is the measured Ni absorption edge. Subtracting a polynomial fit to the background gives the net Mn XAS.

In the initial Mn(acac)₃ powdered compound, Mn has an oxidation state of 3+. When compared to previous L-edge studies of Mn[13], the transmission XAS in figure 5.17 appears to be much more like Mn(II), both in absolute position of the edges and the relative intensities of the bound state lines. Measuring the powdered form of the Mn(acac)₃ compound with TEY

as shown in figure 5.18 reveals that while the Mn is initially Mn(III), it changes rapidly with exposure to the x-ray beam to Mn(II). The transmission XAS does not change with time and appears to be primarily Mn(II) character, suggesting that the compound undergoes reduction upon dissolution into the photoresist matrix. This is not entirely surprising, as the Mn(III) ion is relatively unstable and therefore less common than either Mn(II) or Mn(IV). Since this study is primarily concerned with possible distortions by PFY-XAS, the exact oxidation state of the manganese is not crucial, but the stability over time and x-ray exposure is. This sample is therefore acceptable for this work.

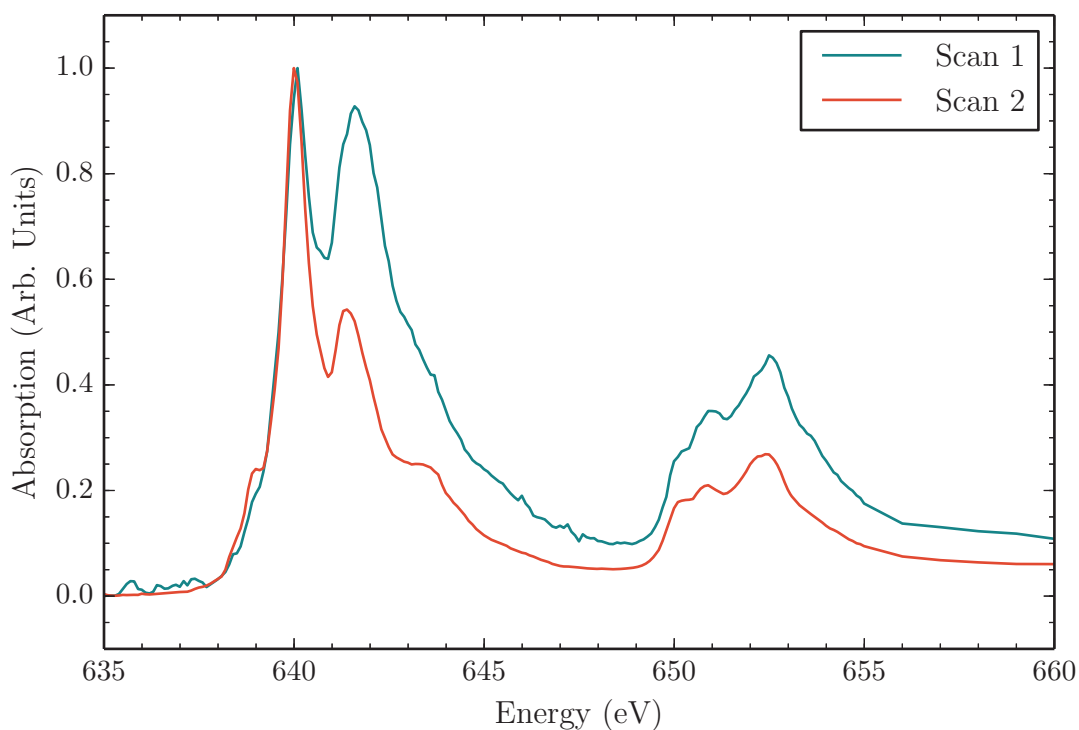


Figure 5.18: TEY $\text{Mn}(\text{acac})_3$ powder. The two spectra are recorded one after the other. The substantial difference is due to the x-ray beam rapidly photoreducing the sample.

Fluorescence spectroscopy of manganese is slightly more challenging than nickel, due to its closer proximity to the bright oxygen K emission and the smaller splitting between the $L_{\alpha,\beta}$ and $L_{i,\eta}$ pairs. The $\text{Mn}(\text{acac})_3$ /photoresist samples were measured with the STJ on ALS beam line 6.3.1. To highlight the different emission bands excited by different regions of the absorption edge, we sum the fluorescence spectra collected during the PFY-XAS scans over regions of beamline (excitation) energy. Using the transmission XAS as a guide for these regions in the

top panel of figure 5.19, we select regions that represent the emission on top of the L_3 and L_2 edge peaks and regions below, between, and above the peaks. The emission spectra shown in the lower panel of figure 5.19 are summed over the regions indicated in the upper panel and normalized to the total collection time in each region.

The Mn L_α and L_β are separable, but with greater difficulty than the nickel $L_{\alpha,\beta}$ as they lie only ≈ 11 eV apart. As with nickel, the L_3 is excited significantly at the L_2 edge due to radiationless Coster-Kronig transitions [14]. The Mn L_ν and L_η lines are only about 30 eV from the strong O K line at 525 eV but are clearly resolvable in figure 5.19. The $L_{\nu,\eta}$ lines are approximately $10\times$ weaker than the $L_{\alpha,\beta}$ which is expected [15]. The strong F K peak at 677 eV is due to stray beam excitation from an adjacent MnF_2 calibration sample. The calibration sample does not however interfere significantly with the $Mn(acac)_3$ measurement, as the amount of beam illuminating the MnF_2 is a small fraction of that on the target sample. The F K peak is strong due to its high fluorescence yield, while the Mn $L_{2,3}$ yields are an order of magnitude smaller [16]. Fe and Ni are visible from the stainless steel sample holder, while a small Cu signal is likely due to scatter from nearby copper on the sample holder mount. Emission from F and higher-energies are excited by higher orders of the beam line.

Figure 5.19 shows shaded extraction windows for the $L_{\alpha,\beta}$ - and $L_{\nu,\eta}$ -gated PFY-XAS. Summing the emission in each window at each beamline excitation energy gives the XAS spectra shown in figure 5.20. The SDD data was collected on beam line 4.0.2 for comparison to the STJ data, but since it has a resolution of approximately 110 eV in this energy range, it cannot separate the $L_{\alpha,\beta}$ and $L_{\nu,\eta}$ regions and so is a sum over all the Mn emission. Since the TEY data is unstable over time, it is not shown for comparison. Figure 5.21 shows the L_2 and L_3 edge regions in detail with the spectra directly overlaid on one another, all normalized to the L_3 peak intensity. The transmission XAS in blue is considered the true XAS to compare to.

The STJ data from beam line 6.3.1 is slightly lower resolution than the other two spectra, but since they are taken from the same data set, the difference between the STJ $L_{\alpha,\beta}$ and $L_{\nu,\eta}$ spectra can be compared to the difference between transmission and SDD spectra. Notable differences in the L_3 edge are seen in the features at ≈ 638 eV and ≈ 643 eV. The 638 shoulder is suppressed in the SDD and $L_{\alpha,\beta}$ spectra, but visible in the transmission and $L_{\nu,\eta}$ spectra. The 643 eV feature is the opposite, with increased intensity in the SDD and $L_{\alpha,\beta}$ compared to their counterpart transmission and $L_{\nu,\eta}$ spectra. At the L_2 edge, both peaks at ≈ 650 and 651.5 eV are enhanced in

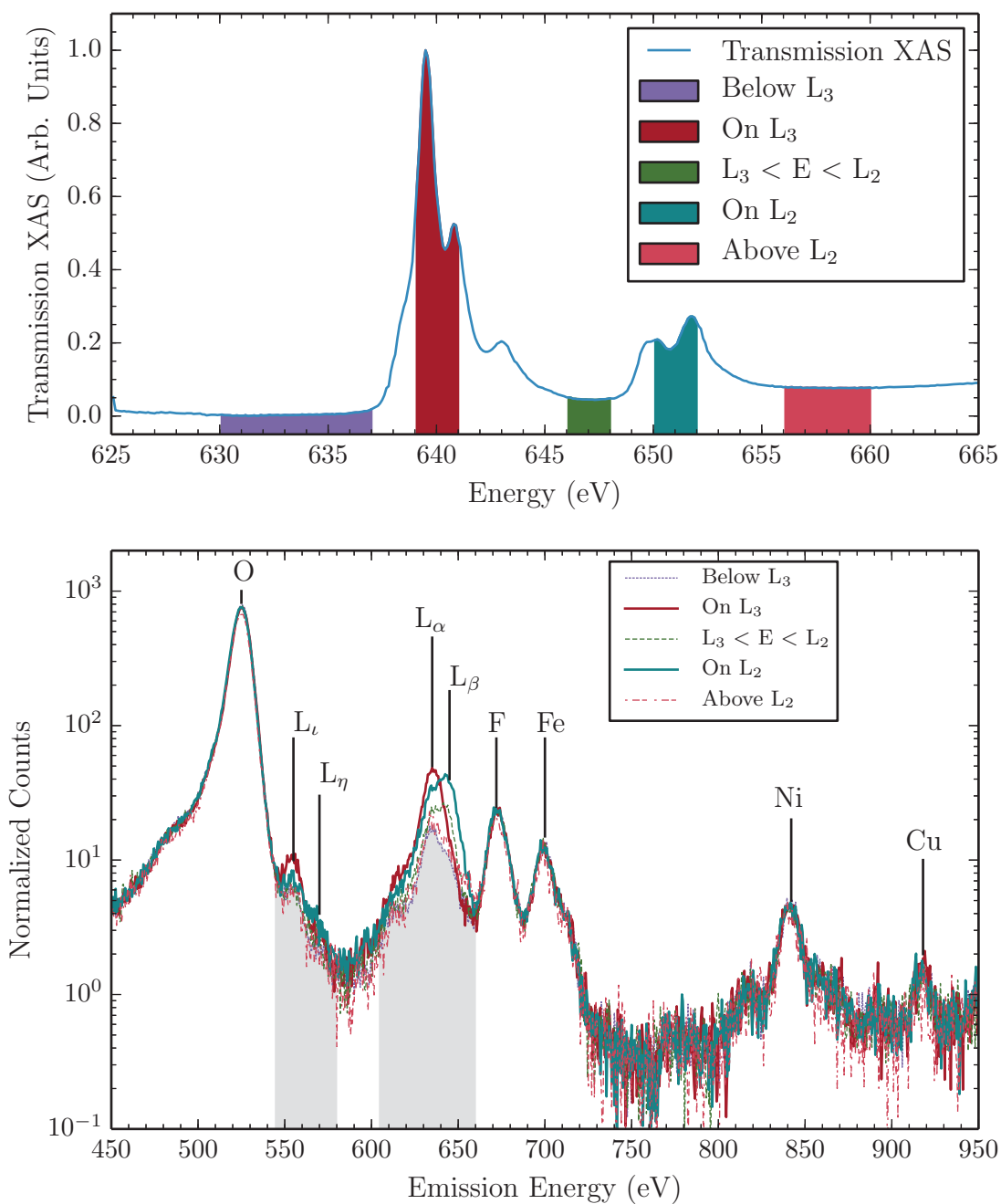


Figure 5.19: Top panel: transmission XAS of $\text{Mn}(\text{acac})_3$ in photoresist with five regions corresponding to pre-, mid-, and post-edge (regions 1 and 5), on top of the L_3 and L_3 edges (regions 2 and 4). Lower panel: Emission spectra recorded with the STJ detector of $\text{Mn}(\text{acac})_3$ during PFY-XAS scans on ALS beam line 6.3.1. Each spectrum summed over the XAS regions indicated in the top panel in order to compare the sample fluorescence across the absorption edge. Lines labeled L_x are from Mn, while other elements are indicated by their L_α or K positions. The shaded regions under the emission spectra correspond to the extraction regions used for PFY-XAS in figure 5.20.

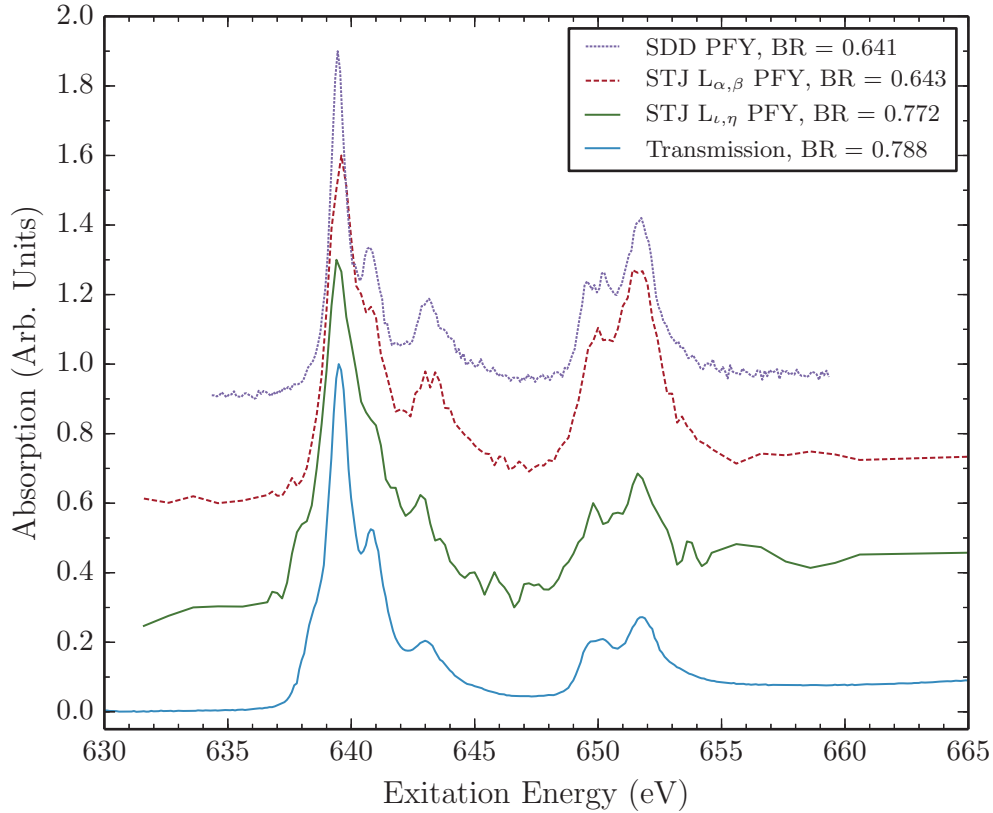


Figure 5.20: Comparison of transmission and PFY-XAS of $\text{Mn}(\text{acac})_3$ in photoresist measured with the STJ with separate extraction regions for the $L_{\alpha,\beta}$ and $L_{\nu,\eta}$ lines, and with a Si drift detector (labeled SDD). The TEY-XAS is not shown as it changes over time as shown in figure 5.18. The different measurement methods are offset so each entire spectrum is visible.

the SDD and $L_{\alpha,\beta}$ data compared to the transmission and $L_{\nu,\eta}$ data, especially at the 651.5 peak. These combined effects at the two L edges alters the inferred DOSs of the bound states as well as the L_3 - L_2 branching ratio. As shown in the legend of figure 5.20, the branching ratio 0.772 of the $L_{\nu,\eta}$ PFY-XAS is very close to the transmission ratio of 0.788, while the SDD and $L_{\alpha,\beta}$ XAS are also similar at 0.641 and 0.643, respectively.

The emission spectra for $\text{Mn}(\text{acac})_3$ in photoresist are shown in figure 5.22 measured with both the STJ and SDD detectors. As in figure 5.16, the Si detector has an energy resolution of approximately 110 eV. The STJ detector is operating at a slightly reduced performance compared to the Ni data, as these spectra were recorded in a short time at the end of an ADR cycle. The resolution of the STJ of ≈ 12 eV is still more than adequate to separate the lines from the different elements around the sample, including the weak $L_{\nu,\eta}$ lines just 30 eV above the O K line. The

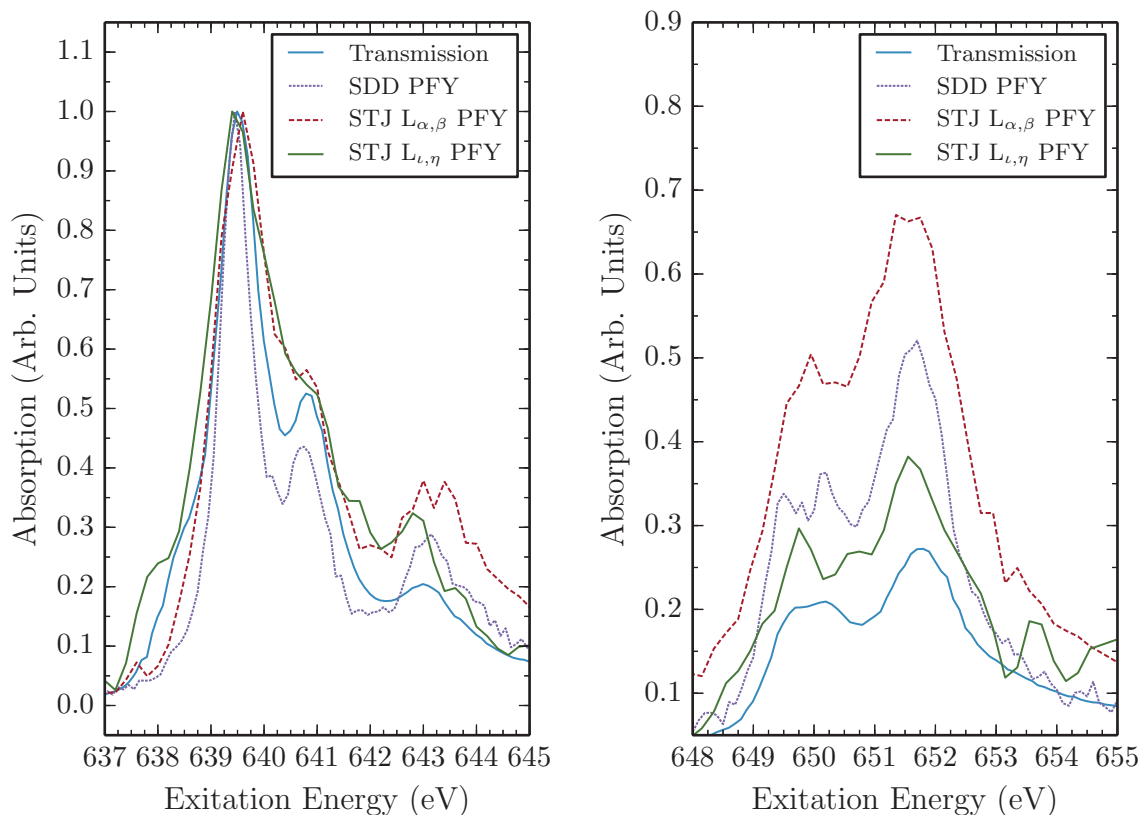


Figure 5.21: Close-up views of the L_3 and L_2 regions of figure 5.20.

presence of the Mn in the Si spectrum is less pronounced than the Ni in figure 5.16, and it is mixed with the nearby F and Fe lines. The STJ detector will have an even greater edge over solid state detectors in detecting trace amounts of Mn.

5.3.3 $\text{Cr}(\text{acac})_3$

Another compound that produced uniform films when dissolved in photoresist is $\text{Cr}(\text{acac})_3$. However, limitations of the beam line optics and detection electronics prevented the collection of transmission or TEY data for this sample, so the results obtained are preliminary. Extremely large Cr edges present in the beamline caused the transmission measurement to generate a badly distorted edge, and the TEY data suffered from strong sample charging effects. Without a transmission spectrum to establish the baseline bound-state transmission intensities, the PFY data may not be evaluated for deviations, but the PFY results are still notable on their own since Cr PFY is technically difficult to obtain due to its close proximity to O.

Figure 5.23 shows emission spectra collected with the STJ and Si drift detectors of the

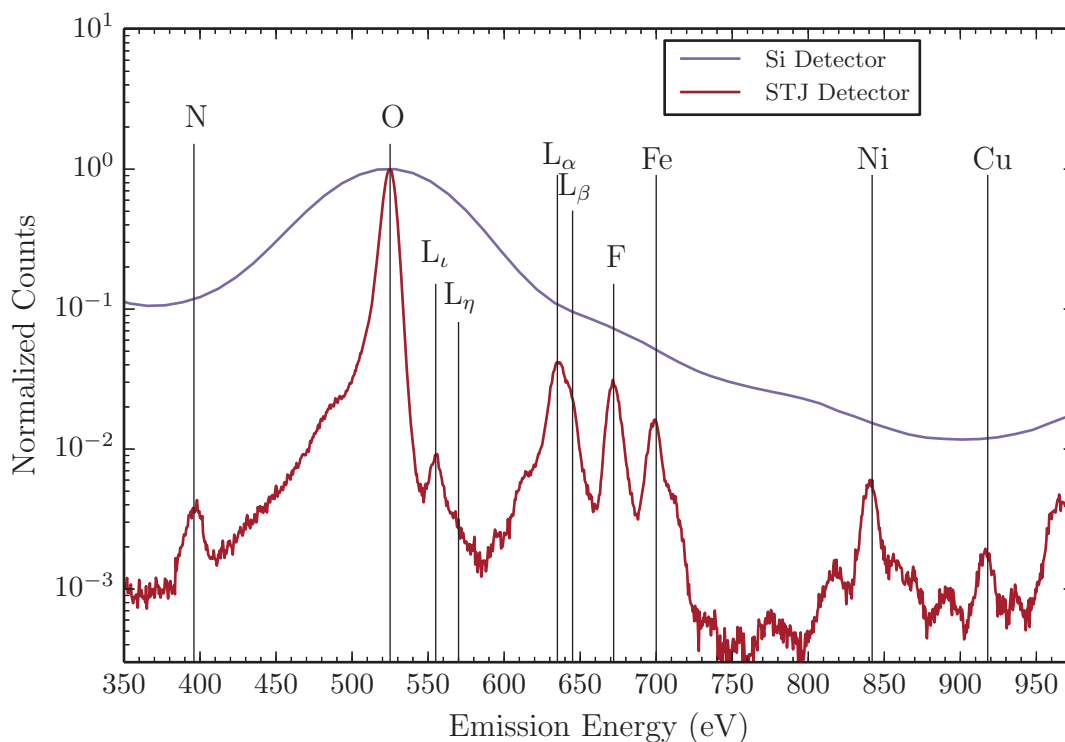


Figure 5.22: Comparison between measured fluorescence spectra of $\text{Mn}(\text{acac})_3$ in photoresist from STJ and Si drift detectors. The spectra are summed over the whole XAS scan and so will show all features highlighted in figure 5.19 simultaneously. Both spectra are normalized to the O K line intensity. Lines labeled L_x are from Mn, while other elements are indicated by their L_α or K positions.

$\text{Cr}(\text{acac})_3$ sample dissolved in photoresist. The STJ can clearly resolve the Cr $L_{\alpha,\beta}$ lines from the O K line, while it is essentially completely covered by the O K in the 110 eV Si spectrum. The $L_{\nu,\eta}$ lines are about 25 eV below the O K edge and are faintly visible in the STJ data. However, as they lie on the low-energy tail of the O K line, the background is too large in this set of measurements to extract an $L_{\nu,\eta}$ -windowed XAS spectrum.

The $L_{\alpha,\beta}$ -windowed XAS acquired with the STJ detector is shown in figure 5.24 along with the Si detector data. The STJ edge is of good quality, especially considering it was acquired in a relatively short time (≈ 1.5 hours) on a dimmer bend magnet beamline, while the Si detector was on a very bright undulator beamline. While the Cr L edges are discernible in the Si detector data, they are very noisy and superimposed on a large background. This is fundamentally limited by the background of the strong O K peak, so increasing the integration times will not aid extraction of meaningful XAS data with a detector of this resolution. Though the number of counts in the

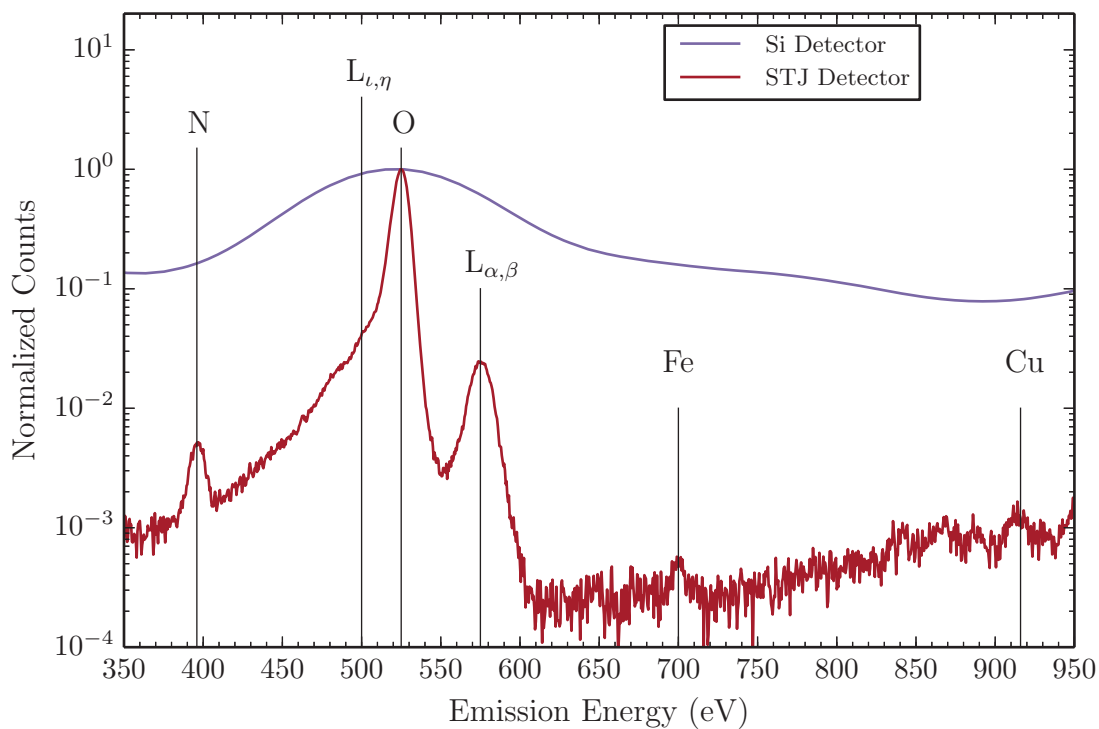


Figure 5.23: Comparison between measured fluorescence spectra of $\text{Cr}(\text{acac})_3$ in photoresist from STJ and Si drift detectors. The spectra are summed over the whole XAS scan, and both spectra are normalized to the O K line intensity.

STJ emission spectrum is less than the Si detector, the greater selectivity of the emission lines allows clean extraction of XAS data in an otherwise very noisy background environment.

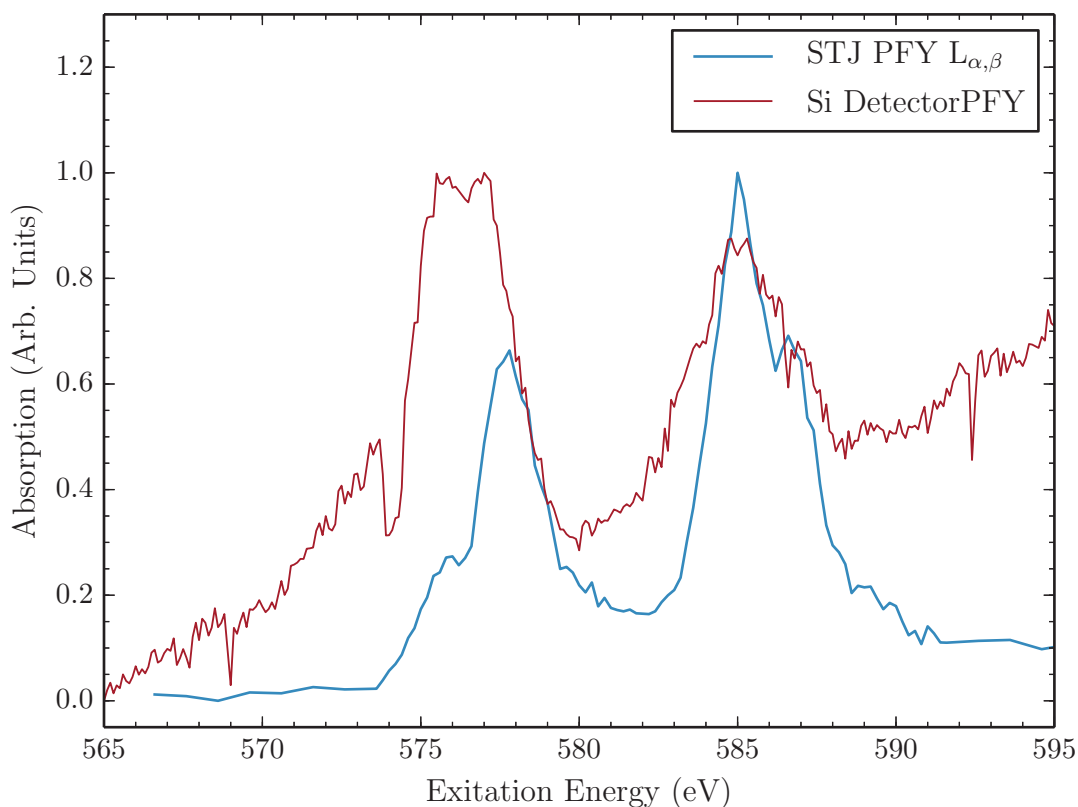


Figure 5.24: PFY-XAS of $\text{Cr}(\text{acac})_3$ dissolved in photoresist, measured with the STJ and Si drift detectors..

5.4 Metal-acac XAS Modeling

The XAS measurements establish that there is a difference between the transmission and PFY-XAS. To show that the observed variations are due to correlation and symmetry effects requires fitting a theoretical model.

The two programs used for modeling these spectra are CTM4XAS 5.5 and CTM4RIXS 0.9 developed by the de Groot group at University of Utrecht [17]. These two programs are interfaces to a modified version of atomic multiplet code first developed by Cowan [18] and extended with charge transfer calculations, hence the abbreviation charge transfer multiplets (CTM). The CTM4XAS program calculates the bound-state wavefunctions and generates the bound-state XAS transitions from them. This model does not include the continuum step. The output wave function definitions may then be input to the CTM4RIXS program to compute the full correlated scattering matrix.

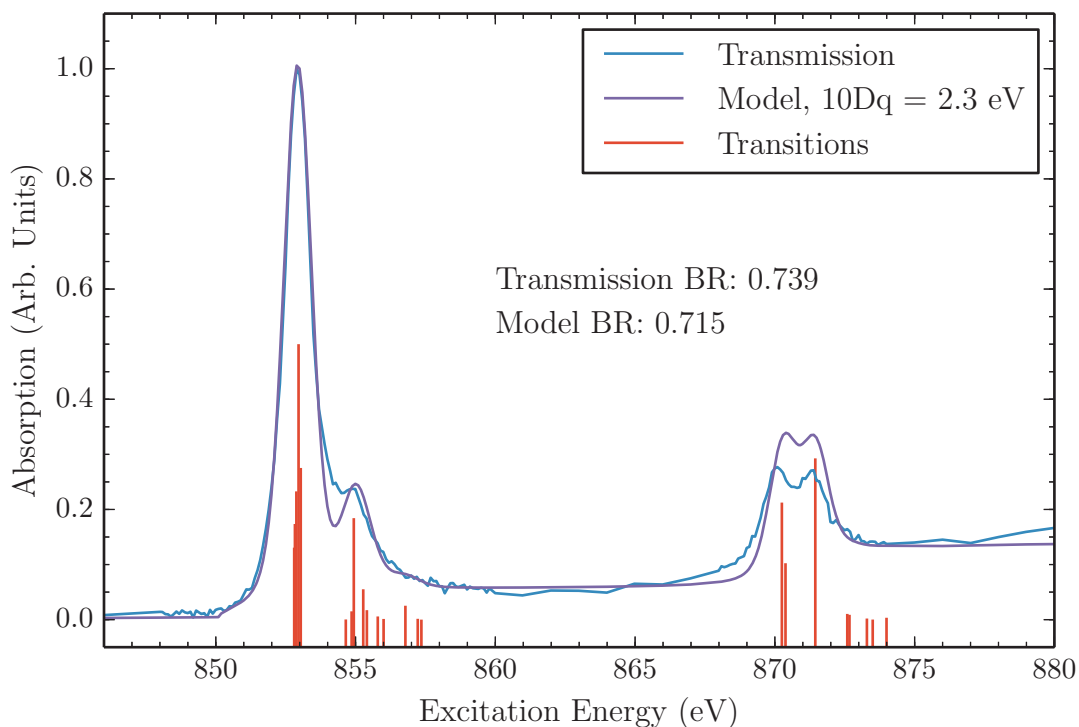


Figure 5.25: Model calculated with charge transfer multiplets fitted to Ni(acac)₂ transmission XAS data.

The XAS portion of the CTM has multiple parameters that affect the complexity of the model. In addition to the basic crystal field splitting energy $10Dq$, the program allows the inclusion/omission of the exchange Coulomb Slater integral G_{pd} and direct Coulomb Slater integrals F_{pd} and F_{dd} , as well as charge transfer (with associated parameters) [19]. When calculating wave functions for the CTM4RIXS package, charge transfer must be omitted in this version of the software. The initial XAS fitting process is an iterative search to find the best-fit parameters for the given data set. The $L_{\nu,\eta}$ lines cannot be simulated with this software at this time, so the discussion here will center around the expected XAS when windowing on the $L_{\alpha,\beta}$ lines.

For the Ni(acac)₂ transmission data, the primary parameter that is changed is the octahedral crystal field splitting energy $10Dq$. The best fit to the transmission spectrum was obtained with $10Dq = 2.3$ eV as shown in figure 5.25. The L_3 and L_2 positions are correct and the relative intensities of the bound-state transitions in each L edge are similar to the measured spectrum, however the L_2 overall intensity is higher in the model than the data. A stepwise edge jump has

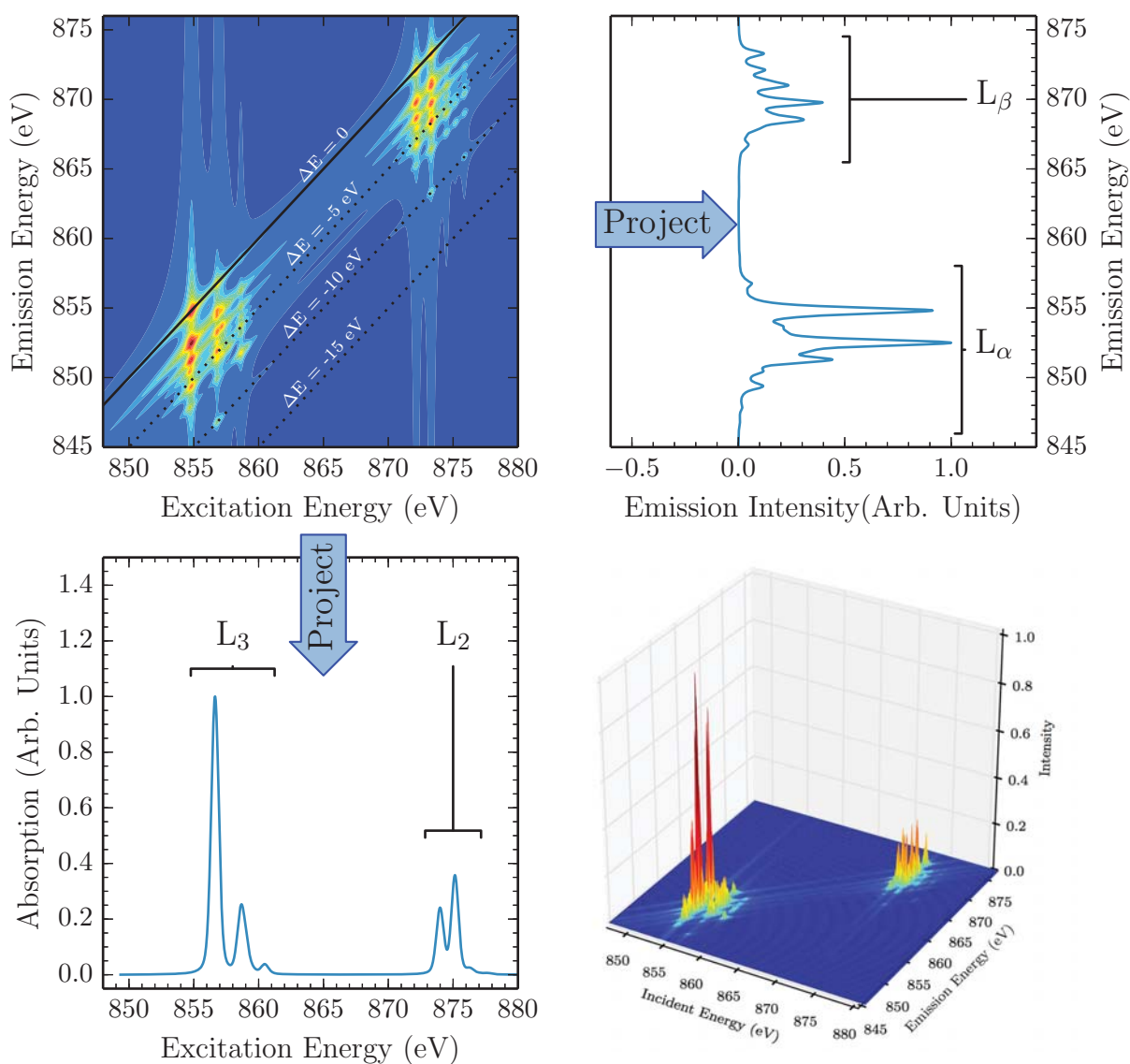


Figure 5.26: Upper Left: Full resonant inelastic x-ray scattering (RIXS)-plane for Ni(II) in octahedral symmetry with $10Dq = 2.3$ eV. The x-axis (excitation energy) is equivalent to the beamline energy while the y-axis is the energy of the scattered photons, equivalent to the emission energy in a fluorescence spectrum. Projecting the plane onto either axis by summing the columns or rows yields the total emission spectrum (upper right) or the absorption spectrum (lower left). The lower right panel is a 3D isometric view of the RIXS plane to highlight the relative intensities of the scattering peaks.

been added to the CTM model to match the data. The branching ratios obtained from the data and model both are in the high-spin range for Ni(II), above 0.7 [12].

The full RIXS calculation may be performed once the XAS model parameters have been fitted. The CTM4XAS program outputs the model wave functions for the initial, intermediate, and

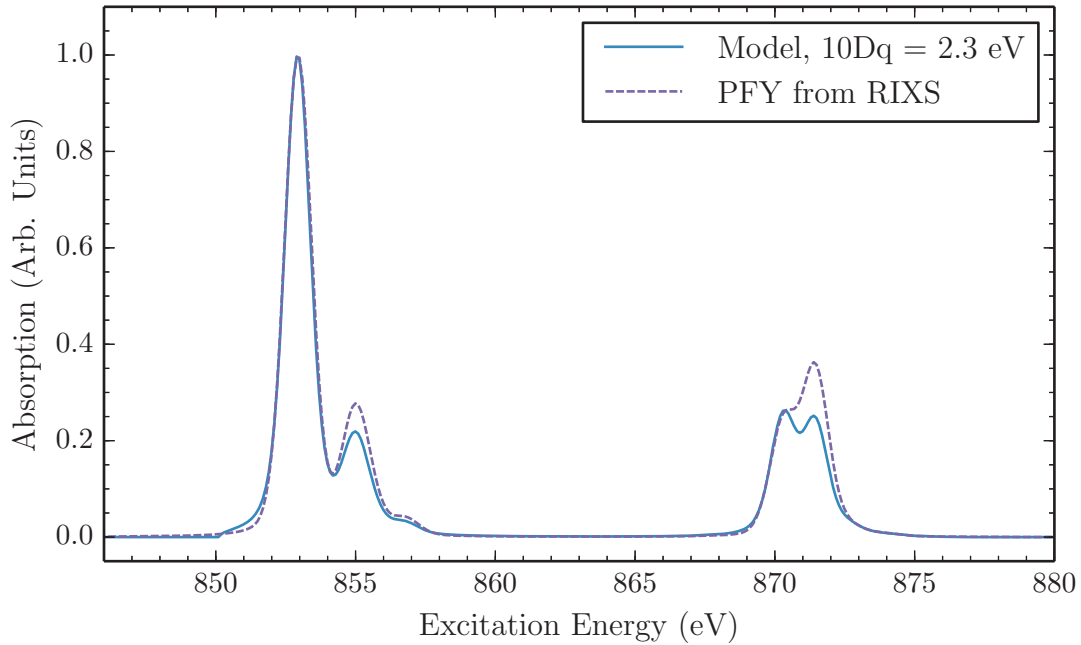


Figure 5.27: Difference between fitted XAS vs. PFY-XAS model derived from full RIXS calculation for Ni(II) with octahedral crystal field parameter $10Dq = 2.3$ eV.

final states to load into the CTM4RIXS program. Most of the parameters in the RIXS calculation involve the scattering energy ranges, broadening factors, and polarization dependence. The output is a 2D array of points containing the scattering intensity at points in the incoming/outgoing energy plane. A photon of incident energy E_i , it may be scattered through interaction with the sample into a different outgoing energy E_o with a probability determined by equation 1.11. This contrasts with the non-coherent picture of interaction, where an incoming photon is absorbed by the excitation of a core electron into a higher state, and then at some time later a decay process occurs to fill the core hole completely independently of the absorption event, generating an outgoing fluorescence photon. Mapping the probability (intensity) of the combinations of E_i and E_o gives the full RIXS plane shown in figure 5.26.

At a given E_i , the set of E_o is the emission spectrum for that element excited at that energy. This spectrum may be summed to produce the fluorescence yield at that point. Generating a projection along the incident energy by summing all the emission spectra for every excitation energy then generates the PFY-XAS from this model. This projection is shown in the lower left panel of figure 5.26. Figure 5.27 compares the PFY-XAS directly to the original CTM model used to derive the RIXS data. As seen in the measured PFY vs transmission XAS, there are differences

in bound-state transition intensities at both the L_3 and L_2 edges, with the simulated PFY data showing increased intensity at 855 and 871.5 eV over the original CTM model. These differences closely match the observed deviations between the PFY and transmission data, confirming the predictions made for this experiment.

The $\text{Mn}(\text{acac})_3$ data is not as straightforward to accurately model due to the apparent mixed oxidation state of the sample dissolved in photoresist. While the XAS has an appearance closer to Mn(II) than Mn(III), modeling it as pure Mn(II) does not produce as close a fit as with the Ni(II) data. To increase the parameter space, a fitting routine was written to optimize a linear combination of Mn(II) and Mn(III) CTM models. The 10Dq values for Mn(II) and Mn(III) were allowed to float, so that the search space is essentially a 2D array of 10Dq values for each ion. The best fit found with this method is approximately 68% Mn(II) with 10Dq = 0.8 eV, with 32% Mn(III) with 10Dq = 0 eV. When using only Mn(II), the best fit is also obtained with 10Dq = 0.8 eV. Figure 5.28 shows this best-fit Mn(II)/(III) composite model to the transmission data, with the pure Mn(II) model for comparison. While the mixed model is technically a better fit to the data, neither fully account for some features such as the transition at 636.5 eV. Better fits might be possible by adding parameters to the CTM model, but this is the best fit that is compatible with the RIXS routines.

To simplify the RIXS calculations, only Mn(II) with 10Dq = 0.8 eV was used instead of the full composite model. This provides qualitative comparison to the observed PFY variations. The full RIXS plane of Mn(II) is shown in figure 5.29. As with nickel, this calculation yields scattering intensity at each (E_i, E_o) point which may be projected onto the incident energy axis to produce the PFY-XAS simulated spectrum.

The comparison between the simulated PFY-XAS and the CTM-XAS model does not yield as much useful information as the nickel simulation, but there are still similarities to note between this model and the differences observed in the real PFY data. The feature at 638 eV is suppressed in both the simulated and real PFY versus the true XAS, while the feature at 643 eV and the entire L_2 edge around 651 eV sees an increase in intensity in the PFY data. The transition at 641 eV has similar behavior between the Si detector data and the simulated PFY, but the STJ $L_{\alpha,\beta}$ -windowed PFY data does not show this same behavior. This feature could be below the resolution of beam line 6.3.1 and is brought up in intensity by the nearby bright line at 639.5. As with the nickel data, these simulations and real measurements show a large degree of agreement

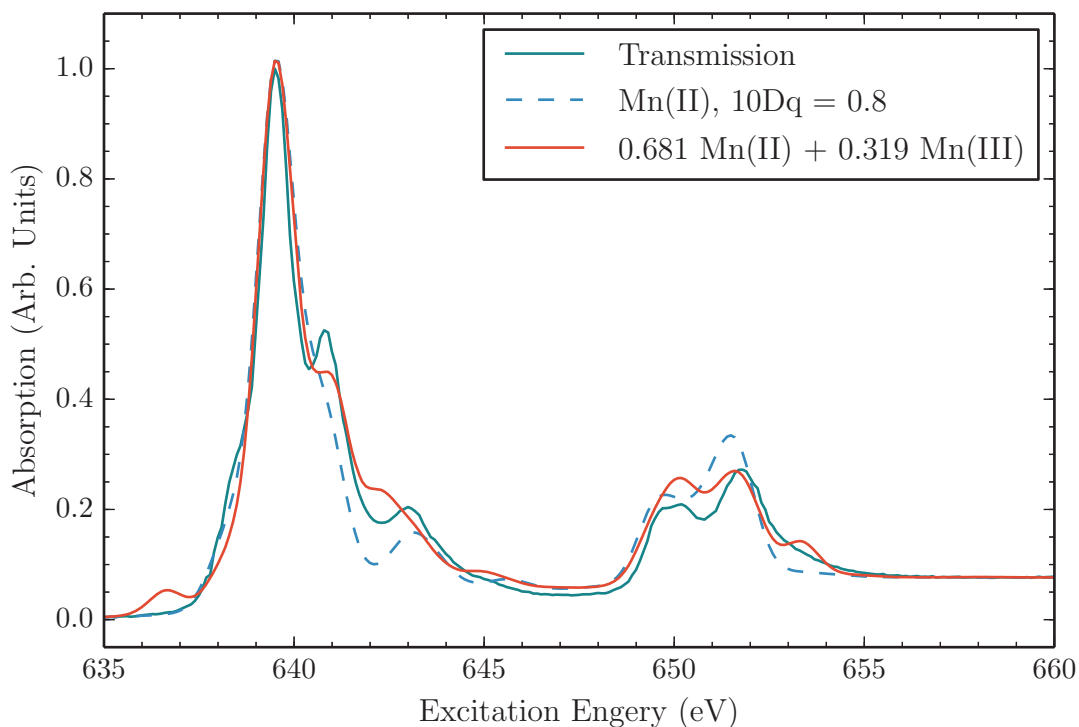


Figure 5.28: Transmission of $\text{Mn}(\text{acac})_3$ with two models. As demonstrated in the TEY spectra, the Mn is reduced from Mn(III) in the pure sample to a form of Mn(II) in the dissolved sample. The first model is pure Mn(II) with a best-fit $10Dq$ value of 0.8 eV, while the second is a mixture of Mn(II) and Mn(III).

in the difference between PFY-XAS and true XAS. In both cases, the $L_{\nu,\eta}$ -windowed PFY also shows improvement over the $L_{\alpha,\beta}$ -windowed PFY.

While it is clear that PFY-XAS measurements yield spectra with significant differences from transmission or TEY measurements, the fact that the CTM approach can successfully model these changes suggests that information such as spin-state, $10Dq$ and so forth can still be readily derived from the spectrum.

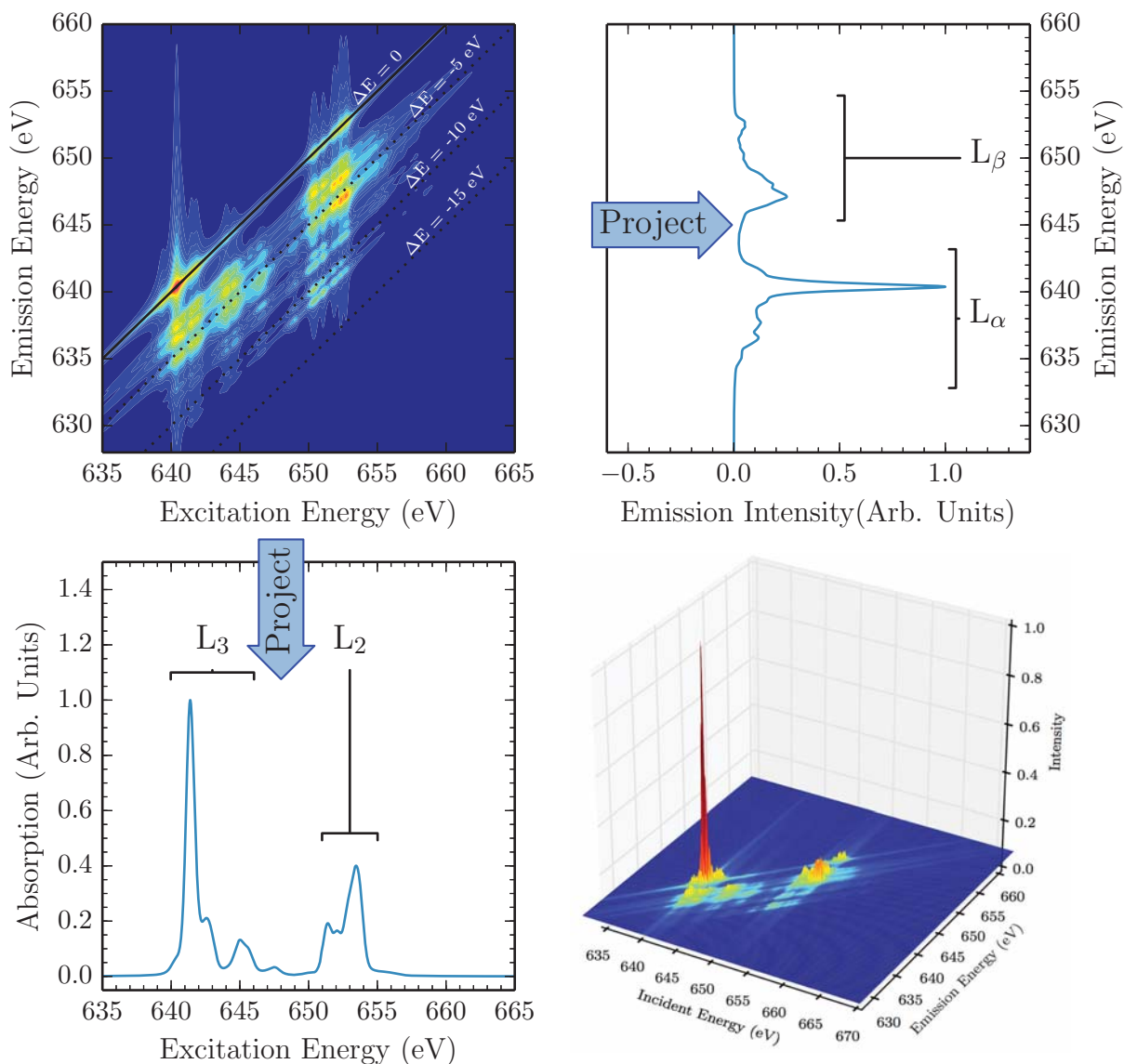


Figure 5.29: Upper Left: Full RIXS-plane for Mn(II) in octahedral symmetry with $10Dq = 0.8$ eV. The x-axis (excitation energy) is equivalent to the beamline energy while the y-axis is the energy of the scattered photons, equivalent to the emission energy in a fluorescence spectrum. Projecting the plane onto either axis by summing the columns or rows yields the total emission spectrum (upper right) or the absorption spectrum (lower left). The lower right panel is a 3D isometric view of the RIXS plane to highlight the relative intensities of the scattering peaks.

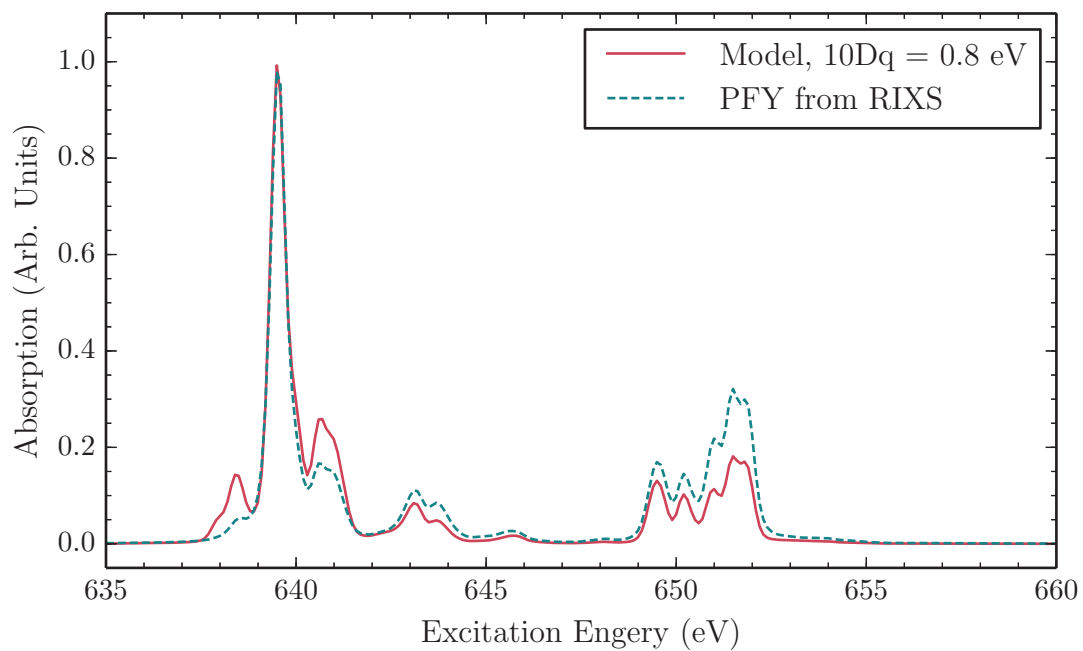


Figure 5.30: Difference between fitted XAS vs. PFY-XAS model derived from full RIXS calculation for Mn(II) with octahedral crystal field parameter $10Dq = 0.8$ eV.

References

- [1] Hoechst Japan Limited, "AZ 1500 Series Positive Photoresists," 2014. (page 114)
- [2] Clariant, "AZ 1500 Series Product Data Sheet," 2014. (page 114, 116)
- [3] CXRO, "Center for X-ray Optics: X-Ray Interactions with Matter," CXRO, 2014. [Online]. Available: http://henke.lbl.gov/optical_constants/ (page 115)
- [4] A. T. Young, E. Arenholz, J. Feng, H. Padmore, S. Marks, R. Schlueter, E. Hoyer, N. Kelez, and C. Steier, "A soft X-ray undulator beamline at the advanced light source with circular and variable linear polarization for the spectroscopy and microscopy of magnetic materials," *Surf. Rev. Lett.*, vol. 9, no. 1, pp. 549–554, 2002. [Online]. Available: <GotoISI>://000177754500085 (page 122)
- [5] A. T. Young, V. Martynov, and H. A. Padmore, "Magnetic high-resolution spectroscopy with Beamline 4.0.1-2: an elliptically polarizing undulator beamline at the Advanced Light Source," *J. Electron Spectros. Relat. Phenomena*, vol. 103, pp. 885–889, 1999. [Online]. Available: <http://www.sciencedirect.com/science/article/B6TGC-3XHH1CT-5H/2/1bd898d2e156fb5c46a41b2a5a9e9253> (page 122)
- [6] P. Nachimuthu, J. H. Underwood, C. D. Kemp, E. M. Gullikson, D. W. Lindle, D. K. Shuh, and R. C. C. Perera, "Performance Characteristics of Beamline 6.3.1 from 200 eV to 2000 eV at the Advanced Light Source," *AIP Conf. Proc.*, vol. 705, pp. 454–457, 2004. [Online]. Available: <http://scitation.aip.org/content/aip/proceeding/aipcp/10.1063/1.1757832> (page 124)
- [7] S. Mitra-Kirtley, O. C. Mullins, J. F. Branthaver, and S. P. Cramer, "Nitrogen Chemistry of Kerogens and Bitumens from X-ray Absorption Near-Edge Spectroscopy," *Energy & Fuels*, vol. 7, no. 6, pp. 1128–1134, 1993. [Online]. Available: <GotoISI>://WOS:A1993MJ57800062 (page 126)
- [8] J. van Elp, G. Peng, Z. H. Zhou, M. W. W. Adams, N. Baidya, P. K. Mascharak, and S. P. Cramer, "Nickel L-Edge X-ray Absorption Spectroscopy of *Pyrococcus furiosus* Hydrogenase," *Inorg. Chem.*, vol. 34, no. 10, pp. 2501–2504, 1995. (page 126)
- [9] H. Wang, D. S. Patil, C. Y. Ralston, C. Bryant, and S. P. Cramer, "L-edge X-ray Magnetic Circular Dichroism of Ni Enzymes: Direct Probe of Ni Spin States," *J. Electron Spectros. Relat. Phenomena*, vol. 114, pp. 865–871, 2001. (page 126)
- [10] A. Volbeda, L. Martin, C. Cavazza, M. Matho, B. W. Faber, W. Roseboom, S. P. Albracht, E. Garcin, M. Rousset, and J. C. Fontecilla-Camps, "Structural differences between the ready and unready oxidized states of [NiFe] hydrogenases," *J. Inorg. Biochem.*, vol. 10, no. 3, pp. 239–249, 2005. (page 126)
- [11] H. Wang, P. H. Ge, C. G. Riordan, S. Brooker, C. G. Woomeer, T. Collins, C. A. Melendres, O. Graudejus, N. Bartlett, and S. P. Cramer, "Counting Holes in Ni Complexes Using Integrated X-Ray L Absorption Spectra," *J. Phys. Chem. B*, vol. 102, no. 42, pp. 8343–8346, 1998. [Online]. Available: <http://pubs.acs.org/cgi-bin/pagelookup?j.phys.chem.b./102/8343http://pubs.acs.org/journals/jpcb/k/index.html> (page 126)

- [12] C. Y. Ralston, H. Wang, S. W. Ragsdale, M. Kumar, N. J. Spangler, P. W. Ludden, W. Gu, R. M. Jones, D. S. Patil, and S. P. Cramer, "Characterization of Heterogeneous Nickel Sites in CO Dehydrogenases from *Clostridium thermoaceticum* and *Rhodospirillum rubrum* by Nickel L-Edge X-Ray Spectroscopy," *J. Am. Chem. Soc.*, vol. 122, no. 43, pp. 10 553–10 560, 2000. [Online]. Available: <http://pubs.acs.org/cgi-bin/pagelookup?j.am.chem.soc./122/10553> (page 126, 142)
- [13] S. P. Cramer, F. M. F. Degroot, Y. Ma, C. T. Chen, F. Sette, C. A. Kipke, D. M. Eichhorn, M. K. Chan, W. H. Armstrong, E. Libby, G. Christou, S. Brooker, V. Mckee, O. C. Mullins, J. C. Fuggle, and F. M. F. de Groot, "Ligand Field Strengths and Oxidation States from Manganese L-Edge Spectroscopy," *J. Am. Chem. Soc.*, vol. 113, no. 21, pp. 7937–7940, 1991. (page 132)
- [14] R. Bruhn, B. Sonntag, and H. Wolff, "3p-excitation of atomic Mn; experimental evidence for the super Coster-Kronig decay," *Phys. Lett. A*, vol. 69, no. 1, pp. 9–11, Nov. 1978. [Online]. Available: <http://www.sciencedirect.com/science/article/pii/0375960178904206> (page 134)
- [15] M. O. Krause J.H., M. O. Krause, and J. H. Oliver, "Natural Widths of Atomic K and L levels, K-alpha X-ray Lines and Several KLL Auger Lines," *J. Phys. Chem. Ref. Data*, vol. 8, no. 2, pp. 329–338, 1979. [Online]. Available: <http://link.aip.org/link/?JPCRB/8/329/1> (page 134)
- [16] M. O. Krause, "Atomic radiative and radiationless yields for K and L shells," *J. Phys. Chem. Ref. data*, vol. 8, no. 2, pp. 307–327, 1979. [Online]. Available: <http://scitation.aip.org/content/aip/journal/jpcrd/8/2/10.1063/1.555594> (page 134)
- [17] E. Stavitski and F. M. F. de Groot, "The CTM4XAS program for EELS and XAS spectral shape analysis of transition metal L edges." *Micron*, vol. 41, no. 7, pp. 687–94, Oct. 2010. [Online]. Available: <http://www.ncbi.nlm.nih.gov/pubmed/20637641> (page 140)
- [18] R. D. Cowan, *The Theory of Atomic Structure and Spectra*. Berkeley: University of California Press, 1981. (page 140)
- [19] P. S. Miedema, P. Wernet, and A. Föhlisch, "State-dependent fluorescence yields through the core-valence Coulomb exchange parameter," *Phys. Rev. A*, vol. 89, no. 5, p. 052507, May 2014. [Online]. Available: <http://link.aps.org/doi/10.1103/PhysRevA.89.052507> (page 141)

Chapter 6

Summary and Outlook

6.1 Summary of Results

This dissertation describes the design, construction, and characterization of a cryogen-free, high-resolution x-ray detector based on superconducting Ta-Al tunnel junctions. The STJ detector has also been operated on beam line 6.3.1 at the ALS synchrotron and has enabled fluorescence-detected XAS of dilute metallo-organic samples.

6.1.1 STJ Detector

The first part of this work involved the design and optimization of Ta-Al-AlO_x-Al-Ta STJ detectors. Test chips with multiple sizes of detector pixels have been fabricated to evaluate the effects of different film deposition parameters, film thickness, mask layout, and edge passivation on the quality of the STJs. Ta is preferred over Nb (which was used in earlier STJ detectors) since it offers higher quantum efficiency due to the higher atomic number of Ta, and improves the intrinsic energy resolution due to the smaller superconducting gap of Ta. Optimized Ta-based STJ x-ray detectors have achieved an energy resolution between 2.5 and 5 eV for soft x-rays below 1 keV. This is an improvement by a factor of ≈ 3 to ≈ 5 over earlier Nb-based STJ x-ray detectors, and is high enough so that the measured resolution is often limited by the line width of the fluorescence x-ray source, and the intrinsic detector resolution can only be measured with a more monochromatic source such as a synchrotron beam line in direct illumination. These STJ detectors can be operated with a high energy resolution of ≈ 10 eV FWHM at count rates up to 5,000 counts/sec. At rates over 10,000 counts/sec, the resolution is reduced to ≈ 25 eV FWHM at 525 eV, still sufficient for many applications and ≈ 3 to 6 times better than typical Si or Ge detectors in this range.

To increase the solid angle for photon collection in PFY-XAS, we have fabricated 36- and 112-pixel arrays of $(208 \mu\text{m})^2$ STJs. We have shown that different pixels in the arrays are very uniform in response and performance. At the highest count rates for high-resolution operation of ≈ 10 eV FWHM, the full 112-pixel array can provide over 500,000 counts/sec. This compares favorably to a Si detector tuned for high-resolution operation, which saturates at around 50,000 counts/sec at a resolution of 100 eV FWHM at 525 eV. The combination of high count rates and high energy resolution make STJs excellent detectors for analyzing dilute samples in measurements where emission lines are closely spaced in energy.

The final phase of spectrometer development involved integration of the STJ detector arrays into a cryogen-free ADR optimized for PFY-XAS. This cryostat uses a mechanical two-stage pulse tube refrigerator for pre-cooling to 3 K, and a two-stage ADR to cool below 100 mK, and allows simple, user-friendly operation for long periods without constant attention. Being free of liquid cryogenics, the cryostat can be controlled from its computer console, allowing remote operation and diagnostics. The cryostat is designed with a 42-cm-long cold finger to insert the detector array chip into a UHV chamber close to the sample for maximum solid angle. This cold finger provides thermal shielding while allowing x-ray transmission to the detector array, and includes superconducting magnets to suppress the dc Josephson effect and Fiske mode resonances. The current design accommodates either 36- or 112-pixel arrays. The cryostat attains a base temperature of ≈ 50 mK, and currently has a hold time of ≈ 9 hours below the maximum STJ operating temperature of 300 mK. Spectrometer tests at ALS beam line 6.3.1 show that the cryogen-free detector attains an average energy resolution of 8-9 eV FWHM at 525 eV, limited by the line width of the fluorescence source and matching the performance achieved in the LLNL wet test cryostat. This confirms that the mechanical pulse tube cryocooler does not degrade the performance of the detectors, and is very encouraging for the prospect of future high-sensitivity experiments with superconducting sensors operated in conjunction with pulse tube cryocoolers.

6.1.2 Scientific Results

In the second part of this dissertation, the STJ x-ray spectrometer has been used to study deviations between PFY and transmission XAS. This work was motivated by concerns about the general assumption behind PFY-XAS is that the measured fluorescence intensity is directly proportional to the x-ray absorption by the sample. This is a reasonable assumption for XAS at the

K edges, where the final state in the fluorescence decay is spherically symmetric and has little overlap with the intermediate states. But for the transition metal L-edges, the intermediate states have higher degrees of symmetry, and the absorption process into partially-filled shells results in coherence between the absorption and emission processes that may distort the observed fluorescence ratios as a function of incident photon energy. Recent theoretical work has therefore suggested that PFY-XAS does not reproduce a correct absorption spectrum if the $L_{\alpha,\beta}$ lines are used as a measure of absorption. On the other hand, gating on the $L_{\nu,\eta}$ lines symmetric shells could reproduce the correct absorption spectrum more accurately since they originate from a completely filled and symmetric shell that does not participate in the absorption process.

To study this question experimentally required the availability of the a STJ detector with an energy resolution sufficiently high to compare the $L_{\alpha,\beta}$ -derived XAS to the $L_{\nu,\eta}$ XAS. These measurements require high resolution to separate the $L_{\alpha,\beta}$ and $L_{\nu,\eta}$ lines as well as high efficiency to collect the scarce photons from the weak $L_{\nu,\eta}$ emission. Grating spectrometers have the required energy resolution but suffer from low efficiency, while Si and Ge detectors have high efficiency but low resolution. The STJ x-ray detector is therefore essential to perform this measurement.

The other requirement for this experiment is to produce samples that can be measured in both transmission and fluorescence yield XAS. In the soft x-ray regime, this is no easy task due to the short attenuation lengths and low concentrations needed to produce PFY spectra free from concentration-related distortions. To accomplish this goal, new methods of sample fabrication were developed and optimized. Photoresist was chosen as a medium to dissolve metal-acac samples and spin them onto thin SiN windows to generate uniform films of order 1 μm thickness. These samples proved robust for both transmission and PFY techniques. With full data sets of $\text{Ni}(\text{acac})_2$ and $\text{Mn}(\text{acac})_3$ comprising transmission, TEY, and PFY windowed on different emission bands, it was shown that the various bound-state bands on the L_2 and L_3 edges can indeed be distorted when measured in fluorescence yield. Additionally, the lack of distortion when measured using the $L_{\nu,\eta}$ -PFY confirms that this is a result of coherence effects in the partially-filled 3d orbitals that participate in the absorption.

These results were corroborated using simulations based on CTM theory. By modeling the true (transmission) XAS with multiplets and using these results to simulate the PFY through full RIXS calculations, two different spectra are simulated which differ in the same manner as the measured PFY and transmission data. This offers strong support to the theory that PFY-

XAS can sometimes be distorted by coherence effects. The degree of distortion may vary and will not always significantly modify the observed spectrum, but because some cases will show large deviations, this is an affect that should be accounted for in all measurements to ensure proper controls, as well as in subsequent analysis of the spectroscopic line shapes by CTM or DFT calculations.

6.2 Outlook

6.2.1 Future STJ Detector Improvements

The performance of this STJ x-ray spectrometer is more than sufficient for the experiments in this dissertation. Still, as it is the first prototype of a Ta-based cryogen-free STJ x-ray detector, there is room for improvement. The first improvement will be to the cold finger to increase the cryostat hold time from the current ≈ 9 hours to > 24 hours per ADR cycle. The first cold finger design was limited by the fact that the snout shields and cold finger need to be installed through the snout port in the lower vacuum case. This places stringent requirements on the way the shields are mounted and heat sunk, and the space for various components is limited. Future cold finger designs will be changed so that they may be installed prior to the radiation shields and the vacuum case. The main areas that need to be modified for this purpose are the lower radiation shields and the vacuum case. Changing the cold finger interface will simplify the installation procedures and improve the thermal performance of the snout shields. To further improve their thermal performance, several parts will be re-manufactured from gold-plated OFHC copper, including the 60 K snout shield, detector magnet bobbins, and covers for the detector suspension. Improving their performance will increase the hold time of the ADR to > 24 hours per cycle and improve the duty cycle and efficiency of the detector.

Another improvement is to the thickness of the IR-blocking windows. The current window design has 350 nm of polyimide coated with 100 nm Al, values chosen conservatively for robustness of the film and strong IR-blocking capabilities without pinholes. However, the transmission of these windows falls to less than 10 % below 500 eV, limits the detector efficiency for very soft x-rays. The Al absorption dominates below 300 eV, while the Kapton dominates above 300 eV. Thinning the Kapton from 350 to 200 nm would improve the transmission by a factor of 2 above 300 eV, while thinning the aluminum adds another improvement of about 50 %. Additional improvements to 20 nm of Al and 100 nm of Kapton are possible. For samples between 300 and 600 eV, free-standing 100 nm Al might be a better choice, at the cost of greatly increased

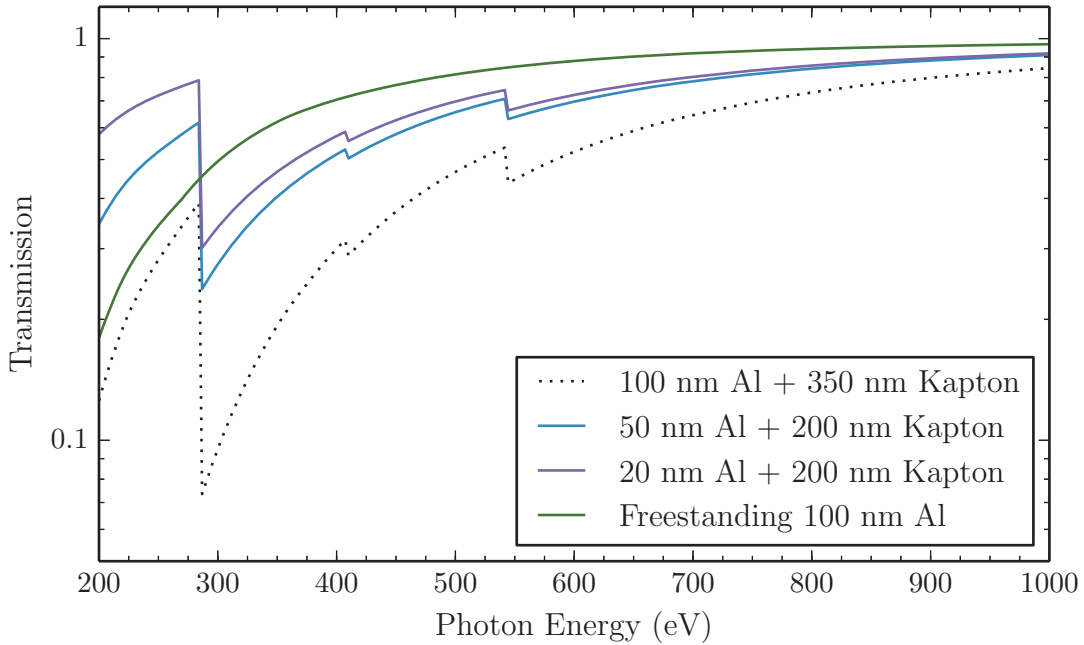


Figure 6.1: Comparison of transmissivities of different filter designs. The plotted transmission is for 1 filter [1].

fragility. This energy range includes K emission from C, N, and O, and L emission from Ti, V, and Cr. For emission below 200 eV, the better choice would be the Al on Kapton but with much thinner Al than the current windows. Elements with emission below 300 eV include B K, S L, and Mo M. For any situation, it is clear that thinner windows could improve the performance and sensitivity of the instrument by a significant factor (figure 6.1).

The instrument in these experiments used a 36-pixel STJ array chip. This choice was made based on the availability of a single 32-channel XIA preamplifier card, and the lower number of wires needed to operate the array to reduce the thermal load on the detector rod. The cryostat is designed to accommodate the full 112-pixel array, so installing the larger array with its extra wiring would immediately increase the available detector area by a factor of 3. This requires the acquisition and programming of additional preamplifier cards, with four cards needed for the full 112-pixel array. Reworking the end of the cold finger to bring the array chip closer to the end could also net a greater solid angle, perhaps up to about 2 times over the current design. Solid angle improvements are a straightforward way to increase the detection sensitivity of the instrument.

A more technical efficiency improvement is to increase the thickness of the top Ta absorber to

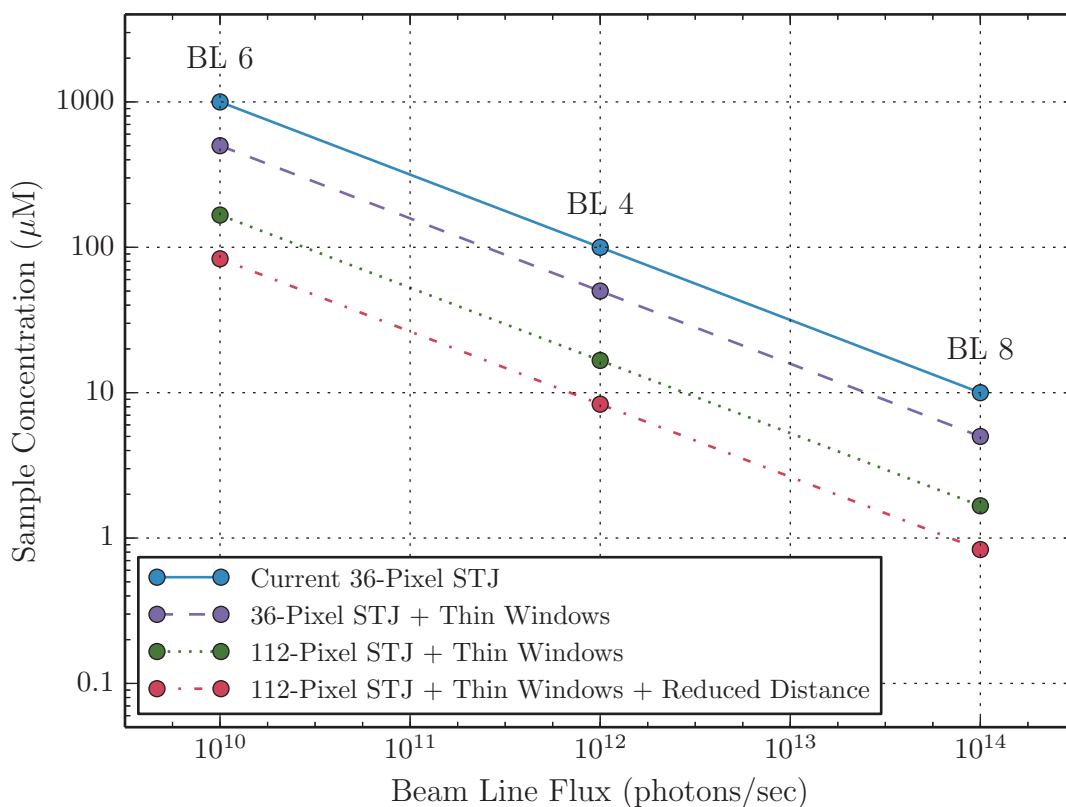


Figure 6.2: Effect of STJ and beam line improvements on experiment sensitivity. The x-axis plots the beam line flux[2, 3], while the y-axis is a measure of the typical sample concentration limit for an experiment. Measurements in this work were made at the ALS beam line 6 with a flux of $\approx 10^{10}$ photons/sec on samples with concentration on the order of 1,000 μM . The different series are generated by combining future efficiency improvements.

reduce or eliminate the line-splitting artifact. For the current array, this artifact may be removed by discriminating against base-layer events based on pulse rise time differences, but this reduces the number of signal photons. If the top Ta is thicker so that it absorbs close to 100 % of incident photons, this artifact is eliminated while the measured signal is increased. Detection efficiency at higher energies (e.g. above 2 keV) would also greatly improve.

Figure 6.2 shows the net result of combining these improvements to increase sensitivity. The values plotted are order of magnitude estimates and are based upon the spectrometer sensitivity measure for this dissertation. The current 36-pixel array was used to characterize samples with a metal concentration of $\approx 1 \text{ mM}$ ($=1,000 \mu\text{M}$) at the fairly weak beam line 6 of the ALS. The projections are plotted by combining future instrument improvements with increases in photon flux at beam lines brighter than 6.3.1 at the ALS, such as an undulator beam line. Improving the

STJ detector and operating it at brighter beam lines will improve the sensitivity to below 1 μM . The high count-rates this detector can withstand are not utilized on a dimmer bend magnet beam line, and the gains that can be made in sample sensitivity are very compelling.

6.2.2 Scientific Outlook

The metal-acac samples studied in this work are important model compounds, but they are well-understood scientifically so that little new information is to be gained. They are well-suited for the demonstration experiments in this dissertation, as prior studies exist to compare the results to. The techniques and instrumentation developed in this work can now be used for PFY-XAS on more complicated and novel samples. Examples that could benefit are metalloproteins such as Ni-Fe hydrogenase, catalytic materials, and environmental samples such as low-concentration Cr contamination. Previous studies required higher sample concentrations and therefore proteins had to be dried into a film. These studies are now possible with samples as a frozen solution or liquid in a flow cell, where they more closely resemble their state in a biological system. Another application requiring high-sensitivity are analytic reactor cells, where a chemical reaction is monitored in a sample cell as it proceeds in real time. The low concentrations and short time scales required for this work demand high photon fluxes and excellent detection efficiency.

This work on the deviations between PFY and transmission XAS does not invalidate prior work on transition metal L-edges, but rather encourages further investigation and modeling of the prior results to determine the extent this phenomenon may have affected the results. Future studies of this class of compounds should be undertaken with this fact in mind. This STJ detector, with its high resolution and great ease of operation for a detector of its class, has proven to be an excellent tool to perform this and future work at the synchrotron.



Figure 6.3: The author analyzes high-resolution x-ray spectra with the STJ detector.

References

- [1] CXRO, "Center for X-ray Optics: X-Ray Interactions with Matter," CXRO, 2014. [Online]. Available: http://henke.lbl.gov/optical_constants/ (page 154)
- [2] A. T. Young, E. Arenholz, J. Feng, H. Padmore, S. Marks, R. Schlueter, E. Hoyer, N. Kelez, and C. Steier, "A soft X-ray undulator beamline at the advanced light source with circular and variable linear polarization for the spectroscopy and microscopy of magnetic materials," *Surf. Rev. Lett.*, vol. 9, no. 1, pp. 549–554, 2002. [Online]. Available: [GotoISI://000177754500085](http://www.got ISI.com/000177754500085) (page 155)
- [3] P. Nachimuthu, J. H. Underwood, C. D. Kemp, E. M. Gullikson, D. W. Lindle, D. K. Shuh, and R. C. C. Perera, "Performance Characteristics of Beamline 6.3.1 from 200 eV to 2000 eV at the Advanced Light Source," *AIP Conf. Proc.*, vol. 705, pp. 454–457, 2004. [Online]. Available: <http://scitation.aip.org/content/aip/proceeding/aipcp/10.1063/1.1757832> (page 155)

LIST OF ABBREVIATIONS

ac	alternating current.
acac	acetylacetonate.
ADR	adiabatic demagnetization refrigerator.
AlO_x	aluminum oxide.
ALS	Advanced Light Source.
ANL	Argonne National Laboratory.
APS	Advanced Photon Source.
bcc	body-centered cubic.
BCS	Bardeen, Cooper, and Schrieffer.
BT	backtunneling.
CFT	crystal field theory.
COM	center of mass.
CTM	charge transfer multiplets.
CXRO	Center for X-ray Optics.
DAC	digital-to-analog converter.
dc	direct current.
DFT	density functional theory.
DOS	density of states.
DT	direct tunneling.
EMI	electromagnetic interference.
EPU	elliptically polarizing undulator.
EXAFS	extended x-ray absorption fine structure.
EY	electron yield.
FAA	ferric ammonium alum.
FEA	finite elements analysis.
FET	field effect transistor.
FT	forward tunneling.
FTIR	Fourier-transform infrared.
FWHM	full width at half maximum.
FY	fluorescence yield.
GGG	gadolinium gallium garnet.
HPGe	high-purity germanium.
HTS	high-temperature superconductor.
IR	infrared.
LBNL	Lawrence Berkeley National Laboratory.
LCAO	linear combination of atomic orbitals.
LLNL	Lawrence Livermore National Laboratory.
NIN	normal-insulator-normal.
OD	outer diameter.
OFHC	oxygen-free high-conductivity.
PCB	printed circuit board.
PDB	Protein Data Bank.
PEY	partial electron yield.

PFY	partial fluorescence yield.
PGMEA	propylene glycol monomethyl ether acetate.
PHA	pulse height analyzer.
PID	proportional-integral-derivative.
qp	quasiparticle.
RCSB	Research Collaboratory for Structural Bioinformatics.
RF	radio frequency.
RIXS	resonant inelastic x-ray scattering.
RT	reverse tunneling.
RTD	resistive temperature detector.
RuOx	ruthenium oxide.
SBIR	Small Business Innovation Research.
SDD	silicon drift detector.
SIN	superconductor-insulator-normal.
SiN	silicon nitride.
SIS	superconductor-insulator-superconductor.
SLS	Swiss Light Source.
SQUID	superconducting quantum interference device.
SSD	solid state detector.
STJ	superconducting tunnel junction.
TEY	total electron yield.
TFY	total fluorescence yield.
UHV	ultra-high vacuum.
UV/Vis	ultraviolet/visible.
VOC	volatile organic compound.
XANES	x-ray absorption near-edge spectroscopy.
XAS	x-ray absorption spectrum.
XAS	x-ray absorption spectroscopy.
XES	x-ray emission spectroscopy.
XMCD	x-ray magnetic circular dichroism.